University of Alberta

Development of a Meteorologic, Hydrologic, and Climatic Framework to Study the Impacts of Environmental Change on Flows in Large River Basins

by

Ernst Nicolas Kerkhoven 

A thesis submitted to the Faculty of Graduate Studies and Research
in partial fulfillment of the requirements for the degree of

Doctor of Philosophy

in

Water Resources Engineering

Department of Civil and Environmental Engineering

Edmonton, Alberta
Fall 2008

Your file Votre référence
ISBN: 978-0-494-46344-4
Our file Notre référence
ISBN: 978-0-494-46344-4

Dedication

To Matheus and Hans, who came after this was started, and to Rudolf Johannes, who left before it was done.

Abstract

A modeling framework for determining the effects of long-term environmental change on the hydrology of large river basins was developed by drawing on meteorologic, hydrologic, and climatic modelling approaches and data sources.

A land surface model, ISBA, was modified to statistically account for sub-grid heterogeneity of soil moisture and rainfall. Simulations in the Athabasca River Basin (ARB) demonstrated that these modifications improve streamflow predictions despite requiring fewer parameters.

The projected changes to climate in from GCMs were applied to the ARB and Fraser River Basin (FRB). Winter snowpacks consistently declined due to a shortened snowfall season and increases in sublimation leading to decreased flows in the summer months. In the ARB, results indicate that streamflows will decline by an average of 41% by the end of the 21st century. Although the wetter and milder FRB was found to be less sensitive on changes to the snowpack, minimum flows are expected to decline by 17% by the end of the century.

The potential effect of vegetation response to climatic change was investigated by applying the predictions of MAPSS under GCM climate simulations. The dominant mechanism was a tendency for increases in grassland area to result in increased snow packs and spring runoff. This can represent a positive feedback mechanism under conditions were warmer and drier climates encourage forest growth at the expense of grassland, but this would be inconsistent with observed behaviour where a negative feedback on streamflow occurs.

ARB and FRB hydrographs were analysed using multifractal detrended fluctuation analysis. The generalized multifractal cascade model could closely model the hydrographs in both river basins. This multifractal model was used to generate artificial time series that had the same periodic, statistical, and fractal properties as the simulated hydrographs. The multifractal hydrographs featured significant departures from the behaviour of long-term statistical independence resulting in a wider range flows over a 30-year time scale than other methods predict.

Acknowledgements

I would like to thank Dr. Thian Gan for his supervision and guidance of this work, and Dr. Gerhard Reuter for his contributions to my work with MM5. I am also grateful to Florence Habets and Aaron Boone at Météo France for providing the ISBA code, and technical support. The University of Alberta, GEWEX/MAGS, the Canadian Water Network, and Alcan Canada provided funding for this research. Kyoto University provided computer resources for early work with MM5.

The archived forecast data from Environment Canada's GEM model and the Peace/Athabasca Digital Elevation Model were provided by GEWEX/MAGS, Météo France provided the Ecoclimap land surface data set, and ECMWF provided the ERA-40 atmospheric re-analysis dataset. Without these datasets, none of this work would have started, let alone completed.

Finally, I wish to thank Eden Koster for the countless sacrifices she made that allowed me to focus on my work when I needed to.

Table of Contents

CHAPTER ONE: INTRODUCTION 1

CHAPTER TWO: LITERATURE REVIEW 5
2.1 Land Surface Models 5
2.2 Project for the Intercomparison of Land-surface Parameterization Schemes (PILPS) 6
2.2.1 PILPS Phase One 7
2.2.2 PILPS Phase 2 9
2.2.3 Summary of the PILPS studies 14
2.3 Land Surface Modelling under the Canadian GEWEX-MAGS Program 16
2.4 Interactions Soil Biosphere Atmosphere Land Surface Model 17
2.4.1 Turbulent Heat Fluxes in ISBA 18
2.4.2 Runoff and Drainage in ISBA 20
2.4.3 Snow in ISBA 22
2.5 Climate Change Science 23
2.6 Bibliography 30

CHAPTER THREE: A MODIFIED ISBA SURFACE SCHEME FOR MODELING THE HYDROLOGY OF ATHABASCA RIVER BASIN WITH GCM-SCALE DATA 43
3.1 Introduction 43
3.2 Research Objectives and Methodology 46
3.3 Athabasca River Basin (ARB) 51
3.4 Hydrological Routing 52
3.5 Modification to ISBA's Sub-grid Heterogeneity Runoff Scheme 53
3.6 Discussion of Results 60
3.6.1 GEM results 60
3.6.2 ERA-40 Results 62
3.6.3 Results of ERA-40 downscaled with respect to GEM Data 65
3.7 Summary and Conclusions 68
3.8 Bibliography 85

CHAPTER FOUR: DIFFERENCES IN THE POTENTIAL HYDROLOGIC IMPACT OF CLIMATE CHANGE TO THE ATHABASCA AND FRASER RIVER BASINS LOCATED ON THE LEEWARD AND WINDWARD SIDES OF THE CANADIAN ROCKY MOUNTAINS RESPECTIVELY 92
4.1 Introduction 92
4.2 Study Basins 93
4.3 Research Methodology 95
4.4 Discussion of Results 98
4.4.1 Athabasca River Basin 98
4.4.2 Fraser River Basin 102
4.4.3 Generalized Equations 107

4.5 Summary and Conclusions 111
4.6 Bibliography 128

CHAPTER FIVE: DIFFERENCES IN THE POTENTIAL HYDROLOGIC IMPACT OF CLIMATE CHANGE TO THE ATHABASCA AND FRASER RIVER BASINS WITH AND WITHOUT CONSIDERING THE EFFECTS OF SHIFTS IN VEGETATION PATTERNS CAUSED BY CLIMATE CHANGE .. 132
5.1 Introduction 132
5.2 Research Methodology 137
5.3 Discussion of Results 141
5.4 Summary and Conclusions 147
5.5 Bibliography 158

CHAPTER SIX: COMPARING FOUR SOURCES OF UNCONDITIONAL UNCERTAINTY IN SIMULATED RIVER FLOWS USING STATISTICAL METHODS AND MULTIFRACTAL ANALYSIS FOR TWO MACRO-SCALE RIVER BASINS TO THE EAST AND WEST OF THE CANADIAN ROCKIES 163
6.1 Introduction 163
6.2 Multifractal Analysis 167
6.2.1 Multifractal Formalism 167
6.2.2 Multifractal Detrended Fluctuation Analysis 168
6.2.3 Generalized Multifractal Cascade Model 169
6.3 |Research Methodology 172
6.3.1 Classical Statistics Method 173
6.3.2 Hurst Exponent Method 174
6.3.3 Autocorrelation Method 174
6.3.4 Multifractal Method 175
6.4 Results 176
6.4.1 Observed and Simulated Historical River Flows 176
6.4.2 SRES Climate Scenarios: Fractal Behaviour 180
6.4.3 Four Methods for Estimating Unconditional Uncertainty 181
6.4.4 Model Structure Uncertainty 182
6.4.5 SRES Climate Scenarios Uncertainty 184
6.5 Summary and Conclusions 186
6.6 Bibliography 204

CHAPTER SEVEN: CONCLUSIONS AND RECOMMENDATIONS 207
7.1 Conclusions 207
7.2 Recommendations 212

APPENDIX A: DERIVATIONS OF EQUATIONS 3.2, 3.6, 3.17, 3.22, AND 6.19 214
Derivation of Equation 3.2 214
Derivation of Equation 3.5 215
Derivation of Equation 3.6 215
Derivation of Equation 3.17 216
Derivation of Equation 3.22 220

Derivation of Equation 6.19 221

APPENDIX B: A COMPARISON OF CUMULUS PARAMETERIZATION SCHEMES IN A NUMERICAL WEATHER PREDICTION MODEL FOR A MONSOON RAINFALL EVENT 223
B.1 Introduction 223
B.2 Methodology and Model Descriptions 226
B.2.1 Methodology 226
B.2.2 Cumulus Parameterization 228
B.2.3 Anthes-Kuo Scheme 230
B.2.4 Betts-Miller Scheme 231
B.2.5 Grell Scheme 231
B.2.6 Fritsch-Chappell Scheme 232
B.2.7 Kain-Fritsch Scheme 233
B.3 Synoptic Situation 234
B.4 Comparison between Predicted and Observed Rainfall 235
B.4.1 Evaluation of Precipitation Simulation 236
B.4.2 Using Different CP Schemes in each Domain 241
B.5 Conclusion 244
B.6 Bibliography 257

List of Tables

Table 3.1 - Calibration and verification errors. All errors are relative to mean observed flow.....71

Table 4.1 - Changes in flow statistics for Athabasca and Fraser River Basins from 2070–2099 with respect to the 1961–1990 climate normal.....114

Table 5.1 - Relationshipa between MAPSS and Ecoclimap Vegetation Classes.....150

Table 6.1 - Estimated 95% confidence limits for observed and simulated stream flows in the Athabasca and Fraser River Basins based on classical, Hurst, Autocorrelation, and Multifractal approaches.....195

Table 6.2 - 95% confidence limits associated with uncertainty in 30-year average flow due to the hydrologic model, SRES scenario, GCM selection, and multifractal sample uncertainty. Quantities are expressed in terms of the percentage difference with respect to the mean flow.....203

Table B.1 - Summary of Cumulus Parameterization Schemes used in this study.....247

Table B.2 - Error Statistics for simulations using the same CP scheme in both domains.....252

Table B.3 - Summary of results based on Error Index and the ratio of total simulated to total observed rainfall over each of three rainfall phases.....253

List of Figures and Illustrations

Figure 3.1 - DEM derived extent of the Athabasca River below Fort McMurray Basin with GEM grid (dashed lines) and ERA-40 grid (solid circles) overlaid. 72

Figure 3.2 - Modified ISBA Runoff mechanism. ΔS is the quantity of new soil moisture expressed in terms of additional soil water retention. 73

Figure 3.3 - ISBA/GEM Calibration (1995-1998) and verification (1998-2001) Hydrographs 74

Figure 3.4 - Observed and OISBA/ERA-40 Simulation Hydrographs 75

Figure 3.5 - Observed and MISBA/ERA-40 Simulation Hydrographs 76

Figure 3.6 - Monthly mean flows and monthly standard deviation of observed flows and (a) OISBA/ERA-40 and (b) MISBA/ERA-40 simulations 77

Figure 3.7 - Observed and OISBA/ERA-40 simulation flows for (a) daily mean flows and (b) standard deviation of flows; and observed and MISBA/ERA-40 simulation flows for (c) daily mean flows and (d) standard deviation of flows 78

Figure 3.8 Annual frequency plots of observed flows and OISBA/ERA-40 simulation for (a) mean annual flow, (b) minimum annual flow, and (c) maximum annual flow; and the same for MISBA/ERA-40 simulation for (d) mean annual flow, (e) minimum annual flow, and (f) maximum annual flow 79

Figure 3.9 - Observed and OISBA/ERA-40/GEM Simulation Hydrographs 80

Figure 3.10 - Observed and MISBA/ERA-40/GEM Simulation Hydrographs 81

Figure 3.11- Monthly mean flows and monthly standard deviation of observed flows and (a) OISBA/ERA-40/GEM and (b) MISBA/ERA-40/GEM simulations 82

Figure 3.12 - Observed and OISBA/ERA-40/GEM simulation flows for (a) daily mean flows and (b) standard deviation of flows; and observed and MISBA/ERA-40/GEM simulation flows for (c) daily mean flows and (d) standard deviation 83

Figure 3.13 - Annual frequency plots of observed flows and OISBA/ERA-40/GEM simulation for (a) mean annual flow, (b) minimum annual flow, and (c) maximum annual flow; and the same for MISBA/ERA-40/GEM simulation for (d) mean annual flow, (e) minimum annual flow, and (f) maximum annual flow 84

Figure 4.1 – Changes in a) annual precipitation (ΔP), b) annual runoff, and c) runoff coefficient against changes in annual temperature (ΔT) in the Athabasca River Basin predicted by SRES climate scenarios 115

Figure 4.2 - Mean annual runoff verses mean annual maximum Snow Water Equivalent (SWE) in the Athabasca River Basin. 116

Figure 4.3 - Mean daily flow rates for 2070–2099 for a) A2 Climate Scenarios and b) CGCM2 climate scenarios and historical flow rates for the 1961–1990 climate normal in the Athabasca River Basin.. 117

Figure 4.4 - Observed and simulated hydrographs for Fraser River at Hope, (a) ERA40 simulation and (b) ERA40-GEM simulation 118

Figure 4.5 - Observed and ERA40-GEM simulated frequency plots for the Fraser River at Hope, (a) mean annual flow rate, (b) minimum annual flow rate, and (c) maximum annual flow rate. 119

Figure 4.6 - Observed and ERA40-GEM 365-day moving average flow rates for the Fraser River at Hope. 120

Figure 4.7 – Projected (a) temperature and precipitation changes and (b) mean annual runoff changes relative to the historical 1961 to 1990 baseline in the Fraser River Basin according to 18 SRES climate scenarios. The blue, green, and red curves envelope the 2010-2039, 2040-2069, and 2070-2099 simulations respectively. 121

Figure 4.8 - Mean monthly flows in the Fraser River at Hope for 2070-2099 of various climate scenarios: (a) A1FI, (b) A2, (c) B2, and (d) B1. 122

Figure 4.9 - Mean annual maximum snow pack in the Fraser River Basin versus (a) change in mean annual temperature and (b) mean winter temperature. The blue, green, and red curves envelope the 2010-2039, 2040-2069 and 2070-2099 simulations respectively 123

Figure 4.10 – (a) Mean annual maximum flow versus and mean annual snow pack and (b) mean annual minimum flow rate versus mean summer precipitation in the Fraser River Basin. The blue, green, and red curves envelope the 2010-2039, 2040-2069 and 2070-2099 simulations respectively. 124

Figure 4.11 - Generalized relationships in the Athabasca River Basin between mean annual runoff, mean annual minimum flow, and mean annual maximum flow; and precipitation and temperature temperature changes. P_{rain} and P_{snow} indicate annual rainfall and snowfall in mm, respectively. ΔT_s and ΔT_w indicate changes in summer and winter temperatures in °C, respectively. 125

Figure 4.12 - Generalized relationship in the Fraser River Basin between mean annual runoff, mean annual minimum flow, and mean annual maximum flow; and precipitation and temperature temperature changes. P_{rain} and P_{snow} indicate annual rainfall and snowfall in mm, respectively. ΔT_s and ΔT_w indicate changes in summer and winter temperatures in °C, respectively. 126

Figure 4.13 - Projected changes in annual precipitation over North America for 2070-2099 according to the (a) HadCM3 A2 and (b) CGCM2 A2 scenarios. Taken from Canadian Climate Impacts and Scenarios (CCIS) Project. 127

Figure 5.1 – Schematic diagram of the MAPSS water budget model (adapted from Neilson, 1995). 151

Figure 5.2 - Relationships between changes in temperature and (a) precipitation and (b) snow water equivalent (SWE); and changes in runoff and changes in (c) precipitation and (d) SWE in the Athabasca (blue) and Fraser (red) River Basins based on the predictions of seven GCMs for SRES B2 climate scenarios using Ecoclimap vegetative cover. 152

Figure 5.3 - MAPSS equilibrium vegetation types under (a) current conditions, (b) GFDL FAR, (c) GISS FAR, (d) HadCmS SAR, (e) OSU FAR, and (f) UKMO FAR. 153

Figure 5.4 - Changes in Ecoclimap vegetation cover types in the (a) Athabasca and (b) Fraser River Basins based on MAPSS model simulations for current and climate change scenarios. 154

Figure 5.5 - Changes in runoff (triangles) and Snow Water Equivalent (SWE, circles) as they relate to changes in (a) Grassland forest area and (b) Conifer Forest , (c) Broadleaf Forest area and (d) Rocks and Bare Soil area in the Fraser (red) and Athabasca (blue) River Basins, based on climate change scenarios using MAPSS vegetative cover. Each symbol represents the average of five SRES GCM climate projections. 155

Figure 5.6 - Changes in runoff as they relate to changes in Snow Water Equivalent (SWE) in terms of (a) percent change and (b) absolute change, based on climate change scenarios using MAPSS vegetative cover. Symbol shape indicates the SRES GCM climate projection and colour indicates the MAPSS vegetation shift scenario. 156

Figure 5.7 - Changes in (a) runoff and (b) SWE with a vegetation shift (averaged across the five MAPSS scenarios) and without a vegetation shift (Ecoclimap current conditions). 157

Figure 6.1 - A typical multifractal spectrum indicating the support dimension, f_{max}, and the multifractal strength, $\Delta\alpha$ (Feder, 1988). 189

Figure 6.2 - 365-day moving averages of observed and simulated flows in the Athabasca and Fraser River Basins. 190

Figure 6.3 - Variation of standard deviation with respect to scale for the observed and simulated historical flows in the Fraser and Athabasca River Basins. Straight lines indicate the line of best fit. 191

Figure 6.4 - Autocorrelation functions of the 365-day moving average of the observed and simulated historical flows in the Athabasca and Fraser River Basins. 192

Figure 6.5 - Generalized Hurst exponents of the observed and simulated historical flows in the Fraser (a) and Athabasca (b) River Basins. Values of parameters a and b indicate the parameters for the best fitting multifractal cascade (lines). 193

Figure 6.6 - Multifractal spectra of the observed and simulated historical flows in the Fraser (a) and Athabasca (b) River Basins. Values of parameters a and b indicate the parameters for the best fitting multifractal cascade (lines).....194

Figure 6.7 - Cumulative probability distributions of observed and fractally generated 365-day moving average flows for the Athabasca and Fraser River Basins 196

Figure 6.8 - The relationship between multifractal strength and change in (a) mean annual flow, (b) mean annual temperature, (c) mean annual precipitation, and (d) mean annual maximum Snow Water Equivalent for 54 SRES climate scenarios in the Athabasca and Fraser River Basins. 197

Figure 6.9 - The relationship between Snow Water Equivalent and the change in the change in January flows for 54 SRES climate scenarios in the Athabasca and Fraser River Basins.....198

Figure 6.10 - Upper and lower 95% confidence bounds for 30-year mean flow for 54 SRES climate scenarios in the Athabasca and Fraser River Basins. 199

Figure 6.11 - Upper and lower 95% confidence bounds for annual mean flow for 54 SRES climate scenarios in the Athabasca and Fraser River Basins.Figure.....200

Figure 6.12 – Predictions of mean annual mean flow for historical conditions (black circle) and for 54 SRES climate scenarios (coloured circles) in the Athabasca River Basin for the MISBA and SAC-SMA models. 201

Figure 6.13 – Generalized relationship describing the difference between the predictions of the SAC-SMA and MISBA models for mean annual runoff (ΔQ) due to climatic change in the Athabasca River Basin. P and ΔT indicate the average annual precipitation and the change in mean annual temperature in the basin. 202

Figure B.1 - Location of MM5 model domains.....248

Figure B.2 - (a) 200 mb wind field and (b) the 850 mb wind field at 0000 UTC 28 June 1998. 'L' and 'H' indicates the locations of 500 mb cyclones and anti-cyclones, respectively. 249

Figure B.3 - (a) 200 mb wind field and (b) the 850 mb wind field at 0000 UTC 28 June 1998. 'L' and 'H' indicates the locations of 500 mb cyclones and anti-cyclones, respectively. 250

Figure B.4 - Location of rainfall gauge stations (squares) in the analysis region. 251

Figure B.5 - Rainfall patterns for (a) Observed station data, (b) AK-AK, (c) BM-BM, (d) FC-FC, (e) GR-Gr, (f) KF-KF, (g) FC-BM, and (h) BM-Gr. Heavy rainfall (hours 24-36) is on the left, moderate rainfall (hours 36-48) is in the middle, and light rainfall (hours 72-84) is on the right. Heavy and moderate rainfall contours are at 10 mm intervals and light rainfall contours are at 5 mm intervals. 256

List of Symbols, Abbreviations and Nomenclature

Symbol	Definition
α	Hölder exponent (Chapter 6)
	Moisture correction factor (Chapter 8)
β	Xinanjiang distribution parameter (Chapter 3)
	Power spectrum slope (Chapter 6)
Γ	Gamma function
γ	Lower incomplete gamma function
ε	Confidence interval variable
λ	Brooks-Corey pore size index
ρ	Box probability
σ^k	Standard deviation at scale k
τ	Scaling exponent
A	Accurate prediction
a	Multifractal cascade parameter
AK	Anthes-Kuo Scheme
AR4	IPCC Fourth Assessment Report
ARB	Athabasca River Basin
B	Over-prediction
b	Multifractal cascade parameter
BM	Betts-Miller Scheme
C	Under Prediction
C_3	Soil drainage coefficient (T^{-1})
CAPE	Convective Available Potential Energy
CP	Cumulus Parameterization
CV	Coefficient of Variation
D	Soil Depth (L)
DEM	Digital Elevation Model
DFA	Detrended Fluctuation Analysis
DGVM	Dynamic General Vegetation Model
ECMWF	European Centre for Mid-range Weather Forecasts
EI	Error Index
ERA-40	40-year ECMWF Re-Analysis project
F	Cumulative probability function
f	Probability density function (Chapter 3)
$f(\alpha)$	Multifractal Spectrum
FAR	IPCC First Assessment Report
FC	Fritsch-Chappell Scheme
FDDA	Four Dimensional Data Assimilation
FRB	Fraser River Basin
GCM	General Circulation Model
GEM	Global Environmental Multiscale Model
Gr	Grell Scheme
H	Hurst exponent

h	Generalized Hurst exponent
i	Precipitation intensity ($L\ T^{-1}$)
IPCC	Intergovernmental Panel on Climate Change
ISBA	Interactions between the Soil-Biosphere-Atmosphere model
K	Hydraulic Conductivity ($L\ T^{-1}$)
k	Fraction of area receiving rainfall (Chapter 3) Characteristic scale (Chapter 6)
KF	Kain-Fritsch Scheme
l(x)	Lower bound of variable x
LAI	Leaf Area Index
MAE	Mean Absolute Error
MAPSS	Mapped Atmosphere Plant Soil System model
MFDFA	Multifractal Detrended Fluctuation Analysis
MISBA	Modified ISBA model
MM5	Fifth-Generation Mesoscale Model
OISBA	Original ISBA model
P	Precipitation depth (L)
PET	Potential Evapotraspiration ($L\ T^{-1}$)
Q	Volumetric flow rate ($L^3\ T\text{-}^{1}$)
q	Moment exponent
q_v	Specific humidity
R_H	Relative humidity
RMSE	Root Mean Square Error
S	Soil water retention
s	Sample standard deviation
SAR	IPCC Second Assessment Report
SRES	IPCC Special Report on Emission Scenarios
SRTM	Shuttle Radar Topography Mission
SVAT	Soil Vegetation Atmosphere Transfer model
T	Temperature
TAR	IPCC Third Assessment Report
t	Time
u(x)	Upper bound of variable x
w	Soil water content
z	Normal distribution quantile
Z_q	q^{th} moment of the box probability

Chapter One: Introduction

Although the linkages of the study of the hydrologic cycle to related fields have long been recognized, the science of hydrology has traditionally been restricted to the study of the portion of the cycle that interacts with the land surface, with a particular emphasis on the vertical and especially horizontal mass fluxes of water. As such, for most of the 20th century hydrologic models were developed in relative isolation from their counterparts in fields such as meteorology and climatology. The complexity of atmospheric processes and the computation effort required to model them precluded the application of meteorological modelling approaches in hydrology, and meteorological models themselves often used highly simplified conceptual models of hydrology to represent their lower boundary conditions. Meanwhile, a much higher emphasis on the accurate simulation of energy fluxes in atmospheric models produced parameterization schemes that treated precipitation (often the single most important variable to a hydrologist) as an incidental by-product of latent heat transfers in the troposphere.

However, the exponentially increasing power of computer processors has slowly encouraged investigators in the previously disparate fields of meteorology, climatology, oceanography, and hydrology to unify their modelling approaches to produce General Circulation Models (GCMs) capable of simulating the entire hydrologic cycle for the first time. In fact, heightened interest in predicting the effects of anthropogenic climate change has encouraged biologists to add their models, allowing for the inclusion of the dynamic effects the living biosphere has on the hydrologic cycle.

At the moment, such grand schemes remain the exclusive domain of giant research organizations and collaboratives. However, with the decline in the relative cost of computational power and the advent of freely available models and the data sets required to run them, it is now becoming possible for an individual investigator to apply these models and techniques at regional and local scales with the aid of a computer that can be purchased by a typical retail consumer. One of the great barriers limiting the scope and power of hydrology is beginning to collapse.

Computational technology was never the only barrier however. Most hydrologists, climatologists, and meteorologists have been trained and continue to practice in isolation, with relatively little understanding of each other's fields and their primary issues of concern. While the previously mentioned exponential growth of computational power may well soon render the technological barrier a historical anachronism for future generations of earth and atmospheric scientists and engineers, the comparatively slow progress of the marriage of these fields at the level of individual people will probably continue long into the future. This is particularly true of engineering hydrologists whose training and practice, at least at the undergraduate level, tend to be more isolated from the fields of the earth and atmospheric sciences.

One of the problems with the traditional approach to answering hydrologic problems is that by focussing on portions of the hydrologic cycle, hydrologic models had to assume a stationary climate because they had no capacity to account for global circulations in the atmosphere and oceans. GCMs, on the other hand, are still run at too coarse a scale to provide a detailed assessment of how climatic change would impact land

surface hydrology at local scales. The objective of this research is to develop a modelling framework that combines the ability of GCMs to capture the large-scale and long-term behaviour of the atmosphere with the ability of hydrologic models to capture land surface processes at smaller scales.

The method proposed here is to use a land surface model, designed to represent the land surface in three-dimensional atmospheric models, to represent the vertical components of land surface hydrologic processes. Since land surface models are designed to be included in atmospheric models, their data requirements are consistent with the output of GCMs and atmospheric re-analysis datasets. The land surface model will then be linked to a distributed hydrologic routing model to create a physically based, distributed hydrologic model appropriate for simulating streamflows in large river basins ($\sim 10^5$ km^2). The modelling framework will be designed to minimize calibration and computational effort while maintaining the key physical processes necessary to ensure it is capable of simulating streamflows under a range of conditions beyond what was historically observed. These conditions include not only changes in temperature and precipitation predicted by GCMs, but also predicted changes in vegetative cover in response to new climatic conditions.

An additional concern is the fact that the modelling approach used by GCMs is incapable of reproducing the specific conditions that control the inter-annual variations in precipitation and temperature at regional scales. Therefore, although GCMs may be capable of simulating long-term trends at regional scales, they cannot reliably predict the annual variations of wet and dry years. The standard approach for incorporating annual

variation is to use the variation in the historical record as the basis to build a new climate time series. However, this method assumes a specific pattern of wet and dry years that is almost certainly not going to be repeated. This introduces a source of uncertainty into the actual range of streamflows that actually would occur even if the GCMs can accurately predict the changes in mean temperature and precipitation. A multifractal approach to the analysis of time series will be applied to estimate the magnitude of this important source of uncertainty.

Chapter 2 is a brief overview of land surface and general circulation models. In Chapter 3, historical re-analysis and forecast data produced by climatic and weather models are used to force a land surface scheme in stand-alone mode in order to reproduce historical streamflows in the Athabasca River Basin. In Chapter 4, the methodology employed in Chapter 3 is extended to the Fraser River Basin. The predictions of general circulation models are then used to evaluate the potential effects of climatic change on streamflows in large river basins. In Chapter 5, the assumption of a stationary biosphere is tested by adjusting the current vegetation characteristics of the Fraser and Athabasca River Basins to match the predictions of a dynamic vegetation model. In Chapter 6, multifractal analysis of streamflow time series is employed to estimate uncertainties due to natural variability relative to uncertainties associated with the selection of individual hydrologic models, climatic models, and future emissions scenarios. Finally, a summary of the conclusions of this work along with a list of recommendations for future research are presented in Chapter 7.

Chapter Two: Literature Review

2.1 Land Surface Models

Land Surface Models (LSMs) have long been recognized as an important component of the Earth's water and energy cycles because the latent and sensible heat fluxes they generate represent the lower boundary conditions for the atmosphere in Numerical Weather Prediction models (NWPs) and General Circulation Models (GCMs). LSMs are also responsible for prediction of important surface parameters, such as surface temperature, humidity, and soil moisture. In addition, soil moisture depends on an accurate partitioning of latent and sensible heat fluxes and is one of the key variables influencing atmospheric variability (Delworth and Manabe, 1988; Delworth and Manabe, 1989; Milly and Dunne, 1994). LSMs are also responsible for representing the rainfall-runoff process and therefore can be seen as a type of hydrologic model. LSMs are generally one-dimensional models (vertical direction) designed to represent the vertical movement of water and energy through the vegetation canopy and the soil column. Because of their fundamental structure, they are not complete hydrologic models because they are incapable of representing the horizontal transport of water. However, when coupled with a horizontal transport model, such as a routing model they have the potential of being a key part of a physically based, distributed hydrologic model.

Manabe (1969) is generally recognized as the first to incorporate a LSM in a GCM. In this model, the land surface is represented conceptually as a bucket with a fixed depth. As precipitation falls, the water level rises accordingly until it spills over

and surface runoff is produced. Water is also removed from the bucket by evapotranspiration in proportion to the depth of water in the bucket.

This simple "bucket" approach has many limitations, including the lack of snow and vegetative covers, and an inability to account for how soil moisture varies with depth. Since the 1980s, a large number of increasingly complex LSMs have been developed (for example, Dickinson et al., 1986; Abranopoulos *et al.*, 1988; Noilhan and Planton, 1989; Pan, 1990; Verseghy, 1991; Xue *et al.*, 1991; Koster and Suarez, 1992; Famiglietti and Wood, 1994; and Liang *et al.*, 1994). The rapid development of numerous and diverse models led the World Climate Research Programme (WCRP) to initiate the Project for the Intercomparison of Land-surface Parameterization Schemes (PILPS) (Henderson-Sellers and Brown, 1992; Henderson-Sellers *et al.*, 1993).

2.2 Project for the Intercomparison of Land-surface Parameterization Schemes (PILPS)

The goal of PILPS was to improve the understanding of water end energy fluxes at the Earth's surface by conducting controlled experiments in which the predictions of numerous LSMs were compared in order to evaluate the relative strengths of various approaches as well as identify processes that may not be adequately accounted for in existing LSMs. PILPS was initiated in four distinct phases. In Phases 1 and 2, experiments were conducted in "off-line" mode with prescribed atmospheric forcings from numerical models (Phase 1) (Pitman *et al.*, 1993, Yang *et al.*, 1995, and Pitman *et al.,* 1999) and observational datasets (Phase 2) (Shao and Henderson-Sellers 1995; Chen *et al.*, 1997; Liang *et al.*, 1998, Lohmann *et al.*, 1998, Wood *et al.,* 1998; Slater *et al.*, 2001; Schlosser *et al.*, 2001; Bowling *et al*, 2003; Luo *et al.*, 2003; Nijssen *et al.*, 2003).

In Phase 3, LSMs were to be coupled with their native atmospheric models and Phase 4 was to consist of coupling different LSMs to a common atmospheric model (Henderson-Sellers *et al.,* 1996). Phase 3 became primarily the analysis of LSMs in another WCRP project, the Atmospheric Model Intercomparison Project (AMIP) in which Atmospheric GCMs are subjected to the same radiative forcings and boundary conditions (Gates 1992 and Gates, 1999). AMIP has in turn become incorporated into the Coupled Model Intercomparison Project (CMIP) (Meehl *et al.*, 2000 and Meehl *et al.*, 2005). Because of these amalgamations, PILPS effectively came to an end after the completion Phase 2 experiments in 2003.

2.2.1 PILPS Phase One

Phase 1(a) of PILPS focused on the control and spin-up tests of LSMs with one-way forcings from the atmosphere, i.e. no feedback from the land surface to the atmosphere (Yang *et al.*, 1995). Model spin-up was defined as the process of the LSM adjusting to equilibrium after the occurrence of a soil moisture anomaly, such as a drought. Twenty-two LSMs were exposed to repeated years of identical meteorological conditions from the NCAR CCM1 GCM until they reached an equilibrium state, which was defined as when the difference in mean annual latent and sensible heat fluxes differed by less than 0.1 W/m^2 from the previous year.

Four experiments were conducted in which each LSM simulated the behaviour of a tropical forest and a grassland. In the control (CNTRL) experiment, soil and canopy moisture was initiated at 50% of capacity with no snow pack. The DRY and WET experiments were identical to CNTRL except the LSMs were initiated at 0% and 100%

moisture capacity. The final experiment, NOP, was identical to CNTRL except the experiment was initiated from the DRY equilibrium state and precipitation was set to zero throughout.

In the CNTRL and WET experiments most LSMs required 2 to 4 years to reach equilibrium. Although several models continued to reach equilibrium quickly in the DRY and NOP experiments, equilibrium times generally increased with several LSMs requiring 40 years or more to reach equilibrium, particularly in the NOP case. It was found that spin-up time varied linearly with the maximum available moisture content in the soil in the CNTRL and WET cases. In the DRY and NOP cases, the spin-up time varied non-linearly with the available moisture content in LSMs that did not use the bucket approach, suggesting that the linear behaviour of bucket-type models is a special case of non-bucket type models. Furthermore, the final equilibrium state could differ depending on the initial conditions and the model used. The wide range in spin-up times between different LSMs and different initial conditions indicates that multiple year simulations are required to compare the behaviour of different LSMs.

These control experiments were repeated in Phases 1(b) and 1(c) with more refinements to the experimental design that ensured the models were physically consistent. In Phase 1(c) (Pitman *et al.*, 1999) 16 remaining LSMs produced a range in latent and sensible heat fluxes of approximately 80 W/m^2 for the tropical forest and 30 W/m^2 for the grassland. Simpler bucket-type schemes tended to produce more evaporation than more complex schemes, although it was found that this could be corrected by adding an additional resistance term to reduce transpiration through the

canopy. It was concluded that the disparity between the models suggested that the LSMs could not agree on the land surface climate even when atmospheric forcing and surface parameters were prescribed, casting doubt on the reliability of all land surface schemes. The priority of future experiments was shifted to understanding the reasons for and decreasing the amplitude of the disparity between LSMs.

2.2.2 PILPS Phase 2

In Phase 2, observed data from numerous sites were used instead of the artificial data used in Phase 1. This meant comparisons could be made between LSMs and observed data, allowing for LSMs to be evaluated on their ability to reproduce observed hydroclimatic behaviour. In Phase 2(a) meteorological data from Cabauw, the Netherlands for the year 1987 was used to force 23 LSMs (Chen *et al.*, 1997) with prescribed physical parameters. Because the soil at the site was saturated throughout the study period, potential initialization problems identified in Phase 1 were minimal. Most schemes exhibited a systematic positive bias in radiative surface temperature, potentially due to the assumed emissivity and the lack of canopy heterogeneity. The ranges in annual latent and sensible heat fluxes were similar to those of grasslands in Phase 1, 25 and 30 W/m^2, respectively. Annual evapotranspiration and runoff across the 23 LSMs varied by more than 300 mm annually, although half of this range could be attributed to three LSMs that did not account for stomatal resistance when water supply was abundant. No surface runoff was observed from the study site and because the terrain was very flat, interflow was negligible. Observed runoff was dominated by vertical drainage to a shallow water table that was drained by ditches. Several models, however, produced

significant volumes of surface runoff or interflow with some models removing water from the water table to produce surface runoff. These few models behaved in this way because of several reasons: using of a parameterization to represent sub-grid variation in saturation at the GCM scale that may not be representative of the relatively homogenous site at Cabauw, a tendency of the near-saturated root-layer to draw water too quickly from the water table, or a tendency to produce significant runoff under non-saturated conditions.

In Phase 2(b) (Shao and Henderson-Sellers, 1995) 13 LSMs were run using measured meteorological forcing from the HAPEX-MOBILHY experimental site in Caumont, France. Once again, the models were subjected to a single year of meteorological data repeated several times until equilibrium was reached. There were large differences between LSMs in the simulation of soil moisture. In particular, results were sensitive to the selection of hydraulic parameters. Qualitatively, all the LSMs described the annual soil moisture cycle correctly but, there were significant seasonal discrepancies between LSMs. LSM predictions of annual runoff and drainage ranged from 100 to 300 mm, with over 2/3 of the models underestimating runoff compared to the observed annual runoff of 250 mm. The range of model predictions of the partitioning of latent and sensible heat flux was 15 to 20 W/m^2, a significant decrease from previous phases but still problematic for long-term climate simulations. The LSMs continued to reach different equilibria under repeated identical atmospheric forcings making it impossible to verify the model performances with the intensive 35-day field data during the growing season. Also, although several models were able to produce a reasonable

simulation of the soil moisture cycle, they did this by partitioning water and energy in very different ways. The treatment of runoff and drainage in the LSMs was found to be generally inadequate and a particular emphasis was put on the importance of further development of hydrologic processes in LSMs.

For Phase 2(c) 10 years (1979-1988) of observed data from the Red-Arkansas Basin in the United States was used to force 16 participating LSMs (Wood *et al.*, 1998; Liang *et al.*, 1998; and Lohmann *et al.*, 1998). This phase represented a significant increase in experimental scope since it involved multiple-year simulations in a diverse, continental-scale basin as well as allowing LSMs to calibrate their parameters from small catchments and transfer them to other catchments and computational grids. The LSMs continued to show significant discrepancies in the partitioning of water and energy. For example, the modeled runoff/precipitation ratio over the 10–year period ranged from 0.02 to 0.41, while the observed ratio was 0.18. (Lohmann *et al.*, 1998). LSMs also disagreed on how evenly and smoothly runoff was distributed across the basin and the partitioning of runoff between soil drainage and surface runoff. During dry summer seasons, the models that were dominated by soil drainage outperformed models that had stronger surface runoff components. LSMs that used observations from small catchments to calibrate their parameters generally performed better than their counterparts that only used predefined values.

Snow cover has a significant influence on local, regional, and global climate, however all the PILPS studies from Phase 1 and 2(a-c) focused on regions where the influence of snow was minimal. Phase 2(d) focused on the treatment of cold climates in

21 LSMs using an 18-year (1966-1983) observational record from Valdai, Russia (Slater *et al.*, 2001, Luo *et al.*, 2003). While the models captured the broad features of the annual snow cycle, significant scatter in the predictions of particularly early season ablation was identified (Slater *et al.*, 2001). The long period of the study allowed for the identification of systematic differences between the LSMs. For example, the rate of sublimation from the snow pack varied from -3 mm to +30 mm per year. The interaction between snow albedo and fractional snow cover, and its influence on the available energy for ablation was identified as a particularly important source of model discrepancy, especially at low snow depths. Other important factors included the treatment of the snow pack within the model structure (for example, whether or not an independent snow temperature was calculated) and sensitivity to downwelling longwave radiation. It was found that once differences in LSM simulations were established they would tend to persist throughout the entire winter season. Luo *et al.* (2003) focused on the treatment of frozen soils in LSMs. The presence of explicit frozen soil processes in LSMS improved the simulation of soil temperature at both seasonal and multi-year scales. Because the study site tended to be saturated throughout the winter period, the influence of frozen soil processes on soil moisture could not be determined. More sophisticated models that included snow metamorphism, variable solar absorption through the depth, phase changes between liquid and solid water, and water transmission through the snowpack produced better snow simulations, especially during ablation. While simpler snow models could reproduce snow accumulation, once snowmelt began they were generally unable to predict the rate and volume of snow melt. Although observations clearly showed snow

cover fraction hysteresis (differences in the rate at which fractional snow cover changes during accumulation and ablation periods), none of the LSMs included such processes. Because snow cover fraction has a significant influence on the energy available for lateral ablation, this was identified as an area where all LSMs could be improved.

In Phase 2(e), 20-years (1979-1998) of data from the Torne-Kalix Basin in northern Scandinavia (approximately, 66 to 69° N and 18 to 25° E) was used to force 21 participating LSMs under high-latitude conditions. While Phase 2(d) focused on observed data at a specific site, Phase 2(e) was designed in a manner similar to the large-scale study in Phase 2(c) (Bowling *et al.*, 2003a; Nijssen *et al.*, 2003). The Torne-Kalix Basin was sub-divided into 218 0.25° by 0.25° grid cells. The first 10 years was used to accommodate model spin-up. Because the region was at high latitude, there were a number of data quality concerns which included a lack of sub-daily precipitation, under-catch of snowfall, and the need to estimate incoming solar radiation. It was found that net radiation, rather than moisture availability, is the primary limitation for estimating latent heat fluxes. The modeled rate of snow sublimation was the most important cause of differences in the simulated annual runoff between models (Bowling *et al.*, 2003a).

As in Phase 2(d), the models were able to capture the general behaviour of the snow cycle and runoff but between the models, large differences in the accumulation and ablation of snow, sensible and latent heat fluxes, and runoff rates continue to exist (Nijssen *et al.*, 2003). Again, differences in simulated runoff between the models were especially noticeable during spring melt due to differences in the treatment of snow processes. Models produced a large range in sublimation rates, ranging from small net

snowpack gains in a few models to a loss of up to one third of the winter snowpack in others. While the models that predicted the highest sublimation rates tended to produce snow accumulation curves that better matched the observed data, they also tended to underestimate the volume of runoff. The models also varied in the timing and rate of snow melt, with most models predicting more rapid melt rates than were observed. How these differences manifested in the predicted hydrographs were further influenced by differences in the treatment of surface and subsurface runoff. The relationship between specific parameterization approaches and their influence on runoff predictions were not identified. The two most important factors leading to differences in annual net radiation were differences in the radiative surface temperature during winter and differences in the surface albedo during spring and early summer. LSMs that produced most of their runoff by surface runoff mechanisms, as opposed to subsurface runoff, showed the greatest variability in runoff (up to double the observed variability).

As in Phase 2(c), LSMs that used observations from small sub-catchments tended to perform better at simulating daily streamflow values than LSMs that only used pre-defined parameter values (Nijssen *et al.*, 2003). Observed runoff appeared to be dominated by slow mechanisms such as subsurface drainage, although the observed data was insufficient to be definitive.

2.2.3 Summary of the PILPS studies

Phase One of PILPS clearly demonstrated that LSMs are capable of exhibiting a wide range of responses under identical environmental conditions, suggesting that most models were not sufficiently robust to reliably represent the land surface in large-scale

Regional Climate Models and GCMs. Many LSMs were found to be particularly sensitive to initial conditions, especially in areas with deep soil layers, often requiring 10 years or more to reach an equilibrium condition. LSMs therefore often cannot be meaningfully inter-compared with field data without several decades of data.

In Phase 2, the inclusion of observed data allowed for the identification of deficiencies in the approaches of individual models. The non-linear nature of most land surface processes resulted in models being unable to capture key features of observed data, such as the timing and intensity of streamflows, without accounting for sub0grid variation of such parameters as soil moisture and vegetative cover. Processes that involved phase changes between snow/ice, liquid water, and water vapor are especially resistant to being accurately modelled with simplified approaches. In general, parameterization approaches that explicitly modelled such processes as canopy storage, multiple soil layers, and detailed snow physics were better able to reproduce observed energy and water fluxes. While simpler approaches, such as the bucket approach, could be fine-tuned to capture hydrologic behaviour at local scales, the calibration requirements become increasingly prohibitive at regional and continental scales.

Phases 2(c, d, and e) focussed on cold regions and the importance of snow and ice processes. A consistent result across these studies was the better performance of LSMs that included more sophisticated snow modelling schemes such as an explicit snow temperature, multiple snow layers, the effects of snow age on snow albedo, density, and thermal conductivity. Although the predicted rates of sublimation varied widely between models, they could not be compared with observed results because such data were

generally unavailable. Because an accurate representation of the timing and intensity of snow melt is so important for the accurate simulation of streamflows in cold regions, the hysteresis of snow accumulation/degradation curves needs to be incorporated into LSMs. A key improvement would be the incorporation of later heat transfer processes between bare and snow-covered ground that can dominate the snow ablation process. LSMs also tend to melt snow too uniformly because they do not include parameterizations for sub-grid variation in the aspect of the land surface resulting in an inability to reproduce the extremely slow melt rates that can occur on slopes that face away from the Sun.

2.3 Land Surface Modelling under the Canadian GEWEX-MAGS Program

Under the Global Energy and Water Cycle Experiment (GEWEX), the Mackenzie GEWEX Study (MAGS) was a collaborative study with the goal of increased understanding and modeling of energy and water cycles in cold region and high-latitude environment, as represented by the Mackenzie River Basin (MRB) in northern Canada (Woo et al., 2008). The study covered a wide range of studies, including atmospheric processes, snow processes, climatic modeling, remote sensing, lake processes, wetland modeling, river ice modeling and hydrologic modeling (Woo, 2008a; Woo, 2008b).

The hydrologic modeling component focussed on the development of LSMs and their coupling with atmospheric and hydrologic models. Soulis and Seglenieks (2008) coupled the hydrologic model WATFLOOD (Kouwen *et al.*, 2003) with the Canadian Land Surface Scheme (CLASS) LSM (Verseghy, 1991) to produce a new model, WATCLASS which would include the detailed vertical physics and the land surface of CLASS with the lateral hydrologic processes of WATFLOOD. In addition to surface

runoff and sub-surface drainage mechanisms of CLASS, WATCLASS introduced the inclusion of an interflow mechanism in which flow was proportional to the slope of the land surface in a manner analogous to a kinematic wave. Other changes to CLASS included the effect of soil ice on effective porosity and hydraulic conductivity, and different snow depletion and degradation curves (Soulis and Seglenieks, 2008). WATCLASS was applied to the major tributaries of the MRB. While it was able to reproduce the hydrographs of the Liard, Peace, and Smoky Rivers reasonably well, it had difficulty reproducing flows in the Athabasca Basin as well as the full MRB (Nash-Sutcliffe coefficients < 0) (Soulis and Seglenieks, 2008).

Kerkhoven and Gan (2008) developed a modified version of the LSM Interactions Soil Biosphere Atmosphere (Noilhan and Planton, 1989) and added a hydrologic routing model to produce a new model called MISBA that was capable of acting as either a hydrologic model in off-line mode or an LSM when coupled with an atmospheric model. A detailed description of MISBA can be found in Chapter 3. The modifications to MISBA focussed on the inclusion of an accounting for sub-grid variation in soil moisture and its influence on runoff generation via the highly non-linear nature of unsaturated flow through porous media. The resulting runoff mechanisms were designed to add no additional calibrated parameters and therefore could be readily transferred to most other LSMs.

2.4 Interactions Soil Biosphere Atmosphere Land Surface Model

Noilhan and Planton (1989) developed the LSM Interactions Soil Biosphere Atmosphere (ISBA) based on the approach of Deardorff (1978) to represent the land

surface in NWPs. The focus of the model design was to reduce the number of parameters to a minimum while preserving the physical processes that control the water and energy budgets. ISBA participated in all phases of PILPS.

2.4.1 Turbulent Heat Fluxes in ISBA

Sensible heat flux away from the land surface in ISBA is determined by applying Monin-Obukhov similarity theory,

$$H = \rho C_p C_H U(T_{skin} - T) \tag{2.1}$$

where, ρ is the air density, Cp is the specific heat at constant pressure, and T_{skin} is the skin temperature, and C_H is the exchange coefficient for heat. T_L and U_L are the temperature and wind speed at the Obukhov length, the height at which the Richardson Number is equal to unity. The above formulation can be written in its resistance form,

$$H = \rho C_p \frac{T_{skin} - T}{r_a} \tag{2.2}$$

where, r_a is the aerodynamic resistance. In ISBA, the skin temperature, T_{skin}, the temperature of an infinitely thin layer of soil with no heat capacity is represented by the temperature of the upper-most soil layer. This soil layer has a fixed depth of 1 cm to minimize the time lag introduced by the thermal heat capacity of the soil (Noilhan and Mahmouf, 1996). The exchange coefficient for heat, C_H, is determined by following the method of Mascart *et al.* (1995) in which the roughness lengths of both heat and momentum are used (Brutsaert, 1982; Beljaars and Viterbero, 1994).

Penman (1948) used an electrical analogy to evaluate the potential evaporation rate from an open water surface as being proportional to the difference in vapor pressure

between two points and inversely proportional to the resistance. If we consider that there are two sources of resistance to evaporation: resistance due to the atmosphere's ability to transport water vapor away from the surface, r_a, and stomatal resistance to water vapor leaving the leaf, r_f, total latent heat flux away from the land surface, LE, can be determined from,

$$LE = \rho \frac{q_{sat}(T_{skin}) - q_L}{r_a + r_s} \tag{2.3}$$

where, q_L is the specific humidity at a height equal to the Obukhov length above the land surface, and $q_{sat}(T_{skin})$ is the saturated specific humidity at the surface. In order to eliminate the need to estimate T_{skin} before calculating the latent heat flux, a first-order Taylor expansion is used,

$$q_{sat}(T_{skin}) = q_{sat}(T_L) + \frac{dq_{sat}(T_L)}{dT}(T_{skin} - T_L) \tag{2.4}$$

Given the energy balance equation at the land surface,

$$R_n = H + LE + G \tag{2.5}$$

where, R_n is the net radiation towards the surface, and G is the ground heat flux away from the surface. It is possible to eliminate $T_{skin} - T_L$ by combining Equations 2.2 and 2.5,

$$T_{skin} - T_L = \frac{r_a}{\rho C_p} H = \frac{r_a}{\rho C_p}(R_n - G - LE) \tag{2.6}$$

Substituting Equation 2.6 into Equation 2.4 gives,

$$q_{sat}(T_{skin}) = q_{sat}(T_L) + \frac{r_a}{\rho C_p}(R_n - G - LE)\frac{dq_{sat}(T_L)}{dT} \tag{2.7}$$

Substituting Equation 2.7 into Equation 2.2 and rearranging to isolate LE give,

$$LE = \frac{\rho \frac{C_p}{r_a}\left[q_{sat}(T_L) - q_L\right] + \left(R_n - G\right)\frac{dq_{sat}(T_L)}{dT}}{C_p\left(1 + \frac{r_s}{r_a}\right) + \frac{dq_{sat}(T_L)}{dT}} \tag{2.8}$$

Equation 2.8 is called the Penman-Monteith equation (Monteith, 1965). In ISBA, the land surface is divided into two "tiles": the fraction of the surface cover by vegetation and the fraction covered by bare soil (i.e. where $r_s = 0$). The total latent heat flux from the land surface is an areally weighted average of the latent heat flux from the vegetated and bare surfaces. Once the latent heat flux has been calculated, the skin temperature and sensible heat flux can be calculated from Equations 2.5 and 2.2.

2.4.2 Runoff and Drainage in ISBA

In ISBA, water is removed from the soil column by two mechanisms, surface runoff and sub-surface drainage. Although the soil column is represented by three layers, the thin, 1 cm upper layer is not distinct from the middle root-layer. Instead, the upper layer is used to represent thermal properties at the surface while the root layer controls surface runoff. In the first version of ISBA (Noilhan and Planton, 1989), surface runoff was generated when the root layer became fully saturated, in a manner similar to the simpler bucket-type models. In order to produce a more realistic mechanism, where surface runoff could be generated when the soil was not completely saturated, Habets *et al.* (1999) incorporated a multi-bucket approach similar to the Variable Infiltration Capacity (Wood *et al.*, 1992) and Xinanjiang (Zhou, 1992) models.

In this approach, the soil moisture capacity, I, of a grid-box is assumed to vary according to a simple, single parameter probability distribution,

$$I = I_{\max}\left[1-\left(1-A(I)\right)^{1/\beta}\right] \tag{2.9}$$

where, I_{max} is the maximum soil moisture capacity in the grid-box, A(I) is the fraction of the grid-box for which the soil moisture capacity is less than I, and β is a calibrated parameter representing the variability of soil moisture capacity in the grid-box. Because porosity is constant throughout the grid-box, this approach can be conceptualized as representing sub-grid variability of soil depth. Furthermore, since the model requires the average soil depth to be given as a parameter and since the distribution of soil depth is bounded by zero and a maximum depth, the single distribution parameter, β, effectively defines the maximum soil depth in the grid-box (see Appendix A for a mathematical proof). In this new mechanism, the distribution of soil column depths fill evenly as water is added by precipitation and snowmelt with surface runoff being generated first at locations where the soil depth is small and last at locations where soil depth is a maximum.

Subsurface drainage in ISBA, Q_{drain}, is generated by removing water from the bottom soil layer at a rate proportional to the available soil moisture,

$$Q_{drain} = C_3 D_3\left(w_3 - w_{drain}\right),\ w_3 > w_{drain} \tag{2.10}$$

where, D_3 is the depth of the bottom soil layer, w_3 is the soil moisture content in the bottom soil layer, w_{drain} is a user defined parameter representing the minimum soil moisture at which drainage occurs. C_3 is a coefficient representing the inverse of the

residence time of soil moisture in the bottom soil layer and is calculated directly from fraction of clay in the grid-box, *CLAY*, after Mahfouf and Noilhan (1996),

$$C_3 = \frac{5.327}{CLAY^{1.043}} days^{-1} \tag{2.11}$$

It can be seen that subsurface drainage in ISBA is linearly proportional to the volume of available storage in the bottom soil layer and therefore follows a linear reservoir approach.

2.4.3 Snow in ISBA

ISBA originally used a single layer snow model in which the temperature of the snow pack was equal to the temperature of the upper soil layer. This approach was identified in PILIS Phase 2(d) as physically problematic (Slater *et al.*, 2001). Boone (2002) developed a three-layer snow model where the depth, density, and temperature of each layer were explicitly modeled independent of the upper soil layer.

The fraction of the land surface covered by snow, f_{snow}, is calculated from,

$$f_{snow} = \frac{D_{snow}}{D_{snow} + D_{ref}} \tag{2.12}$$

where, D_{snow} is the depth of snow and D_{ref} is a reference depth that is proportional to the roughness height of the land surface. This is a standard approach used by many LSMs (e.g. Dickinson *et al.*, 1986; Pitman *et al.*, 1991; and Verseghy, 1991) however its lack of a hysteresis mechanism has been identified as being inconsistent with field observations (Luo *et al.*, 2003).

The upper snow layer is set to 25% of the total snow depth, to a maximum of 5 cm to capture diurnal variations, while the second snow layer varies from 34% to 50%

depending on the total snow depth, to a maximum of 50 cm. Snow density varies from 150 km/m^3 for fresh snow, exponentially approaching a maximum snow density of 450 kg/m^3 with an e-folding time of approximately 4 days. Further density increases can be produced by melting processes and the infiltration of rainwater.

The upper layer served as the interface between the snow pack and the atmosphere and the lower layer interfaced with the soil surface. Ground and turbulent heat fluxes were transmitted between the layers by thermal diffusion while the fraction of shortwave radiation absorbed by each layer was proportional to their depth. Snow albedo for dry snow decreased linearly (Baker et al., 1990) and exponentially for wet snow (Verseghy, 1991).

The latent and sensible heat fluxes from the snow surface are treated in a similar manner as for a bare soil surface. The main difference is that the latent heat flux must be partitioned between evaporation and sublimation processes. Evaporation occurs when the upper snow layer temperature is at the freezing point and is proportional to the liquid water content in the upper snow layer. The remaining latent heat is sublimated from the upper layer. The temperature of each snow layer is limited to the freezing point of water. Any additional available heat is put towards melting. Any liquid water produced by either melting or rainfall is allowed to infiltrate through the lower snow layers until they reach the soil surface.

2.5 Climate Change Science

The ability of the atmosphere to potentially act to increase surface temperatures due to differences in the absorption of shortwave and longwave radiation was first

indentified in the 17th century and by the 18th century experimental evidence confirmed that this effect could be produced by glass (Fleming, 1998; Weart, 2003). In the 19th century, Tyndall (1861) showed that water vapour and CO_2 could trap sufficient quantities of heat to explain the Earth's surface temperature and Arrhenius (1895) postulated that relatively moderate increases or decreases in CO_2 concentration could be sufficient to cause glacial advances or retreats.

In the early 20th Century, Bjeknes (1900) and Richardson (1922) developed the fundamental equations and many of the techniques that would later be used in GCMs. Data and computation limitations, however, prevented their application to practical weather forecasting until the development of the computer in the mid-20th century (Edwards, 2000). Charney *et al.* (1950) used ENIAC, generally recognized as the first operational computer, to conduct the first large-scale atmospheric simulations using a simplified two-dimensional version of the finite difference approach developed by Richardson. The model used a grid with a horizontal resolution of 700 km and a 3-hour time step to produce forecasts for North America. Philips (1956) developed the first three-dimensional GCM consisting of two vertical layers with a 625 km by 375 km grid spacing and a time step of 2 hours (or less, if required for numerical stability). The model was able to reproduce the easterly-westerly zonal winds, jet streams, and the net transfer of energy towards the poles but over-estimated the latitudinal mean annual temperature gradient. By the 1960s, GCM development was led by research groups such as the General Fluid Dynamics Laboratory (Manabe *et al.*, 1965; Smagorinsky *et al.*, 1965), UCLA (Arakawa, 1970), and the National Center for Atmospheric Research

(Kasahara and Washington, 1967). This era saw the introduction of coupled atmosphere-ocean models using simple 1-layer, "swamp", and 2-layer ocean models (Manabe and Bryan, 1969).

Meanwhile, the theory behind how CO_2 influenced climate through differences in its absorption of solar and thermal radiation was developed (Callandar, 1949; Seuss, 1953; Plass, 1956) and methane, nitrous oxide, and chlorofluorocarbons were identified as greenhouse gasses while clouds and atmospheric aerosols were identified as promoting cooling due to their ability to reflect and scatter radiation away from the Earth (Ramanathan, 1975; Wang *et al.*, 1976; Twomey, 1977; Charlson *et al.*, 1990).

By the 1980s, further advances in computers led many countries to establish meteorological research centres and develop new GCMs such as the UK's European Center for Medium Range Weather Forecasts (ECMWF), Germany's Max Planck Institute, the Australian Numerical Meteorological Research Center, and the Canadian Climate Centre (Boer and McFarlane, 1979). Developments during this era primarily focused on the improvement of existing techniques such as the treatment of land surface processes and hydrology, boundary layer turbulence, coupling the ocean and the atmosphere, atmospheric chemistry, and cumulus convection. Global climate simulations with doubled CO_2 concentration became a common method of estimating the potential effect of anthropogenic climate change (Edwards, 2000).

The Intergovernmental Panel on Climate Change (IPCC) was set up by the World Meteorological Organization and the United Nations Environment Programme in 1988 with the mandate to assess the most recent scientific literature relating to climate change

in order to present an objective source of information for anyone interested in climate change. The IPCC has released four assessment reports commencing with the First Assessment Report (FAR) in 1990 (IPCC, 1990), followed by the Second Assessment Report (SAR) in 1995 (IPCC, 1995), the Third Assessment Report (TAR) in 2001, (IPCC, 2001) and the Fourth Assessment Report (AR4) in 2007 (IPCC, 2007), which lead to the IPCC winning the 2007 Nobel Peace Prize.

The GCMs used in FAR featured atmospheric models with a horizontal resolution of approximately 500 km coupled with single layer ocean models and included ice parameterizations and the effect of clouds (IPCC, 2007). The report concluded that the authors were certain that there is a natural greenhouse effect and human activities were causing an increase in the global concentration of greenhouse gasses such as CO_2, methane, and nitrous oxide. Under the "business as usual" case and based on the GCM projections, it was estimated that global mean temperature would rise by 2 to 5°C, with a mean of 3°C, by the end of the 21st century, although this could be reduced to as little as 1°C if emissions were to be controlled. Analysis of historic observations suggested that global mean temperature had increased by 0.3 to 0.6°C during the 20th century, which was consistent with model simulations but also within the range of natural variability.

By the release of the SAR (IPCC, 1995) GCM models had reduced their horizontal resolutions to approximately 250 km and added multi-layer ocean models, and the influences of volcanic activity and aerosols (IPCC, 2007). The scientific report stated that greenhouse gasses have continued to increase, and that anthropogenic aerosols produce a negative effect on global temperature. In addition, it concluded that global

climate has changed in the 20th century and that this change includes a noticeable effect from human activity and that climate will continue to change in the next century, although many sources of uncertainty remain (IPCC, 1995). The inclusion of aerosols was credited as the reason for being able to detect human influence on global climate. The best estimate of the change in the mean global temperature by 2100 was decreased from 3°C in FAR to 2°C in SAR, due to the inclusion of aerosols and a reduction in the estimated concentrations of greenhouse gasses.

IPCC (2000) issued a special report defining six emission scenario families comprising 40 different scenarios for the 21st century based on different assumptions about regional economic and technologic development patterns. The six families are: A1T, AIB, A1FI, A2, B1, and B2. IPCC has made no attempt to quantify the probability of occurrence of any of these scenarios. Instead, they are meant to represent a wide range of political and economic decisions and thereby reflect the range of potential impacts. These scenarios formed the basis of both TAR and AR4 (IPCC, 2000).

The A1 families all feature rapid economic growth and spread of new technologies, peak global population of 9 billion, and regional convergence in economic development. The three A1 families differ in what technologies are emphasized however with A1T emphasizing non-fossil fuel technologies, A1FI emphasizing fossil fuel sources, and A1B representing a balance of both energy sources. The A2 family assumes a regionally divided world with continual population growth, divergent economic growth, and relatively slow transfer of new technologies (IPCC, 2000).

The B1 family represents a scenario in which economic and population growth matches the A1 families but with an emphasis on growth in the service and information industries while featuring decreases in the intensity of resource consumption, increased use of clean and efficient technologies, and the rapid transfer of new technologies to developing regions. The B2 family represents a world with continual population growth at a slower rate than A2 and intermediate economic development. While the B2 family places an emphasis on the development of clean technologies, like A2 it features more regional divergence and slower rates of technology transfers (IPCC, 2000).

By the release of TAR (IPCC, 2001), horizontal resolutions in GCMs had been further reduced to approximately 180 km and model features included ocean overturning, rivers, and enhanced carbon cycle modeling (IPCC, 2007). The report concluded unequivocally that the Earth's climate was changing with an observed increase in the global mean surface temperature of 0.6°C over the 20^{th} century. Analysis of satellite imagery data showed that snow cover in the Northern Hemisphere had decreased 10% since the 1960s with strong evidence that a major decline in glaciers was underway in response to global temperature increases. Collectively, the combination of temperature, precipitation, snow and ice extents, and sea level changes consistently presented evidence of a warming global climate during the last century. At the same time, global concentrations of CO_2, methane, and nitrous oxide have continued to increase at rates that were expected to have a long-term impact on global climate (IPCC, 2001).

Comparison of observed temperature trends with GCM simulations under natural and anthropogenic forcings led to the conclusion that most of the observed warming since

1950 was likely to be due to increases in greenhouse gas concentrations in the atmosphere. Overall, the global mean surface temperature was estimated to increase by 1.5 to 5.8 °C by 2100. This range includes the variability due to different climate scenarios as well as differences between GCMs. When ensembles of the GCM simulations were averaged for each SRES family, this range decreased to 2.0 to 4.5°C. Western North America, which includes the Athabasca and Fraser River basins, was expected to see small increases in winter precipitation and above average increases in winter and summer temperature (IPCC, 2001).

AR4 is the most recent assessment report from the IPCC (2007). Horizontal resolution decreased to approximately 110 km and model features were further expanded to include atmospheric chemistry and interactive vegetation (IPCC, 2007). Analysis of observed data confirmed the conclusions from TAR. In addition, the report concluded that global land surface temperatures have been warming at double the rate of ocean surface temperatures, tropospheric water vapor has increased since the 1980s, increases have occurred in the number of heavy precipitation events, and droughts have become more common since the 1970s. Furthermore, temperatures at the top of the arctic permafrost layer has increased by 3°C since the 1980s while the extent of seasonally frozen ground in the Northern Hemisphere as decreased by 7% in the 20th century (IPCC, 2007).

Further comparisons of GCM simulations of historic climate under natural and anthropogenic forcings led to the conclusion that that the observed warming since 1950 is very likely to be due to increases in greenhouse gas concentrations and it is extremely

unlikely (less than 5%) that warming trends can be explained without external forcing, that this warming has occurred during a time that natural forcings alone would likely have resulted in global cooling, and that it is very likely that a substantial portion of the variation in Northern Hemisphere temperature over the previous 700 years is due to natural forcings such as volcanic eruptions and solar variability (IPCC, 2007).

In addition to the SRES scenarios used in TAR, GCM projections were conducted under the assumption that global concentrations were held at levels observed in 2000 to estimate the extent warming that cannot be mitigated by emission reductions alone. The estimated increases in global mean surface temperature by the end of the 21st century for the seven scenario families were: 0.3 to 0.9°C (2000 concentrations), 1.1 to 2.9°C (B1), 1.4 to 3.8°C (A1T and B2), 1.7 to 4.4°C (A1B), 2.0 to 5.4°C (A2), and 2.4 to 6.4°C (A1FI). The range of ensemble averaged model results across the six SRES families was 1.8 to 4.0°C, representing a slightly more optimistic and less uncertain projection than TAR (2.0 to 4.5°C). As with TAR, the GCMs continue to project above average increases in winter and summer temperatures and small increases in winter precipitation in the regions of Canada that include the Athabasca and Fraser River Basins (IPCC, 2007).

2.6 Bibliography

Abramopoulos, F., C. Rosenzweig, and B. Choudhury, (1988), Improved ground hydrology calculations for global climate models (GCMs): Soil water movement and evaporation, *J. Climate*, 1, 921-941.

Arakawa, A., (1970), Numerical Simulation of Large-Scale Atmospheric Motions, Numerical Solution of Field Problems in Continuum Physics, *SIAM-AMS Proceedings*, American Mathematical Society, 2, 24-40.

Arrhenius, S., (1895), On the Influence of Carbonic Acid in the Air upon the Temperature of the Ground, *Philosophical Magazine and Journal of Science*, 41, 237-276.

Baker, D.G., D.L. Ruschy, and D.B. Wall, (1990), The albedo decay of prairie snows, *J. Appl. Meteor.*, 29, 179-187.

Beljaars, A.C.M., and P. Viterbo, (1994), The sensitivity of winter evaporation to the formulation of aerodynamic resistance in the ECMWF model. *Bound. Lay. Meteor.*, 71, 135-149.

Bjerknes, V., (1900), The circulatory movements in the atmosphere. *Monthly Weather Review*. 28(12), 532-535.

Boer, G.J., and N.A. McFarlane, (1979), *The AES atmospheric general circulation model.* Report of the JOC Study Conference on Climate Models: Performance, Intercomparison and Sensitivity Studies, Vol. I, GARP Publ. Ser. No. 22, 409-460.

Boone, A., (2002), *Description du schema de neige ISBA-ES (Explicit Snow). (Description of the ISBA-ES Explicit snow scheme)*, Note de Centre, Meteo-France/CNRM, 70, 53p.

Bowling, l., D. Lettenmaier, B. Nijssen, L.P. Graham, D. Clark, M. El Maayar, R. Essery, S. Goers, Y. Gusev, F. Habets, B. van den Hurk, J. Jin, D. Kahan, D. Lohmann,

X. Ma, S. Mahanama, D. Mocko, O. Nasonova, G.-Y. Niu, P. Samuelsson, A. Shmakin, K. Takata, D. Verseghy, P. Viterbo, Y. Xia, Y. Xue, Z.-L. Yang, (2003), Simulation of high-latitude hydrological processes in the Torne-Kalix basin: PILPS Phase 2(e) 1: Experiment description and summary intercomparisons, *Global and Planetary Change*, 38, 1-30.

Brutsaert, W., (1982), *Evaporation into the atmosphere: Theory, History, and Applications*, Boston, D. Reidel, 299 pp.

Callendar, G.S., (1949), Can Carbon Dioxide Influence Climate, *Weather*, 4, 310-314.

Charney, J.G., R. Fjörtoft, and J. von Neumann, (1950), Numerical integration of the barotropic vorticity equation, *Tellus*, 2, 237-254

Charlson, R.J., J. Langner, and H. Rodhe, (1990), Sulphate Aerosol and Climate, *Nature*, 348, 22.

Chen, T.-H., and A. Henderson-Sellers, P.C.D. Milly, A.J. Piman, A.C.M. Beljaars, J. Polcher, F. Abramopoulis, A. Boone, S. Chang, F. Chen, Y. Dai, C.E. Desborough, R.E. Dickinson, L. Du Menil, M. Ek, J.R. Garratt, N. Gedney, Y.M. Gusev, J. Kim, R. Koster, E.A. Kowalczyk, K. Laval, J. Lean, D. Lettenmeier, X. Liang, J.-F. Mahouf, H.-T. Mengelkamp, K. Mitchell, O.N. Nasonova, J. Noilhan, A. Robock, C. Rosenzweig, J. Schaake, C.A. Schlosser, J.-P. Schultz, Y. Shao, A.B. Shmakin, D.L. Verseghy, P. Wetzel, E.F. Wood, Y. Xue, Z.-L. Yand, and Q. Zeng, (1997), Cabauw experimental results from the Project for Intercomparison of Land-surface Parameterization Schemes (PILPS). *J. Climate*, 10, 1194–1215.

Deardorff, J.W., (1978), Efficient prediction of ground surface temperature and moisture, with inclusion of a layer of vegetation, J. Geophys. Res., 83, 1889-1903.

Delworth, T.L., and S. Manabe, (1988), The influence of potential evaporation on the variabilities of simulated soil wetness and climate, *J. Climate*, 1, 523-547.

Delworth, T.L., and S. Manabe, (1989), The influence of soil wetness on near-surface atmospheric variability, *J. Climate*, 2, 1447-1462.

Dickinson, R.E., A. Henderson-Sellers, P.J. Kennedy, and M.F. Wilson, (1986), *Biosphere-atmosphere transfer scheme (BATS) for the NCAR Community Climate Model*, National Center for Atmospheric Research, NCAR Tech. Note NCAR/TN-387+STR.

Edwards, P.N., (2000), A Brief History of Atmospheric General Circulation Modeling, in David A. Randall, ed., *General Circulation Development, Past Present and Future: The Proceedings of a Symposium in Honor of Akio Arakawa*, New York, Academic Press, 67-90.

Famiglietti, J.S., and E.F. Wood (1994), Multiscale modeling of spatially variable water and energy balance processes, *Water Resour. Res.*, 30(11), 3061–3078.

Fleming, J.R., (1998), *Historical Perspectives on Climate Change*. New York and Oxford: Oxford Univ. Press. 200p.

Gates, W.L., 1992: AMIP: The Atmospheric Model Intercomparison Project. *Bull. Amer. Meteor. Soc.*, 73, 1962–1970.

Gates, W.L., J.S. Boyle, C. Covey, C.G. Dease, C.M. Doutriaux, R.S. Drach, M. Fiorino, P.J. Gleckler, J.J. Hnilo, S.M. Marlais, T.J. Phillips, G.L. Potter, B.D. Santer, K.R. Sperber, K.E. Taylor, and D.N. Williams, (1999), An Overview of the Results of the

Atmospheric Model Intercomparison Project (AMIP I), *Bull. Amer.Meteor. Soc.*, 80, 29–55.

Habets F., Noilhan J. , Golaz C., Goutorbe J.P., Lacarrère P., Leblois E., Ledoux E., Martin E., Ottlé C., and Vidal-Madjar D., (1999) The ISBA surface scheme in a macroscale hydrological model applied to the Hapex-Mobilhy area Part 1: Model and database, *J Hydrol*, 217, 75-96.

Henderson-Sellers, A., Brown, V.B., (1992), *Project for Intercomparison of Landsurface Parameterization Schemes (PILPS): First Science Plan*, GEWEX Technical Note, IGPO Publication Series No. 5, 53 p.

Henderson-Sellers, A., Z.-L. Yang, and R. E. Dickinson, The Project for Intercomparison of Land-surface Parameterization Schemes, (1993), *Bull. Amer. Meteorol. Soc.*, 74, 1335.

Henderson-Sellers, A, McGuffie, K. and A.J. Pitman, (1996), The Project for Intercomparison of Land-surface Parameterization Schemes (PILPS): 1992 to 1995, Climate Dynamics, 12, 849-859.

Intergovernmental Panel on Climate Change, (1990), *Climate Change 1990: The Intergovernmental Panel on Climate Change Scientific Assessment*, Cambridge University Press, Cambridge.

Intergovernmental Panel on Climate Change, (1995), *Climate Change 1995: the Science of Climate Change*, Contribution of Working Group I to the Second Assessment Report of the Intergovernmental Panel of Climate Change, Cambridge University Press, Cambridge.

Intergovernmental Panel on Climate Change, (2000), *Emissions Scenarios*, A Special Report of Working Group II of the Intergovernmental Panel on Climate Change. Cambridge University Press, Cambridge.

Intergovernmental Panel on Climate Change, (2001), *Climate Change 2001: The Scientific Basis*, Contribution of Working Group 1 to the Third Assessment Report of the Intergovernmental Panel on Climate Change, Cambridge University Press, Cambridge.

Intergovernmental Panel on Climate Change, (2007), *Climate Change 2007 - The Physical Science Basis*, Contribution of Working Group 1 to the Fourth Assessment Report of the Intergovernmental Panel on Climate Change, Cambridge University Press, Cambridge.

Kasahara, A., and W.M. Washington, (1967), NCAR Global General Circulation Model of the Atmosphere, *Monthly Weather Review*, 95, 389-402.

Kerkhoven, E.N., and Gan, T.Y., (2008), Development of a Hydrologic Scheme for Use in Land Surface Models and its Application to Climatic Change in the Athabasca River Basin, in *Cold Region Atmospheric and Hydrologic Studies The Mackenzie GEWEX Experience, Volume 2: Hydrologic Processes*, Woo, M.K (ed.), Springer-Verlag, Berlin, 411-434.

Koster, R. D., and M. J. Suarez, (1992), Modeling the land surface boundary in climate models as a composite of independent vegetation stands, *J. Geophys. Res.*, 97, 2697.

Kouwen, N., Soulis, E.D., Pietroniro, A., Donald, J., and Harrington, R.A., (1993), Grouped Response units for distributed hydrologic modeling, *J Water Resources*, 119, 289-305.

Liang, X., D. Lettenmaier, E.F. Wood, and S.J. Burges, (1994), A simple hydrologically based model of land surface water and energy fluxes for general circulation models. *J. Geophys. Res.*, 99D, 14415-14428.

Liang, X., E. Wood, D. Lettenmaier, D. Lohmann, A. Boone, S. Chang, F. Chen, Y. Dai, C. Desborough, R. Dickinson, Q. Duan, M. Ek, Y. Gusev, F. Habets, P. Irannejad, R. Koster, K. Mitchell, O. Nasonova, J. Noilhan, J. Schaake, A. Schlosser, Y. Shao, A. Shmakin, D. Verseghy, K. Warrach, P. Wetzel, Y. Xue, Z.-L. Yang, Q. Zeng, (1998), The Project for Intercomparison of Land-surface Parameterization Schemes (PILPS) phase 2(c) Red-Arkansas River basin experiment: 2. Spatial and temporal analysis of energy fluxes, *Global Planetary Change*, 19, 137-159.

Lohmann, D., D. Lettenmaier, X. Liang, E. Wood, A. Boone, S. Chang, F. Chen, Y. Dai, C. Desborough, R. Dickinson, Q. Duan, M. Ek, Y. Gusev, F. Habets, P. Irannejad, R. Koster, K. Mitchell, O. Nasonova, J. Noilhan, J. Schaake, A. Schlosser, Y. Shao, A. Shmakin, D. Verseghy, K. Warrach, P. Wetzel, Y. Xue, Z.-L. Yang, Q. Zeng, (1998), The Project for Intercomparison of Land-surface Parameterization Schemes (PILPS) phase 2(c) Red-Arkansas River basin experiment: 3. Spatial and temporal analysis of water fluxes, *Global Planetary Change*, 19, 161-179.

Luo, l., A. Robock, K. Y. Vinnikov, C.A. Schlosser, A. G. Slater, A. Boone, H. Braden, P. Cox, P. de Rosnay, R. E. Dickinson, Y. Dai, Q. Duan, P. Etchevers, A.

Henderson-Sellers, N. Gedney, Y. M. Gusev, F. Habets, J. Kim, E. Kowalczyk, K. Mitchell, O. N. Nasonova, J. Noilhan, A. Pitman, J. Schaake, A. B. Shmakin, T. G. Smirnova, P. Wetzel, Y. Xue, Z.-L. Yang, Q. Zeng, (2003), Effects of Frozen Soil on Soil Temperature, Spring Infiltration, and Runoff: Results from the PILPS 2(d) Experiment at Valdai, Russia, *Journal of Hydrometeorology*, 4, 334- 351.

Manabe, S., , J. Smagorinsky, and R.F. Strickler, (1965), Simulated Climatology of General Circulation with a Hydrologic Cycle, *Monthly Weather Review*, 93, 769-798.

Manabe, S., (1969), Climate and the ocean circulation I. The atmospheric circulation and the hydrology of the Earth's surface, *Mon. Wea. Rev.*, 97, 739-774.

Manabe, S., and K. Bryan, (1969), Climate Calculations with a Combined Ocean-Atmosphere Model, *Journal of the Atmospheric Sciences*, 26, 786-789.

Mascart, P., J. Noilhan, and H. Giordani, 1995: A modified parametrization of the surface layer flux-profile relationships using different roughness length values for heat and moisture. *Boundary-Layer Meteorology* 72(4): 331.

Meehl , G.A., G. J. Boer, C. Covey, M. Latif, and R. J. Stouffer, (2000), The Coupled Model Intercomparison Project (CMIP). *Bull. Amer.Meteor. Soc.*, 81, 313–318.

Meehl , G.A., C. Covey, B. McAvaney, M. Latif, and R. J. Stouffer, (2005), Overview of the Coupled Model Intercomparison Project, *Bull. Amer.Meteor. Soc.*, 86, 89-93.

Milly, P.C.D., and K.A. Dunne, (1994), Sensitivity of the global water cycle to the water-holding capacity of land, *J. Climate*, 7, 506-526.

Monteith, J.L., (1965), Evaporation and environment. *19th Symp. Soc. Exp. Bio.*, 205-234.

Nijssen, B., L. Bowling, D. Lettenmaier, D. Clark, M. El Maayar, R. Essery, S. Goers, Y. Gusev, F. Habets, B. van den Hurk, J. Jin, D. Kahan, D. Lohmann, X. Ma, S. Mahanama, D. Mocko, O. Nasonova, G.-Y. Niu, P. Samuelsson, A. Shmakin, K. Takata, D. Verseghy, P. Viterbo, Y. Xa, Y. Xue, Z.-L. Yang, (2003), Simulation of high latitude hydrological processes in the Torne-Kalix basin: PILPS Phase 2(e) 2: Comparison of model results with observations, *Global Planetary Change*, 38, 31-53.

Noilhan, J., Mahfouf, J.F., (1996). The ISBA land surface parameterization scheme. *Global and Planetary Change* 13, 145–159.

Noilhan J., and Planton S., (1989), A simple parameterization of land surface processes for meteorological models, *Mon Wea Rev*, 117, 536-549.

Pan, H.-L., (1990), A simple parametrization scheme of evapotranspiration over land for the NMC medium-range forecast model. *Mon. Wea. Rev.*, 118, 2500-1512.

Penman, H.L., (1948), Natural evaporation from open water, bare soil and grass. *Proc. Roy. Soc. London*, A193, 120-145.

Phillips, N.A., (1956), The General Circulation of the Atmosphere: A Numerical Experiment, *Quarterly Journal of the Royal Meteorological Society*, 82, 123-164.

Pitman, A., and Coauthors, (1993), Project for Intercomparison of Land-Surface Parameterization Schemes, Results from offline control simulations (Phase 1a), GEWEX/WCRP, International GEWEX Project Office, Publication Series No. 7.

Pitman, A.J., Z.-L. Yang, J.G Cogley, and A. Henderson-Sellers, (1991), *Description of bare essentials of surface transfer for the Bureau of Meteorology Research Centre AGCM.* Bur. Meteor. Res. Rep. No.32, 86pp.

Pitman, A.J., Henderson-Sellers, A., Yang, Z-L., Abramopoulos, F., Boone, A., Desborough, C.E., Dickinson, R.E., Gedney, N., Koster, R., Kowalczyk, E., Lettenmaier, D., Liang, X., Mahfouf, J-F., Noilhan, J., Polcher, J., Qu, W., Robock, A., Rosenzweig, C., Schlosser, C., Shmakin, A.B., Smith, J., Suarez, M., Verseghy, D., Wetzel, P., Wood, E., Xue, Y., (1999), Key Results and Implications from Phase 1(c) of the Project for Intercomparison of Land-surface Parameterization Schemes, *Climate Dynamics*, 15, 673-684.

Plass, G.N., (1956), The Carbon Dioxide Theory of Climatic Change, *Tellus*, 8, 140-154.

Ramanathan, V., (1975), Greenhouse Effect Due to Chlorofluorocarbons: Climatic Implications, *Science*, 190, 50-52.

Richardson, L.F., (1922), *Weather prediction by numerical process*. Cambridge Univ. Press, reprinted Dover, 1965, 236 pp.

Schlosser, C.A., A. G. Slater, A. Robock, A. Pitman, K. Y. Vinnikov, A. Henderson-Sellers, N. A. Speranskaya, K. Mitchell, (2000), Simulations of a Boreal Grassland Hydrology at Valdai, Russia: PILPS Phase 2(d), *Monthly Weather Review*, 128, 301- 321.

Shao, Y., and Henderson-Sellers, A., (1995), Modeling Soil Moisture : A Project for Intercomparison of Land Surface Parameterization Schemes Phase 2(b), *JGR*, 101, 7227-7250.

Slater A.G., Schlosser C.A., Desborough C.E., Pitman A.J., Henderson-Sellers A., Robock A., Vinnikov K.Y., Mitchell K., Boone A., Braden H., Chen F., Cox P.M., de Rosnay P., Dickinson R.E., Dai Y.-J., Duan Q., Entin J., Etchevers P., Gedney N., Gusev Y.M., Habets F., Kim J., Koren V., Kowalczyk E.Y., Nasonova O.N., Noilhan J., Schaake S., Shmakin A.B., Smirnova T.G., Verseghy D., Wetzel P., Xue Y., Yang Z.-L., and Zeng Q., (2001), The Representation of Snow in Land Surface Schemes: Results from PILPS 2(d), *J Hydrometeorology*, 2, 7-25.

Smagorinsky, J., S. Manabe, and J.L. Holloway, (1965), Numerical Results from a Nine-Level General Circulation Model of the Atmosphere, *Monthly Weather Review*, 93, 727-768.

Soulis, E.D., and Sedlenieks, F.R, (2008), The MAGS Integrated Modeling System, in *Cold Region Atmospheric and Hydrologic Studies The Mackenzie GEWEX Experience, Volume 2: Hydrologic Processes*, Woo, M.K (ed.), Springer-Verlag, Berlin, 445-474.

Suess, H.E., (1953), *Natural Radiocarbon and the Rate of Exchange of Carbon Dioxide Between the Atmosphere and the Sea, in Nuclear Processes in Geologic Settings*, ed. National Research Council Committee on Nuclear Science, Washington, D. C, National Academy of Sciences, 52-56.

Twomey, S. A., (1977), The Influence of Pollution on the Shortwave Albedo of Clouds, *J. Atmospheric Sciences*, 34, 1149-52.

Tyndall, J., (1861), On the Absorption and Radiation of Heat by Gases and Vapours, and on the Physical Connection of Radiation, Absorption, and Conduction, *Phil. Mag,*. 4(22), 273–85.

Verseghy, D.L. (1991), CLASS-A Canadian land surface scheme for GCMs. I. Soil model. *Int. J.Climatol.*, 11 111-133.

Wang, W. C., Y. L. Yung, A. A. Lacis, T. Mo, and J. E. Hansen, (1976.), Greenhouse effects due to man-made perturbations of trace gases, *Science*, 194, 685-90.

Weart, Spencer R. (2003), *The Discovery of Global Warming*, Cambridge, MA, Harvard University Press.

Woo, M.K., (2008a), *Cold Region Atmospheric and Hydrologic Studies The Mackenzie GEWEX Experience, Volume 1: Atmospheric Dynamics*, Springer-Verlag, Berlin, 470p.

Woo, M.K., (2008b), *Cold Region Atmospheric and Hydrologic Studies The Mackenzie GEWEX Experience, Volume 2: Hydrologic Processes*, Springer-Verlag, Berlin, 507p.

Woo, M.K., Rouse W.R., Stewart. R.E., and Stone J.M.R., (2008), The Mackenzie GEWEX Study: a Contribution to Cold Region Atmospheric and Hydrologic Sciences, in *Cold Region Atmospheric and Hydrologic Studies The Mackenzie GEWEX Experience, Volume 1: Atmospheric Dynamics*, Woo, M.K (ed.), Springer-Verlag, Berlin, 1-23.

Wood, E. F., D. P. Lettenmaier, and V. G. Zartarian, (1992), A Land-Surface Hydrology Parameterization With Subgrid Variability for General Circulation Models, *J. Geophys. Res.*, 97(D3), 2717–2728.

Wood E.F., Lettenmaier D.P., Liang X., Lohman D., Boone A., Chang S., Chen F., Dai Y., Dicikinson R.E., Duan Q., Ek M., Gusev Y.M., Habets F., Irannejad P., Koster R., Mitchel K.E., Naonova O.N., Noilhan J., Schaake J., Schlosser A., Shao Y., Shmakin A.B., Verseghy D., Warrach K., Wetxel P., Xue X., Yang Z.-L., and Zeng Q., (1998), The Project for Intercomparison of Land-Surface parameterization Schemes (PILPS) Phase 2(c) Red-Arkansas River basin experiment, *Global and Planetary Change*, 19, 115-179.

Xue, Y., M.J. Fennessy, and P.J. Sellers, (1996), Impact of vegetation properties on U.S. Summer weather prediction. *J. Geophys. Res.*, 101D, 7419-7430.

Yang, Z.L., and R. E. Dickinson, (1995), Preliminary study of spin-up processes in land surface models with the first stage data of Project for Intercomparison of Land Surface Parameterization Schemes Phase 1(a), *JGR*, 1995 100, 16553-16578.

Zhao R.J., (1992), The Xinanjiang model applied in China, *J Hydrology*, 135, 371-381.

Chapter Three: A Modified ISBA Surface Scheme for Modeling the Hydrology of Athabasca River Basin with GCM-scale Data[1]

3.1 Introduction

The exchange of water, energy, and carbon fluxes between the atmosphere and the land surface directly controls global and regional climate patterns. Because of this, if we want to be able to make accurate predictions of climate at any spatial or temporal scale, we must be able to accurately model these exchanges. Furthermore, given the increase in concern in recent years that extreme climatic events may have become more frequent worldwide, one of the questions commonly asked of hydrologists today is to predict the effect of climate change on water resources, such as streamflow. Because the best tools we have to answer these questions are the predictions of General Circulation Models (GCMs), it is important that we are capable of reproducing the historically observed streamflows using data predicted by GCMs. Furthermore, it is preferable to use physical/process based rather than conceptual/empirical hydrologic models to minimize the need of calibrating model parameters because such parameters may become invalid when extended beyond the hydroclimatic regime of calibration experience.

Land surface processes were first included in GCMs in the 1960s when it was recognized that atmospheric processes are sensitive to the conversion of radiative energy

---

[1] A version of this chapter has been published as, Kerkhoven, E., and Gan, T.Y., (2006), A Modified ISBA Surface Scheme for Modeling the Hydrology of Athabasca River Basin with GCM-scale Data, Advances in Water Resources, 29(6), 808-826.

into sensitive and latent heat (Manabe, 1969). Over the last 40 years the development and application of ever more sophisticated models has shown that these water, energy, and carbon exchanges are tightly coupled (Pitman 2003). Land surface models can generally be classified into three categories (Foley, 1995): soil-vegetation-atmosphere transfer models (SVATs), terrestrial biogeochemistry models, and potential vegetation models. This paper is limited to the discussion of SVATs because these models focus on the water and energy processes of the hydrologic cycle rather than the dynamics of vegetation. Generally, SVATs partition the incoming solar and long wave radiation into ground, sensible, and latent heat fluxes and the movement of water between canopy, soil, snow storage, evapotranspiration, and runoff. Because of the wide variety of SVATs, numerous intercomparison studies have been undertaken, especially in the last 10 years (Wetzel and Chang, 1988; Henderson-Sellers, *et al.*, 1995; Chen *et al.*, 1997; Koster *et al.*, 1997; Liang *et al*, 1998, Lohmann *et al.*, 1998, Wood *et al.,* 1998; Slater et al., 2001; Schlosser *et al.*, 2001; Bowling *et al*, 2003; Luo *et al.*, 2003; Nijssen *et al.*, 2003;). These studies highlighted the importance of multi-year runs, interactions between evaporation and runoff formulations, the effect of sub-grid variability, the use of *a priori* parameters, and sensitivity to soil moisture and snow physics.

SVATs are usually based on one-dimensional physics meant for point or field scale applications, but are applied to scales on the order of 100 km^2 to 10,000 km^2. Since small-scale variations cannot be expected to be averaged out at larger scales, heterogeneity plagues SVAT applications, as it does all numerical modeling involving nonlinear relationships. Conversely, when a SVAT is applied to coarse grid cells, sub-

grid heterogeneity should be accounted for. Several studies had been conducted regarding the effects of sub-grid parameter variability on the output of SVATs (Charpentier and Groffman, 1992; Noilhan and Lacarrère, 1995). However, most studies were conducted in mid-latitude croplands or grasslands, usually under summer conditions, and over varying scales ranging from an 11.7 km^2 watershed (Famiglietti and Wood, 1995) to a typical GCM grid scale of up to 100,000 km^2 (Ghan *et al.*, 1997; Noilhan and Lacarrère, 1995).

Parameters that tend to have significant heterogeneity are hydraulic conductivity, soil moisture, precipitation, vegetative cover, snowcover, and topography. The simplest approach to this problem is to assign a single number to each parameter to represent the bulk or average value in the grid area. Noilhan and Lacarrère (1995) found that averaging the surface parameters produced better results than prescribing surface properties associated with a dominant land use. Beyond the aforementioned approach, there are two basic ways to account for sub-grid variability. If adequate data is available, a more realistic approach is to divide grids into sub-grids, each with its own set of parameters, or partition a grid cell into tiles, with each tile having distinct landuse and physics, just like Koster and Suarez (1992) who represented sub-grid variability by a 'mosaic' of homogenous vegetation 'tiles'. Effectively, this means that several parallel simulations are conducted and the resulting fluxes are combined using an area-weighted average. Alternatively, sub-grid parameter variation can be described statistically (Entekhabi and Eagleson, 1989; Mohr *et al.*, 2001; Sivapalan and Woods, 1995; Zhou, 1992). This paper draws from both these approaches.

The earliest SVATs used variations of the simple bucket scheme of Manabe (1969) in which the soil column is assumed to be analogous to a bucket of fixed size that produces runoff whenever it fills. More recently, many SVATs have implemented a variable bucket approach based on the Xinanjiang hydrological model (Yarnal *et al.*, 2001) to represent sub-grid variability of soil moisture and its effect on surface runoff generation. This method is used by ISBA (Habets *et al.*, 1999), VIC-3L (Liang *et al.*, 1996), and SEWAB (Mengelkamp *et al.*, 1999). The use of a Xinanjiang model based approach also requires the modeller to define a shape parameter that describes the sub-grid variation of soil moisture capacity. Unfortunately, this parameter is difficult to estimate accurately (Feyen *et al.*, 2006). This approach also only considers Dunne runoff mechanisms in which surface runoff only occurs when the soil becomes saturated. Liang and Xie (2001) developed a runoff parameterization scheme incorporating both Dunne and Horton runoff mechanisms and showed that this improved the performance of VIC-3L's runoff predictions during high rainfall events and reduced model sensitivity to the choice of the shape parameter.

With the above background, Section 2 presents the research objectives and methodology, Section 3 the study site and Section 4 the Hydrological routing. Section 5 presents the sub-grid heterogeneity in ISBA's runoff generation scheme, Section 6 the results, and Section 7 the summary and conclusions.

3.2 Research Objectives and Methodology

SVATs are often run in stand alone mode with no feedback to the atmosphere. Meteorological data used with SVATs in stand alone mode typically come from GCM

output, global re-analysis datasets, weather model forecasts, or regional re-analysis datasets. GCM output and global re-analysis data are typically available at spatial scales on the order of 1° to 3°, while weather model forecasts and regional re-analysis data are available at spatial scales of 10 to 50 km. Coarse resolution datasets are typically easier to acquire and easier to apply over extended time periods due to computer memory, storage, and speed limits. Furthermore, coarse resolution datasets usually offer global rather than regional coverage and cover much longer time periods. However, finer resolution datasets provide superior reproduction of local variation, particularly for precipitation. It would therefore be useful to develop techniques using coarse resolution datasets that produce results comparable to those of finer resolution datasets.

The primary objective of this paper is to improve the simulation of streamflow in the Athabasca River Basin (ARB) below Fort McMurray (Figure 3.1) by developing a new approach to the treatment of sub-grid moisture variability and its role in the production of surface and sub-surface runoff that can easily be incorporated into any SVAT without adding any new calibrated parameters. This approach is then applied to an existing SVAT which is then driven by observed data and data supplied by atmospheric models to simulate the interaction between the atmosphere and ARB. The local runoff predicted by the SVAT is then routed using a hydrological routing model to simulate the total streamflow at the basin outlet.

Two sources of meteorological data with a significant difference in spatial scale were used. The first is a set of archived forecasts from the Meteorological Survey of Canada's atmospheric model Global Environmental Multiscale Model (GEM), and the

second is the ERA-40 historical re-analysis data set developed by European Centre for Mid-range Weather Forecasts (ECMWF). The GEM archive covers Western Canada from October 1995 to September 2001 while ERA-40 has global coverage from January 1961 to August 2002. The GEM data has a spatial resolution of 0.33° latitude and 0.50° longitude and a temporal resolution of 3 hours. The ERA-40 data has a spatial resolution of 2.5° latitude and 2.5° longitude and a temporal resolution of 6 hours. The GEM dataset is typical for weather forecasting applications and the ERA-40 dataset is typical of GCM applications.

The SVAT used in this study was the Interactions between the Soil-Biosphere-Atmosphere (ISBA) scheme developed by Noilhan and Planton (1989). ISBA explicitly models the energy and water processes at the land surface using formulations based on the physics of each process and is therefore both physically and process based. Modelled processes include soil water and heat transfer, solid-liquid storage and phase changes, and vegetative interaction with soil water. Recently, the model has been extended to include a sub-grid runoff scheme (Habets *et al.*, 1999), a third soil layer (Boone *et al.*, 1999), and a multi-layer snow scheme (Boone and Etchevers, 2001).

The standard ISBA scheme requires eight parameters: soil clay content, soil sand content, fraction of land covered by surface water, depth of soil column, heat capacity of vegetation, and three stomatal resistance parameters. Important initial conditions, which are often unknown and therefore act as model parameters, are: initial soil moisture, initial soil ice content, and initial deep soil temperature. Surface albedo, Leaf Area Index

(LAI), vegetative cover fraction, and the vegetative roughness length can be treated as either input data or as calibrated parameters.

As the model complexity of a SVAT grows, so do the number of parameters. To overcome the challenge of parameter estimation, *a priori* relationships linking parameters with land surface and soil characteristics are available with many SVATs. The Ecoclimap land use dataset (Masson *et al.*, 2003) that includes all the physical parameters needed to run ISBA was used to define the surface parameters of ISBA. Ecoclimap, which covers the entire globe with a horizontal resolution of 30 arc-seconds (approximately 1 km), was derived by combining existing land-cover and climate maps, in addition to using the AVHRR satellite data. ISBA parameters are divided into two categories: four primary parameters that are specified at each grid point (% sand, % clay, vegetation type, and land-water ratio), and 22 secondary parameters, which are determined from the primary parameters.

Basin characteristics such as areal extent and the drainage network were derived from the 6 arc-second (approximately 200 m in resolution) Digital Elevation Model (DEM) of the Peace-Athabasca River Basin. To facilitate cross-referencing across the data sets, each DEM square was linked to its nearest land use data square, and each land use data square was linked to its nearest Meteorological grid square according to the following methodology:

1) Determine the portion of each meteorological square that is within the basin from the DEM dataset.

2) Cross reference the meteorological, DEM, and land use datasets to determine the distribution of land surface parameters in each meteorological grid square.

3) Generate a mosaic of land cover tiles by group averaging the land surface parameters (including DEM elevation) based on common land cover type in each meteorological square. For example, the land surface parameters for all grassland squares were averaged to derive a 'typical' grassland tile for each meteorological square.

4) For each land cover type, adjust the meteorological data for elevation. Surface pressure was adjusted using the hypsometric equation, temperature was adjusted using a moist lapse rate, longwave radiation was adjusted using the Stephan-Boltzmann equation, specific humidity was adjusted to keep relative humidity constant, and precipitation was adjusted using a relation derived by Golder Associates [12] for the region around Fort McMurray, Alberta in the Athabasca River Basin in which precipitation is increased by 1% for every 12.5 metre increase in elevation to account for orographic effects.

5) Run the SVAT once for each land cover type present in each meteorological grid square.

6) Aggregate the runoff generated by each land cover tile in each grid of the flow routing network and route the total predicted runoff through the hydrological routing model.

Representing the land cover as a mosaic of tiles and adjusting the meteorological data for each tile's mean elevation can account for a large part of the spatial heterogeneity of land cover and topography. This accounting is primarily limited by the variation in topography within each land cover tile.

3.3 Athabasca River Basin (ARB)

ARB is of key interest to the province of Alberta mainly because of its multi-billion dollar, oil sand industry at Fort McMurray. The basin area according to the Water Survey Canada is 133 000 km^2, and its main channel length is about 1154 km (Kellerhals *et al.*, 1972). ARB has a continental climate with significant seasonal variation in temperature, with daily mean temperature dropping below freezing after mid-October and remaining below zero until early April. Typical January temperature is about -20°C while that of July is about 17°C. Typically, June to October are the wet months in ARB, with an average total precipitation of about 300 mm, while winter and spring only experience about 150mm of precipitation in an average year. Coniferous forest, mixed wood and deciduous forest are the dominant vegetation especially in the upland areas (elevation ranging from 350 to 850m) and willow brush, shrubs, black spruce and sphagnum moss dominate the lowland areas which is often poorly drained. For lowland dominated by muskeg, interflow tends to constitute a significant component of the sub-surface runoff. The southwest corner of the basin extends well into the Rocky Mountains (Golder Associates, 2002). Dominant surficial soils are glacial soils (silt, clay and sands), glaciolacustrine soils (clay loam to heavy clay) and glaciofluvial soils (sandy loam to sands) (Fulton, 1995).

Natural watersheds in many parts of ARB are characterized by peat soils that vary in depth from 0.3m (upland terrain) to over 1 m (lowland terrain). Upland watersheds typically have ground slopes of 0.5% or more, while lowland areas typically have an average slope of less than 0.5%. Lowland areas normally have thick peat soils with near-surface groundwater table. As a result, a significant amount of runoff (e.g., could be more than 70%) from lowland watersheds occurs as interflow through deep peat, or for areas dominated by muskeg, irrespective of the sub-soil types (Golder Associates, 2002).

3.4 Hydrological Routing

The 6 arc-second (200 m) resolution DEM of the Peace-Athabasca Basin developed by National Water Research Institute was used to determine the extent and flow network of the ARB. Flow directions were determined using a simple steepest descent algorithm. With the flow directions determined, the basin extent was determined by finding all the squares in the DEM that drained to the outlet. The area of the Athabasca River Basin below Fort McMurray was calculated to be 133 606 km^2 with a main channel length of 1119 km.

Channel routing was performed using the Ponce and Yevjevich (1978) variation of the Muskingum-Cunge scheme (Cunge, 1969). The scheme is essentially a kinematic routing scheme that approximates a diffusive wave by equating the numerical diffusion of the scheme with the physical diffusion. This scheme was applied to each of the hydrologic grid squares in the basin starting with the farthest upstream, and ending at the basin outlet. Channel reach lengths are on the order of 2000 m and all channel cross-sections are assumed rectangular in shape. Channel characteristics were assumed to be

simple power functions of drainage area. These functions were determined from Kellerhals *et al.* (1972), which includes channel characteristics for 21 reaches in the Athabasca River Basin.

3.5 Modification to ISBA's Sub-grid Heterogeneity Runoff Scheme

Habets et al. (1999) developed a sub-grid runoff scheme that statistically considers the sub-grid heterogeneity of the moisture capacity of the soil, x (metres), to follow the Xinanjiang distribution (Zhao, 1992),

$$F(x) = 1 - \left(1 - \frac{x}{x_{\max}}\right)^{\beta} \qquad 0 \le x \le x_{\max} \tag{3.1}$$

$$\frac{x_{ave}}{x_{\max}} = \frac{1}{\beta + 1} \tag{3.2}$$

where β is an empirical parameter, and $F(x)$ is the cumulative probability distribution of x. This distribution is completely defined by the maximum (x_{max}) and mean (x_{ave}) values of x. Effectively, this scheme acts like a multi-bucket scheme in which the Xinanjiang distribution defines the distribution of bucket sizes and surface runoff occurs whenever a bucket fills to capacity. When the modellers set the parameter β they are effectively defining the maximum bucket size (or soil depth) in the grid. A gravity drainage scheme was also developed to represent sub-surface runoff,

$$Q = C_3 (w - w_{drain}) D \tag{3.3}$$

where Q is the sub-surface runoff in metres/second, D is the depth of the deep soil layer in metres, w is the soil water content, w_{drain} is the minimum soil water content where drainage will occur, and C_3 is a coefficient and is a function of soil texture and has units

of seconds^{-1}. ISBA therefore treats sub-surface runoff as a linear reservoir. In ISBA, w_{drain} is not a property of soil texture but an empirical parameter that must be calibrated. Although w_{drain} operates similarly in the model to the concept of the residual soil moisture content of a gravity drained soil the two should not be confused with each other. Furthermore, because sub-surface runoff is treated as a linear reservoir, it was found that ISBA tends to drain too quickly, leading to excessive peaks and steep recessions, which was also the experience of researchers from the University of Waterloo (e.g., E. Rodriquez, personal communication). This approach may work well in French watersheds where ISBA's runoff scheme was developed and specifically tested (Habets *et al.*, 1999), but not so in ARB, which is relatively dry.

The ISBA runoff scheme requires two parameters: the Xinanjiang distribution parameter, β, and the minimum soil water content for drainage, w_{drain}. Both of these parameters need to be calibrated by the user and therefore become problematic when applied to large river basins where they could vary widely. To eliminate this difficulty, these two parameters were removed by altering the basic approach to sub-grid moisture variability in such a way that they could be calculated directly from the soil characteristics.

It is here proposed that the Xinanjiang distribution be applied to sub-grid variation of residual soil moisture rather than the traditional variation in soil moisture capacity. This represents a significant conceptual departure. Whereas the traditional application of the Xinanjiang distribution may be conceived as a distribution of buckets of various sizes all filled to the same level, this application suggests a number of identical buckets filled

to a distribution of different levels. This change allows for statistical representations of soil moisture variability that can be integrated analytically as shown below.

First, runoff was made a function of soil water retention, S,

$$S = \left(\frac{w - w_r}{w_{sat} - w_r} \right) \tag{3.4}$$

where, w is the soil water content, w_r is the residual water content, and w_{sat} is the saturated water content. The Xinanjiang distribution is used to represent the sub-grid variation in soil water retention. Because the maximum possible retention is 1, and since the model predicts the average water retention at each time step, β can be derived from Equation 3.2 for each time step as,

$$\beta = \frac{1}{S_{ave}} - 1 \tag{3.5}$$

Figure 3.2 is a graphical representation of the new surface runoff mechanism.

The assumption that sub-grid moisture variation can be approximated by the Xinanjiang probability distribution can be shown to be reasonable by comparing its coefficient of variation (CV) with that of observed field studies. Several field studies have found an inverse relationship between CV and the mean of soil moisture content (Bell *et al.*, 1980; Charpentier and Groffman, 1992; Famiglietti *et al.*, 1999). Famiglietti et al. (1999) found that in a field study in Central Oklahoma the CV decreased from around 1 for dry soils (moisture contents of approximately 0.05) to near 0 for wet soils (moisture contents over 0.40). The coefficient of variation for the Xinanjiang distribution for soil water retention can be shown to be

$$CV^2 = \frac{1 - S_{ave}}{1 + S_{ave}} \tag{3.6}$$

The Xinanjiang distribution therefore predicts that the coefficient of variation for a dry soil (S_{ave} equals 0, or soil moisture equals the residual moisture content) is 1 and for a saturated soil is 0. The Xinanjiang distribution therefore represents a reasonable description of soil moisture variation.

Any new depth of water added to the soil column is first converted to additional soil water retention, ΔS,

$$\Delta S = \frac{P_{ave} \Delta t}{D_{eff}(w_{sat} - w_r)} \tag{3.7}$$

where P_{ave} is the average intensity of rainfall in metres/second, Δt is the model time step in seconds, and D_{eff} is the effective depth of the soil in metres. In the runoff scheme of Habets *et al.* (1999) the entire root depth was used to calculate runoff, effectively assuming that additional water penetrated the rooting depth in the model time step. This may not be realistic for vegetative covers with deep roots and soils with low permeability. To account for this, an effective depth was calculated based on the kinematic wave velocity of the wetting front of Smith (1983),

$$D_{eff} = \frac{K_{sat} - K(w)}{w_{sat} - w} \Delta t \tag{3.8}$$

where, K_{sat} and $K(w)$ are the saturated and unsaturated hydraulic conductivities respectively with units of metres/second.

From Equation 3.1 with x replaced by S and noting that S_{max} is always 1, the soil moisture distribution is the sum of the initial soil moisture distribution plus the additional water, ΔS,

$$S = 1 - (1 - F)^{1/\beta} + \Delta S \tag{3.9}$$

Surface runoff, expressed in terms of a change in soil moisture retention in a single model time step, S_r, is equal to the area where S exceeds 1,

$$S_r = \int_{F_1}^{1} \left[1 - (1 - F)^{1/\beta} + \Delta S - 1\right] dF \tag{3.10}$$

where, F_1 is the point where S in Equation 3.9 equals 1,

$$F_1 = 1 - \Delta S^{\beta} \tag{3.11}$$

Integrating Equation 3.10 yields,

$$S_r = \frac{\Delta S^{\beta+1}}{\beta + 1} \tag{3.12}$$

Equation 3.12 is only valid when ΔS is less than or equal to 1. When the additional water exceeds the storage capacity of the soil column to the effective depth, runoff is simply,

$$S_r = S_{ave} + \Delta S - 1 = \Delta S - \frac{\beta}{\beta + 1} \tag{3.13}$$

In Habets *et al.* (1999), snowmelt and rainfall were each assumed to be evenly distributed over the grid square. To account for spatial distribution of these important quantities, melting snow was assumed to be uniformly distributed over the snow covered area only, while rainfall was assumed to follow an exponential distribution after Entekhabi and Eagleson (1989),

$$f(i) = \frac{k}{P_{ave}} exp\left(-\frac{ki}{P_{ave}}\right) \quad i \geq 0 \tag{3.14}$$

where, k is the fraction of the total area that receives rainfall, and i is the rate of rainfall in metres/second. For simplicity, k was assumed to be 1. Substituting i for P_{ave} in Equations 3.7, 3.12, and 3.13 and integrating over Equation 3.14 yields,

$$S_r = \frac{k^2}{P_{ave}(\beta+1)}\left(\frac{\Delta t}{D_{eff}(w_{sat}-w_r)}\right)^{\beta+1}\int_0^{i_{max}} i^{\beta+1} exp\left(-\frac{ki}{P_{ave}}\right)di + \frac{k^2}{P_{ave}}\int_{i_{max}}^{\infty}\left(\frac{i\Delta t}{D_{eff}(w_{sat}-w_r)} - \frac{\beta}{\beta+1}\right)exp\left(-\frac{ki}{P_{ave}}\right)di \tag{3.15}$$

where, i_{max} is the rate of rainfall, in metres/second, where ΔS is equal to 1,

$$i_{max} = \frac{D_{eff}(w_{sat}-w_r)}{\Delta t} = K_{sat} - K(w) \tag{3.16}$$

Equation 3.15 represents the surface runoff due to exponentially distributed precipitation over an area in which soil water retention is distributed according to the Xinanjiang distribution.

The first term in Equation 3.15 is similar to the definition of Euler's lower incomplete gamma function, $\gamma(a,x)$, from which the integral, after some simplification, can be shown to be,

$$S_r = \frac{\Delta S^{\beta+1}}{\beta+1}\frac{\gamma(\beta+2, k/\Delta S)}{k^{\beta}} + exp\left(-\frac{k}{\Delta S}\right)\left[\Delta S + \frac{k}{\beta+1}\right] \tag{3.17}$$

It should be noted that i_{max} is equal to the maximum rate that water can infiltrate into the soil. The first term in Equation 3.17 therefore represents locations where the rate of precipitation is less than the infiltration capacity and runoff occurs because the soil

becomes saturated (Dunne runoff). The second term represents locations where the rate of precipitation exceeds the infiltration capacity of the soil (Horton runoff). Equation 3.17 therefore includes both Dunne and Horton runoff mechanisms.

This method eliminates β as a user defined parameter. The other parameter was eliminated by assuming that w_{drain} equals w_r, which can be calculated from the soil texture using one of several pedo-transfer functions. Drawing an analogy to the Brooks-Corey equation for hydraulic conductivity of unsaturated soils (Brooks and Corey, 1964), Equation 3.3 for subsurface runoff was altered into a function of soil water retention,

$$Q = C_3 \left(\frac{w - w_r}{w_{sat} - w_r} \right)^{3+\frac{2}{\lambda}} D = C_3 D S^n \tag{3.18}$$

where, λ is the Brooks-Corey pore-size index which can also be calculated from the soil texture using a pedo-transfer function. This general approach has also been used to represent sub-surface flow in the VIC model (Huang and Liang, 2006). If we continue our assumption that the sub-grid distribution of soil water retention follows the Xinanjiang distribution, the total subsurface runoff produced is,

$$Q = \int_0^1 Q(S) f(S) dS \tag{3.19}$$

where, by differentiating Equation 3.1,

$$f(S) = \beta (1 - S)^{\beta - 1} \tag{3.20}$$

Therefore,

$$Q = \beta C_3 D \int_0^1 S^n (1 - S)^{\beta - 1} dS \tag{3.21}$$

Equation 3.21 represents subsurface runoff from an area in which soil water retention, S, follows the Xinanjiang distribution. The integral in Equation 3.21 is similar in form to the Euler's beta function, from which the solution to Equation 3.21 can be found to be,

$$Q = C_3 D \frac{\Gamma(n+1)\Gamma(\beta+1)}{\Gamma(n+\beta+1)} \tag{3.22}$$

where $\Gamma(x)$ is Euler's gamma function, where $\Gamma(x)=(x-1)!$ when x is an integer. This equation is highly non-linear and produces much lower runoff rates under dry conditions than the original ISBA scheme. Under moist conditions, when β approaches 0, the two methods will predict similar runoff rates.

3.6 Discussion of Results

3.6.1 GEM results

The GEM meteorological data was divided into a calibration period (October 1996 to June 1998) and a verification period (July 1998 to September 2001). The calibration and verification runs were both initialized on 1 October 1995. One set of calibration and verification runs were made using the Original ISBA (OISBA) scheme and the Modified ISBA scheme (MISBA) described in Section 5.

In the calibration runs, the only parameters that were calibrated were the β and w_{drain} parameters of the sub-grid runoff scheme developed by Habets *et al.* (1999). The calibrated values were 1.0 and 0.1 respectively. All other parameters were defined by the Ecoclimap dataset. MISBA, therefore, had no calibrated parameters and is included in the calibration primarily for comparison purposes.

Figure 3.3a shows the calibration hydrographs for both OISBA and MISBA. OISBA responds very quickly to precipitation and snowmelt events, and predicts a much steeper recession curve with much lower winter streamflows than are observed. OISBA is particularly sensitive to mid-winter ablation events, predicting unrealistically high runoff. MISBA, however, matches the observed streamflow much better, even though it has fewer calibrated parameters. This difference is primarily due to the way MISBA treats sub-surface runoff because in both cases runoff is dominated by the sub-surface schemes. OISBA effectively uses a linear reservoir approach, while MISBA uses a non-linear approach. This non-linear approach results in a longer retention time and a more realistic recession curve. Even with the sub-grid runoff scheme developed by Habets et al. (1999), the soil rarely becomes moist enough to produce any noticeable surface runoff. MISBA, although dominated by sub-surface runoff, does predict some surface runoff during periods of rapid snowmelt and intense precipitation and this runoff was found to improve MISBA's performance.

Calibration statistics are summarized in Table 3.1. MISBA outperforms OISBA significantly in terms of all four measures: coefficient of determination, absolute error (ABSE), root-mean-square error (RMSE), and log error.

$$ABSE = \frac{\sum |Q_{obs} - Q_{sim}|}{\sum Q_{obs}} \tag{3.23}$$

$$RMSE = \frac{\sqrt{\sum (Q_{obs} - Q_{sim})^2}}{\sum Q_{obs}} \tag{3.24}$$

$$\log error = \frac{\sum |\ln Q_{obs} - \ln Q_{sim}|}{\sum \ln Q_{obs}} \tag{3.25}$$

While the coefficient of determination and the absolute error are sensitive to all flows, the root-mean-square and log error statistics are particularly sensitive to peak and low flows, respectively. The fact that MISBA is better by all four measures indicates that it represents a fundamental improvement over OISBA mainly because it more accurately models the sub-surface runoff of ARB dominated by interflow.

Figure 3.3b shows the verification hydrographs for both OISBA and MISBA. From Table 3.1 it can be seen that both schemes improve significantly, especially OISBA, in terms of the coefficient of determination. This improvement in performance during verification is due to a combination of the fact that the calibration period had a much shorter spin up time, the fact that the verification years were significantly drier than the calibration years, and the fact that almost all of the parameters were defined *a priori* from the Ecoclimap data set. Because the verification years are drier, OISBA's tendency to over predict runoff during the more extreme events is muted but it can still be seen in the log error statistic. Despite the improvement of OISBA, MISBA still outperforms OISBA by all four measures.

3.6.2 ERA-40 Results

For the ERA-40 OISBA simulation the calibrated values for β and w_{drain} from the GEM simulation were used, while for MISBA all parameters were defined by the Ecoclimap data set and so no parameters were calibrated. Comparing the error statistics in Table 3.1 for the GEM and ERA-40 simulations during the overlap period (October

1995 to September 2001) reveals similar overall skill with the ERA-40 simulations generally performing better during the GEM calibration period and worse during the verification period. Unlike the GEM simulations, there is no significant improvement in performance between the GEM calibration and GEM verification periods in the ERA-40 simulations and therefore Table 3.1 only shows the error statistics for the full overlap period.

Figure 3.4 is a plot of the full hydrograph from January 1961 to August 2002 for the OISBA/ERA-40 simulation. The OISBA hydrograph is generally a series of runoff events with rapid recession and rarely predicts sustained flow over 1000 m^3/s during the summer months. During the winter months it is quite common for the OSIBA hydrograph to approach zero flow interspersed with one or two significant mid-winter runoff events. Figure 3.5 is the same as Figure 3.4 but for the MISBA/ERA-40 simulation. The MISBA hydrograph matches the observed hydrograph much better than OISBA as evidenced by the error statistics in Table 3.1, which are roughly 40% lower for MISBA than OISBA. As mentioned in Section 3.6.1, most of this improvement is due to the changes to the treatment of sub-surface runoff, which dominates the long-term flow behaviour in the ARB. MISBA reproduces the recession of streamflow after a peak much better than OISBA, particularly when flows drop below approximately 1000 m^3/s. Figure 3.6 shows the monthly variation of monthly mean flow and its standard deviation for the OISBA/ERA-40 and MISBA/ERA-40 simulations. MISBA reproduces the annual variation of monthly flows better than OISBA from August to April. Most

notable is the significant improvement in the reproduction of the late winter and early spring flows and the annual variation in the standard deviation of monthly flows.

Figures 3.7 shows the daily variation of mean flow and its standard deviation for the OISBA/ERA-40 and MISBA/ERA-40 simulations. Once again, MISBA reproduces the mean annual hydrograph and its standard deviation much better than OISBA, particularly the standard deviation, which OISBA consistently overestimates. From the observed record it can be seen that peak flows occur at three different times. The first is in late April and is due to the melting of snow in the lowlands, the second occurs in June and is due to snowmelt in the mountainous southwest, and the third is in July and is due to convective summer storms. It is this last period that usually results in the annual maximum flow rate. Both OISBA and MISBA reproduce the first two peaks but miss the third one almost entirely. This is most likely due to the coarse resolution of the ERA-40 data, which tends to diffuse the convective storms both spatially and temporally and therefore significantly underestimates their intensity. The OISBA simulation adds a new peak in March that does not correlate to any observed flows in the basin.

Statistical t- and F-tests were performed for each day for both the OISBA and MISBA simulations. The t- and F-tests are designed to show statistically whether the means and variances respectively of two samples (simulated and observed streamflow for each day) are drawn from the same population. The t-test is often chosen as a 2-sided test while the F-test as a 1-sided test, but usually both at a significant level, α, of 0.05. Test statistics greater than the significant level (e.g., $\text{t-test}_{0.025,40} = \pm 2.0211$, $\text{F-test}_{0.05,40,40} = 1.69$) causes the hypothesis that two samples coming from the same population to be

rejected, and vice versa. Solid circles indicate the days on which the simulations passed the t-test in Figures 3.7a and 3.7c and the F-test in Figures 3.7b and 3.7d. OISBA passed the t-test for 121 days of the year and the F-test 67 days of the year while MISBA passed the t-test 202 days of the year and the F-test 235 days of the year. The superior t-test and F-test probabilities for MISBA indicate that streamflows predicted by MISBA reflect the statistical properties of the observed flows much better than OISBA.

3.6.3 Results of ERA-40 downscaled with respect to GEM Data

At 2.5^{o} x 2.5^{o}, ERA-40 data is of GCM resolution, and so downscaling the data could potentially improve the simulation of ARB's streamflow. Even though there are complex, dynamical approaches, only simple statistical downscaling schemes will be considered here. This approach is computationally modest, parsimonious, but lacking in physical processes. Usually the idea is to develop empirical relationships either between large-scale atmospheric variables and sub-grid elements of local surface environment, or variables of GCM scale to local scale. The complexity of this approach would depend on the climate variables considered, e.g., downscaling precipitation is more involved than downscaling temperature data, since precipitation is affected by both local and mesoscale processes and skewed distributed. Downscaling precipitation could involve large-scale predictors such as sea level pressure, 500 mb geopotential heights, or relative humidity (Yarnal *et al.*, 2001).

In our situation, given that the GEM archive is of much higher resolution than ERA-40 data, instead of using predictors as mentioned above, we can directly compare the mean monthly meteorological GEM data for each grid point with the mean monthly

meteorological data for the nearest ERA-40 grid point during the period that the two datasets overlap (October 1995 to September 2001). Downscaling was achieved by simply shifting the ERA-40 data to match the monthly mean of each GEM point. For example, if the January precipitation of a GEM point was 10% higher than its closest ERA-40 point during the overlap period, all the January ERA-40 precipitation rates for this point were increased by 10%. Radiation, humidity, air pressure, and wind speed data were handled in the same way while temperature was simply shifted by the difference in mean temperature.

This algorithm does not address limitations of ERA-40's temporal scales and spatial variability and therefore should not improve the simulation of summer storms. However, it will better represent the spatial distribution of land cover, topography, and local climate and should therefore improve the simulation of snowmelt and evaporation. For the OISBA simulation, the calibrated values for β and w_{drain} from the GEM simulation were used. Comparing the error statistics in Table 3.1 for the GEM and ERA-40/GEM simulations during the overlap period shows that the ERA-40/GEM simulations are just as accurate as the GEM simulations. This suggests that this simple algorithm accounts for the majority of the heterogeneity between the ERA-40 and GEM scales. Comparing the error statistics for the ERA-40 and ERA-40/GEM simulations shows that the ERA-40/GEM simulations are superior by every error measure. The improvement in the OISBA simulation however is not enough to surpass the performance of the MISBA/ERA-40 simulation.

Figures 3.9 and 3.10 are similar to Figures 3.4 and 3.5 except they show the ERA-40/GEM hydrographs. The OISBA hydrograph is still dominated by a series of peaks and troughs but it is not as extreme as in the OISBA/ERA-40 hydrograph. The most noticeable improvement in the MISBA hydrograph is the reduction of a number of anomalous peaks in the MISBA/ERA-40 hydrograph (Figure 3.5) without compromising the non-anomalous peaks.

Figure 3.11 is similar to Figure 3.6 except it shows the ERA-40/GEM mean monthly hydrographs. Again, the improvement in the OISBA plot is significant but it is not enough to surpass the MISBA/ERA-40 simulation (Figure 3.6b) and the MISBA simulation greatly reduces the most significant aberrations of the ERA-40 simulation. Figure 3.12 is similar to Figure 3.7 except it shows the ERA-40/GEM mean daily hydrographs. Although the standard deviations of flow in the OISBA case are greatly improved they are still more severe than the MISBA/ERA-40 simulation (Figure 3.7d). Although the anomalous March peak is greatly reduced from the OISBA/ERA-40 simulation it still represents a significant mode for producing a maximum annual flow and thus compromises the quality of the OISBA/ERA-40/GEM predictions for these flows. Once again, the MISBA/ERA-40/GEM simulation is the best but, as expected, it still cannot consistently account for the observed runoff from convective summer storms partly because of the coarse resolution of ERA-40 data.

Solid circles indicate the days on which the ERA-40/GEM simulations passed the t-test in Figures 3.12a and 3.12c and the F-test in Figures 3.12b and 3.12d. OISBA passed the t-test for 182 days of the year and the F-test 133 days of the year while

MISBA passed the t-test 287 days of the year and the F-test 242 days of the year. Again, the MISBA/ERA-40/GEM simulation is the best of all the simulations in this study while the OISBA/ERA-40/GEM performs much better than the OISBA/ERA-40 simulation but still not as well as MISBA/ERA-40.

Figure 3.13 is similar to Figure 3.8 except it shows the frequency plots for the ERA-40/GEM simulation. The mean and minimum annual flow plots are virtually indistinguishable from their ERA-40 counterparts. The maximum annual flows, however, are both significantly lower than in the ERA-40 simulations. Figure 3.13c shows a near perfect match between observed and simulated, but as was previously stated, this is compromised by its heavy bias towards spring runoff events. For example, from 1961 to 2002 the earliest observed peak annual flow was April 30. This is also the earliest peak flow from the MISBA/ERA-40/GEM simulation, but the OISBA/ERA-40/GEM simulation includes 7 annual maximums before this date including three in March. The MISBA/ERA-40/GEM simulation itself is biased towards May peak flows with approximately one third of the annual peaks occurring in this month. The observed record shows only one annual peak flow occurring in May.

3.7 Summary and Conclusions

A modelling scheme was developed to simulate historically observed streamflows in a large northern basin of 133,000 km^2 in area, the Athabasca River Basin (ARB), using gridded meteorological data from both a numerical weather prediction model, the Canadian GEM model, and a GCM scale re-analysis data called ERA-40 of ECMWF. Modifications were made to the original land surface model ISBA of Météo France,

referred to as OISBA, so that the modified, MISBA, could better simulate the sub-surface runoff of ARB dominated by muskeg hydrology with an emphasis on the treatment of sub-grid heterogeneity.

Heterogeneity of land cover was accounted for by using a variation of the mosaic approach. The effects of heterogeneity of rainfall, and soil moisture on surface and sub-surface runoff were treated statistically. New highly non-linear formulations for surface and sub-surface runoff were derived based on the assumption that sub-grid variation of soil water retention follows the Xinanjiang distribution. In the process, two previously user defined parameters became internal functions. Despite this reduction in the number of calibrated parameters, MISBA performed significantly better than OISBA by all statistical measures for both GEM and ERA-40 data. Although the method proposed was applied to ISBA, it could easily be applied to any SVAT as long as soil texture data is available.

Simulations using the GCM scale ERA-40 data set showed that it is possible to reconstruct the observed streamflow in a large river basin without using downscaling methods. The simulations were particularly effective in reproducing the onset of snowmelt runoff, autumn and winter baseflow recession, and the annual variation of mean and minimum flows. The simulations could not account for runoff produced by convective summer storms due to the low temporal (6-hourly) and spatial (2.5^{o} x 2.5^{o}) resolutions of ERA-40 data. As a result of this, the model predictions of maximum annual flows are biased towards peaks generated by snowmelt events. Despite this

limitation, the simulated maximum flows still indicate the variation of size of the dominant annual spring runoff flood wave very well.

Finally, a simple downscaling algorithm was employed to downscale the ERA-40 data to the GEM data's scale, e.g., ERA-40/GEM, and thus improve the model's accounting of local variation of land cover, topography, and climate. Again, MISBA/ERA-40/GEM significantly outperformed OISBA/ERA-40/GEM. The overall simulations showed significant improvement in modelling seasonal variation of streamflow but they did not significantly improve the timing of snowmelt runoff, baseflow recession, or the annual variation of mean and minimum flows. The simple downscaling approach could not effectively account for the high spatial variability of summer convective storms. Further refinement of the model's predictions would require either an algorithm for downscaling ERA-40's to a scale appropriate for convection, or a method for calculating the effective area and duration of a storm, which is beyond the scope of this study. Both these approaches would require significantly more data than is currently readily available and would not necessarily result in more accurate predictions under future climate scenarios since the algorithms used would have to be calibrated from historical data and may only be valid for the climate they were derived from.

Table 3.1 - Calibration and verification errors. All errors are relative to mean observed flow.

			R^2	Absolute Error	RMS Error	Log Error
GEM	Calibration	Original ISBA	0.290	0.604	0.808	0.159
		Modified ISBA	0.592	0.402	0.576	0.078
	Verification	Original ISBA	0.750	0.350	0.501	0.091
		Modified ISBA	0.774	0.263	0.438	0.050
ERA-40	GEM period	Original ISBA	0.458	0.554	0.880	0.131
		Modified ISBA	0.622	0.355	0.643	0.062
	1961-2002	Original ISBA	0.323	0.608	0.928	0.128
		Modified ISBA	0.565	0.376	0.628	0.060
ERA/GEM	GEM period	Original ISBA	0.577	0.441	0.717	0.104
		Modified ISBA	0.771	0.285	0.495	0.050
	1961-2002	Original ISBA	0.431	0.490	0.754	0.103
		Modified ISBA	0.680	0.313	0.515	0.051

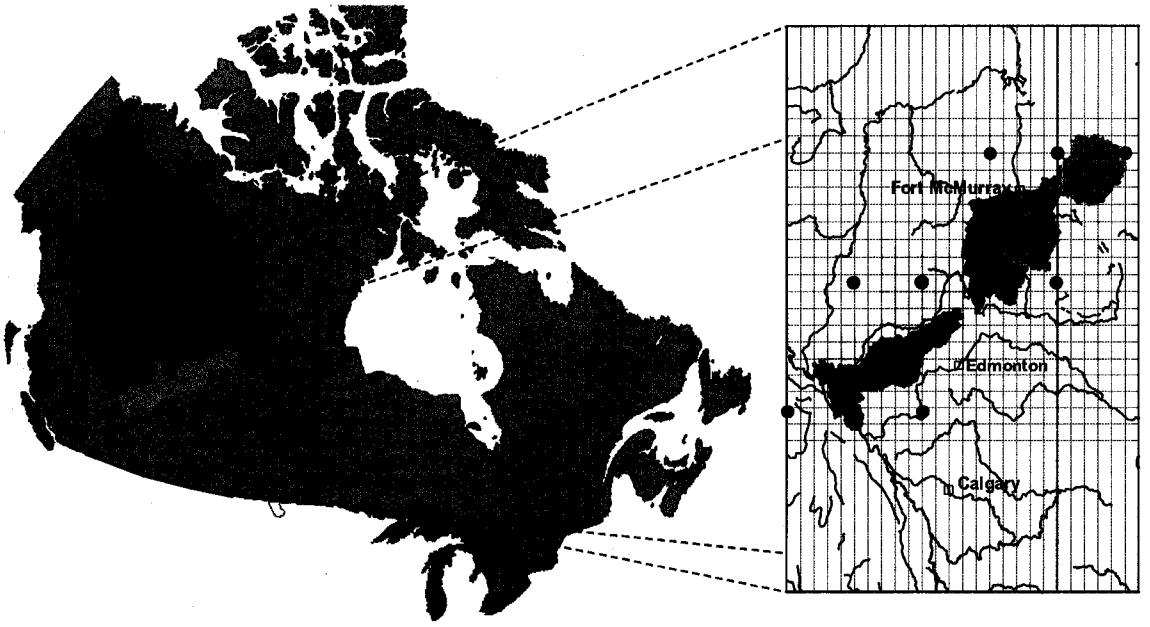

Figure 3.1 - DEM derived extent of the Athabasca River below Fort McMurray Basin with GEM grid (dashed lines) and ERA-40 grid (solid circles) overlaid.

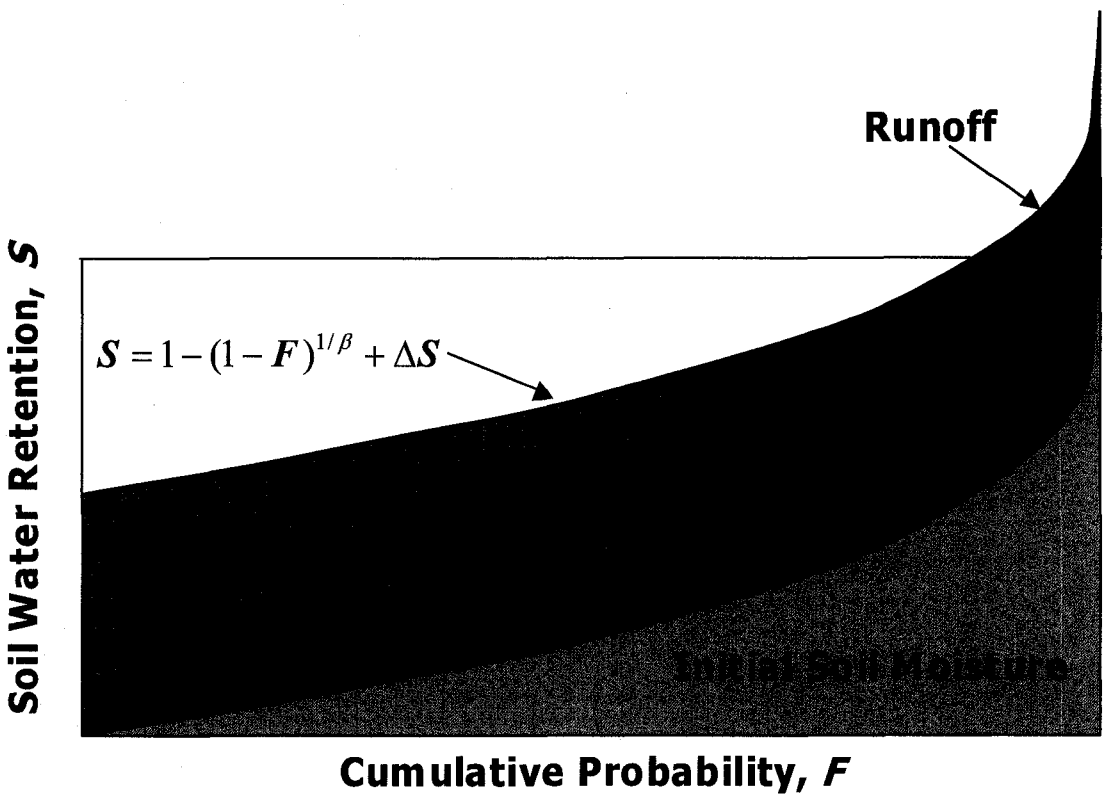

Figure 3.2 - Modified ISBA Runoff mechanism. ΔS is the quantity of new soil moisture expressed in terms of additional soil water retention.

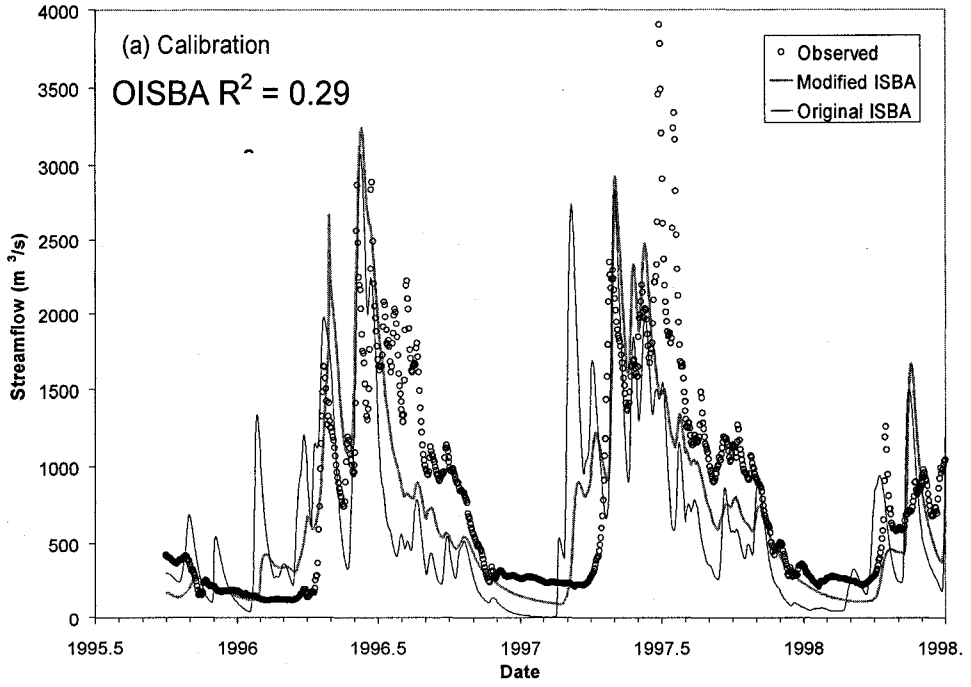

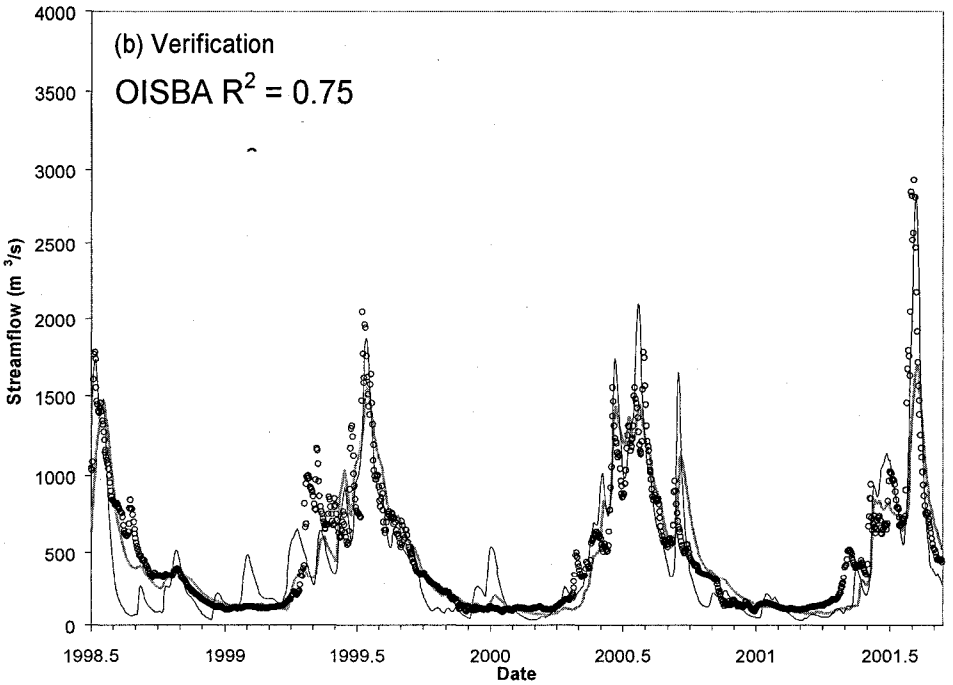

Figure 3.3 - ISBA/GEM Calibration (1995-1998) and verification (1998-2001) Hydrographs

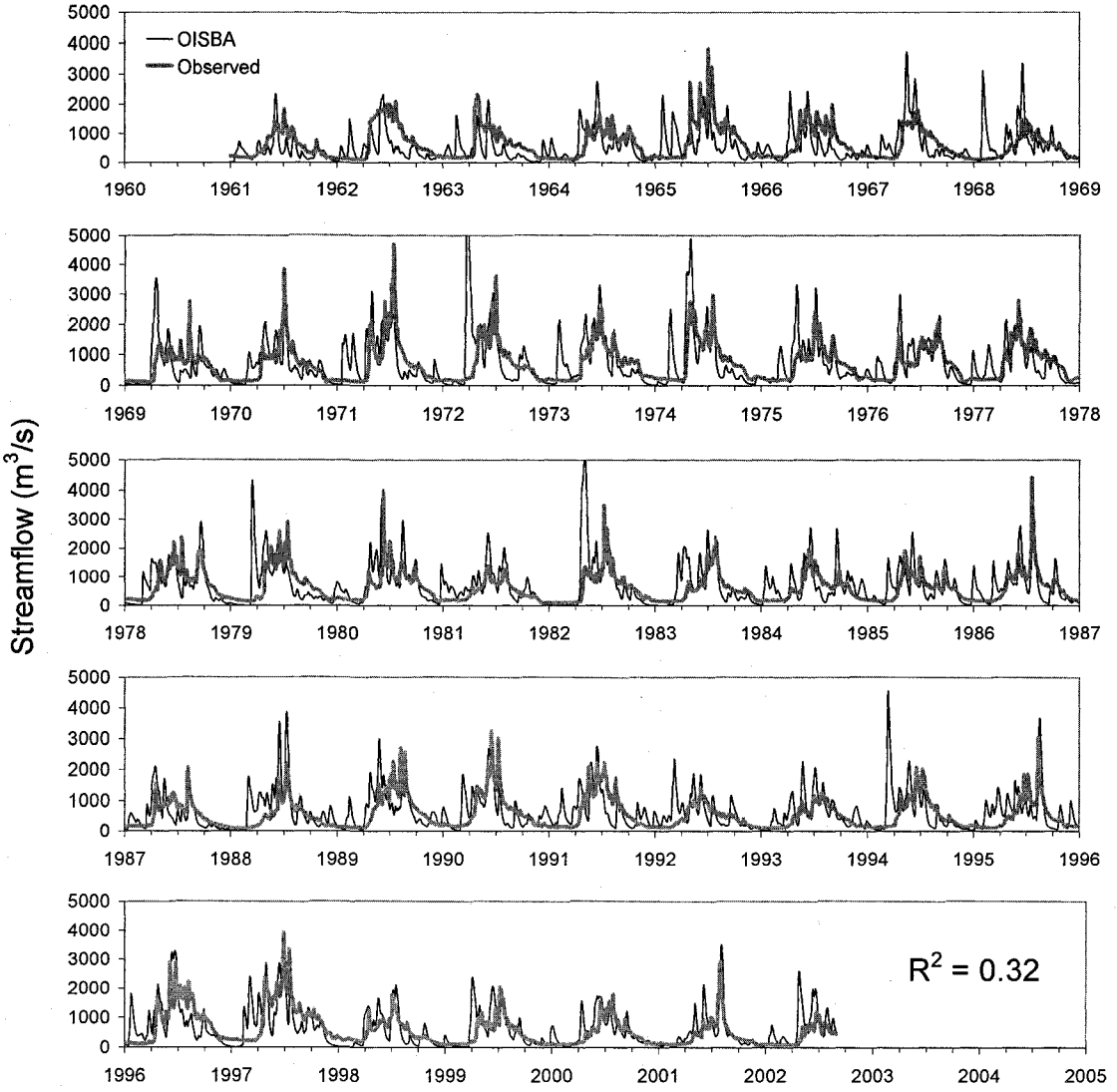

Figure 3.4 - Observed and OISBA/ERA-40 Simulation Hydrographs

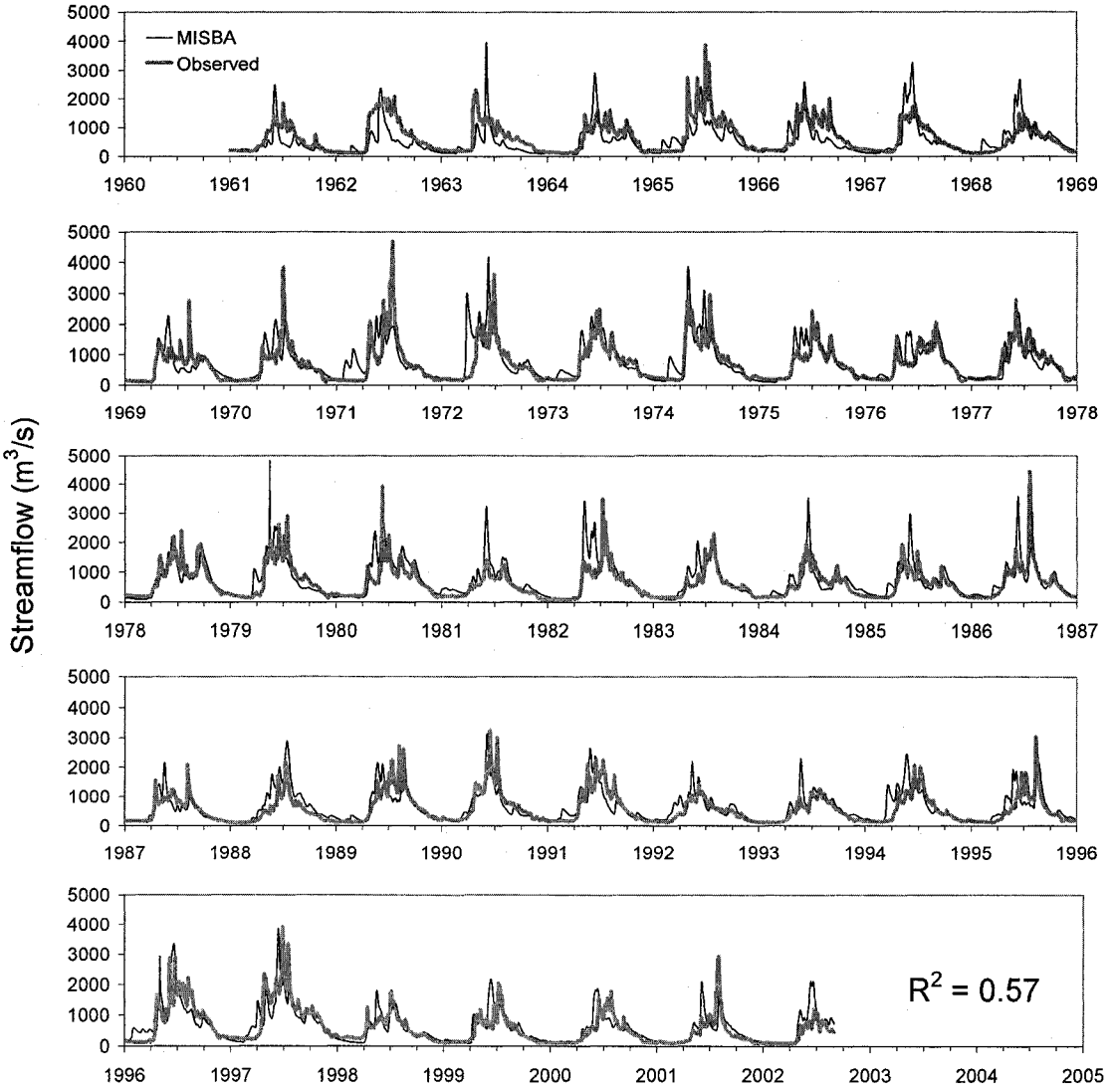

Figure 3.5 - Observed and MISBA/ERA-40 Simulation Hydrographs

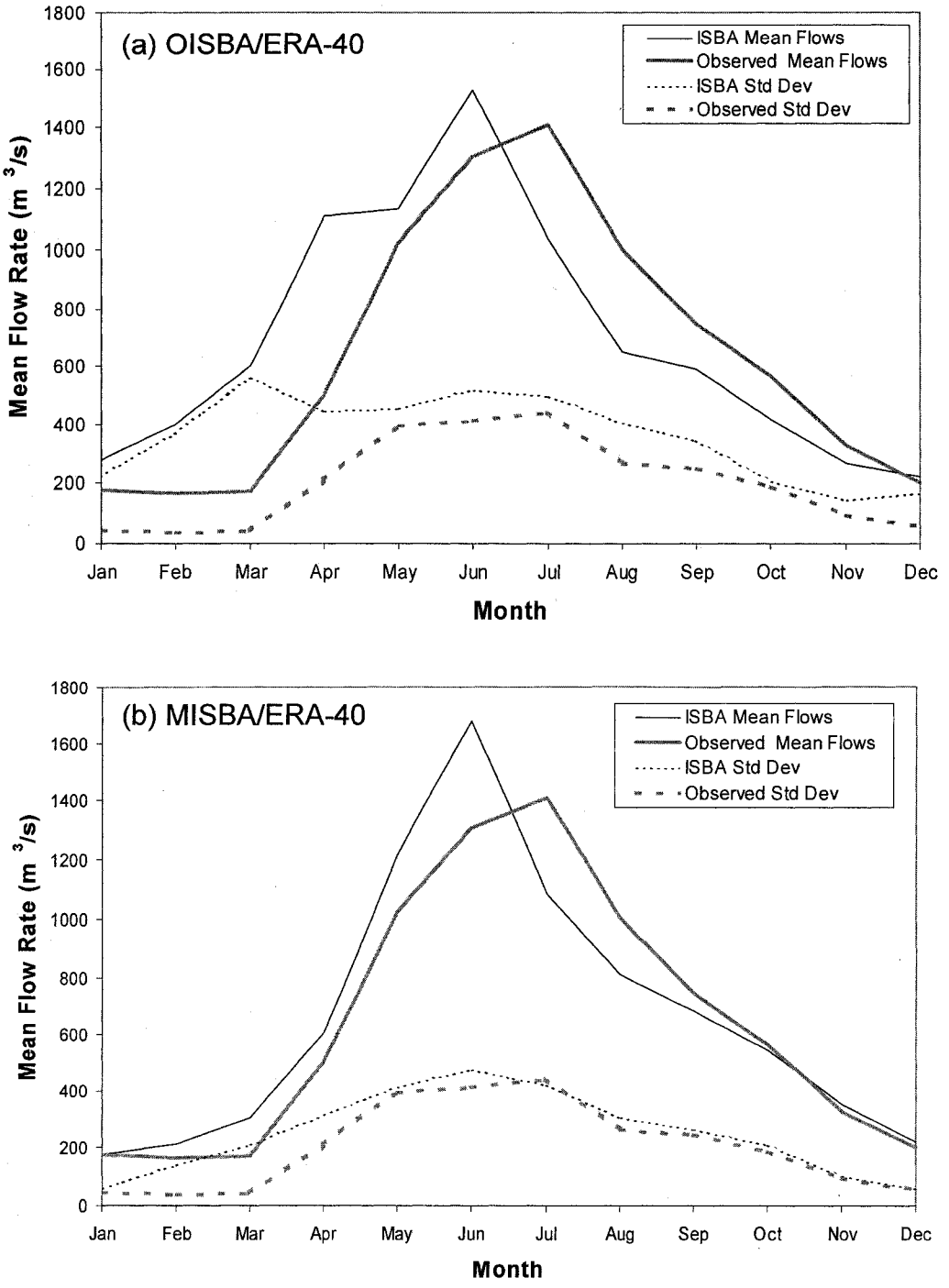

Figure 3.6 - Monthly mean flows and monthly standard deviation of observed flows and (a) OISBA/ERA-40 and (b) MISBA/ERA-40 simulations

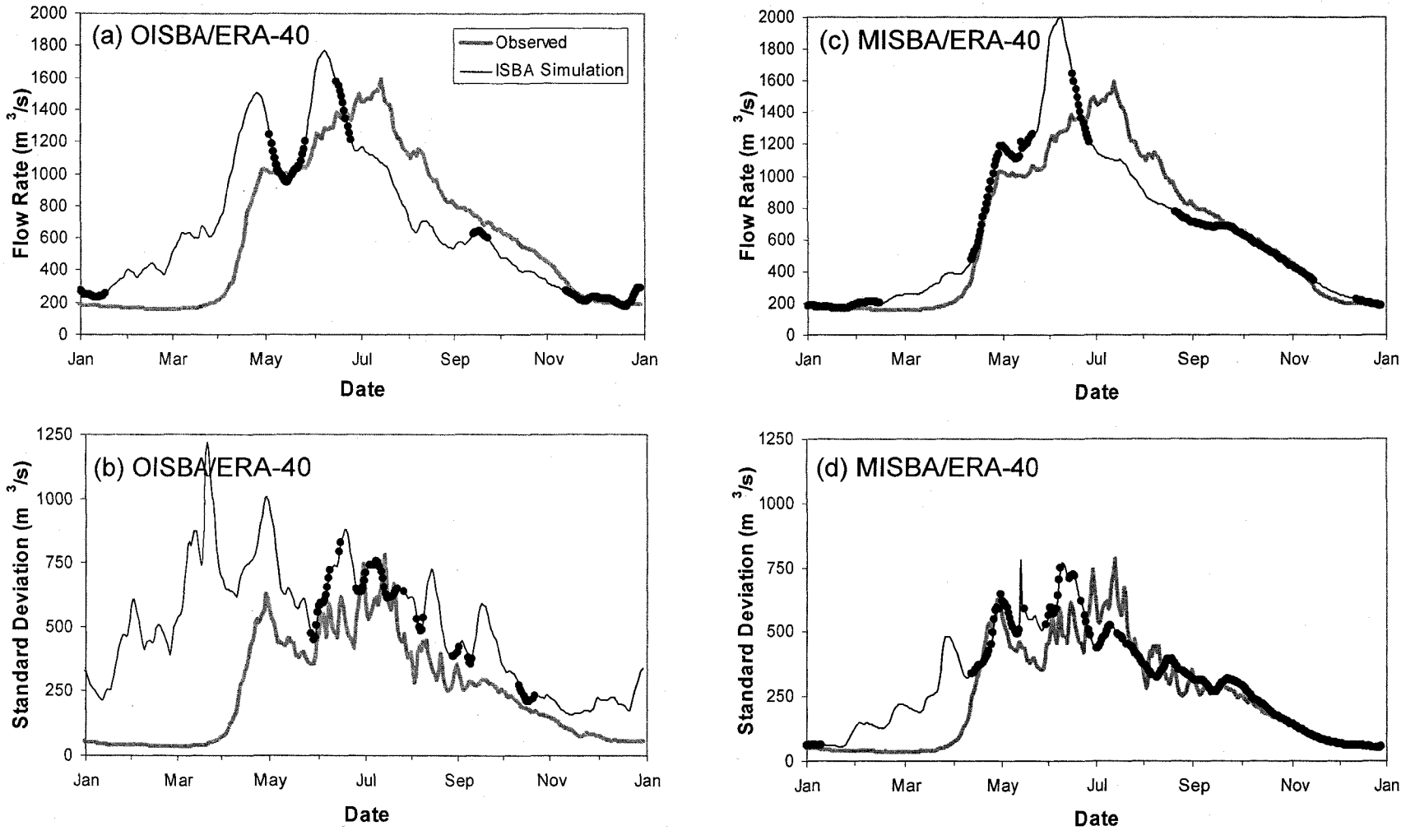

Figure 3.7 - Observed and OISBA/ERA-40 simulation flows for (a) daily mean flows and (b) standard deviation of flows; and observed and MISBA/ERA-40 simulation flows for (c) daily mean flows and (d) standard deviation of flows.

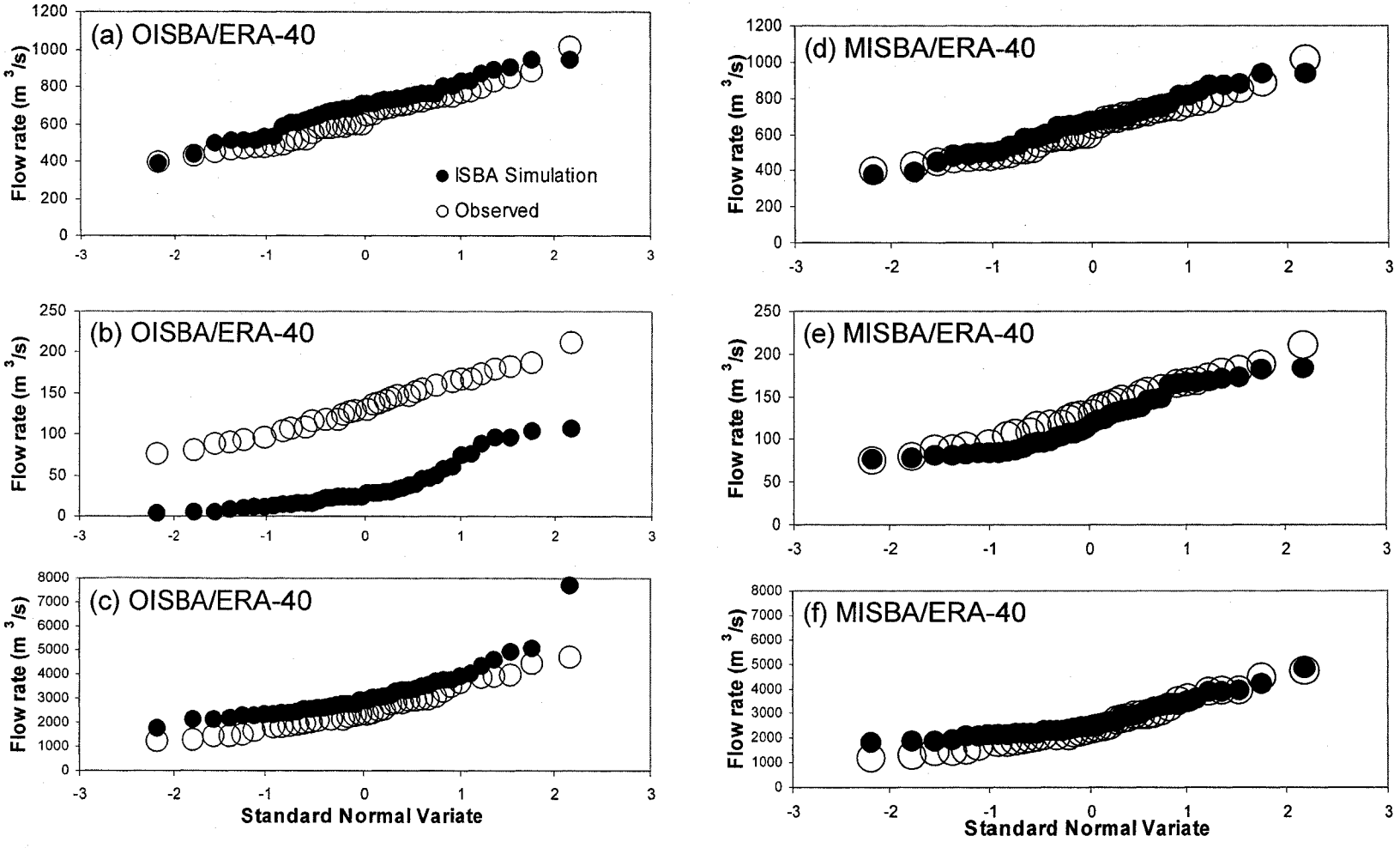

Figure 3.8 Annual frequency plots of observed flows and OISBA/ERA-40 simulation for (a) mean annual flow, (b) minimum annual flow, and (c) maximum annual flow; and the same for MISBA/ERA-40 simulation for (d) mean annual flow, (e) minimum annual flow, and (f) maximum annual flow

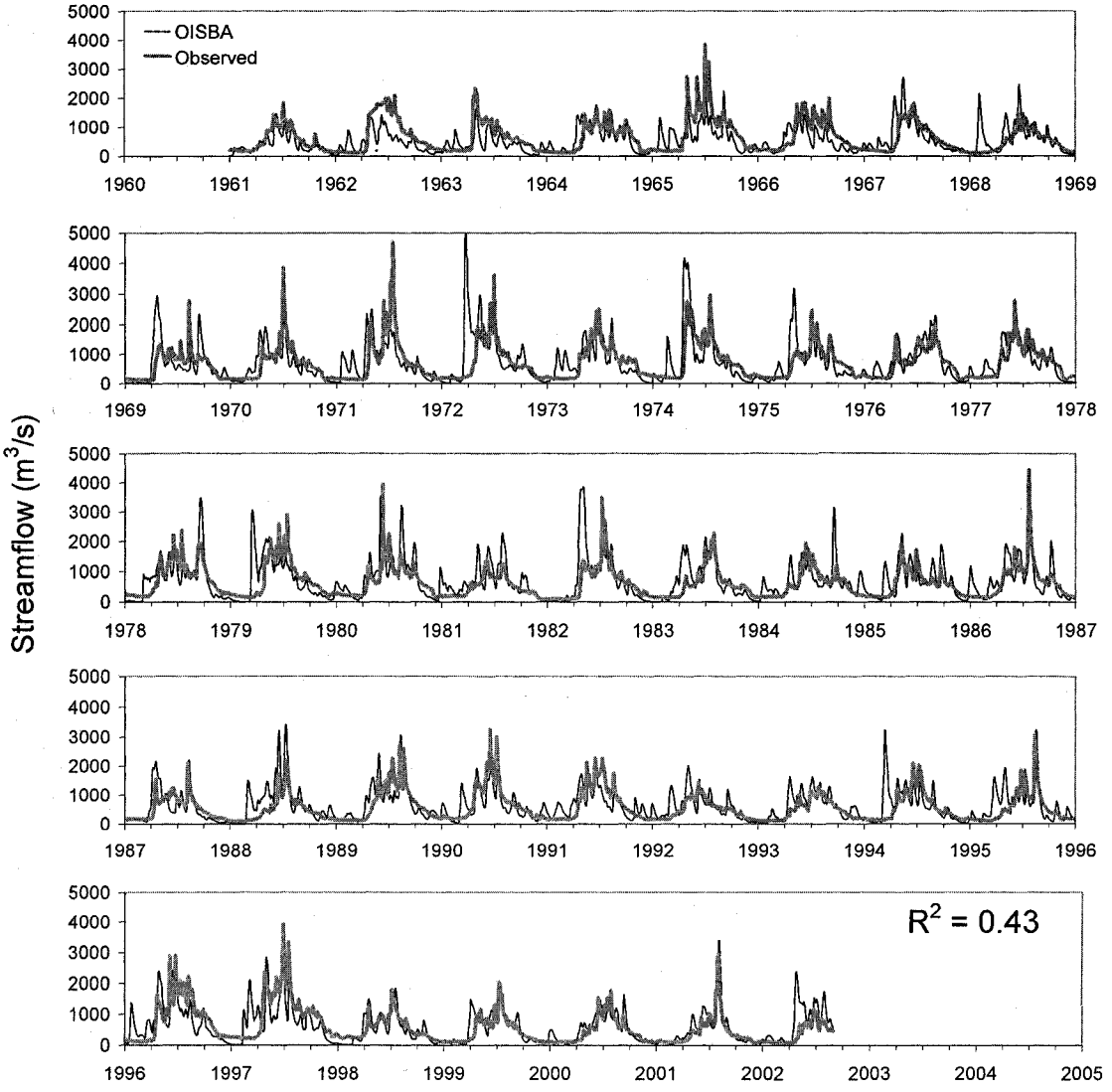

Figure 3.9 - Observed and OISBA/ERA-40/GEM Simulation Hydrographs

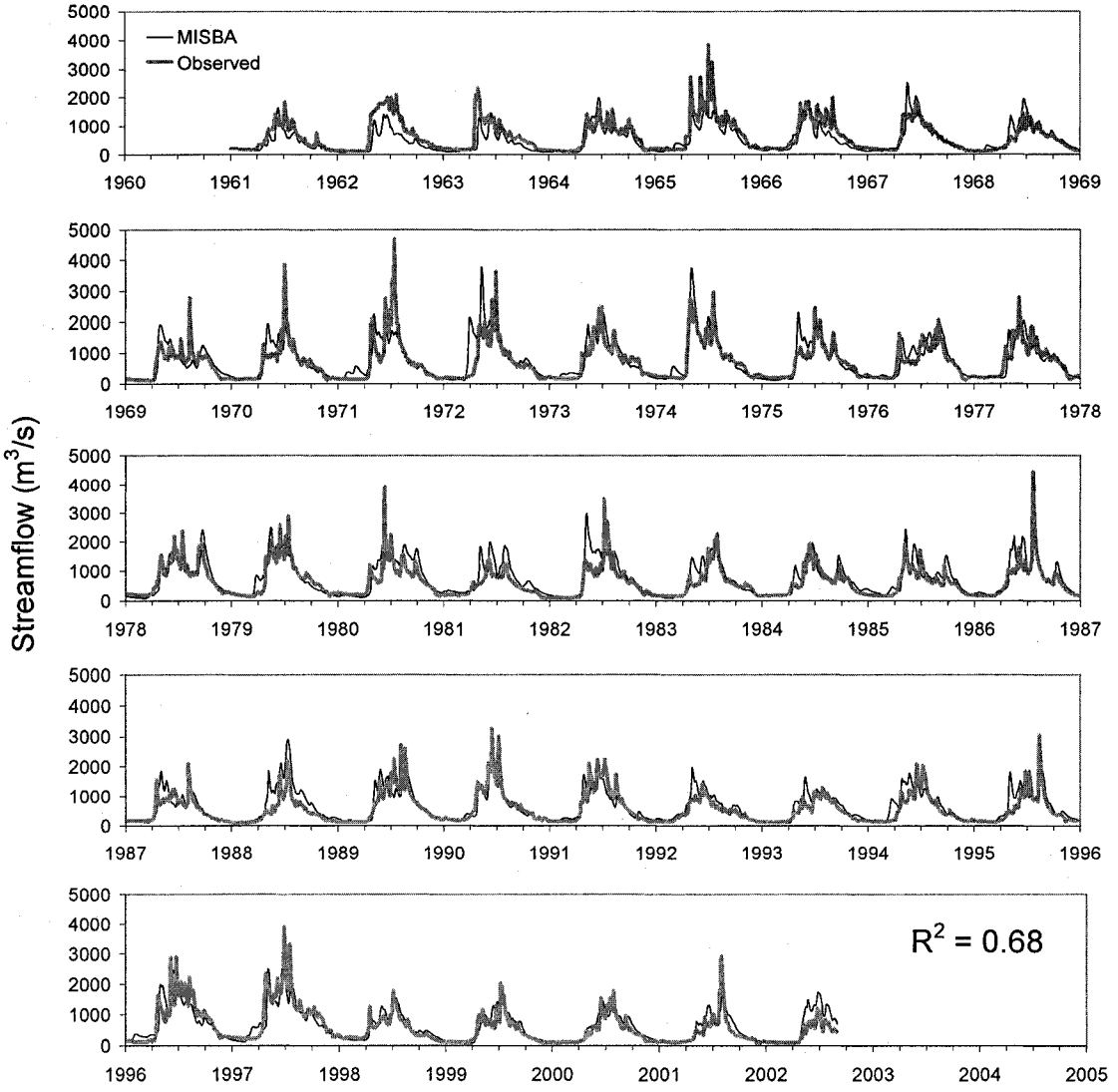

Figure 3.10 - Observed and MISBA/ERA-40/GEM Simulation Hydrographs

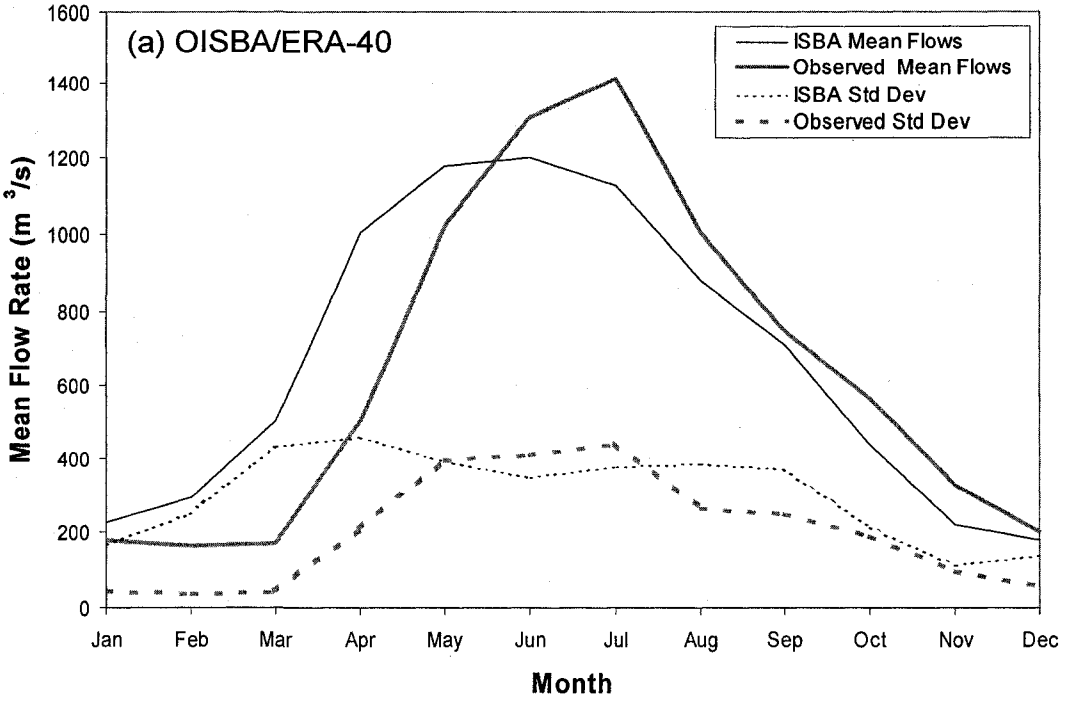

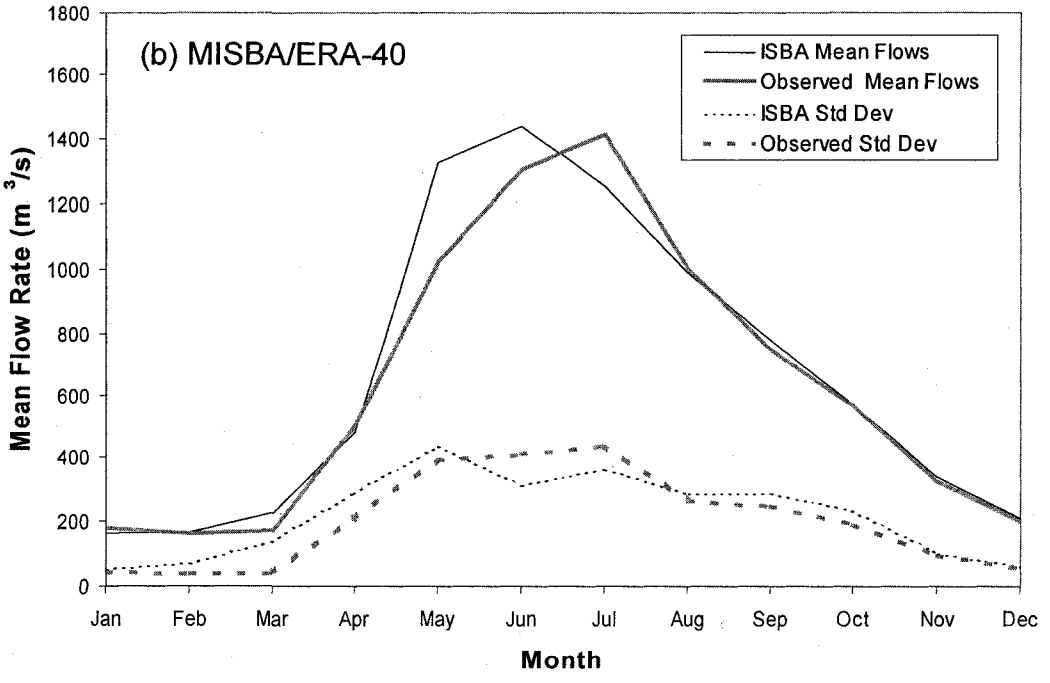

Figure 3.11- Monthly mean flows and monthly standard deviation of observed flows and (a) OISBA/ERA-40/GEM and (b) MISBA/ERA-40/GEM simulations

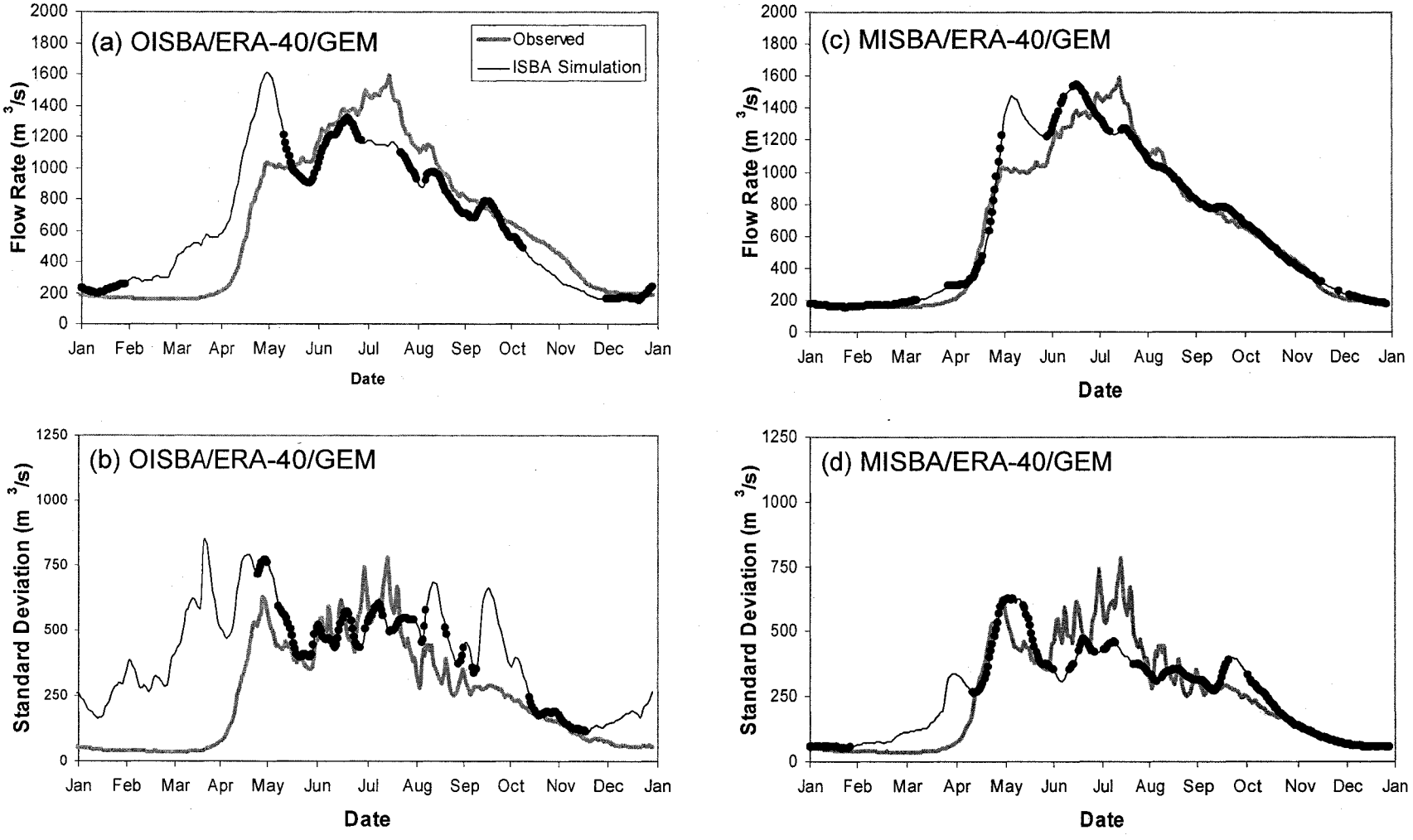

Figure 3.12 - Observed and OISBA/ERA-40/GEM simulation flows for (a) daily mean flows and (b) standard deviation of flows; and observed and MISBA/ERA-40/GEM simulation flows for (c) daily mean flows and (d) standard deviation

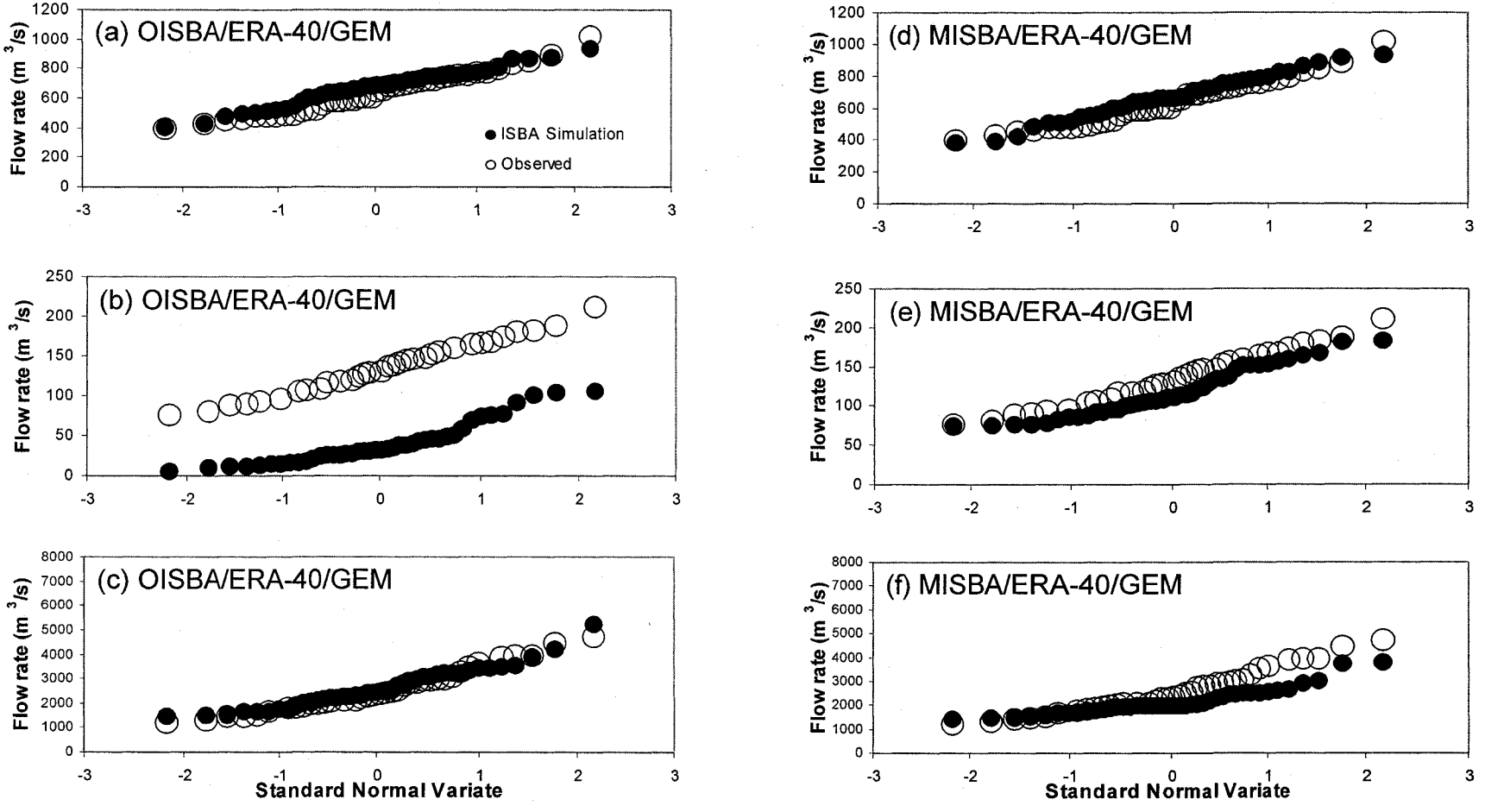

Figure 3.13 - Annual frequency plots of observed flows and OISBA/ERA-40/GEM simulation for (a) mean annual flow, (b) minimum annual flow, and (c) maximum annual flow; and the same for MISBA/ERA-40/GEM simulation for (d) mean annual flow, (e) minimum annual flow, and (f) maximum annual flow

3.8 Bibliography

Bell K.R., B.J. Blanchard, T.J. Schmugge, and M.W. Witczak, (1980), Analysis of surface moisture variations within large-field sites, *Water Resour Res*, 16, 796-810.

Boone A., J.-C. Calvet, and J. Noilhan, (1999), The inclusion of a third soil layer in a Land Surface Scheme using the Force-Restore method, *J Appl Meteor*, 38, 1611-1630.

Boone A., and P. Etchevers, (2001), An inter-comparison of three snow schemes of varying complexity coupled to the same land-surface model: Local scale evaluation at an Alpine site, *J Hydrometeor*, 3, 374-394.

Bowling, l., D. Lettenmaier, B. Nijssen, L. P. Graham, D. Clark, M. El Maayar, R. Essery, S. Goers, Y. Gusev, F. Habets, B. van den Hurk, J. Jin, D. Kahan, D. Lohmann, X. Ma, S. Mahanama, D. Mocko, O. Nasonova, G.-Y. Niu, P. Samuelsson, A. Shmakin, K. Takata, D. Verseghy, P. Viterbo, Y. Xia, Y. Xue, Z.-L. Yang, (2003), Simulation of high-latitude hydrological processes in the Torne-Kalix basin: PILPS Phase 2(e) 1: Experiment description and summary intercomparisons, *Global and Planetary Change*, 38, 1-30.

Chen, T.-H., and A. Henderson-Sellers, P.C.D. Milly, A.J. Piman, A.C.M. Beljaars, J. Polcher, F. Abramopoulis, A. Boone, S. Chang, F. Chen, Y. Dai, C.E. Desborough, R.E. Dickinson, L. Du Menil, M. Ek, J. R. Garratt, N. Gedney, Y.M. Gusev, J. Kim, R. Koster, E. A. Kowalczyk, K. Laval, J. Lean, D. Lettenmeier, X. Liang, J.-F. Mahouf, H.-T. Mengelkamp, K. Mitchell, O.N. Nasonova, J. Noilhan, A. Robock, C. Rosenzweig, J. Schaake, C.A. Schlosser, J.-P. Schultz, Y. Shao, A. B. Shmakin, D. L. Verseghy, P. Wetzel, E.F. Wood, Y. Xue, Z.-L. Yand, and Q. Zeng, (1997), Cabauw

experimental results from the Project for Intercomparison of Land-surface Parameterization Schemes (PILPS). *J. Climate*, 10, 1194–1215.

Brooks R.H., and A.T. Corey, (1964), *Hydraulic properties of porous media, Hydrology Papers, no. 3*, Colorado State University, USA.

Charpentier M.A., and P.M.. Groffman, (1992), Soil moisture variability within remote sensing pixels. *J Geophys Res*, 97, 18987-95.

Cunge J.A., (1969), On the Subject of a Flood Propagation Computation Method (Muskingum Method), *J Hyd Res* , 7(2), 205-230.

Entekhabi D., and P.S. Eagleson, (1989), Land Surface Hydrology Parameterization for Atmospheric Models Including Subgrid Scale Spatial Variability. *J Climate*, 2, 816-831.

Famiglietti J.S., J.A. Devereaux, C.A. Laymon, T. Tsegaye, P.R. Houser, T.J. Jackson, S.T. Graham, M. Rodell, and P.J.V. Oevelen (1999), Ground-based investigation of soil moisture variability within remote sensing footprints during the Southern Great Plains 1997 (SGP97) Hydrology Experiment, *Water Resour Res*, 35, 1839-51.

Famiglietti J.S., and E.F. Wood, (1995), Effects of Spatial Variability and scale on areally averaged evapotranspiration, *Water Resour Res*, 31(3), 699-712.

Feyen, L., J.A. Vrugt, B.O. Nualláin, J. van der Knijff and A. De Roo, (2006), Parameter optimisation and uncertainty assessment for large-scale streamflow simulation with the LISFLOOD model, *Journal of Hydrology*, 332, 276-289.

Foley J.A., (1995), Numerical models of the terrestrial biosphere, *J Biogeogr*, 22, 837-842.

Fulton, R.J., (1995), *Surficial materials of Canada, Geological Survey of Canada, "A" Series Map 1880A*, Natural Resources Canada.

Ghan, S.J., J.C. Liljegren, W.J. Shaw, J.H. Hubbe, and J.C. Doran, (1997), Influence of Subgrid Variability on Surface Hydrology, *J Climate*, 10(12), 3157-3166.

Golder Associates, (2002), *Regional surface water hydrology study by re-calibration of HSPF model*, Calgary, Golder Associates.

Habets F., J. Noilhan, C. Golaz, J.P. Goutorbe, P. Lacarrère, E. Leblois, E. Ledoux, E. Martin, C. Ottlé, and D. Vidal-Madjar, (1999) The ISBA surface scheme in a macroscale hydrological model applied to the Hapex-Mobilhy area Part 1: Model and database, *J Hydrol*, 217, 75-96.

Henderson-Sellers A., Pitman A.J., Love P.K., Irannejad P., and Chen T.H., (1995), The Project for the Intercomparison of Land Surface Parameterization Schemes (PILPS): Phases 2 and 3, *Bull Am Met Soc*, 76(4), 489-503.

Hunag, M., and X. Liang, (2006), On the assessment of the impact of reducing parameters and identification of parameter uncertainties for a hydrologic model with applications to ungauged basins, *Journal of Hydrology*, 320, 37-61.

Kellerhals R., C.R. Neill, and D.I. Bray, (1972), *Hydraulic and Geomorphic Characteristics of Rivers in Alberta*, Edmonton, Research Council of Alberta.

Koster R., and P. Milly, (1997), The interplay between transpiration and run-off formulations in land-surface schemes used in atmospheric models, *J Climate*, 10, 1578-1591.

Koster R., and M.J. Suarez, (1992), Modeling the land surface boundary in climate models as a composite of independent vegetation stands, *J Geo Res*, 97(D3), 2697-2715.

Liang X., D.P. Lettenmaier, and E.F. Wood, (1996), One-dimensional statistical dynamic representation of subgrid spatial variability of precipitation in the two-layer variable infiltration capacity model, *J Geophys Res*, 101(D16), 21,403-22.

Liang, X., E. Wood, D. Lettenmaier, D. Lohmann, A. Boone, S. Chang, F. Chen, Y. Dai, C. Desborough, R. Dickinson, Q. Duan, M. Ek, Y. Gusev, F. Habets, P. Irannejad, R. Koster, K. Mitchell, O. Nasonova, J. Noilhan, J. Schaake, A. Schlosser, Y. Shao, A. Shmakin, D. Verseghy, K. Warrach, P. Wetzel, Y. Xue, Z.-L. Yang, Q. Zeng, (1998), The Project for Intercomparison of Land-surface Parameterization Schemes (PILPS) phase 2(c) Red-Arkansas River basin experiment: 2. Spatial and temporal analysis of energy fluxes, *Global Planetary Change*, 19, 137-159.

Liang, X., and Z. Xie, , (2001) A new surface runoff parameterization with subgrid-scale soil heterogeneity for land surface models, *Advances in Water Resources*, 24(9-10), 1173-1193.

Lohmann, D., D. Lettenmaier, X. Liang, E. Wood, A. Boone, S. Chang, F. Chen, Y. Dai, C. Desborough, R. Dickinson, Q. Duan, M. Ek, Y. Gusev, F. Habets, P. Irannejad, R. Koster, K. Mitchell, O. Nasonova, J. Noilhan, J. Schaake, A. Schlosser, Y. Shao, A. Shmakin, D. Verseghy, K. Warrach, P. Wetzel, Y. Xue, Z.-L. Yang, Q. Zeng, (1998), The Project for Intercomparison of Land-surface Parameterization Schemes (PILPS) phase 2(c) Red-Arkansas River basin experiment: 3. Spatial and temporal analysis of water fluxes, *Global Planetary Change*, 19, 161-179.

Luo, l., A. Robock, K. Y. Vinnikov, C.A. Schlosser, A. G. Slater, A. Boone, H. Braden, P. Cox, P. de Rosnay, R. E. Dickinson, Y. Dai, Q. Duan, P. Etchevers, A. Henderson-Sellers, N. Gedney, Y. M. Gusev, F. Habets, J. Kim, E. Kowalczyk, K. Mitchell, O. N. Nasonova, J. Noilhan, A. Pitman, J. Schaake, A.B. Shmakin, T.G. Smirnova, P. Wetzel, Y. Xue, Z.-L. Yang, Q. Zeng, (2003), Effects of Frozen Soil on Soil Temperature, Spring Infiltration, and Runoff: Results from the PILPS 2(d) Experiment at Valdai, Russia, *Journal of Hydrometeorology*, 4, 334- 351.

Manabe S., (1969), Climate and the ocean circulation: 1, the atmospheric circulation and the hydrology of the Earth's surface, *Mon Wea Rev*, 97, 739–805.

Masson V., J.-L. Champeaux, F. Chauvin, C. Meriguet, and R. Lacaze, (2003), A Global Database of Land Surface Parameters at 1km Resolution in Meteorological and Climate Models, *J.Climate*, 16: 1261-1282.

Mengelkamp H.T., K. Warrach, and E. Raschke, (1999), SEWAB – a parameterization of the Surface Energy and Water Balance for atmospheric and hydrologic models, *Adv Water Res*, 23, 165-75.

Mohr K.I., J.S. Famiglietti, and A. Boone, (2001), The Effect of Sub-Grid Variability of Soil Moisture on the Simulation of Mesoscale Watershed Hydrology: A Case Study From the Southern Great Plains 1997 Hydrology Experiment, in *Land Surface Hydrology, Meteorology, and Climate: Observations and Modeling*, Editors (Lakshmi, Albertson, Schaake), Water Science and Application, Washington, AGU.

Nijssen, B., L. Bowling, D. Lettenmaier, D. Clark, M. El Maayar, R. Essery, S. Goers, Y. Gusev, F. Habets, B. van den Hurk, J. Jin, D. Kahan, D. Lohmann, X. Ma, S. Mahanama, D. Mocko, O. Nasonova, G.-Y. Niu, P. Samuelsson, A. Shmakin, K. Takata,

D. Verseghy, P. Viterbo, Y. Xa, Y. Xue, Z.-L. Yang, (2003), Simulation of high latitude hydrological processes in the Torne-Kalix basin: PILPS Phase 2(e) 2: Comparison of model results with observations, *Global Planetary Change*, 38, 31-53.

Noilhan J., and P. Lacarrère, (1995), GCM Grid-Scale Evaporation from Mesoscale Modeling, *J Climate*,8(2), 206-223.

Noilhan J., and S. Planton, (1989), A simple parameterization of land surface processes for meteorological models, *Mon Wea Rev*, 117, 536-549.

Pitman A.J., (2003), The Evolution of, and Revolution in, Land Surface Schemes Designed for Climate Models, *Int J Climatol*, 23, 479-510.

Ponce V.M., and V. Yevjevich, (1978), Muskingum-Cunge Method with Variable Parameters, *J Hyd Div*, 104, 1663-1667.

Schlosser, C.A., A.G. Slater, A. Robock, A. Pitman, K.Y. Vinnikov, A. Henderson-Sellers, N.A. Speranskaya, K. Mitchell, (2000), Simulations of a Boreal Grassland Hydrology at Valdai, Russia: PILPS Phase 2(d), *Monthly Weather Review*, 128, 301- 321.

Sivapalan M., and R.A. Woods, (1995), Evaluation of the effects of general circulation models' subgrid variability and patchiness of rainfall and soil moisture on land surface water balance fluxes, *Hydrol Proc*, 9, 697-717.

Slater A.G., C.A. Schlosser, C.E. Desborough, A.J. Pitman, A. Henderson-Sellers, A. Robock, K.Y. Vinnikov, K. Mitchell, A. Boone, H. Braden, F. Chen, P.M. Cox, P. de Rosnay, R.E. Dickinson, Y.-J. Dai, Q. Duan, J. Entin, P. Etchevers, N. Gedney, Y.M. Gusev, F. Habets, J. Kim, V. Koren, E.Y. Kowalczyk, O.N. Nasonova, J. Noilhan, S. Schaake, A.B. Shmakin, T.G. Smirnova, D. Verseghy, P. Wetzel, Y. Xue, Z.-L. Yang,

and Q. Zeng, (2001), The Representation of Snow in Land Surface Schemes: Results from PILPS 2(d), *J Hydrometeorology*, 2, 7-25.

Smith R.E., (1983), Approximate soil water movement by kinematic characteristics, *Soil Sci Soc Am Proc*, 47, 3-8.

Wetzel P.J., and J.-T. Chang, (1988), Evapotranspiration from Nonuniform Surfaces: A First Approach for Short-Term Numerical Weather Prediction, *Mon Wea Rev*, 116(3), 600-621.

Wood E.F., D.P. Lettenmaier, X. Liang, D. Lohman, A. Boone, S. Chang, F. Chen, Y. Dai, R.E. Dicikinson, Q. Duan, M. Ek, Y.M. Gusev, F. Habets, P. Irannejad, R. Koster, K.E. Mitchel, O.N. Naonova, J. Noilhan, J. Schaake, A. Schlosser, Y. Shao, A.B. Shmakin, D. Verseghy, K. Warrach, P. Wetxel, X. Xue, Z.-L. Yang, and Q. Zeng, (1998), The Project for Intercomparison of Land-Surface parameterization Schemes (PILPS) Phase 2(c) Red-Arkansas River basin experiment, *Global and Planetary Change*, 19, 115-179.

Yarnal B. , A.C. Comrie, B. Frakes, and D.P. Brown, (2001), Developments and prospects in synoptic climatology, *Int J Climatology*, 21, 1923-50.

Zhao R.J., (1992), The Xinanjiang model applied in China, *J Hydrology*, 135, 371-381.

Chapter Four: Differences in the Potential Hydrologic Impact of Climate Change to the Athabasca and Fraser River Basins Located on the Leeward and Windward Sides of the Canadian Rocky Mountains Respectively

4.1 Introduction

Water managers regularly use historical streamflows to facilitate watershed planning. Strictly speaking, such approaches are only valid when the historical and future climates are stationary. However, anthropogenic climate change due to ever increasing greenhouse gas emissions (from about 315 ppmv in 1959 to 390 ppmv in 2007, IPCC(2007)) has the potential to drastically alter climates at all spatial scales and thereby invalidate hydrological analysis methods that depend on the assumption of a stationary climate (e.g., Dettinger et al. 2004; Stewart et al. 2004).

In the First Assessment Report of the IPCC (Intergovernmental Panel on Climate Change) atmospheric General Circulation Models (GCMs) were run to equilibrium under current ($1xCO_2$) and doubled ($2xCO_2$) emissions forcings (Cusbach and Cess, 1990) to estimate the potential effect of these emissions on global climate. These models were then coupled with Oceanic Circulation Models in the Second Assessment Report (Gates *et al.*, 1996) and forced with transient greenhouse emissions to allow for the estimation of the rate at which climate changes might occur. In the Third Assessment Report (TAR), a series of emission scenarios from the Special Report on Emission Scenarios (SRES) (IPCC, 2000) were used to evaluate the effects of a range of government policy options through their effects on population growth, technological, and economic development (IPCC, 2001). The results of each GCM used in the TAR were summarized as monthly changes in mean state variables (for example, near-surface temperature and precipitation) with respect to the 1961-1990 baseline climate normal. The Fourth Assessment Report

(AR4) the SRES scenarios were again used to force the most recent generation of GCMs, which feature improvements in grid resolution and process treatment but no fundamental advances comparable to the inclusion of ocean dynamics in FAR and TAR (IPCC, 2007). The projected global average temperature change by the end of the 21st century ranged from 1.4 to 5.8°C in TAR and 1.1 to 6.4°C in AR4.

The projections of these relatively coarse resolution GCMs have been used to drive land surface hydrology models to estimate the potential impact of climatic change on hydrology in mid-latitude regions such as California (e.g., Lettenmaier and Gan, 1990; Brekke *et al.* 2004; Knowles and Cayan 2004; Maurer, 2007) and the Europe (e.g., Middelkoop *et al.*, 2001; Etchevers *et al.*, 2002; Beniston *et al.*, 2003; Zierl and Bugmann, 2005). This paper will focus on the effects of climatic change on large river basins on either side of the Rocky Mountains of western Canada: the Athabasca River Basin (ARB) of Alberta, and the Fraser River Basin (FRB) of British Columbia. Because of the Rocky Mountains, these basins experience quite different climate and thus contain different vegetation, boreal forest in the ARB and coniferous forest in the FRB.

4.2 Study Basins

The ARB is of key interest mainly because of its multi-billion dollar, oilsands industry at Fort McMurray. The basin area of ARB is 133 000 km^2 and its main channel length is about 1154 km (Kellerhals *et al.*, 1972). ARB has a continental climate with daily mean temperature dropping below freezing between mid-October and early April. Typical January temperature is -20°C while July is 17°C. June to October are the wet months, with an average total precipitation of about 300 mm, while winter and spring

only experience about 150mm of precipitation in an average year. Coniferous, mixed wood and deciduous forests are the dominant vegetation especially in the upland areas (elevation ranging from 350 to 850m) and willow brush, shrubs, black spruce and sphagnum moss dominate the lowland areas which are often poorly drained. For lowland dominated by muskeg, interflow tends to constitute of a significant component of the sub-surface runoff (Golder Associates, 2002). Dominant surficial soils are glacial soils (silt, clay and sands), glaciolacustrine soils (clay loam to heavy clay) and glaciofluvial soils (sandy loam to sands) (Fulton, 1995).

Natural watersheds in many parts of ARB are characterized by peat soils that vary from 0.3m (upland) to over 1 m (lowland). Upland watersheds typically have ground slopes of 0.5% or more, while lowland areas typically have average slope less than 0.5%. Lowland areas normally have thick peat soils with near-surface groundwater table. As a result, a significant amount of runoff (e.g., could be more than 70%) from lowland watersheds occurs as interflow through deep peat, or muskeg, irrespective of the sub-soil types (Golder Associates, 2002).

The Fraser River Basin (FRB) is the principle river of British Columbia (BC). Rising in the Rocky Mountains and flowing northwest through the Rocky Mountain Trench to Prince George, the Fraser River then turns south and west to Vancouver where it flows into the Strait of Georgia 1370 km from its headwaters, draining an area of 230,000 km^2. The river contains the chief spawning grounds in North America for the Pacific salmon and logging is important along the upper course. The Fraser delta, the

most fertile agricultural region of BC, contains the largest concentration of people in Western Canada.

The FRB lies between the Coast and Rocky Mountain ranges. As a result, the basin valley is quite dry with an average annual precipitation between 300 and 500 mm. The upper reaches of the basin, in the Rocky Mountains, are by far the wettest, averaging 1500 mm of precipitation annually. Average January temperatures vary from –15 °C in the northern, mountainous regions to 0 °C at the mouth. In June, temperatures range from 20 °C in the interior to 10 °C in the high mountains. The FRB is heavily forested, with coniferous forests dominating the Western regions, and mixed forests in the Eastern regions. There is also significant agriculture along the Fraser River's main channel. The upper reaches of the Nechako River is regulated by Kennedy Dam, affecting 6.7% of the river basin area and 2.6% of the FRB's mean annual flow. Surficial soils are dominated by glacial till deposits in the interior plateau and alpine rock outcrops along the eastern and western boundaries of the basin. The region surrounding the confluence of the Nechako and Fraser Rivers is dominated by fine grained glaciolacustine deposits (Fulton, 1995).

4.3 Research Methodology

The Modified Interactions between the Soil–Biosphere–Atmosphere (MISBA) model, described in the previous chapter, was used to simulate the hydrology of the ARB and FRB. MISBA was forced by climate scenarios projected by selected general circulation models (GCM) described below and downscaled to the regional scale to simulate the future water supply under the impact of climate change. From the results,

the projected impact of climate change were assessed using statistics such as annual flow means and variances, seasonal flow means and variances, peak flows, low flows, goodness-of-fit statistics, flow duration curves, and frequency analysis.

The meteorological datasets used were Meteorological Survey of Canada's Global Environmental Multiscale Model (GEM), and ERA-40 historical re-analysis data developed by the European Centre for Mid-range Weather Forecasts (ECMWF). All land use data was derived from the Ecoclimap dataset (Masson *et al.*, 2003). Basin characteristics, such as areal extent and the drainage network, were derived from the 6 arc-second (approximately 200-m resolution) Digital Elevation Model (DEM) of the Peace-Athabasca River basin and the 3 arc-second (approximately 100 m) Shuttle Radar Topography Mission (SRTM) DEM.

Attempts to quantify hydrologic uncertainties in the ARB and FRB and their tributaries under the potential impact of climate change can be very challenging since the consequences are decades away, associated uncertainties are many and are often unpredictable, and GCMs are of coarse resolution, simplified version of nature, and so are prone to errors. The simulated runoffs are subjected to possible errors caused by uncertainties in the model structure of MISBA which is a simplified version of nature, hydrologic and topographic data errors, and most importantly, uncertainties associated to projected future climate scenarios. As a means to assess uncertainties to model results, and to obtain a sense of realistic possible changes induced by climatic warming in the hydrologic signals of the ARB and FRB, projections of climate change of 7 major GCMs (Japan's CCSRNIES, Canada's CGCM2, Australia's CSIROMk2b, Germany's

ECHAM4, the USA's GFDLR30, the UK's HadCM3, and the USA's NCARPCM) driven under four SRES climate scenarios (A1FI, A2, B1, and B2) over three 30-year time periods (2010-2039, 2040-2069, 2070-2100) were used in this study.

Given the relatively coarse resolution of the ERA-40 reanalysis data (2.5°x2.5°), the data were adjusted with respect to the higher resolution GEM forecast archive (0.329° x 0.500°) using a simple statistical approach. The ECMWF and GEM data sets overlap from the September 1995 to August 2001. For this period, the differences in monthly temperature, humidity, pressure, wind speed, precipitation, and radiation values between each ECMWF point and its surrounding GEM points were calculated. These differences were then applied to the entire ECMWF data set. The basic assumption is that the time series at each ECMWF grid point is representative of the climate of all the areas located within each grid. Incorporating the higher resolution GEM data in this way can correct for biases in latitude and elevation as well as any systematic biases in the ECMWF data. This method is similar to the one used in the previous chapter for historical flows in the ARB. However, instead of adjusting the ECMWF data for each GEM point, the ECMWF data is adjusted to match the basin area weighted average of the surrounding GEM points. The final simulations are therefore still run at the 2.5° scale. This is therefore not a downscaling scheme but an assimilation scheme. This approach was taken in order to reduce the time required to conduct all 54 simulations in each river basin while incorporating most of the additional information that the GEM archive provides, mainly any temperature and precipitation biases produced by using a single grid point to represent climate conditions over a large area.

The SRES GCM scenarios predict the monthly change in near-surface air temperature and precipitation for three 30-year time periods (2010-2039, 2040-2069, 2070-2100) with respect to a historical 30-year period (1961-1990). These predicted changes were used to adjust the historical ERA-40 data to produce new meteorological datasets for each future time period.

4.4 Discussion of Results

MISBA/ERA-40 was used to simulate a number of SRES climate scenarios for the Athabasca and Fraser River basins. The predicted changes to mean monthly temperature and precipitation from seven GCM models (CCSRNIES, CGCM2, CSIROMk2b, ECHAM4, GFDLR30, HadCM3, and NCARPCM) for four SRES climate scenarios (A1FI, A21, B11, B21) over the 1961–1990 base period were used to adjust the adjusted ERA-40 temperature and precipitation over three 30-year time periods: 2010–2039 (early 21st century), 2040–2069 (mid 21st century), and 2070–2099 (late 21st century). Results are available from all seven GCMs for the A2 (fragmented world) and B2 (local sustainability) scenarios, but only the HadCM3 and CCSRNIES models have provided results for the A1FI (fossil fuel intensive) and B1 (global environmental emphasis) scenarios. In total, 18 future climates scenarios were run for each 30-year period (two A1FI predictions, seven A2 predictions, two B1 predictions, and seven B2 predictions) for a total of 54 simulations for each river basin.

4.4.1 Athabasca River Basin

The historic reconstruction of streamflows in the ARB was conducted in Chapter 3 and in Kerkhoven and Gan (2006). In general, the predicted future streamflows were

more sensitive to the GCM used than the scenario selected. However, most of the GCMs predict continuing decreases in average, maximum, and minimum flows over the next 100 years. A summary of the GCM predictions for annual temperature and precipitation changes in the ARB is shown in Figure 4.1a. The three enveloping curves indicate the three time periods of the 2020s, the 2050s, and the 2080s. In general, the GCMs predict an increase in both temperature and precipitation. HadCM3 is the wettest, ECHAM4 is the driest, and CCSRNIES is the warmest. CGCM2's predictions fall in the middle. Changes in predicted runoff are weakly correlated with precipitation changes. However, driving MISBA with input data adjusted with all these GCM scenarios lead to decreased streamflow by the end of the 21st century, and two-thirds of the scenarios predict stream flows to decline by over 20% (Figure 4.1b). Even though ΔP are mostly positive (Figure 4.1a), the runoff coefficient seems to be strongly correlated to changes in temperature such that for every degree of temperature rise, the runoff coefficient drops by about 8% (Figure 4.1c).

As can be seen in Figure 4.2, the amount of the mean annual snowpack in the basin is strongly correlated with mean annual flow in the basin. With the exception of the HadCM3 GCM (which is by far the wettest in December and January) the scenarios predict a strong decrease in the snow pack over the 21st century resulting in less water available for spring snowmelt runoff. This reduction in snow pack is primarily due to increases in winter temperatures that result in less snow accumulation and increased evaporation loss, which could offset a positive ΔP. The correlation between winter precipitation (December–January) and maximum snow pack (R = +0.345) is much lower

than the correlation between winter temperature (December–January) and maximum snow pack ($R = -0.800$).

Figure 4.3a shows the mean daily stream flow predictions for the A2 scenario for three of the GCMs for the last 30 years of the 21st century. The 1961–1990 hydrograph exhibits two distinct peaks. The first is associated with snowmelt freshets in the lowlands and the second is associated with snowmelt in the mountainous southwest. The GCMs tend to predict snowmelt freshets to occur approximately 10 to 15 days earlier than during the historical baseline, and with the exception of the wet HadCM3 model, the amplitude of the lowlands freshet decreases significantly. All the GCMs predict significant declines in flows from June through November, and most predict significant declines in February and March.

Given that among the GCMs' results, CGCM2's are representative of an average simulation for ARB, the mean daily streamflow for all the CGCM2 scenarios were examined (Figure 4.3b). Both scenarios depict very similar patterns with streamflows become progressively smaller as the century progresses. These results are representative of the general tendency of streamflows to vary more between different GCMs within the same emissions scenario than between different emission scenarios from the same GCM. The lowland snowmelt event becomes weaker and the mountain snowmelt comes earlier until the two-peak behaviour disappears, which likely implies that uncertainties associated with climate scenarios are more related to GCMs than the assumed emissions.

In both cases, mean annual flows are predicted to decrease by almost 25% by the last third of the 21st century. The high flow season also becomes much shorter.

Historically, in an average year ARB stream flows could be expected to stay over 1000 $m^3 s^{-1}$ for nearly 5 months from late April until mid-August. For both climate scenarios, the CGCM2 predict a high flow season that lasts less than 2 months from early May to mid-June. This behaviour is consistent with the findings of paleo-climatologic research in the Peyto Glacier basin on the western slopes of the Alberta Rocky Mountains (Demuth and Keller, 2006; Luckman, 2006) where the extent of the glacier was found to be much more sensitive to declines in winter snowfall than increases in summer temperature.

In terms of mean annual flow by the end of the 21st century, the ECHAM4 A2 scenario predicted the largest decrease at –36.6%, while HadCM4 and NCAR B2 predicted the smallest decrease at –5.0% (Table 4.1). As expected (Figure 4.1a), the average change in annual flow by 2070–2099 was –21.1%. The HadCM3 and NCARPCM consistently predicted the highest flow rates, while the ECHAM4 predicted the lowest. In terms of mean annual maximum flow, the CCSRNIES B2 scenario predicted the largest decrease at –17.9%, while HadCM4 B21 predicted the largest increase at +10.5%. The average change in annual maximum flow by 2070-2099 was –4.4%. In terms of mean annual minimum flow, the climate scenarios usually predicted changes ranging from –17.6 to –57.5%, with –41.0% as the average predicted change.

Under the terms of the Lower Athabasca Management Plan (Alberta Environment, 2007) cumulative consumptive water withdrawals from the Athabasca River below Fort McMurray are limited to 8 $m^3 s^{-1}$ when winter flows fall below the historic 95% exceedence flow, which ranges between 100 $m^3 s^{-1}$ and 110 $m^3 s^{-1}$ from December to February. Active, approved, and proposed water licenses along this reach

of the Athabasca total 6 $m^3 s^{-1}$, 10 $m^3 s^{-1}$, and, 14 $m^3 s^{-1}$, respectively, as of December 2007 (Pat Marriott, Alberta Environment, personal communication, 2007). The SRES climate scenarios suggest that the mean minimum annual flow will drop from the current 138 $m^3 s^{-1}$ to averages of 111 $m^3 s^{-1}$, 90 $m^3 s^{-1}$, and 81 $m^3 s^{-1}$ by the 2020s, 2050s, and 2080s, respectively. Industrial operations in the Lower Athabasca, which typically expect to continue operations for the next 25 to 50 years, could therefore face severe water shortages far more often than once every 20 years for much of their future operational lifespan. Given the fact that most of these operations do not currently include accommodations for water storage, the newer operations with their lower licence priority under Alberta water law could suffer extended shutdowns far more often than the analysis of historic flows would suggest.

4.4.2 Fraser River Basin

As a first step, the ERA-40 re-analysis data was used to simulate historical river flows at the Fraser River at Hope gauging station from 1 September 1957 to 31 August 2001. Initial results showed that the low resolution of the ERA-40 data is highly problematic for the mountainous Fraser basin. Precipitation on the windward side of the Rocky Mountains is much higher than that on the leeward side. However, the ERA-40 data set cannot distinguish these differences. Precipitation is consistently overestimated when the nearest ERA-40 point is on the windward side and underestimated when it is on the leeward side. In the case of the preliminary simulations, the western part of the basin was subjected to coastal precipitation patterns. This resulted in runoff patterns that did not match those observed in the basin. Figure 4.4a is a typical example of the observed and simulated hydrographs. The two hydrographs fit poorly ($R^2 = 0.001$).

Next, the assimilation scheme used for the ARB was applied to produce a new meteorological data set (ERA40-GEM) to simulate stream flows of the Fraser River at Hope, BC from September 1957 to August 2001. Figure 4.4b shows a typical example of the observed and simulated daily hydrographs. The incorporation of the GEM data significantly improves the results (R^2 = 0.39 versus 0.001 before the adjustment). The most notable improvement is the reduction on the size of the anomalous winter runoff events and much better simulation of the spring runoff peaks. Some of the error can be attributed to the fact that the FRB is a regulated river basin and the methodology described here cannot account for man made effects on the Nechako Rivers, which accounts for less than 3% of the FRB annual runoff volume.

Figure 4.5 shows the observed ERA40-GEM simulated mean annual flow, minimum annual flow, and maximum annual flow frequency plots for the Fraser River at Hope. The simulations reproduce the annual variation in mean flow very well and, to a lesser extent, the minimum annual flow except for the fluxes of high return period. With the exception of three excessive peak flows in 1967, 1971 and 1974 the annual maximum flow series is also well reproduced. The simulations also tend to improve in later years when better data became available to construct the ERA40 data set.

Figure 4.6 shows the observed and ERA40-GEM simulated 365 day moving average flow rate of the Fraser River at Hope. The early significant discrepancy before 1964 can be attributed to a combination of model spin up, particularly the time required to build up snow packs in the mountains, and systematic biases in the ERA40 data set. After 1964, the simulation reproduces the annual variations in stream flow very well for

the wet and dry periods both in terms of timing and severity ($R^2 = 0.80$, after 1964). This indicates the modelling scheme described here can reproduce the large-scale behaviour of the FRB.

Although these historical simulations are not as accurate as for the ARB (see Section 4.4.1), Figures 4.5 and 4.6 show they are of sufficient accuracy to produce meaningful results from the SRES climate scenarios. Figure 4.7a is a plot of the predicted changes in annual precipitation and temperature in the FRB based on the results from the GCMs scenarios. On average, the scenarios predict average temperature increases of 4.0°C and precipitation increase of 8.4% in the FRB over the next 100 years. The GCMs all predict increasing temperatures and precipitation in the basin throughout the next century; however the magnitude of these increases varies widely between models. Generally, for the A2 and B2 scenarios, CCSRNIES predicts the largest temperature increases (+5 to +7 °C) and NCARPCM the smallest temperature increases (+2.2 to 3.2 °C) by the end of the 21st century. CCSRNIES, CSIROMk2b, and GFDLR30 consistently predicted the largest increase in the precipitation of the FRB (+9 to 14% by the end of the century) and CGCM2 the least increase (+0.5 to 3.5% by the end of the century).

The seasonal variations in these changes also vary widely between models. For the A2 scenarios, The NCARPCM, CCSRNIES, and CSIROMk2b models predict the bulk of the warming to occur in the winter months (November to February); the CGCM2 model predicts most of the warming to occur in the spring (March to May); and the HadCM3 and ECHAM4 models predict most of the warming to occur in the summer

(July to September). Only the GFDLR30 model predicts warming to occur relatively evenly over the year. Most of the models predict that the largest increases in precipitation will occur in the winter months with moderate decreases occurring in the summer.

These scenarios generally predict small to moderate changes in mean annual flow in the FRB by the end of the 21st century, with all eighteen scenarios predicting changes within ±10% of the historical mean annual flow (Table 4.1) with an average change in annual flow of –0.5%. As the wettest GCM, HadCM3 A1FI and B1 scenarios produced the largest increases (+9.6% and +7.7%, respectively) while only CGCM2 consistently predicted decreased annual flow rates (A2 -7.2%, and B2 -8.8%). The other models tended to predict small positive or negative changes. All eighteen scenarios, however, predicted declines in the mean annual maximum and minimum flow rates, with maximum flows declining by an average of 29% and minimum flows declining by 17%.

Figure 4.7b shows the predicted mean annual flow rate and annual precipitation. As was the case in the ARB, changes in annual flow under climate change scenarios are weakly correlated with changes in precipitation. Figure 4.7b also depicts the enveloping curves for each 30-year simulation. The increased spread is a reflection of differences between the individual GCMs and the different climate scenarios; however, inter-GCM variation appears to dominate. Overall, the projected annual precipitation tends to increase with time even though the spread between GCMs also increases with time. However, changes to the mean annual runoff are relatively modest compared to

precipitation, and as a whole, the predicted mean annual flow marginally decreases with time.

Figure 4.8 is a plot of the mean monthly flow rates in the FRB for 2070 to 2099 predicted by the seven GCMs for the four SRES climate scenarios. All the scenarios show a similar earlier onset of spring snowmelt in the annual flow pattern, differing primarily in the magnitude of the shift, and a decrease in peak flows during spring and early summer. Mean monthly flows increase during the winter and early-spring months (November to April) and decrease from the late-spring to the fall (May to October). HadCM3 is the only model to predict relatively minor changes in seasonal flow patterns.

Figure 4.9a shows that all climate scenarios predict a decrease in the mean annual maximum snow pack in the FRB against temperature increases over the century. The smallest decreases are predicted by HadCM3, which is the only one of the cooler GCMs to emphasize summer warming. For the other GCM scenarios, the general tendency towards especially warm winters more than offsets the increases in winter precipitation, resulting in a decreased snowpack.

Figure 4.9b shows a decrease in the mean annual maximum snow pack against increasing winter (November to March) temperature despite the predicted increases in winter precipitation, which is attributed to large increases in winter temperature. For example, three scenarios predicted the mean winter temperature to rise above 0°C by the end of the century from the historical -5.6°C, resulting in a large shift away from winter snowfall to rainfall, causing MISBA to predict higher than historical flows during winter months at the expense of lower flows during spring and summer months.

Figure 4.10a shows a general decline in the mean annual maximum flow rate in the FRB against a decreasing mean annual maximum snow pack but this decline in mean annual flow could stop, as can be seen in the CCSRNIES case in the 2080s, which exhibits mean snowpacks less than 60 mm of Snow Water Equivalent (SWE). In these cases, the amplitude of the spring freshet declines dramatically due to a combination of increased winter and decreased late spring (May and June) flows (Figure 4.8).

Simulated annual minimum flows in the FRB show strong correlation with summer precipitation, and both tend to decline for all 18 scenarios (Figure 4.10b) by the end of the century. However, differences in the predicted extent of this decline vary widely, ranging from as little as -3.5% (NCARPCM B2) to as much as -36.1% (HadCM3 A1FI).

4.4.3 Generalized Equations

For the ARB and FRB, nonlinear relationships between mean annual runoff and mean annual minimum and maximum flows to mean annual rainfall, mean annual snowfall and changes to mean annual winter and summer temperature were developed using a variation of the Shuffled Complex Evolution algorithm (Nelder and Mead, 1964; Duan *et al.*, 1992, and Duan *et al.*, 1993) (see Figures 4.11 and 4.12).

For the ARB,

$$Q_{mean,ARB} = 0.276P_{rain}\exp(-0.00612\Delta T_s) + 0.604P_{snow}\exp(-0.165\Delta T_w) \quad (4.1)$$

$$Q_{\min,ARB} = 0.186P_{rain}\exp(-0.00181\Delta T_s) + 0.654P_{snow}\exp(-0.304\Delta T_w) \quad (4.2)$$

$$Q_{\max,ARB} = 4.25P_{rain}\exp(0.0396\Delta T_s) + 12.4P_{snow}\exp(-0.0719\Delta T_w) \quad (4.3)$$

For the FRB,

$$Q_{mean,FRB} = 0.347P_{rain}\exp(-0.0227\Delta T_s) + 0.600P_{snow}\exp(-0.0398\Delta T_w) \quad (4.4)$$

$$Q_{\min,FRB} = 1.22P_{rain}\exp(-0.0987\Delta T_s) + 0.104P_{snow}\exp(-0.388\Delta T_w) \quad (4.5)$$

$$Q_{\max,FRB} = 3.71P_{rain}\exp(0.0747\Delta T_s) + 16.8P_{snow}\exp(-0.130\Delta T_w) \quad (4.6)$$

where, Q_{mean} is mean annual runoff in mm, Q_{min} and Q_{max} are the mean annual minimum and maximum flow in m^3/s, P_{rain} and P_{snow} are the mean annual rainfall and snowfall in mm, and ΔT_s and ΔT_w are the changes in mean annual summer and winter temperature from the 1960-1990 baseline in °C. The correlations between these equations and the modelled results are generally high (R^2 values range from 0.82 to 0.94), and generally only a small fraction of the hydrologic behaviour that cannot be explained by these equations because of the spatial and temporal variability of temperature and precipitation patterns across the scenarios.

Many of the coefficients are similar for both basins, except for the coefficients for P_{rain} and P_{snow} for minimum flows. The temperature coefficients in these equations show that flow rates in the both basins are more sensitive to changes in winter temperature than changes in summer temperature, suggesting that increased sublimation of the snow pack has a greater impact on the streamflows in both basins than increases in summer evapotranspiration. This can be best explained by the fact that an exposed snow surface can continually sublimate at the potential rate while a surface soil quickly dries out in the absence of sustained rainfall. Changes in winter temperature therefore have much more time to produce large reductions in water storage than changes in summer temperature, as is evident in the larger winter temperature coefficients for minimum than for average and maximum flows. In order for snowfall to contribute to minimum flows, snowmelt must

enter the near-surface water table and persist for several months since minimum flows usually occur in months with little or no snowmelt. Since increasing winter temperatures result in both smaller snowpacks and earlier snowmelt it becomes exceedingly difficult for snowfall to contribute to minimum flows because more time will have elapsed since melting occurred and the initial contribution will be smaller.

All the temperature coefficients are negative in both basins, except for summer temperature in the maximum flow equations. This reflects the importance of evaporation and sublimation losses for mean and minimum flows, which are sensitive to hydrologic processes at seasonal time scales. In the case of maximum flows, the temperature coefficient is positive because evaporation is generally less under humid conditions and so not as important as the increase in rainfall rates (P_{rain}) associated with increased temperatures.

The rainfall coefficients for mean annual and maximum flows are also similar in both basins. In the case of mean annual flows, under historical climate conditions, approximately 60% of annual snowfall contributes to streamflow, while the rainfall contribution is about 35% in the FRB and 28% in the ARB. Similarly, in both basins the contribution of snowfall to maximum flows is much higher than that of rainfall, although large differences in the temperature coefficients reduce this effect as the climates warm.

Some fundamental differences in the hydrology of the two basins are apparent in differences in the coefficients of these equations. In the ARB, under historical conditions, precipitation that falls as rain is less likely to leave the basin as streamflow in the FRB where a unit of rainfall generally produces about 25% more runoff than a unit of

rainfall in the ARB because the FRB is wetter than the ARB and therefore rainfall is more likely to fall on wet soils in the FRB than in the ARB and produce more runoff in an average year. This is especially true in the plains regions of the ARB where summer rains often fall on very dry soils and produce little runoff relative to the precipitation intensity of these events. Annual flow in the ARB is also more sensitive to changes in winter temperatures because snowpacks have more time to sublimate before the melting occurs. Overall, the proportional influence of P_{snow} over P_{rain} for the ARB is higher than for the FRB, especially for the minimum flows (compare Equations 4.2 and 4.5). Furthermore, as expected, the influence of P_{rain} and P_{snow} are the strongest for the maximum flows and weakest for the minimum flows, in both basins.

The two basins differ in their sensitivities to rainfall and snowfall on the minimum flow rates, which reflects the long-term storage of water in the surface water table, since this is the only water source that can consistently supply water to a river during periods with little rainfall, either due to a general lack of precipitation or during cold winter months. In the ARB, minimum flows are mostly supplied by the spring snowmelt, while in the FRB they are more dependent on summer rains. In the absence of rapid river ice freeze-up events, low flows in the ARB usually occur in the late winter, almost a full year after the previous snowmelt. Because this water must persist for such a long period in order to maintain late winter flows, the basin is very sensitive to sublimation losses as much of this water would otherwise recharge the soil making it easier for summer rainfall to maintain soil groundwater storage for the winter. In the wetter FRB, summer rainfall has a much better chance of recharging any moisture deficit that may have occurred due to a low winter snowpack and so summer evaporation is a

much more important factor than in the ARB.

4.5 Summary and Conclusions

The potential effects of anthropogenic climatic change on streamflows of two regional Canadian river basins, Athabasca and Fraser River Basins, were estimated by applying the projections of seven GCMs under four SRES emission scenarios of IPCC over three 30-year periods in the 21st century to the ERA-40 re-analysis dataset downscaled with the GEM data. For both basins, the GCMs project average increases in temperature and precipitation of approximately 5°C and 10%, respectively, although the GCM precipitation projections show far more variation in the FRB than the ARB. Despite this similar change in climate, the simulated streamflow responses in the two basins differ.

In the ARB, mean annual flows are expected to decline as the shortened snowfall season and increased sublimation together lead to a decline in the spring snowpack. Although the wettest scenarios predict mild increases in annual runoff in the first half of the century, all GCM and emission combinations predict large declines by the end of the 21st century with an average change in annual runoff, mean maximum annual flow and mean minimum annual flow of –21%, –4.4%, and –41%, respectively.

The climate scenarios in the FRB present a less clear picture of streamflows in the 21st century. All 18 GCM projections suggest mean annual flows in the FRB should change by ±10% with 8 projections suggesting increases and 10 projecting decreases in mean annual flow. The primary reason for this stark contrast with the ARB results is the fact that the FRB currently has a much milder climate. Under the warmest scenarios,

much of the FRB is projected to become warmer than 0°C for most of the calendar year, resulting in a decline in the amplitude of the FRB's characteristic snow fed annual hydrograph response. The fact that the FRB is also much wetter than the ARB means that the FRB is not as dependent on winter snowfall because the shift to winter rains happens at a wetter time of year in the FRB and so these rains are more likely to produce runoff than in the ARB. The decline in the amplitude of the snow melt flood wave in the FRB also results in a large decline in the average maximum flow rate as summer rainfall events build upon reduced baseflow.

The impact of climatic change on the mean annual minimum flow in the FRB is much more varied than in the ARB due to the FRB's sensitivity to summer rainfall and the relatively high variance between GCMs for this predictor. Unfortunately, there are great disagreements between climate scenarios projected by different GCMs on how global increases in temperature are manifested in regional precipitation changes. For example, HadCM3 predicts dramatic increases in precipitation under the A2 emissions scenario in the Arctic regions of North America and large decreases in Central America and northern South America, while CGCM2 predicts much milder changes in these regions (Figure 4.13). CGCM2 also predicts wetter conditions along the Pacific Coast of the United States and drier conditions along the Atlantic Coast, while HADCM3 predicts the opposite.

Overall, the nonlinear relationships between annual mean, minimum and maximum flows to mean annual rainfall, snowfall and changes to mean annual winter and summer temperature changes show that flow rates in both basins are more sensitive to

winter and summer temperatures (due to the greater impact of increased sublimation of the snowpack than increased summer evaporation) and the contribution of snowfall to maximum flows is much higher than the contribution than that of rainfall.

Differences in the predictions of temperature and precipitation of different GCMs at regional spatial scales is currently the most important factor limiting the application of GCM model output to water management and planning. Although many key hydrologic variables show much variation between different GCMs by the end of the 21st century, the models consistently predict similar seasonal changes in flow patterns, due primarily to temperature induced phase shifts from snow to rain. These changes include the earlier onset of snowmelt, a decline in the amplitude of the snowmelt flood wave, a reduction in flow during the summer months, and declines in flows during low flow months.

Table 4.1 - Changes in flow statistics for Athabasca and Fraser River Basins from 2070–2099 with respect to the 1961–1990 climate normal under various combinations of GCM model and SRES emission scenarios.

		% Change in					
		Athabasca River basin			Fraser River Basin		
Model	SRES Scenario	Mean Annual Flow	Maximum Annual Flow	Minimum Annual Flow	Mean Annual Flow	Maximum Annual Flow	Minimum Annual Flow
NCARPCM	A2	-16.4	-11.7	-33.6	-7.3	-35.2	-5.6
	B2	-5.0	10.0	-17.6	0.8	-24.4	-3.5
ECHAM4	A2	-36.6	-12.4	-57.5	-2.1	-24.5	-35.3
	B2	-32.5	-10.4	-56.9	1.6	-18.7	-20.9
GFDLR30	A2	-22.3	-6.4	-53.6	-0.2	-37.5	-14.3
	B2	-26.1	-4.5	-47.5	1.0	-26.6	-7.1
HadCM3	A1FI	-14.7	1.3	-36.2	9.6	-19.4	-36.1
	A2	-8.9	8.1	-25.8	3.2	-16.1	-29.7
	B1	-7.6	4.8	-22.9	7.7	-18.5	-14.5
	B2	-5.0	10.5	-18.3	-1.2	-23.5	-24.8
CSIROMk2b	A2	-23.7	-5.9	-50.9	4.9	-36.0	-10.3
	B2	-22.8	-3.1	-50.2	-0.7	-36.2	-7.0
CGCM2	A2	-24.8	-6.1	-45.6	-7.2	-36.5	-18.2
	B2	-26.6	-8.5	-47.7	-8.8	-32.8	-12.8
CCSRNIES	A1FI	-27.0	-10.3	-34.0	-1.6	-33.9	-22.6
	A2	-27.3	-7.7	-36.8	0.9	-33.9	-20.5
	B1	-29.5	-17.9	-50.6	-5.8	-34.2	-14.9
	B2	-22.0	-9.8	-52.8	-2.9	-36.2	-4.6
Mean		-21.1	-4.4	-41.0	-0.5	-29.1	-16.8
Median		-23.3	-6.3	-46.6	-0.5	-33.4	-14.7

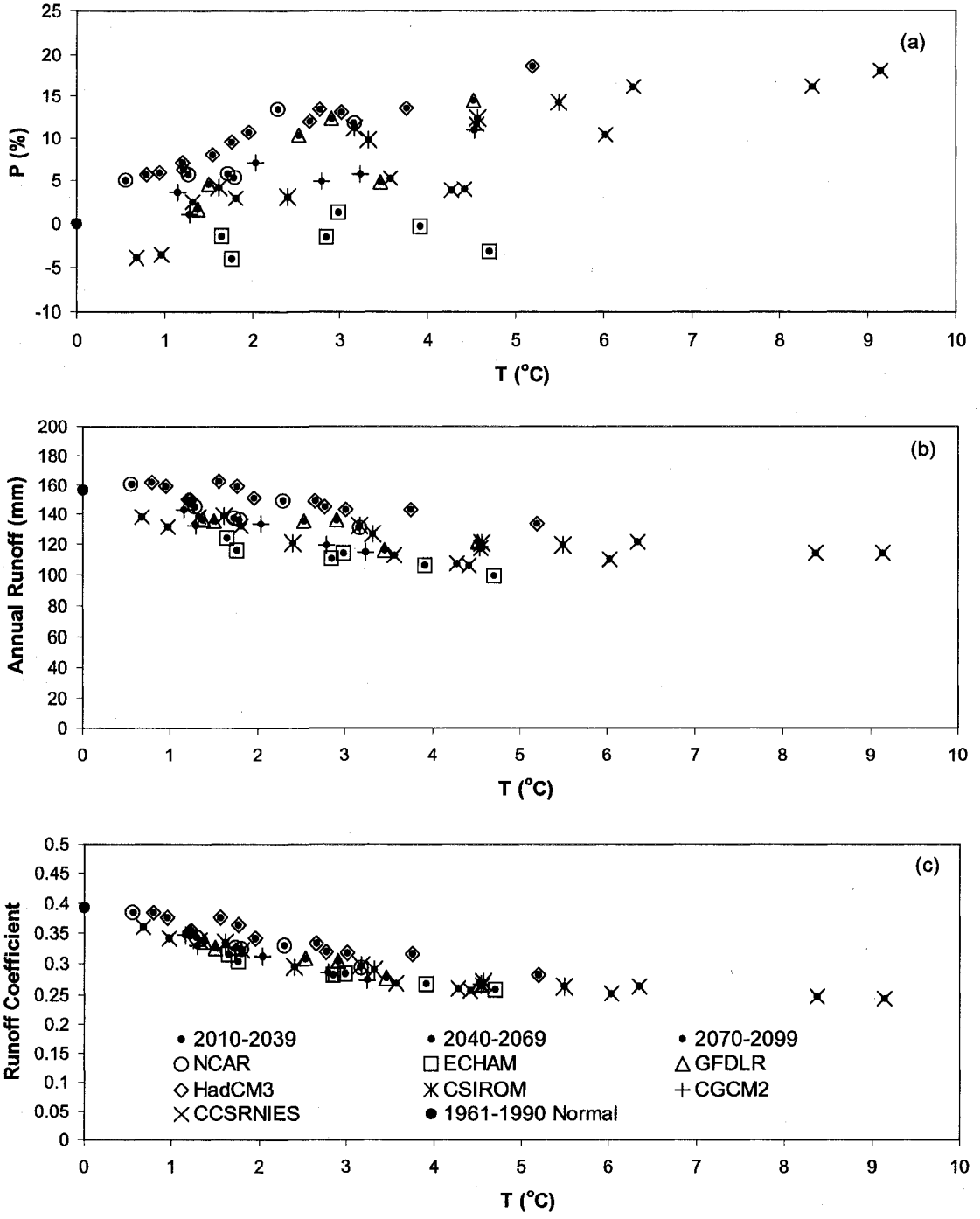

Figure 4.1 – Changes in a) annual precipitation (ΔP), b) annual runoff, and c) runoff coefficient against changes in annual temperature (ΔT) in the Athabasca River Basin predicted by SRES climate scenarios

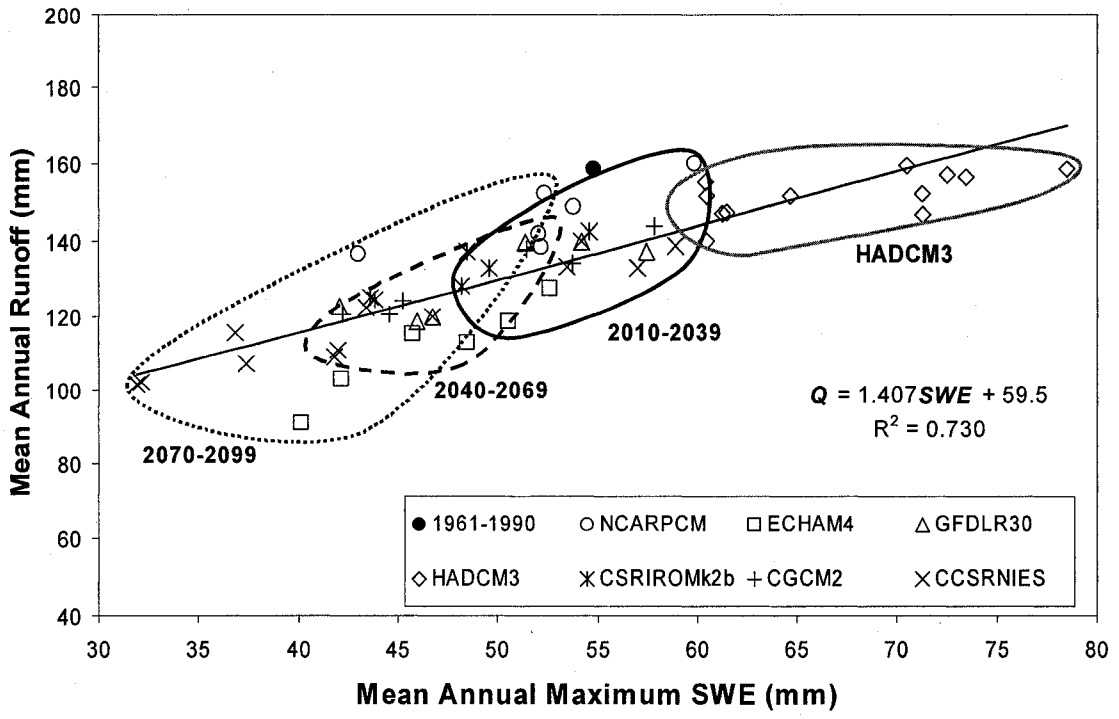

Figure 4.2 - Mean annual runoff verses mean annual maximum Snow Water Equivalent (SWE) in the Athabasca River Basin.

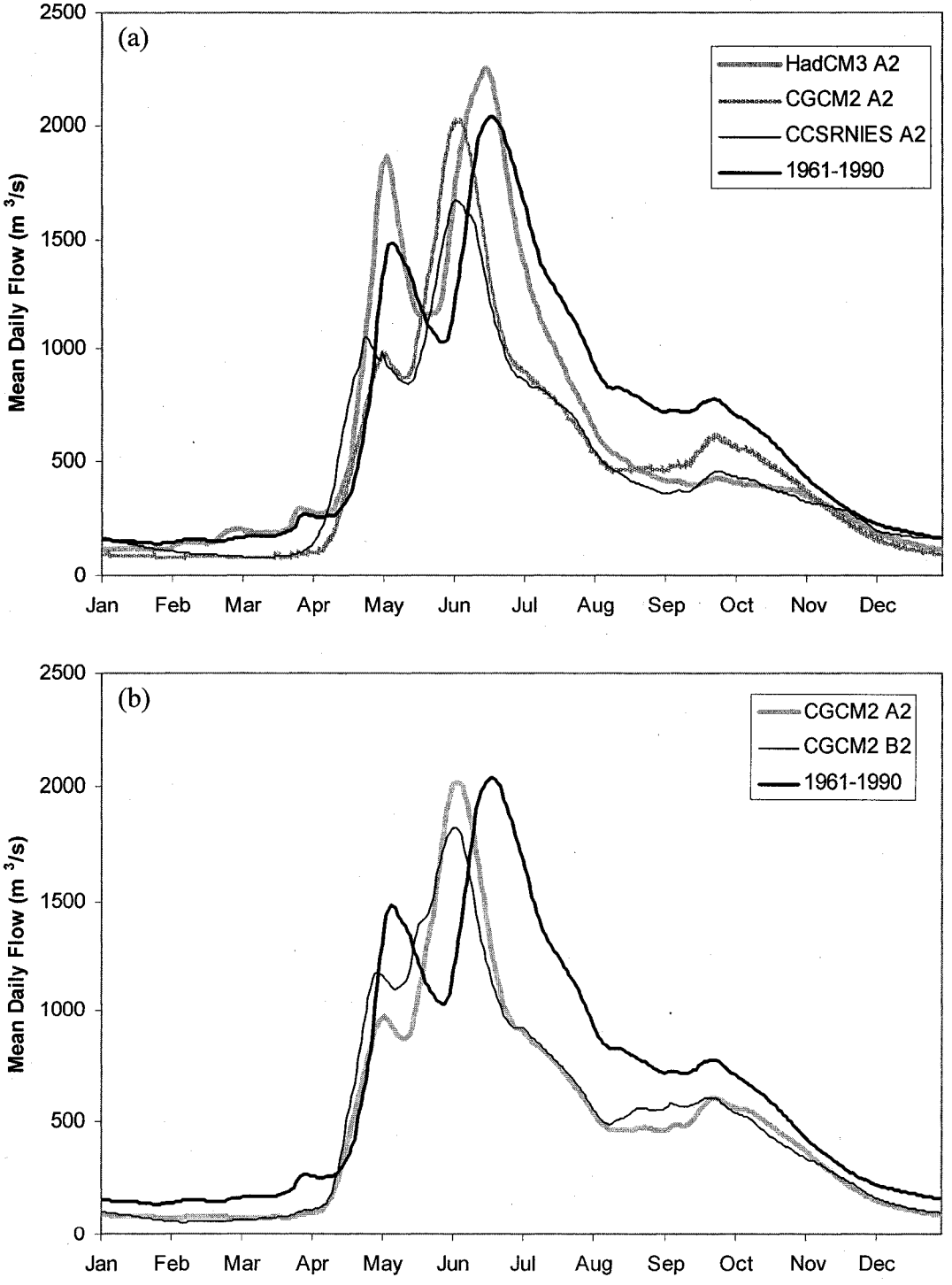

Figure 4.3 - Mean daily flow rates for 2070–2099 for a) A2 Climate Scenarios and b) CGCM2 climate scenarios and historical flow rates for the 1961–1990 climate normal in the Athabasca River Basin.

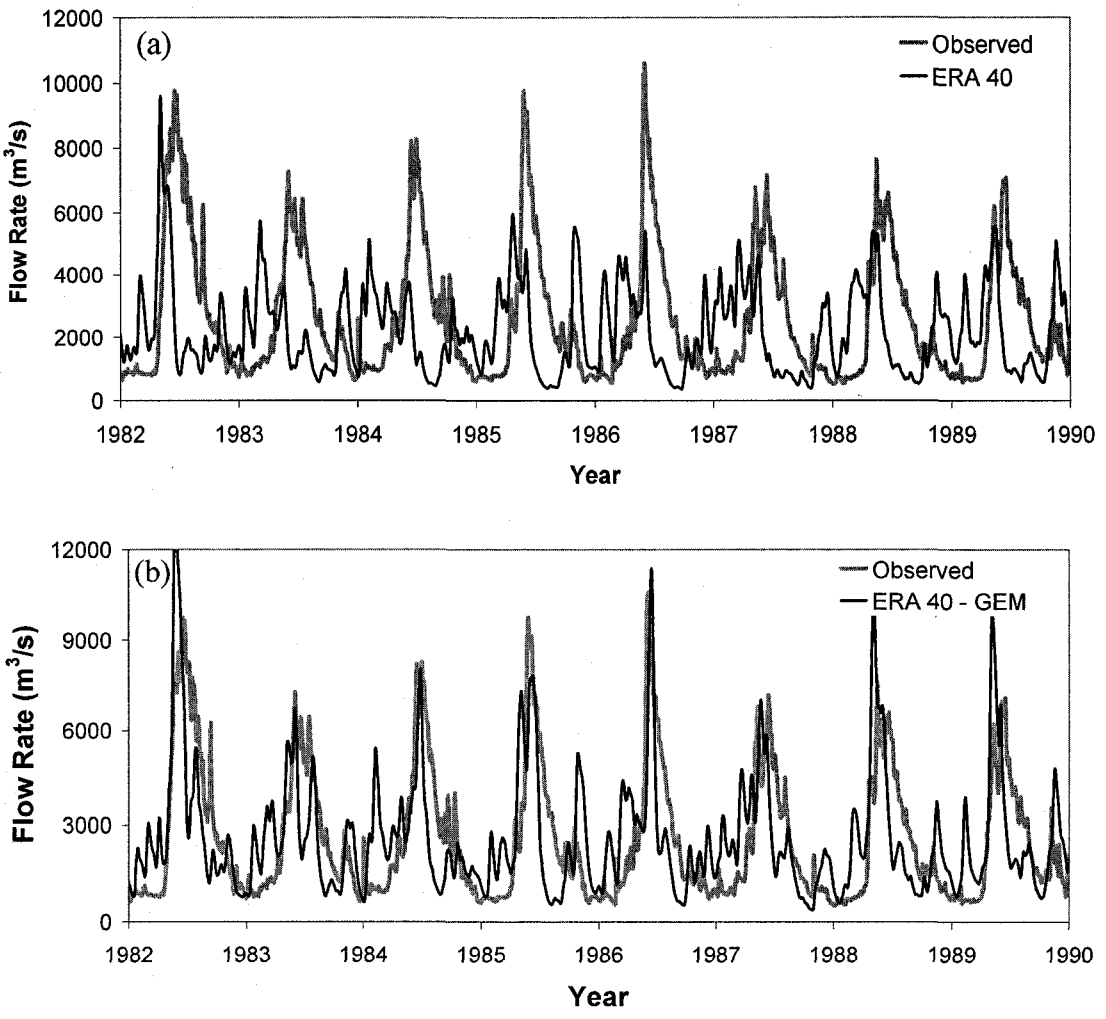

Figure 4.4 - Observed and simulated hydrographs for Fraser River at Hope, (a) ERA40 simulation and (b) ERA40-GEM simulation

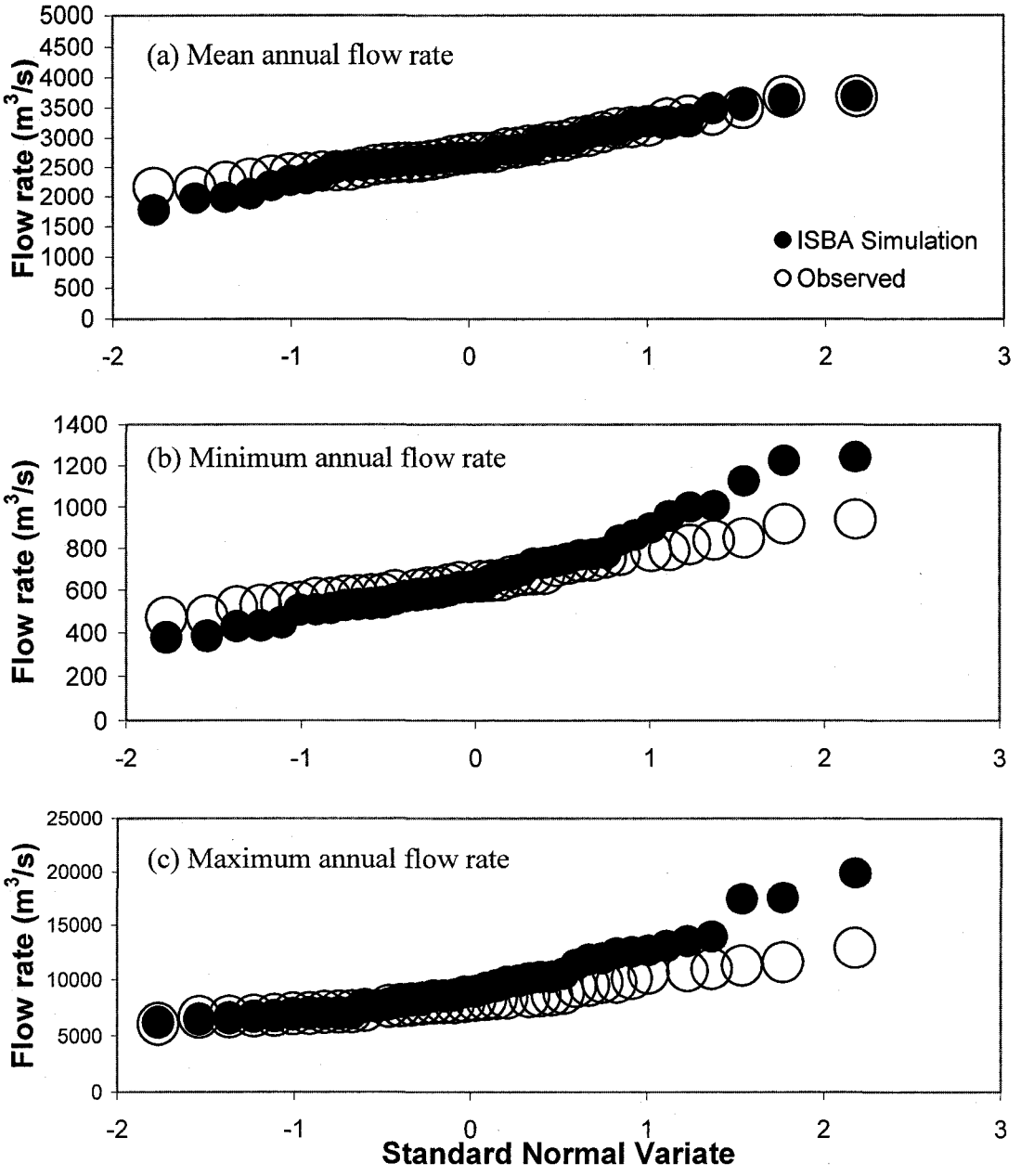

Figure 4.5 - Observed and ERA40-GEM simulated frequency plots for the Fraser River at Hope, (a) mean annual flow rate, (b) minimum annual flow rate, and (c) maximum annual flow rate.

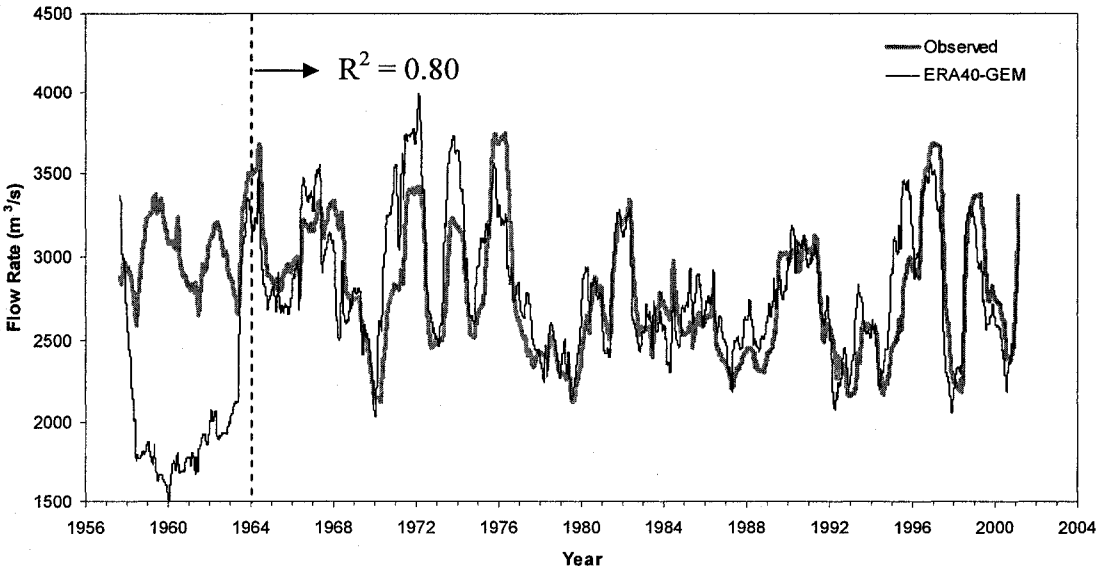

Figure 4.6 - Observed and ERA40-GEM 365-day moving average flow rates for the Fraser River at Hope.

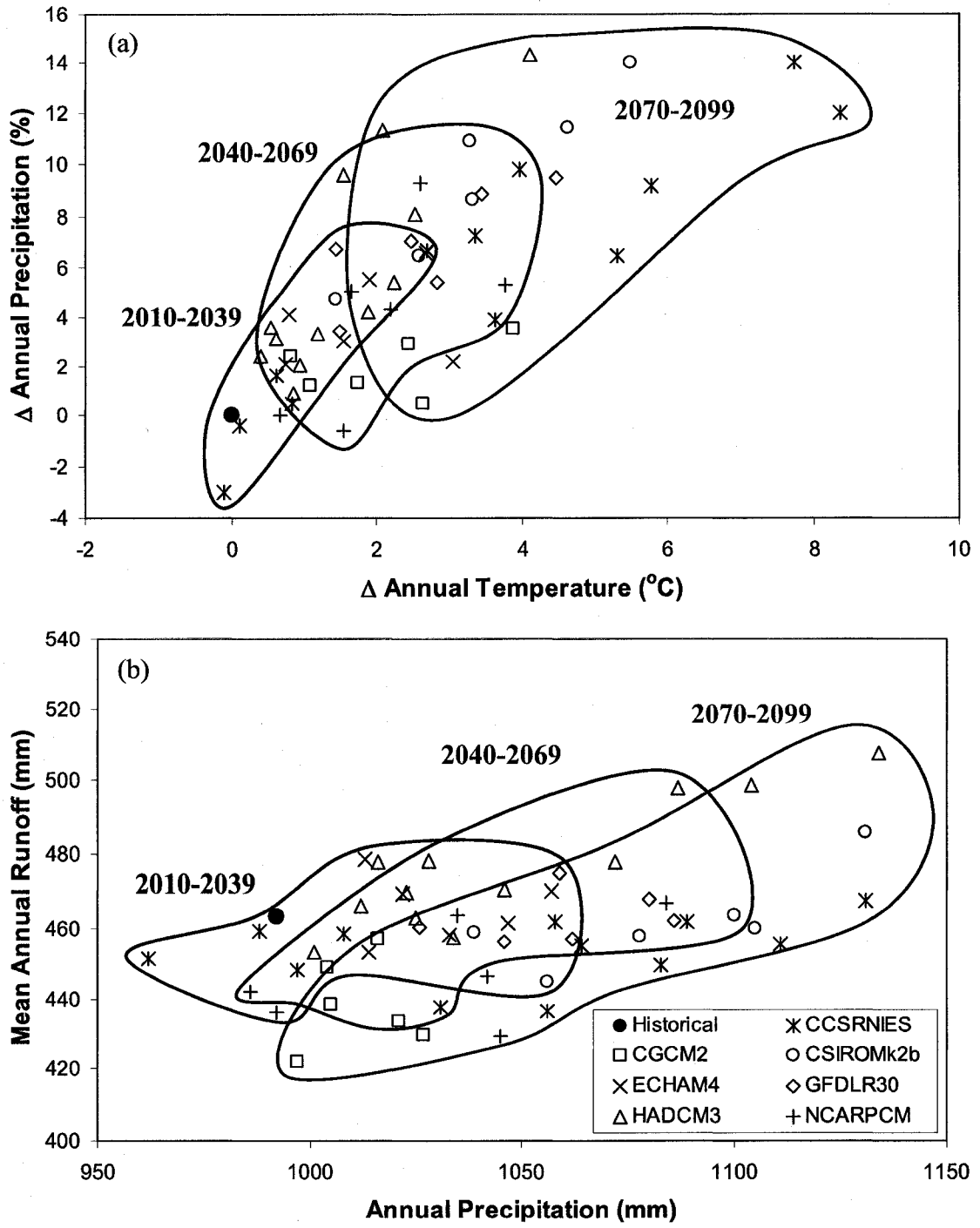

Figure 4.7 – Projected (a) temperature and precipitation changes and (b) mean annual runoff changes relative to the historical 1961 to 1990 baseline in the Fraser River Basin according to 18 SRES climate scenarios. The blue, green, and red curves envelope the 2010-2039, 2040-2069, and 2070-2099 simulations respectively.

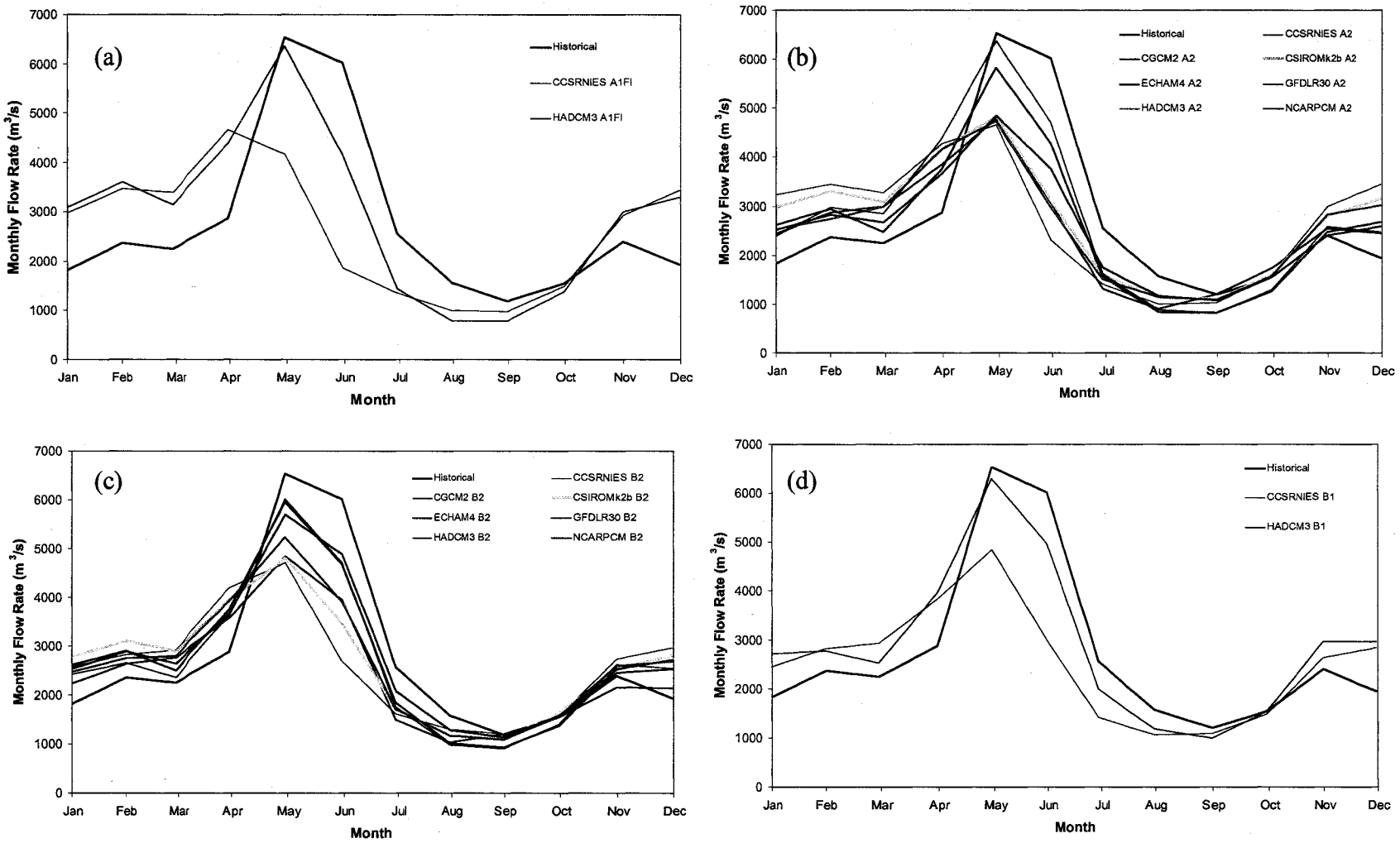

Figure 4.8 - Mean monthly flows in the Fraser River at Hope for 2070-2099 of various climate scenarios: (a) A1FI, (b) A2, (c) B2, and (d) B1.

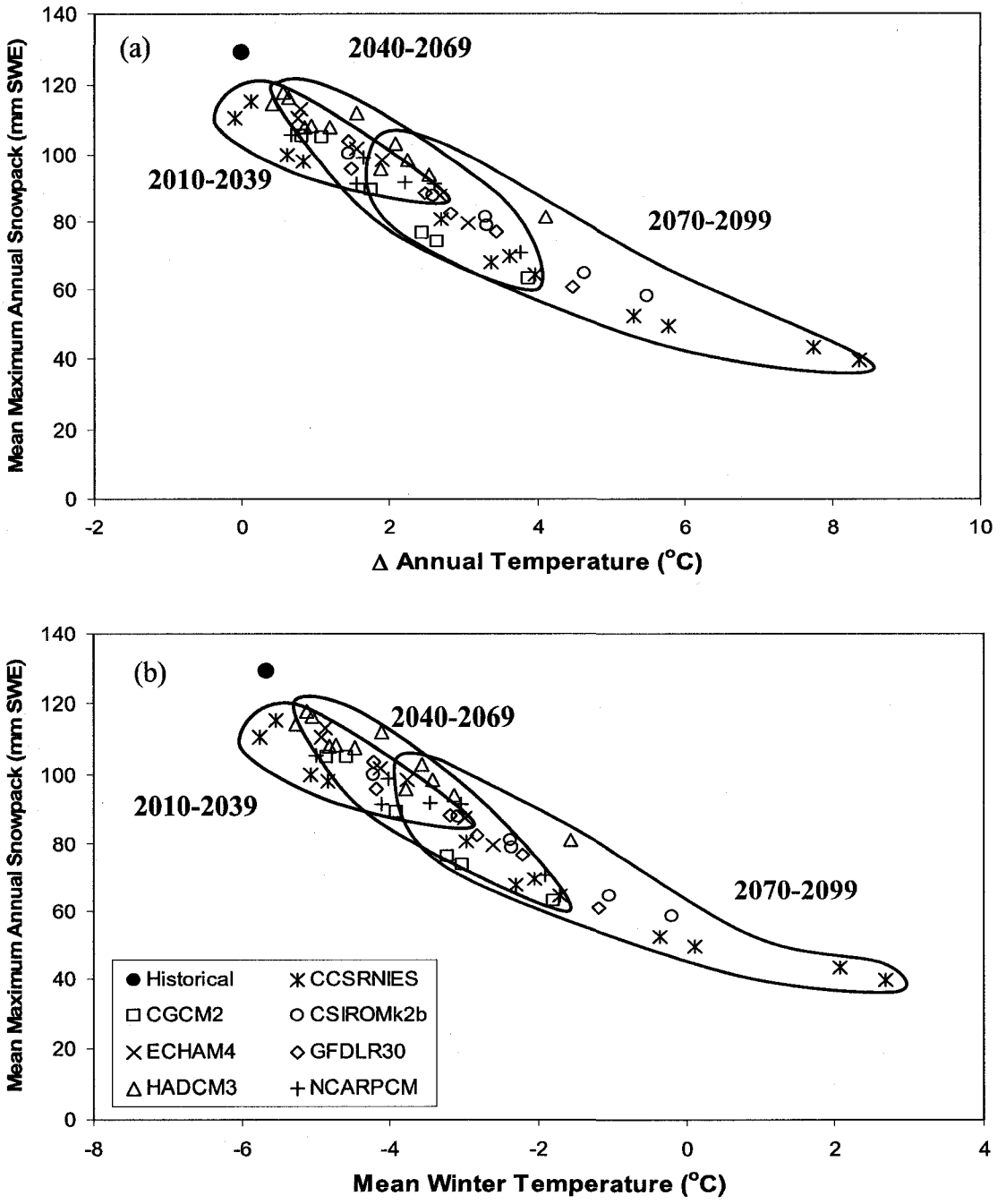

Figure 4.9 - Mean annual maximum snow pack in the Fraser River Basin versus (a) change in mean annual temperature and (b) mean winter temperature. The blue, green, and red curves envelope the 2010-2039, 2040-2069 and 2070-2099 simulations respectively.

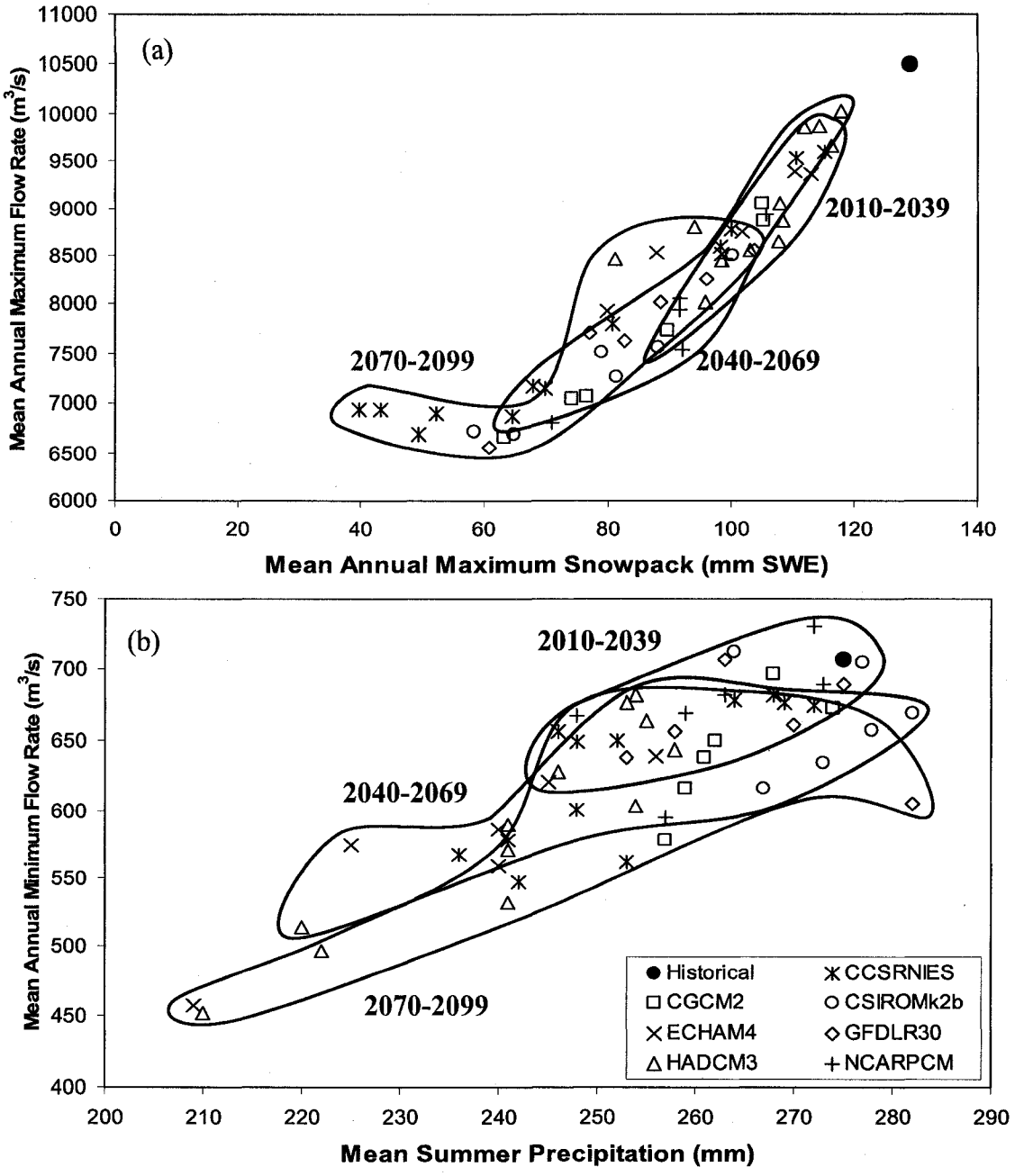

Figure 4.10 – (a) Mean annual maximum flow versus and mean annual snow pack and (b) mean annual minimum flow rate versus mean summer precipitation in the Fraser River Basin. The blue, green, and red curves envelope the 2010-2039, 2040-2069 and 2070-2099 simulations respectively.

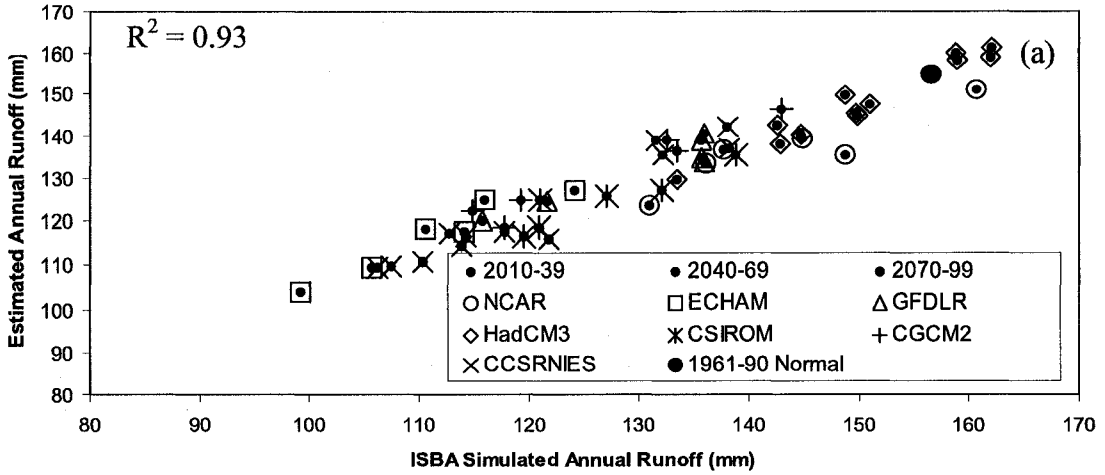

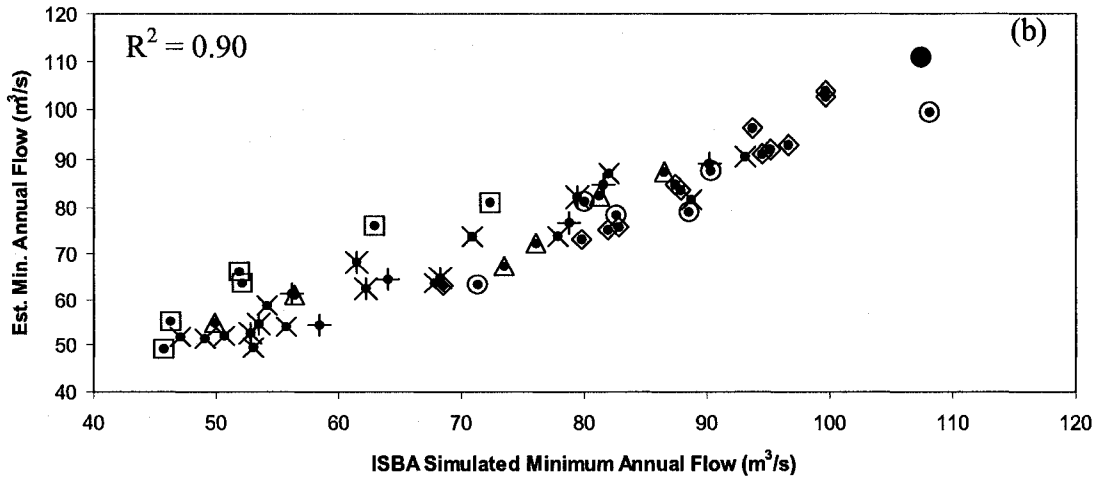

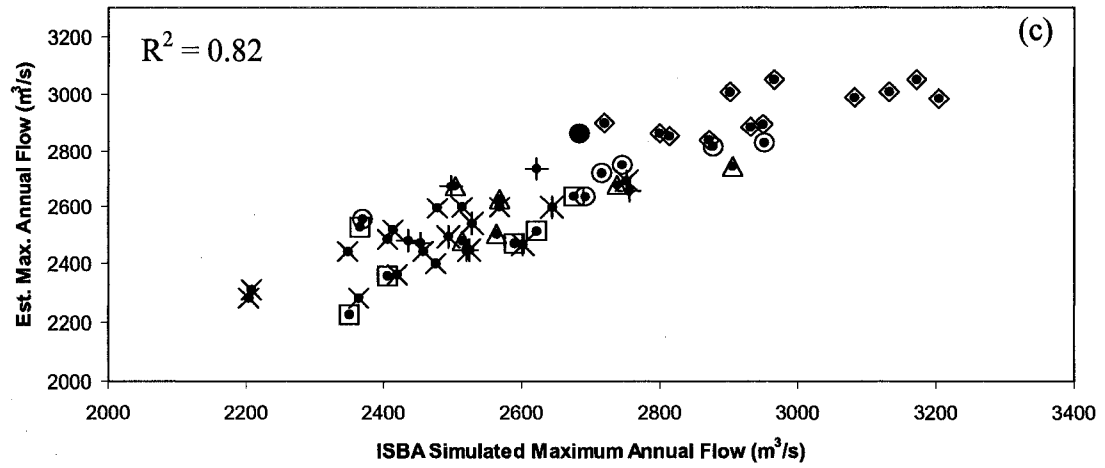

Figure 4.11 - Generalized relationships in the Athabasca River Basin between mean annual runoff, mean annual minimum flow, and mean annual maximum flow; and precipitation and temperature temperature changes. P_{rain} and P_{snow} indicate annual rainfall and snowfall in mm, respectively. ΔT_s and ΔT_w indicate changes in summer and winter temperatures in °C, respectively.

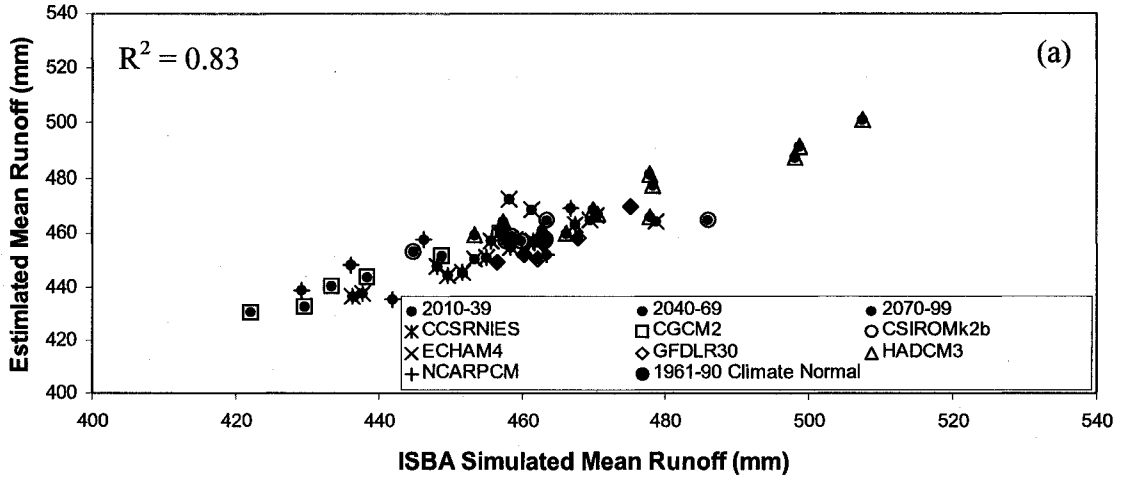

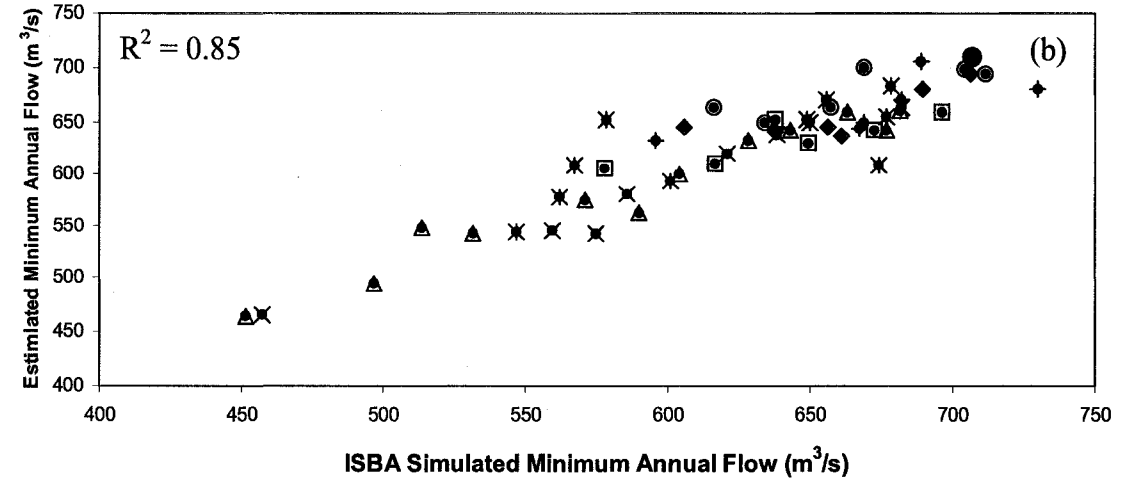

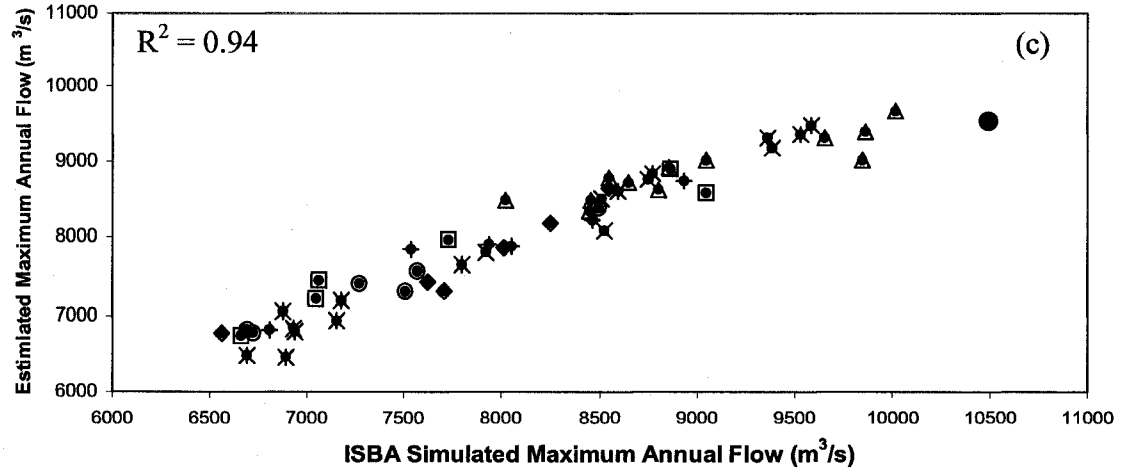

Figure 4.12 - Generalized relationship in the Fraser River Basin between mean annual runoff, mean annual minimum flow, and mean annual maximum flow; and precipitation and temperature temperature changes. P_{rain} and P_{snow} indicate annual rainfall and snowfall in mm, respectively. ΔT_s and ΔT_w indicate changes in summer and winter temperatures in °C, respectively.

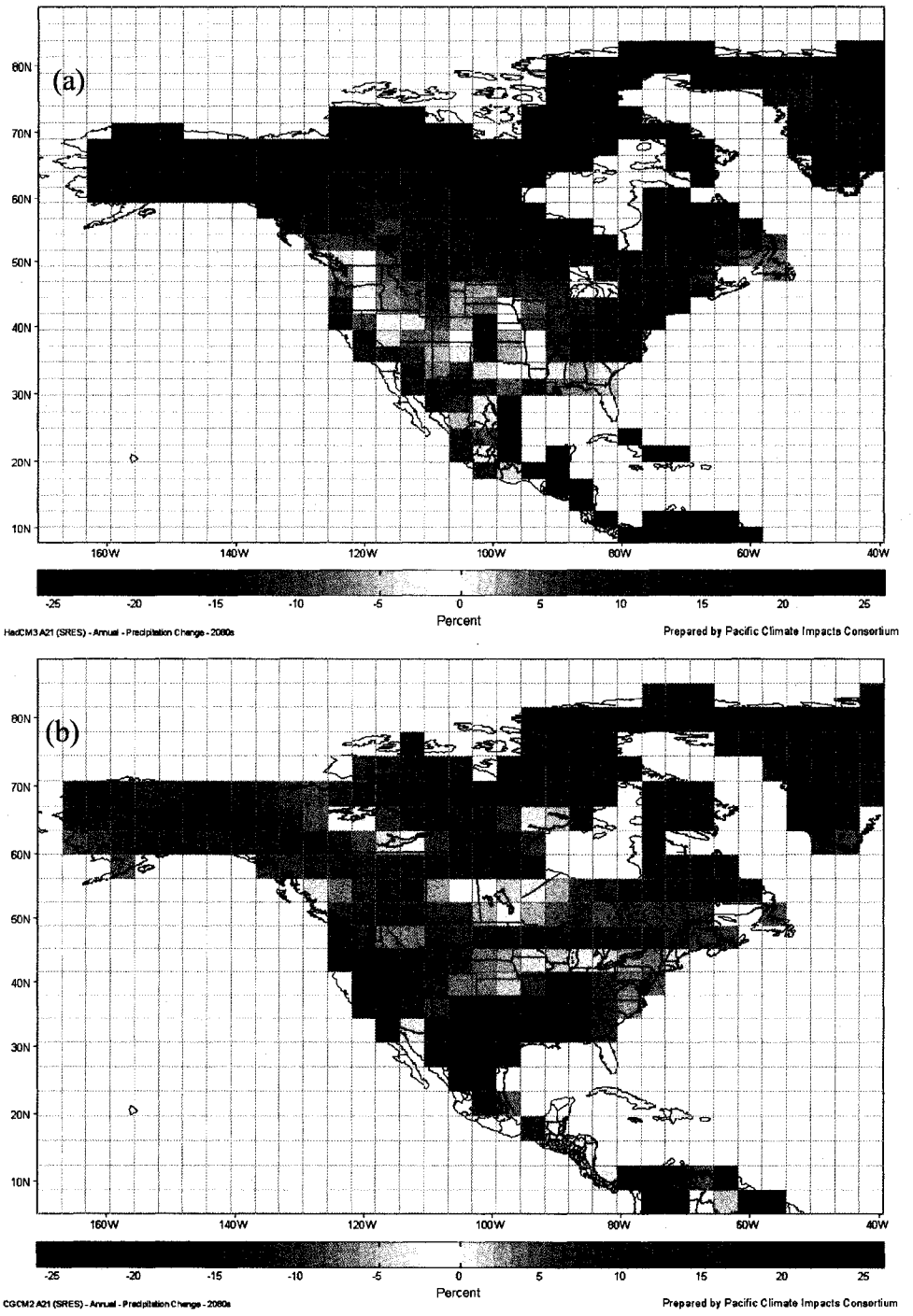

Figure 4.13 - Projected changes in annual precipitation over North America for 2070-2099 according to the (a) HadCM3 A2 and (b) CGCM2 A2 scenarios. Taken from Canadian Climate Impacts and Scenarios (CCIS) Project.

4.6 Bibliography

Alberta Environment, (2007), *Lower Athabasca Management Plan*, Alberta Environment, Edmonton, Canada.

Beniston, M., F. Keller, B. Koffi, and S. Goyette, (2003), Estimates of snow accumulation and volume in the Swiss Alps under changing climatic conditions, *Theoretical Applications in Climatology*, 76, 125–140.

Brekke, L.D., N.L. Miller, K.E. Bashford, N.W.T. Quinn, and J.A. Dracup, (2004), Climate change impacts uncertainty for water resources in the San Joaquin River basin, California, *J Am Water Resour Assoc*, 40, 149–164

Cunge, J.A., (1969), On the subject of a flood propagation computation method (Muskingum Method), *J. Hydraul. Res.* 7(2), 205–230.

Cubasch, U., and R.D. Cess, (1990), Processes and Modeling, In: *Climate Change: the IPCC Scientific Assessment*, edited by: Houghton, J.T., Jenkins, G.J. , Ephraums, J.J. , Cambridge University Press, Cambridge, 69-91.

Demuth, M., and R. Keller, (2006), An assessment of the mass balance of Peyto Glacier (1966-1995) and its relations to recent and past-century climatic variability, *Peyto Glacier-One Century of Science*, edited by: Demuth, M., D. Munro, and G. Young, , National Hydrology Research Institute, Science Report 8, 83-132.

Dettinger, M.D., D.R. Cayan, M.K. Meyer, and A.E. Jeton, (2004), Simulated hydrologic responses to climate variations and change in the Merced, Carson, and American River basins, Sierra Nevada, California, 1900–2099, *Climatic Change*, 62, 283–317.

Duan, Q., V.K. Gupta, and S. Sorooshian, (1992), A Shuffled Complex Evolution Approach for Effective and Efficient Optimisation, *J. Optimization Theory Appl.*, 76(3), 501-521.

Duan, Q., S. Sorooshian, and V.K. Gupta, , (1993), Effective and efficient global optimisation for conceptual rainfall-runoff models, *Water Resources Research*, 28(4), 1015-1031.

Etchevers, P., C. Golaz, F. Habets, and J. Noilhan, (2002), Impact of a climate change on the Rhone river catchment hydrology, *Journal of Geophysical Research*, 107(D16), 4293, doi:10.1029/2001JD000490.

Fulton, R.J., (1995), *Surficial materials of Canada, Geological Survey of Canada, "A" Series Map 1880A*, Natural Resources Canada.

Gates, W.L., A. Henderson-Sellers, G.J. Boer, C.K. Folland, A. Kitoh, B.J. McAvaney, F. Semazzi, N. Smith, A.J. Weaver, and Q.-C. Zeng, (1996) Climate Models - Evaluation, In: *Climate Change 1995: the Science of Climate Change. Contribution of Working Group I to the Second Assessment Report of the Intergovernmental Panel of Climate Change*, edited by: Houghton, J.T., L.G. Meira Filho, B.A. Callander, N. Harris, A. Kattenberg, , K. Maskell, Cambridge University Press, Cambridge, 235-284.

Intergovernmental Panel on Climate Change, (2000), *Emissions Scenarios*, A Special Report of Working Group II of the Intergovernmental Panel on Climate Change. Cambridge University Press, Cambridge.

Intergovernmental Panel on Climate Change, (2001), *Climate Change 2001: The Scientific Basis*, Contribution of Working Group 1 to the Third Assessment Report of the Intergovernmental Panel on Climate Change, Cambridge University Press, Cambridge.

Intergovernmental Panel on Climate Change, (2007), *Climate Change 2007 - The Physical Science Basis*, Contribution of Working Group 1 to the Fourth Assessment Report of the Intergovernmental Panel on Climate Change, Cambridge University Press, Cambridge.

Kellerhals R., C.R. Neill, and D.I. Bray, (1972), Hydraulic and Geomorphic Characteristics of Rivers in Alberta, Edmonton: Research Council of Alberta, 383p.

Kerkhoven, E., and T.Y. Gan, (2006), A Modified ISBA Surface Scheme for Modeling the Hydrology of Athabasca River Basin with GCM-scale Data, *Advances in Water Resources*, 29(6), 808-826.

Knowles N., and D.R. Cayan, (2004), Elevational dependence of projected hydrologic changes in the San Francisco estuary and watershed, *Climatic Change*, 62, 319–336.

Lettenmaier, D.P., and T.Y. Gan, (1990), Hydrologic sensitivities of the Sacramento-San Joaquin River Basin to global warming, *Water Resources Research*, AGU, 26(1), 69-86, 1990.

Luckman, B.H, (2006), The Neoglacial history of Peyto Glacier, *Peyto Glacier-One Century of Science*, edited by: Demuth, M., D. Munro, and G. Young, National Hydrology Research Institute, Science Report 8, 25-58.

Masson V., J.-L. Champeaux, F. Chauvin, C. Meriguet, and R. Lacaze, (2003), A Global Database of Land Surface Parameters at 1km Resolution in Meteorological and Climate Models, *J Climate*, 16, 1261-1282.

Maurer, E,, (2007), Uncertainty in hydrologic impacts of climate change in the Sierra Nevada, California, under two emissions scenarios, *Climatic Change*, 82, 309–325.

Middelkoop, H., K. Daamen, D. Gellens, W. Grabs, J.C.J. Kwadijk, H. Lang, B. Parmet, B. Schadler, J. Schulla, and K. Wilke, (2001), Impact of climate change on hydrological regimes and water resources management in the Rhine basin, *Climatic Change,* 49, 105–128.

Nelder, J.A., and R. Mead, (1964), A Simplex Method for Function Minimization, *Computer Journal*, 7, 308-313.

Stewart, I.T., D.R. Cayan, and M.D. Dettinger, (2004), Changes in snowmelt runoff timing in western North America under a 'business as usual' climate change scenario, *Climatic Change*, 62, 217–232.

Zierl, B., and H. Bugmann, (2005), Global change impacts on hydrological processes in Alpine Catchments, *Water Resour Res*, 41, W02028, doi:10.1029/2004WR003447.

Chapter Five: Differences in the Potential Hydrologic Impact of Climate Change to the Athabasca and Fraser River Basins with and without Considering the Effects of Shifts in Vegetation patterns Caused by Climate Change

5.1 Introduction

Energy and mass transfer feedbacks between the Earth's ecosystem and the atmosphere, ocean, and land surface systems have long been recognized as having impacts on future projections of climatic change. The Intergovernmental Panel on Climate Change (IPCC) has been working towards dynamic, coupled modeling of all these systems since the First Assessment Report (FAR) when Atmospheric General Circulation Models were run to equilibrium under current and doubled CO_2 forcings with fixed land and ocean properties (IPCC, 1990). By the Second Assessment Report (SAR) coupled Atmosphere-Ocean General Circulation Models were run under transient forcing scenarios of a variety of greenhouse gasses with fixed land-surface properties (IPCC, 1995). The Third (TAR) and Fourth Assessment Reports have seen the addition of increasingly complex Soil-Vegetation-Atmosphere-Transfer schemes (SVAT) that can dynamically model energy and mass transfers between the Atmosphere and the land surface; however, Dynamic General Vegetation Models (DGVM), which would allow for the inclusion of the effect of ecological dynamics, have not yet been coupled to General Circulation Models (GCM) because their development has lagged behind those of the other systems (Neilson and Drapek, 1998; IPCC, 2001; IPCC, 2007).

DGVMs are transient vegetation models unlike their conceptual predecessors, Static Biogeographical Models (SBMs), which used equilibrium climatic conditions to determine equilibrium vegetation (Peng, 2000). Competition between various plant life forms in different environments is simulated based on ecological constraints, such as a

plant's ability to survive frost events, and resource limitations, such as the availability of water. In recent years, a variety of DGVMs have been developed (Woodward *et al.*, 1995; Foley *et al.*, 1996; Bachelet *et al.*, 2001; and Stich *et al.*, 2003) and various intercomparison projects have begun, such as the Vegetation/Ecosystem Modeling and Analysis Project (VEMAP) (Gordon *et al.*, 2004), and the Vulnerability and Impacts of North American Forests to Climate Change: Ecosystem Responses and Adaptation (VINCERA) (Neilson *et al.*, 2007). Preliminary results indicate that a DGVM's performance can be improved by incorporating evaporation and snow routines as well as a more realistic representation of sub-grid soil moisture variability (Gordon *et al.*, 2004).

Ecological dynamics influence future climate predictions by altering the distribution of vegetation species on the land surface which in turn changes the rates of water and energy transfers via changes in surface albedo, surface roughness, and transpiration rates. For example, a northern shift in forest coverage would bring about significant carbon sequestration (negative temperature feedback), a decrease in albedo (positive temperature feedback) and an increase in surface roughness, potentially resulting in a shift from sensible to latent heat fluxes (negative temperature feedback) and a potential increase in cloud coverage due to increased transpiration (positive or negative temperature feedback, depending on cloud type) (Neilson and Drapek, 1998; Cox *et al.*, 2000; Peng, 2000; Neilson *et al.*, 2005).

Species change can result from either subdominant species being replaced by previously dominant species or by species migration. Generally, diverse ecosystems are considered to be more adaptable to rapid changes by allowing for local dominance shifts

to retain critical ecosystem functions due to their increased redundancy. Ecosystem simulations under future climate scenarios have suggested the long-term equilibrium ranges of many species could shift an order of magnitude faster than after the last glaciation environment (Neilson *et al.*, 2005). The potential die off of species that cannot migrate fast enough to keep up with these changes could reduce the ability of some ecosystems to adapt to these climatic changes. DGVMs typically concentrate on relating historic climate with vegetation patterns to estimate critical factors that determine the preferred range of dominant species. If climate conditions change more rapidly than species can migrate, local vegetation could either flourish or dwindle depending on whether growing conditions improve or worsen.

Most DGVMs do not account for migration processes and those that do are too simple to adequately describe the effects of sudden changes in an ecosystem's environment. Furthermore, the development of migration models has been limited by the lack of data describing plant migration processes and a lack of our understanding of the phenology of various species with respect to climate. A detailed understanding of the migratory behaviour of plant types with climatic change requires long-term extensive field observations that in most situations are not available due to the enormous cost and manpower required. Some ongoing questions that have not been adequately addressed include: appropriate triggering mechanisms for catastrophic fires, the treatment of insect infestations, the differing migration rates of plant species with similar ecological functions, the timing and magnitude of increases in plant growth due to increases in water use efficiencies associated with higher CO_2 concentrations, and the interaction between

transient vegetation patterns and ocean-atmosphere general circulation patterns (Hogg and Bernier, 2005; Neilson *et al.*, 2005).

The Mapped-Atmosphere-Plant-Soil-System model (MAPSS) developed by Neilson (1995) can simulate the thermal and water balance constraints that act on individual plant types (e.g., trees, shrubs, grasses, etc.) and biome physiognomy (e.g., forest, savannas, etc.). MAPSS has been the basis of a variety of climate change studies, including forest management in the Canadian Boreal Forest (Scott and Lemieux, 2007), plant migration rates under climate change (Malcolm *et al.*, 2002), vegetation responses in China (Zhao *et al.* 2002), and shifts in the ranges of mammals in the Western Hemisphere (Lawler *et al.*, 2006).

The fundamental assumption underlying how MAPSS treats water balance constraints is that Leaf Area Index (LAI), the surface area of leaf canopy per unit of land surface area, will reach a maximum when all the available soil water is utilized (Neilson, 1995). Trees, shrubs, and grasses compete for areal coverage based on their respective rates of transpiration (i.e. soil moisture use) under different Potential Evapotranspiration (PET) conditions. Grass area is further limited by the presence of trees due to sunlight competition. The effects of fires are incorporated by removing all shrubs and trees whenever there is sufficient fuel (grass and shrubs) and an ignition trigger (indexed by summer rainfall). Competition between needle and broad leaf forms is determined by the presence of cold winters (where temperatures below the supercooled freezing point of water, -40°C, occur at least once in an average year), dry summers (indexed by summer rainfall as a measure of humidity), and the length and warmth of the frost-free season.

Cold winters, dry summers, and short, cool frost free seasons favour conifer forests while mild winters, wet summers, and long, warm frost free seasons favour broadleaf forests. Vegetation is further classified into one of six thermal zones: tundra, taiga, boreal, temperate, sub-tropical and tropical based on the mean annual number of frost free degree-days and the mean annual minimum monthly temperature (Neilson, 1995).

Under most conditions in MAPSS, LAI is controlled by water availability. Since LAI is the key mechanism in MAPSS of assessing competition between trees, shrubs, and grasses, the water budget model used in MAPSS has a strong influence on the performance of the model. MAPSS uses a relatively complex process model to calculate the water budget at the land surface (Figure 5.1). Snowmelt is modelled using the degree-day approach, and surface runoff is assumed to be proportional to the degree of saturation of the upper soil layer (i.e. all precipitation and snowmelt becomes runoff if the soil is saturated and no runoff is generated if the soil is very dry). The infiltration rate is calculated as the difference between the moisture flux at the surface (precipitation and snowmelt) and surface runoff. This is in contrast to the more standard approach of directly calculating the infiltration and applying the residual to surface runoff. Percolation is estimated based on the degree of saturation in the upper soil layer and the available moisture capacity in the lower soil layer. Water percolating through the lowest soil layer is removed as baseflow.

Although the MAPSS water budget model includes most of the processes used in current SVAT schemes, it has some important limitations. The process formulations are conceptual and therefore are reliant on calibration. Unlike current SVATs such as

Modified-Interactions-Biosphere-Soil-Atmosphere (MISBA) (Noilhan and Planton, 1989; Kerkhoven and Gan, 2006), BATS (Dickinson et al., 1986), and SiB (Sellers *et al.*, 1986), the model does not calculate an energy budget. Finally, the water budget model operates on the same monthly time step as the vegetation model, although the runoff and percolation processes are calculated three times in each monthly time step, which is still crude for modelling runoff.

MAPSS has been used to model the equilibrium vegetation distribution of the United States (Neilson, 1995), global vegetation distribution under the $2xCO_2$ scenarios from FAR (Neilson and Marks, 1994), and global vegetation distribution under the transient scenarios from SAR (Neilson and Drapek, 1998). More recently, MAPSS has been combined with the bio-geochemical cycling model CENTURY (Parton *et al.*, 1987) to produce a DGVM called MC1 that has been used to simulate the ecosystem dynamics of Alaska under the SAR scenarios (Bachelet *et al.*, 2005). Although MC1 is currently being tested under the IPCC's Special Report on Emission Scenarios (SRES) climate scenario results, only the MAPSS simulations under the FAR and SAR scenarios are publically available at the moment. Furthermore, preliminary results with TAR scenarios produce similar vegetation shifts as the FAR and SAR scenarios in Canada (Neilson, 2008, personal communication).

5.2 Research Methodology

In Chapter 4, the effects of climatic change on stream flows in the Athabasca (ARB) and Fraser River Basins (FRB) under a variety of SRES climate scenarios from the IPCC's TAR have been estimated using a modified version of the SVAT ISBA. All

these simulations assumed that vegetation distribution of the two basins would not change from the current pattern. In this chapter, the potential effects of vegetation shifts on these simulations will be estimated using the MAPSS simulated model results based on the FAR and SAR GCM scenarios of the IPCC.

Global MAPSS vegetation data is available at a 0.5^{o} resolution, vegetation is classified into 63 categories, and it provides the dominant vegetation type in each grid square. The Ecoclimap data set used in the previous climate change simulations has a 30 arc-second resolution, vegetation is classified into 11 categories, and it provides a distribution of vegetation types in each grid square. Before simulations could be conducted with a modified vegetative cover, the MAPPS data had to be reclassified in a manner consistent with the Ecoclimap dataset. This was done by combining the 29 MAPSS classes present in the Fraser and Athabasca Basins into a total of 11 generalized categories, which were then related to the 5 dominant Ecoclimap classes in the two basins. The Ecoclimap classes Permanent Snow and C3 Cropland were assumed to be unchanged because the MAPSS resolution was too low to resolve mountain glaciers and the MAPSS methodology was designed to predict natural vegetation patterns. Table 5.1 summarizes the relationship used in this study, which were derived by comparing the Ecoclimap and MAPSS vegetation distributions in the Fraser and Athabasca River Basins.

For each ERA-40 meteorological grid square, the change in the areal coverage of each vegetation class between the current and future climate distributions predicted by the MAPSS model was calculated. The vegetation distribution of each Ecoclimap square

was then adjusted by first reducing the coverage of those classes that lost area and then replacing this lost area with vegetation classes that gained area. Vegetation classes that lost area were calculated based on the percent change in areal coverage lost by each class while vegetative classes that gained area were calculated based on their share of area gained.

For example, assume an Ecoclimap square currently consists of 30% broadleaf trees, 60% conifer trees, and 10% grassland and that MAPSS predicted that conifer trees lost 10% of their area while broadleaf trees and grasslands took over 1/3 and 2/3 of the area lost by other classes respectively. The future distribution of vegetation would become, for conifer trees,

$$= (60\%)(1 - 0.1) = 54\%$$

for broadleaf trees,

$$= 30\% + (60\% - 54\%)(1/3) = 32\%$$

and for grasslands,

$$= 10\% + (60\% - 54\%)(2/3) = 14\%$$

MAPSS climate scenarios were based on the predictions of 5 GCM simulations: the Geophysical Fluid Dynamics Laboratory (GFDL) model (Manabe and Stouffer, 1994), the Goddard Institute of Space Studies (GISS) model (Schmidt *et al.*, 2006), the Oregon State University (OSU) model (Sperber and Hameed, 1991), the United Kingdom Meteorological Office (UKMO) model (Cullen, 1993), and the Hadley Centre with Sulphate forcing (HCS) GCM (Johns *et al.*, 1997). The GFDL, GISS, OSU, and UKMO

GCM simulations were from the FAR and represent equilibrium climates with doubled CO_2 concentrations. The HCS model was a transient simulation from the SAR. Because the HCS model was a transient simulation, the MAPSS predictions are based on the GCM results at the end of the HCS simulation, 2070-2099, which approximately coincides with a doubling of atmospheric CO_2 (Neilson and Drapek, 1998).

The climate scenarios used to predict streamflows in the Athabasca and Fraser River Basins in Chapter 4 were based on SRES simulations from the TAR. To minimize the effect of this inconsistency, only the B2 scenarios for 2070-2099 from the TAR were used because this scenario assumes a steady increase in equivalent CO_2 concentrations reaching 915 ppmv by 2100 and best approximates the effects of an atmosphere with double equivalent CO_2 concentrations relative to 1990 (476 ppmv) (CCCma, 2007). The late time period (2070-2099) allows for sufficient time for vegetation shifts to occur. A total of 35 hydrologic simulations (each combination of 5 vegetation scenarios and climate forcings from the SRES B2 climate projections of 7 GCMs) were performed on each basin. Since this methodology mixes the results of different GCM simulations (for example, vegetation from a relatively warm and dry GCM with climate forcings from a relatively cool and wet GCM) the range of final results will tend to be an overestimate of the actual potential range, especially if the process is dominated by negative feedbacks on runoff since this will tend to exaggerate the predictions of inconsistent combinations of GCMs.

The predicted change in the mean temperature between the 50°N and 60°N latitudes for the FAR and SAR simulations used by MAPSS were 3.2°C (HCS and OSU),

4.3°C (GISS), 5.0°C (GFDL), and 7.4°C (UKMO) (Neilson and Drapek, 1998). The seven SRES B2 scenarios ranged from 2.3 to 6.3°C in the Athabasca Basin and 2.6°C to 5.0°C in the Fraser Basin (Figure 5.2a). The B2 scenarios of TAR therefore typically predict less severe climate change than most of the other FAR scenarios but more severe change than the SAR scenario indicating that vegetative shifts under the B2 scenario probably lie somewhere in the middle of the ranges predicted by the five MAPSS scenarios.

5.3 Discussion of Results

Figure 5.2a is a plot of changes in temperature and precipitation in the Athabasca and Fraser River basins with respect to the 1961-1990 baseline under the B2 SRES scenario by the end of the 21st century (2070-2099). The GCMs consistently predict temperature increases in both basins averaging +3.3°C and 3.2°C in the Athabasca and Fraser River basins respectively, and an almost consistent prediction of an increase in annual precipitation, averaging +8% and +7% in Athabasca and Fraser River Basins, respectively. Differences between these GCM predictions vary quite widely in both precipitation and temperature. These increased temperatures result in significant decreases in snow water equivalent in both basins (Figure 5.2b). These results are consistent with the predictions of the other SRES climate scenarios from Chapter 4.

As was seen in Chapter 4, how these changes translate to changes in runoff differ significantly between the two basins. In both basins, when comparing runoff at the end of the century, runoff is higher when precipitation is higher (Figure 5.2c) but in the Athabasca Basin there are significant declines in runoff relative to the 1961-1990

baseline even when precipitation increases significantly relative to the baseline. The relationship between runoff and SWE is also different in the two basins. In the Athabasca, the simulations generally predict runoff declines that are directly proportional to declines in SWE, except for the anomalous HADCM3 GCM that predicts very large increases in winter precipitation that over come the effects of a shorter winter snow season resulting from rising winter temperatures. However, while this increase in maximum winter snow pack translates into stronger spring runoff, much warmer and slightly drier summers result in a net decline in annual flow. Although increased temperatures dramatically reduce the size of the winter snow pack in the Fraser Basin, some of the GCMs produce significant increases in annual flows, while the other GCMs predict small declines despite much larger SWE declines than occur in the Athabasca. The Fraser basin, however, is much wetter than the Athabasca, especially in the winter months. As a result, winter and spring rainfall often falls on a saturated surface, unlike in the Athabasca basin where a much higher proportion of rainfall never reaches the river network system because it falls on relatively dry soils. Again, these results are consistent with the prediction of the other SRES scenarios from Chapter 4.

MAPSS's predictions of the changes in equilibrium vegetative cover in Western Canada under the five projected future climates are shown in Figure 5.3. All the scenarios predict the encroachment of temperate conifer forest in areas currently dominated by mountain taiga forest and the conversion of conifer forest on the Pacific Coast to mixed forest. Most of the scenarios predict large increases in grassland in the British Columbia Interior and a southern and eastern movement of conifer parkland savanna into areas currently dominated by mixed parkland savanna. The scenarios differ

in their predictions of the changes in the Boreal Forest. GISS and HCS predict large increases in mixed forest while GFDL and OSU predict an expansion of parkland conifer savanna. There are also significant differences at the interface between prairie grasslands and parkland savanna. GFDL, GISS, and UKMO predict relatively small changes in prairie grassland area while HCS and OSU predict significant expansion of conifer savanna.

The differences in the prairies can best be explained as a reflection of the sensitivity of vegetation to the precise water balance on the leeward side of the Rocky Mountains, which usually are projected to become warmer and receive more precipitation. Warmer temperatures lead to increased evaporation rates that may or may not be able to overcome the effects of increased precipitation. In the wetter models, trees can expand into what is now dry prairie land. In the boreal forests, predicted changes depend on the balance between winter and summer warming. Winter warming reduces the number of killer frosts and encourages the expansion of broadleaf forests, while summer warming can increase fires, which encourage the expansion of savanna and grassland.

The effect of these changes on vegetative cover in the two basins is summarized in Figure 5.4. In the Athabasca Basin, under some scenarios, the areal coverage of broadleaf (GISS and HCS) or conifer (UKMO) forests are predicted to increase at the expense of grasslands, while others (GFDL and OSU) predict modest increases in grassland area. In the Fraser Basin, most of the scenarios predict moderate increases in grassland area (GFDL, HCS, OSU) while GISS predicts a significant increase in conifer

forest at the expanse of grassland and broadleaf forest. Unlike the other scenarios that predict conifer forest to maintain its dominance of most of the basin, the warm UKMO scenario predicts conifer forested area to drops to 45% of the basin due to a dramatic expansion of grasslands in the central Fraser Basin as well as significant increase in broadleaf forest in the north-western region of the basin.

Each of the five MAPSS vegetation scenarios was used to define the vegetation cover for the seven GCM simulations of the B2 emission scenarios for the 2070-2099 time period. Changes in the simulated mean annual maximum snow pack and mean annual runoff are strongly effected by changes in basin area covered by grassland (Figure 5.5a). This is a reflection of the tendency for more snow to accumulate in open grassland areas than forested areas, due primarily to differences in sublimation rates (Pomeroy et al., 1998). Most of the scenarios predict relatively modest changes in annual runoff and SWE, however the UKMO projection, with its large increase in grassland area in the British Columbia Interior, produces a 58% increase in the mean annual snow pack and a 13% increase in mean annual flow while the GISS and HCS projections, which predict large decreases in grassland area in the Upper Athabasca, produce 30 to 35% less snow and 7 to 8% less annual runoff.

None of the other vegetation types show a similar, consistent strong relationship (Figures 5.5b, 5.5c, and 5.5d). In most of the scenarios there is a strong inverse relationship between changes in conifer forest area and runoff and SWE, except in the cases of the GISS and HCS scenarios in the Athabasca Basin that predict large increases in broadleaf forest area at the expense of conifer and grassland area. Most of the

apparent relationships between changes in conifer forested area can therefore be attributed to the fact that in most cases changes in grassland area arise due to direct competition between grasslands and conifer forests. Changes in conifer forest area therefore have a strong inverse relationship with changes in grassland area. Since changes in grassland area are very highly co-related with changes in SWE and runoff, this results in an inverse relationship between conifer area and SWE and runoff.

Another variation on this can be seen in the effect of broadleaf forest area on SWE and runoff (Figure 5.5c). In the Fraser Basin, increases in broadleaf area co-relates with increases in both SWE and runoff, while the opposite is seen in the Athabasca basin. This can be explained by differences in the relationship between grasslands and broadleaf forests in the two basins. In the Athabasca, grassland area tends to decline in scenarios where broadleaf forests expand into the boreal forest while in the Fraser basin, scenarios that predict large increases in grassland area in the British Columbia Interior also predict increases in broadleaf forested areas on the leeward side of the Coastal and Rocky Mountain Ranges (e.g. Figures 5.3b and 5.3f).

Overall, broadleaf area change is relatively modest (Figure 5.5c) compared to changes in conifer area (Figure 5.5b) and the dominant mechanism for changes in SWE and runoff is competition between grassland and total forested area. Although the runoff generation characteristics of broadleaf and conifer forests are not identical, they are much more similar with each other than they are with runoff generation characteristics of grasslands.

There is also a strong linear relationship between changes in annual maximum SWE and annual runoff, both in terms of percent change (Figure 5.6a) and absolute change (Figure 5.6b). Generally, a 4% change in SWE due to a vegetation shift results in a 1% increase in mean annual runoff and a 1 mm increase in SWE results in a 1.1 mm increase in mean annual runoff. These relationships hold true in both basins over a wide range of GCM predicted climate conditions and vegetation responses, suggesting that almost all the changes in mean annual flow can be attributed to changes in SWE.

This all suggests that the primary mechanism for runoff changes due to a vegetation shift is the higher rate of snow pack sublimation in forested areas relative to grassland areas (Pomeroy *et al.*, 1998; Pomeroy *et al.*, 2002). As the area of grassland in a basin increases, a basin's overall average snow sublimation rate decreases throughout the winter leaving more snow available for melting in the spring. This results in more spring runoff, which leads to more annual runoff.

The general impact of including the effect of vegetation response to climatic change is to increase runoff in the FRB and decrease runoff in the ARB (Figure 5.7a), a reflection of differences in how snow packs in these basins respond to vegetation shifts (Figure 5.7b). However, the differences in runoff between the shifted vegetation and historic vegetation scenarios is relatively small, as can be seen from the fact that all the points in Figure 5.7a fall very close to the dashed line (all changes within the range -6% to + 3%).

The results presented in this study have several limitations. The simulations involve the combination of different GCM projections under different emission scenarios and often at different timescales (i.e. steady-state equilibrium vs. transient simulations).

Such a methodology will almost certainly result in unrealistic combinations of relatively cool and wet scenarios with warm and dry scenarios. If the dominant feedback mechanism were positive (for example, if warm and dry climate conditions favoured vegetations shifts that resulted in less runoff) this would be relatively unimportant because the range of final results would be dominated by consistent combinations of GCMs. However, if the relationship between vegetation shifts and stream flows is negative, the outliers in the final results would be dominated by inconsistent combinations of GCMs and the estimated range of potential outcomes would be exaggerated.

5.4 Summary and Conclusions

Vegetation cover plays an important role in land surface hydrology and vegetation types are expected to change in response to climatic change. The degree to which vegetation shifts may amplify or mitigate changes in river flows however has remained an open question. In this study, the sensitivity of two large river basins was evaluated with the hydrologic model MISBA under climate change projections from the IPCC's TAR and vegetation shifts predicted by the vegetation model MAPSS.

It was found that the dominant mechanism driving changes in runoff in response to vegetation shifts under a changed climate involved forest retreat and grassland expansion due to drier conditions created by increased temperatures. Since open grasslands tend to have deeper snow packs than forested areas, yielding increased spring runoff and mean annual flow, a negative feedback is produced that can mitigate some of the flow losses that might otherwise occur. This process was most evident in the central Fraser River Basin, which is considerably drier than the mountainous regions along the

basin's outer boundary. However, under several GCM projections, flow in the Fraser River is expected to increase due to significant increases in rainfall that overcome decreases in the winter snow pack. Vegetation shifts in mountainous regions are expected to be dominated by conifer/broadleaf competition, which were not found to translate into significant changes in annual runoff yield. The shift to grassland will therefore tend to result in even larger increases in runoff in the FRB as a whole.

In the ARB, several scenarios predicted a southern expansion of the conifer forest into area currently classified as conifer savannah. The resulting loss of grassland area resulted in decreased flows in three of the vegetation scenarios (GISS, HCS, and UKMO). Since all the GCMs predict significant increases in annual temperatures in the mid latitudes, this behaviour suggests that the simple water budget model used in MAPSS to represent available soil moisture predicts that soils will become wetter in much of the ARB. This is inconsistent with the predictions of the more comprehensive and physically-based hydrologic modeling employed in MISBA, which predicts drier conditions in the ARB. In this case, the negative feedback mechanism produces unrealistic interactions between inconsistent hydrologic models where the relatively wet model used in MAPSS predicts vegetation shifts that moderate increases in soil moisture while the relatively dry model in MISBA predicts even drier conditions and decreased stream flows. This inconsistency highlights the importance of the consistent treatment of the water balance in hydrologic and vegetation models and suggests that the treatment of hydrologic factors in vegetation models needs to be improved before detailed conclusions can be drawn from a series of stand-alone simulations. Ideally, a more physically-based hydrologic land surface scheme should be coupled with the vegetation model.

Overall, the changes in runoff volume due to shifts in vegetation are relatively small, even in cases where an unrealistic interaction between different hydrologic models is probably overestimating the likely range of flows (e.g. probably GISS and HCS in the ARB and possibly UKMO in the FRB). Half the scenarios predict changes in runoff between -1% and +3% and even the most extreme combinations predict changes within ±15%, despite the tendency of the employed methodology to overestimate the potential range of changes.

These results, however, cannot account for the response of humans to climatic change. While declining forested area will tend to mitigate stream flow declines, much of this decline would be due to increased forest fires, which are often actively suppressed by government agencies. The vegetation models are also understandably unable to account for changes in forestry and agricultural practices as foresters and farmers change activities in response to climatic change. Finally, the vegetation models used in this study assumed equilibrium conditions that may take more than a century to occur and, in some cases, may never occur if species migration rates are too slow and key ecological functions are lost and never replaced.

Table 5.1 - Relationships between MAPSS and Ecoclimap Vegetation Classes in the Fraser and Athabasca River Basins.

			Ecoclimap Classification					
			Bare Soil	Rocks	Perm Snow	Broadleaf	Conifer	Grassland
MAPSS Classification	Forest	Broadleaf				0.80	0.10	0.10
		Mixed				0.45	0.45	0.10
		Conifer				0.10	0.80	0.10
	Savanna	Broadleaf				0.45	0.05	0.50
		Mixed				0.25	0.25	0.50
		Conifer				0.05	0.45	0.50
	Shrubland					0.30	0.30	0.40
	Grassland					0.10	0.10	0.80
	Taiga/Tundra		0.25	0.25			0.50	
	Tundra		0.30	0.30	0.30		0.10	

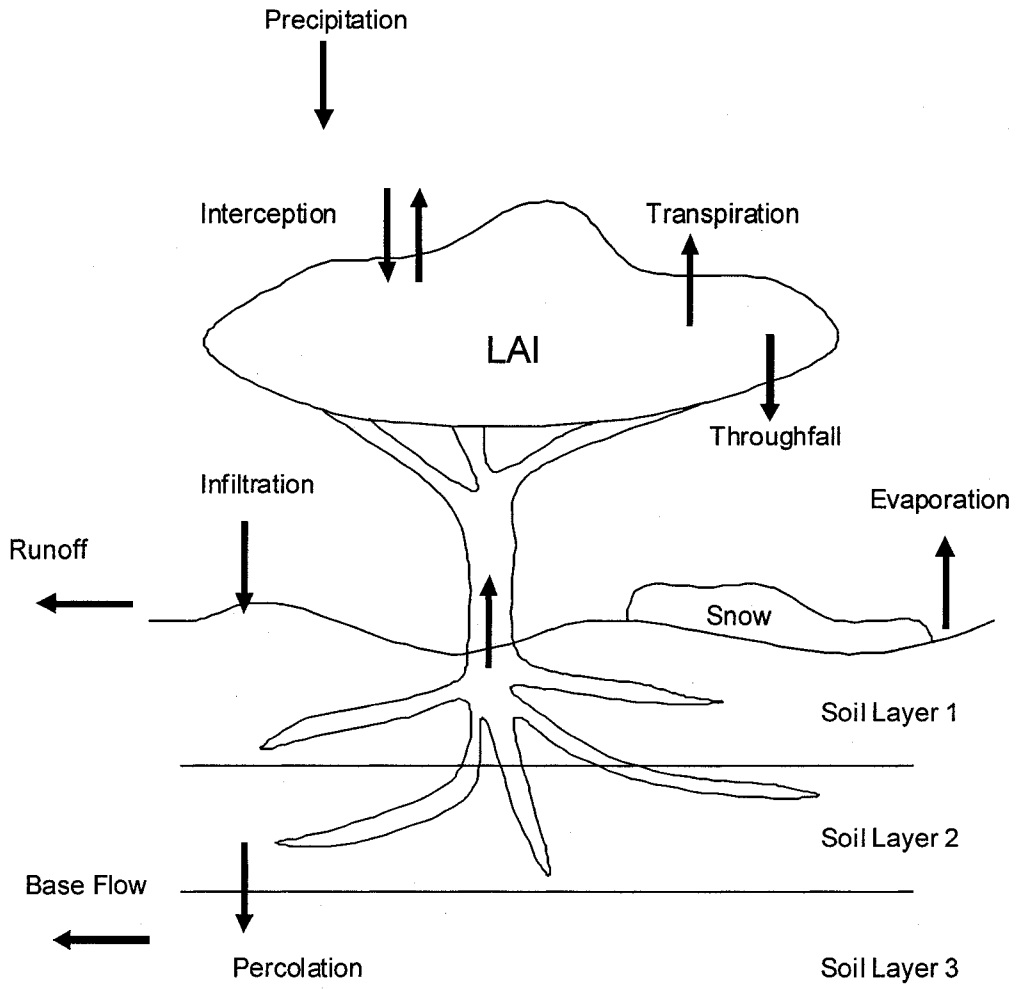

Figure 5.1 – Schematic diagram of the MAPSS water budget model (adapted from Neilson, 1995).

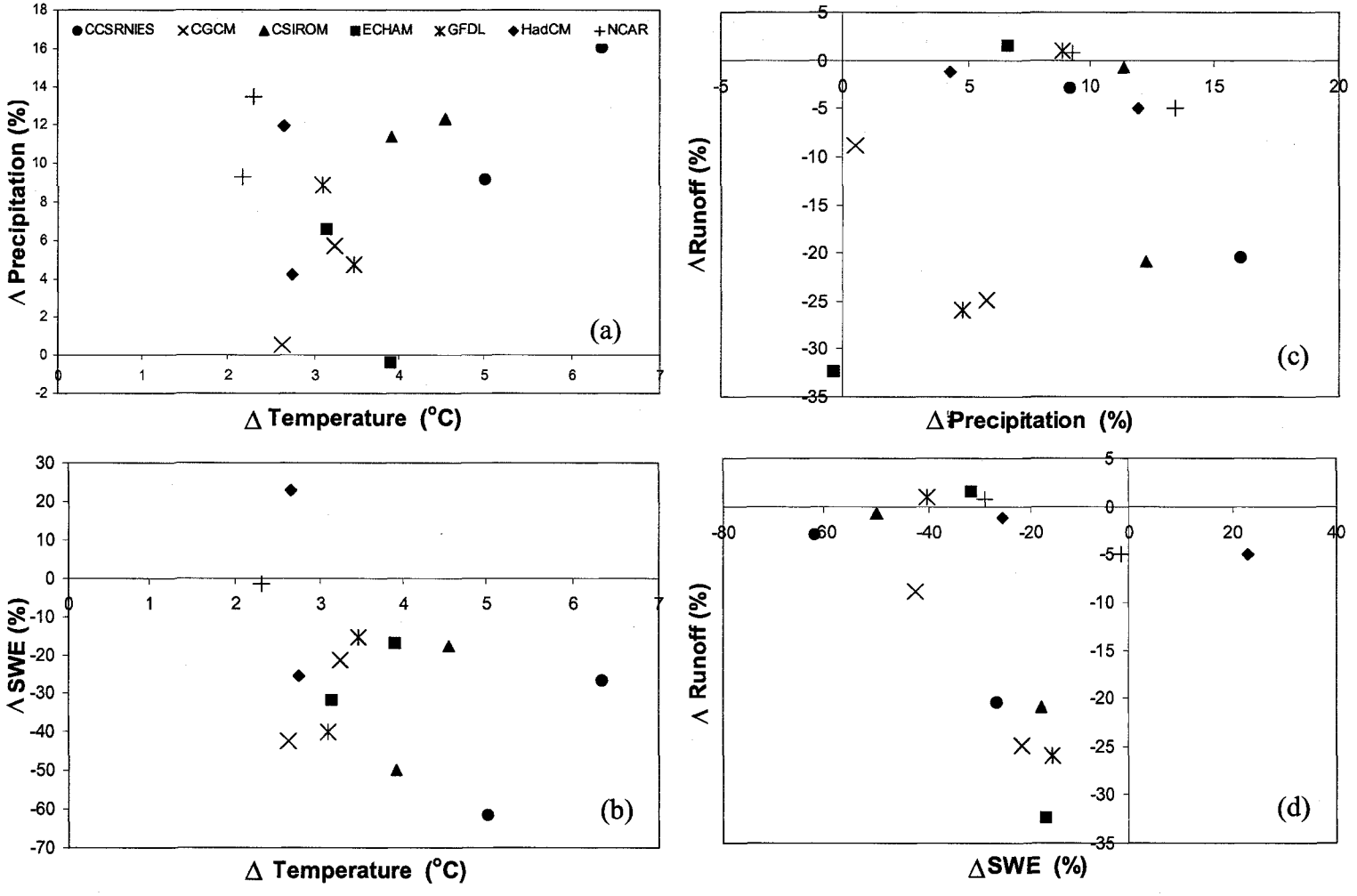

Figure 5.2 - Relationships between changes in temperature and (a) precipitation and (b) snow water equivalent (SWE); and changes in runoff and changes in (c) precipitation and (d) SWE in the Athabasca (blue) and Fraser (red) River Basins based on the predictions of seven GCMs for SRES B2 climate scenarios using Ecoclimap vegetative cover.

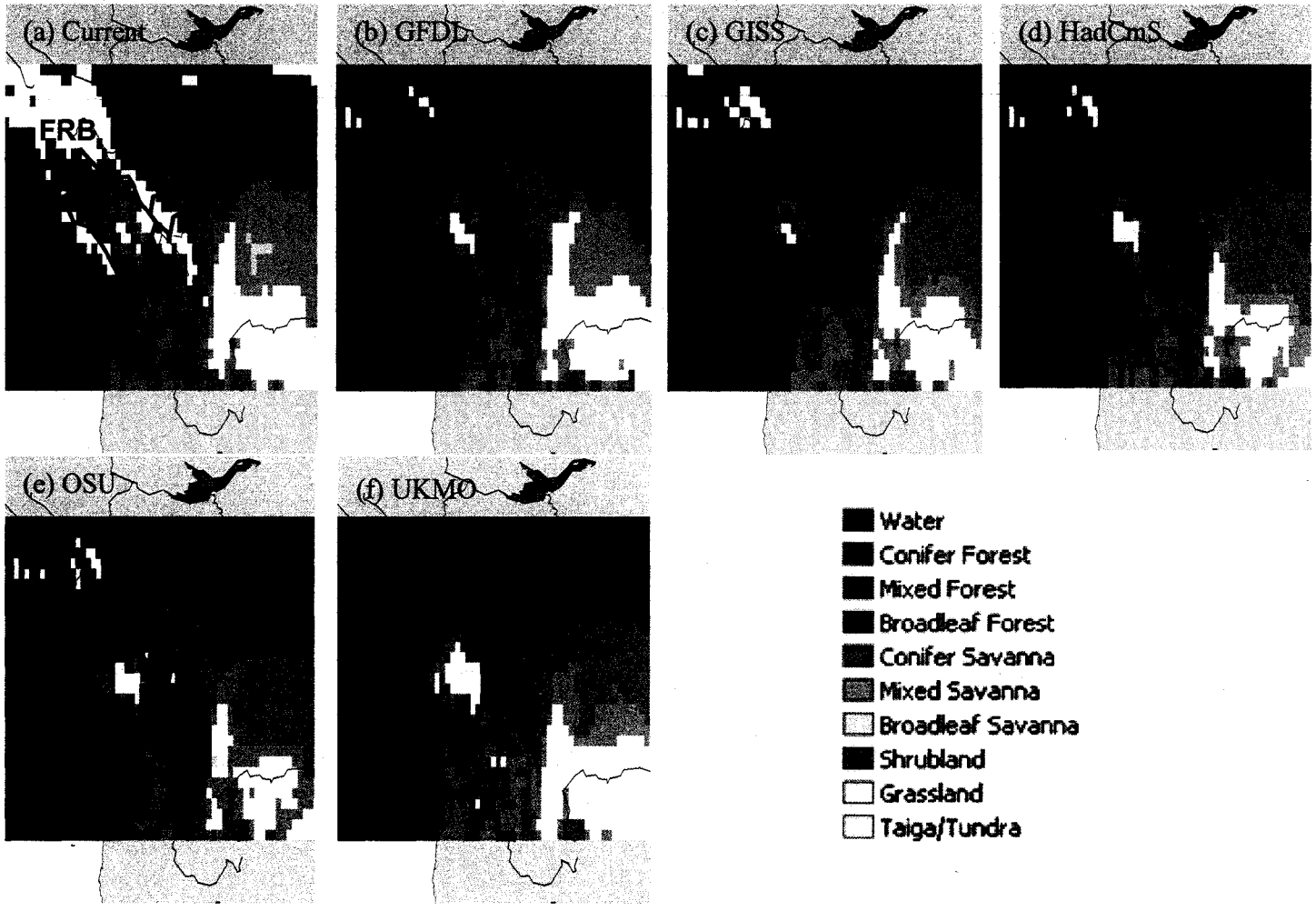

Figure 5.3 - MAPSS equilibrium vegetation types under (a) current conditions, (b) GFDL FAR, (c) GISS FAR, (d) HadCmS SAR, (e) OSU FAR, and (f) UKMO FAR. Solid lines indicate the Athabasca River Basin (ARB) and the Fraser River Basin (FRB).

(a) Athabasca River Basin

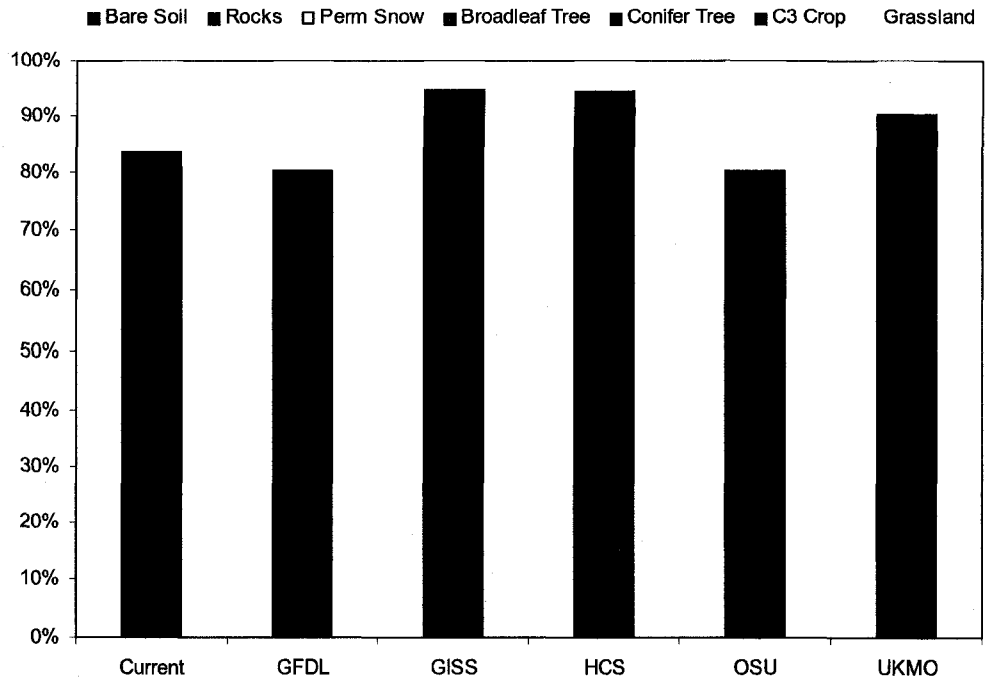

(b) Fraser River Basin

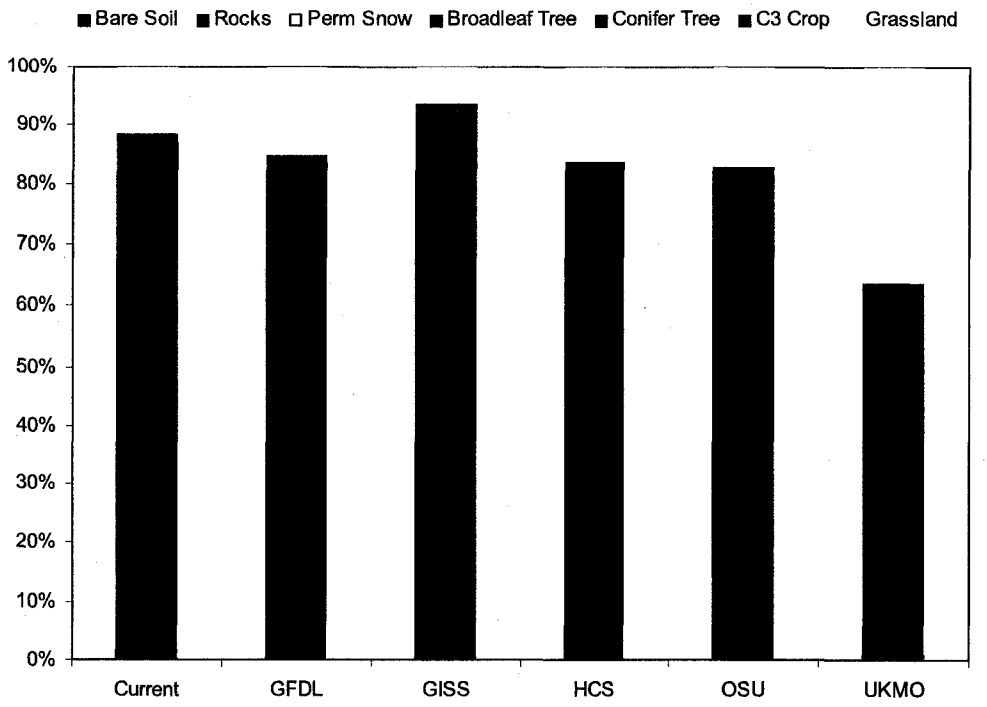

Figure 5.4 - Changes in Ecoclimap vegetation cover types in the (a) Athabasca and (b) Fraser River Basins based on MAPSS model simulations for current and climate change scenarios.

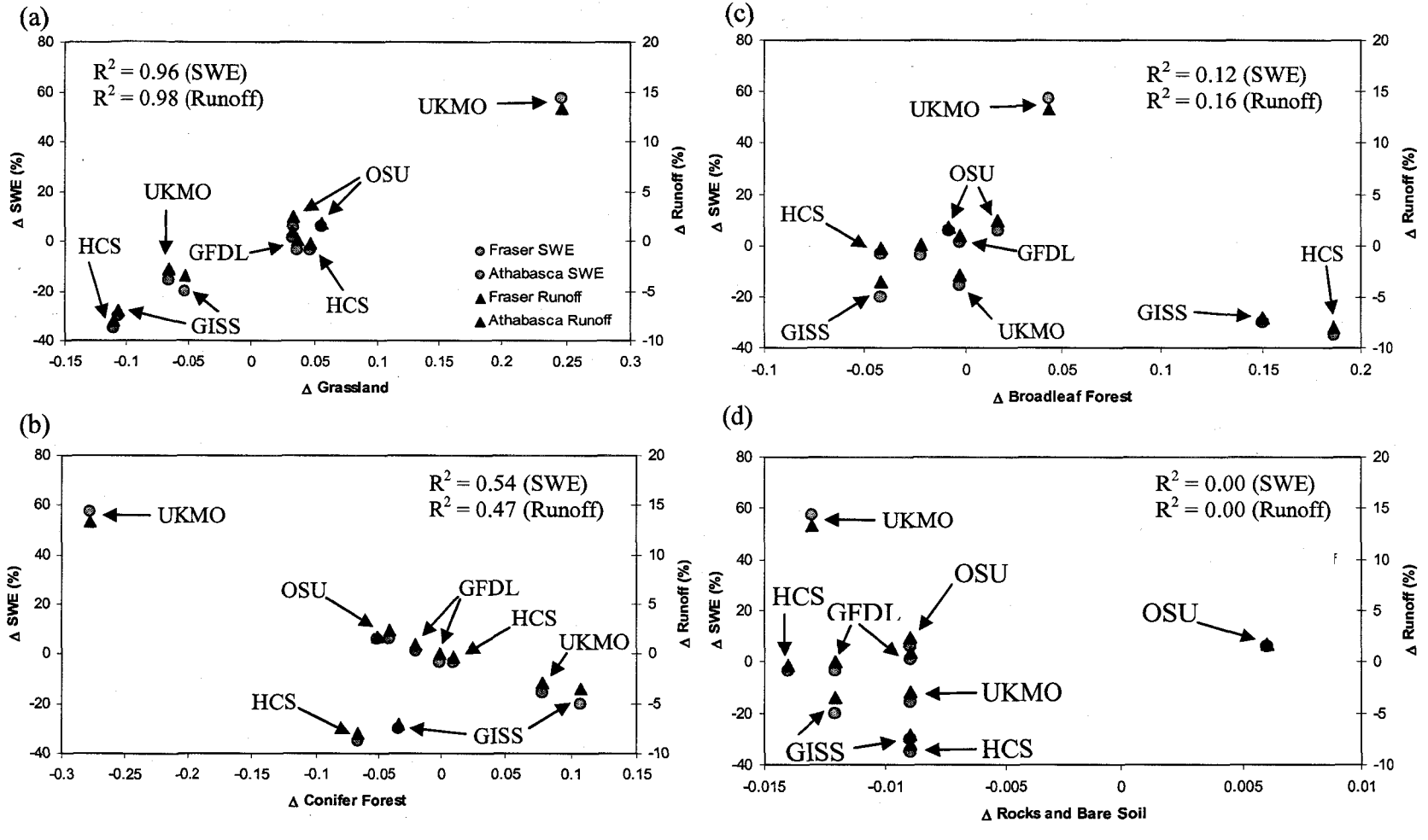

Figure 5.5 - Changes in runoff (triangles) and Snow Water Equivalent (SWE, circles) as they relate to changes in (a) Grassland forest area and (b) Conifer Forest , (c) Broadleaf Forest area and (d) Rocks and Bare Soil area in the Fraser (red) and Athabasca (blue) River Basins, based on climate change scenarios using MAPSS vegetative cover. Each symbol represents the average of five SRES GCM climate projections.

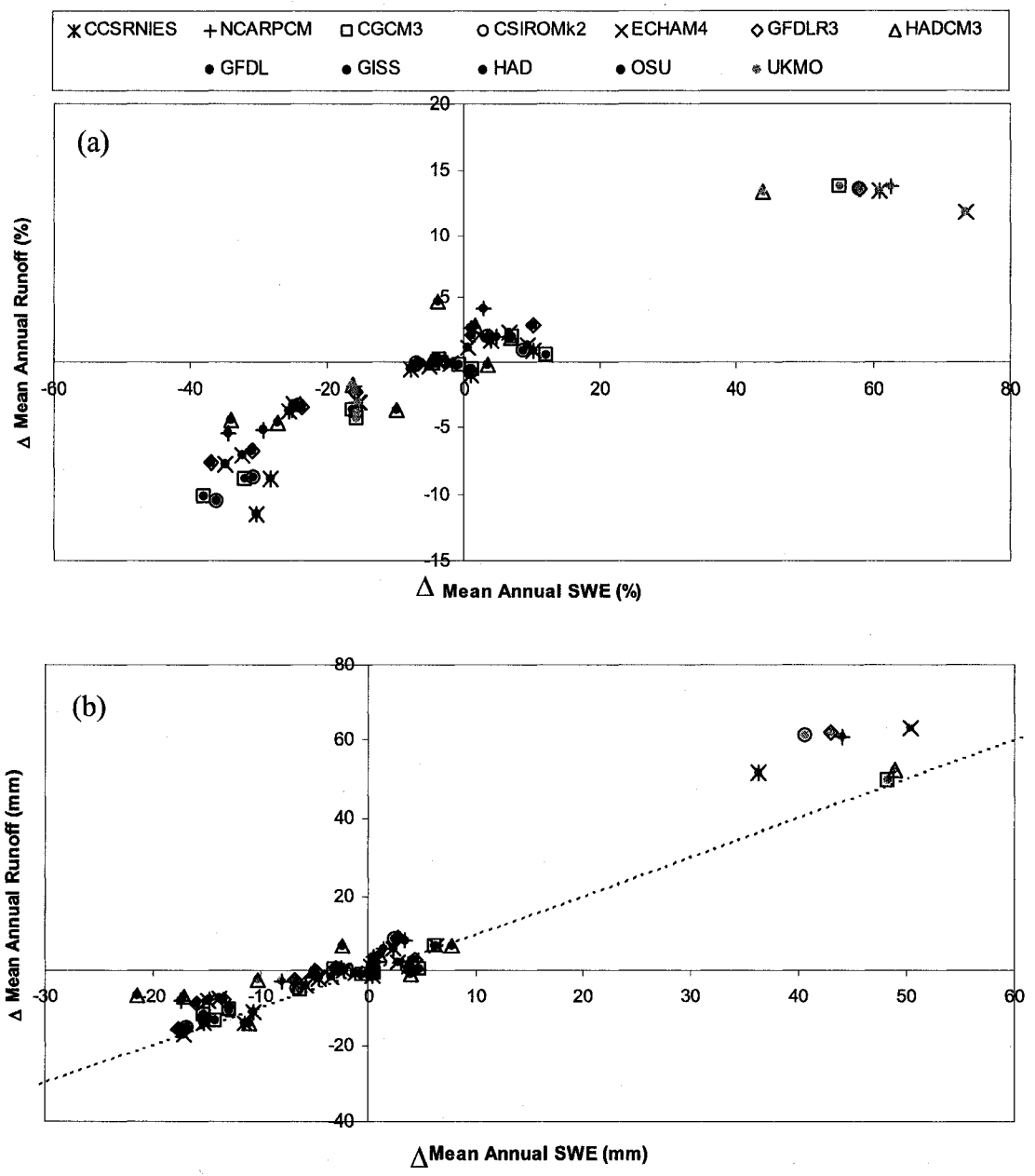

Figure 5.6 - Changes in runoff as they relate to changes in Snow Water Equivalent (SWE) in terms of (a) percent change and (b) absolute change, based on climate change scenarios using MAPSS vegetative cover. Symbol shape indicates the SRES GCM climate projection and colour indicates the MAPSS vegetation shift scenario.

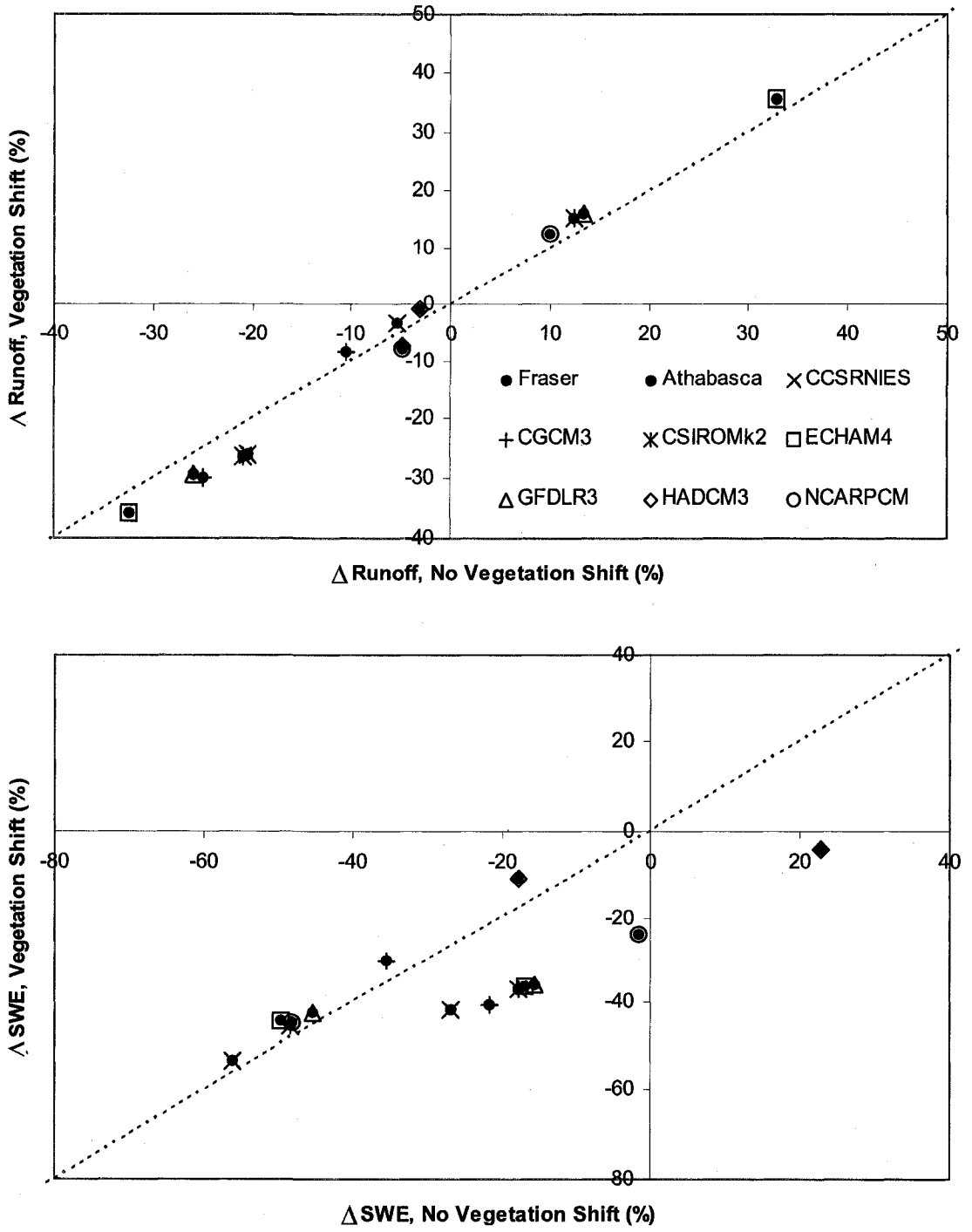

Figure 5.7 - Changes in (a) runoff and (b) SWE with a vegetation shift (averaged across the five MAPSS scenarios) and without a vegetation shift (Ecoclimap current conditions).

5.5 Bibliography

Bachelet, D., J.M. Lenihan, Daly, C. Neilson, R.P. Ojima, D.S. and Parton, W.J.,(2001), *MC1: A Dynamic Vegetation Model for Estimating the Distribution of Vegetation and Associated Ecosystem Fluxes of Carbon, Nutrients, and Water, Technical Documentation, Version 1.0*, United States Department of Agriculture, Forest Service, 95p.

Bachelet, D., J.M. Lenihan, R.P. Neilson, R.J. Drapek, and T. Kittel, (2005), Simulating the response of natural ecosystems and their fire regimes to climatic variability in Alaska, *Can. J. For. Res.*, 35, 2244-2257.

Canadian Centre for Climate Modelling and Analysis, (2007), *CGCM1 and CGCM2 Runs Forcing Equivalent CO2 concentrations used in CCCma coupled global climate model simulations*, http://www.cccma.ec.gc.ca/data/cgcm/cgcm_forcing.shtml, last accessed: 26 May 2008.

Cox, P.M., R.A Betts. C.D. Jones, S.A. Spall, and I.J Totterdell,. (2000), Acceleration of global warming due to carbon-cycle feedbacks in a coupled climate model, *Nature*, 408, 184-187.

Cullen, M.J.P., (1993), The Unified Forecast/Climate Model, *Meteor. Mag.*, 122, 81-94.

Dickinson, R.E., A. Henderson-Sellers, P.J. Kennedy, and M.F. Wilson, (1986), *Biosphere-atmosphere transfer scheme (BATS) for the NCAR Community Climate Model*, National Center for Atmospheric Research, NCAR Tech. Note NCAR/TN-387+STR.

Foley, A.F., I.C Prentice, N. Ramankutty, S. Levis, D. Pollard, S. Sitch, and A. Haxeltine, (1996), An integrated biosphere model of land surface processes, terrestrial carbon balance, and vegetation dynamics, *Global Biochemical Cycles*, 10(4), 603-628.

Gordon, W.S., J.S. Famiglietti, N.L. Fowler, T.G.F. Kittel, and K.A. Hibbard, (2004), Validation of Simulated Runoff from Six Terrestrial Ecosystem Models: Results from VEMAP, *Ecological Applications*, 14(2), 527-545.

Sellers, J. P., D.A. Randell, G.J. Collatz, J.A. Berry, C.B. Field, D.A. Dazlich, C. Zhang, G.D. Collelo and L. Bounua, (1996), A revised land surface parametrization (SiB 2) for atmospheric GCMs. Part I:Model formulation, *J. Climate*, 9, 676-705.

Hogg, T.H., and P.Y. Bernier, (2005), Climate change impacts on drought-prone forests in western Canada, *Forestry Chronicle*, 81(5), 675-682.

Intergovernmental Panel on Climate Change, (1990), *Climate Change 1990: The Intergovernmental Panel on Climate Change Scientific Assessment*, Cambridge University Press, Cambridge.

Intergovernmental Panel on Climate Change, (1995), *Climate Change 1995: the Science of Climate Change*, Contribution of Working Group I to the Second Assessment Report of the Intergovernmental Panel of Climate Change, Cambridge University Press, Cambridge.

Intergovernmental Panel on Climate Change, (2001), *Climate Change 2001: The Scientific Basis*, Contribution of Working Group 1 to the Third Assessment Report of the Intergovernmental Panel on Climate Change, Cambridge University Press, Cambridge.

Intergovernmental Panel on Climate Change, (2007), *Climate Change 2007 - The Physical Science Basis*, Contribution of Working Group 1 to the Fourth Assessment

Report of the Intergovernmental Panel on Climate Change, Cambridge University Press, Cambridge.

Johns, T.C., R.E. Carnell, J.F. Crossley, J.M. Gregory, J.F.B. Mitchell, C.A. Senior, S.F.B. Tett, and R.A. Wood, (1997), The second Hadley Centre coupled ocean-atmosphere GCM: Model description, spinup and validation. *Climate Dyn.*, 13, 103-134.

Kerkhoven, E., and T.Y. Gan, (2006), A Modified ISBA Surface Scheme for Modeling the Hydrology of Athabasca River Basin with GCM-scale Data, *Advances in Water Resources*, 29(6), 808-826.

Lawler, J.J., D. White, R.P. Neilson, and A.R. Blaustein, (2006), Predicting climate-induced range shifts: model differences and model reliability, *Global Change Biology*, 12, 1568-1584.

Malcolm, J.R., A. Markham, R.P. Neilson, and M. Garaci, (2002), Estimated migration rates under scenarios of global climate change, *Journal of Biogeography*, 29, 835-849.

Manabe, S., and R.J. Stouffer, (1994), Multiple-Century Response of a Coupled Ocean-Atmosphere Model to an Increase of Atmospheric Carbon Dioxide, *J. of Climate*, 7, 5-23.

Neilson, R.P., (1995), A Model for Predicting Continental-Scale Vegetation Distribution and Water Balance, *Ecological Applications*, 5(2), 362-385.

Neilson, R.P., and R.J. Drapek, (1998), Potentially complex biosphere responses to transient global warming, *Global Change Biology*, 4 (5), 505–521.

Neilson, R.P., and D. Marks, (1994), A Global Perspective of Regional Vegetation and Hydrologic Sensitivities from Climatic Change, *Journal of Vegetation Science*, 5(5), 715-730.

Neilson, R.P., L.F. Pitelka, A.M. Solomon, R. Nathan, G.F. Midgley, J.M.V. Fragoso, H. Lihchke, and K. Thompson, (2005), Forecasting Regional to Global Plant Migration in Response to Climate Change, *BioScience*, 55(9), 749-759.

Neilson, R.P., J.M. Lenihan, D. Bachelet, R.J. Drapek, F.I. Woodward, and M. Lomas, (2007), Perpetual Growth, or Potential Catastrophic Dieback of North American Forests, *U.S. North American Carbon Program (NACP) Investigators Meeting, 2007*, Colorado Springs, Colorado, USA.

Noilhan J., and S. Planton (1989), A simple parameterization of land surface processes for meteorological models, *Mon Wea Rev*, 117, 536-549.

Parton, W.J., D.S. Schimel, C.V. Cole, and D.S. Ojima, (1987), Analysis of factors controlling soil organic matter levels in Great Plains grasslands, *Soil Science Society of America Journal*, 51, 1173-1179.

Peng, C., (2000), From static biogeographical model to dynamic global vegetation model: a global perspective on modelling vegetation dynamics, *Ecological Modelling*, 135, 33-54.

Pomeroy, J.W., J. Parviainen, N. Hedstrom and D.M. Gray, (1998), Coupled modelling of forest snow interception and sublimation, *Hydrological Processes*, 12, 2317-2337.

Pomeroy, J.W., D.M. Gray, N.R. Hedstrom, and J.R. Janowicz, (2002), Prediction of seasonal snow accumulation in cold climate forests, *Hydrological Processes*, 16, 3543-3558.

Schmidt, G.A., R. Ruedy, J.E. Hansen, I. Aleinov, N. Bell, M. Bauer, S. Bauer, B. Cairns, V. Canuto, Y. Cheng, A. Del Genio, G. Faluvegi, A.D. Friend, T.M. Hall, Y. Hu, M. Kelley, N.Y. Kiang, D. Koch, A.A. Lacis, J. Lerner, K.K. Lo, R.L. Miller, L. Nazarenko, V. Oinas, Ja. Perlwitz, Ju. Perlwitz, D. Rind, A. Romanou, G.L. Russell, Mki. Sato, D.T. Shindell, P.H. Stone, S. Sun, N. Tausnev, D. Thresher, and M.-S. Yao, (2006), Present day atmospheric simulations using GISS ModelE: Comparison to in-situ, satellite and reanalysis data, *J. Climate*, 19, 153-192.

Sperber, K.R., and S. Hameed, (1991), Southern Oscillation simulation in the OSU coupled upper ocean-atmosphere GCM, *Climate Dynamics*, 6(2), 83-97.

Scott, D., and C. Lemieux, (2007), Climate change and protected areas policy, planning and management in Canada's boreal forest, *Forestry Chronicle*, 83(3), 347-357.

Stich, S., B. Smith, C. Prentice, A. Arneth, A. Bondeau, W. Cramer, J.O. Kaplans, S. Levise, W. Lucht, M.T. Sykes, K. Thinicke, and S. Venevsky, (2003), Evaluation of ecosystem dynamics, plant geography and terrestrial carbon cycling in the LPJ dynamic global vegetation model, *Global Change Biology*, 9, 161-185.

Woodward, F.I., T.M. Smith, and W.R. Emanuel, (1995), A global land primary productivity and phytogeography model, *Global Biochemical Cycles*, 9(4), 471-490.

Zhao M., R.P. Neilson, X. Yan, W. Dong, (2002), Modeling the vegetation of China under changing climate, *J Geogr Sci*, 57(1), 28–38.

Chapter Six: Comparing Four Sources of Unconditional Uncertainty in Simulated River Flows using Statistical Methods and Multifractal Analysis for Two Macro-scale River Basins to the East and West of the Canadian Rockies

6.1 Introduction

All estimates of future hydrological behaviour (forecasts) are associated with several sources of uncertainty, which may be due to one of many sources such as the limitations of the models used or the quality and resolution of the input data and initial conditions. As such, most forecasts are inherently statistical in nature, even if they are not explicitly described as such. For example, the standard method for estimating how stream flows will change under the climate predicted by a General Circulation Model (GCM) scenario is to adjust the observed meteorological record (e.g. 1961-1990) to match the predicted changes in monthly temperature and precipitation and use this adjusted data to force a hydrological model that has been calibrated and verified with historical observations. The resulting hydrograph is meant to represent the future climate scenario and is expected to have the same statistical properties as would actually be observed under the new climate. The meteorological data used to derive this forecast however is only one sample of a virtually infinite set of future meteorological conditions that satisfy the climatology predicted by the GCM. There is therefore a sample error, or uncertainty, associated with the date used to force the hydrological model as well as the estimated stream flows.

Uncertainty in a forecast can be categorized into two types: conditional uncertainty and unconditional uncertainty (Koutsoyannis *et al.*, 2007). The distinction between these categories is analogous to the distinction between conditional and unconditional probability. In systems with significant long-term memory, the influence

of known recent conditions reduces the uncertainty of relatively short-term forecasts. When one uses this knowledge one is estimating conditional uncertainty. As a forecast looks further into the future, the influence of current conditions becomes progressively smaller and conditional uncertainty approaches a maximum range: the unconditional uncertainty, in which the influence of current conditions is negligible.

For a series of statistically independent events, the sample error decreases with the square root of the sample size. Daily stream flows however are not independent events. One common approach to such data sets is to evaluate the autocorrelation of the time series and estimate an effective sample size. In the case of a time series with positive autocorrelation, such as stream flow, the effective sample size is smaller than the actual sample size resulting in a higher sampling error than for an independent series.

An alternative approach to estimate uncertainty is to employ the concept of the Hurst phenomenon. By analyzing how river flows varied over large time scales, Hurst (1951) first demonstrated that rivers exhibit long-range statistical dependencies that could be characterized by an exponent now commonly called the Hurst exponent, H (Mandelbrot and Wallis, 1968). Following Hurst, the standard deviation of a time series decreases with the time scale to the power of $1 - H$ (Koutsoyiannis *et al.*, 2007). For a series of statistically independent events, since the standard deviation (and the sample error) decreases with the square root of the sample size, H is 0.5. In the case of a time series with $H > 0.5$, such as stream flow, standard deviation decreases with sample size to an exponent smaller than 0.5, again resulting in a higher sampling error than for an independent series.

Hurst's discovery is now recognized as the first example of fractal behaviour in an empirical time series (Feder, 1988). Despite this observation, the 1970s saw the development of rainfall and runoff models that were incapable of accounting for scaling, resulting in the need to use different probability distributions for normal and extreme events (Tessier *et al.*, 1996). However, the Hurst's observations formed the basis of the fractal approach of Mandelbrot and Wallis (1968) wherein the statistical properties of river flows, including extreme events, were represented as generalizations of Brownian motion with H acting as a single scaling factor. In the 1980s, there were studies attempted to estimate the fractal dimension of rainfall (e.g. Lovejoy and Mandelbrot, 1985). Although it was clear that fractals were the correct theoretical framework for analyzing the simple geometric scaling properties, the appropriate framework for scaling in geophysics was multifractals (Tessier *et al*, 1996). In a multifractal, scaling properties are represented by a range of scaling exponents instead of a single value.

The structure of turbulence is commonly described as an energy cascade in which energy that is generated by large scale phenomena are transferred down through progressively smaller scales until it is dissipated by viscosity at the Kolmogorov scale (Kolmogorov, 1962). A similar argument has been applied to rainfall by several researchers (Schertzer and Lovejoy, 1987; Lovejoy and Schertzer, 1990; and Gupta and Waymire, 1993) in which clusters of intense cloud scale rainfall is embedded in clusters of mesoscale rainfall, which are embedded in clusters of low intensity synoptic-scale rainfall. Gan *et al.* (2007) detected multifractal behaviour in Canadian precipitation data. Tessier *et al.* (1996) observed that both rainfall and runoff time series exhibit two distinct features in their power spectra: a strong annual peak (especially for stream flows), and a

sudden change in slope at a time scale of approximately 16 days, which they associated with the time scale of atmospheric structures of planetary extent (i.e. the synoptic scale). These characteristics strongly indicate that the scaling properties of rainfall are transferred through the rainfall-runoff process to stream flows.

Although both the autocorrelation and Hurst exponent approaches represent a significant improvement over the assumption of statistical independence, these methods can fail in the presence of systematic trends such as seasonal cycles, regulation, or climatic change. Monotonic trends tend to result in an overestimation of the Hurst exponent and uncorrelated data superimposed on a long-term trend will exhibit autocorrelation (Bhatthacharya *et al.*, 1983). Recently, analysis techniques that are able to detect long-term correlations in the presence of trends such as Detrended Fluctuation Analysis (DFA) have been developed. Kantelhardt *et al.* (2002) developed Multifractal Detrended Fluctuation Analysis (MFDFA) to determine the underlying multifractal behaviour of time series in the presence of long-term trends. In a subsequent study, Kantelhardt *et al.* (2003) first applied this analysis methodology to rainfall and stream flow data where they found that the multifractal behaviour of stream flows was well represented by the binomial multifractal cascade model. Koscielny-Bunde *et al.* (2006) used MFDFA to analyze stream flow measurements throughout the world and detected significant multifractal behaviour in 40 of the 41 rivers studied. MFDFA has also been applied to wind data (Kavasseri, 2005) and traffic flows (Shang *et al.*, 2008).

6.2 Multifractal Analysis

6.2.1 Multifractal Formalism

Suppose the series, x, is a stationary time series of length N that has been normalized such that,

$$\sum_{i=1}^{N} x_i = 1 \tag{6.1}$$

If the time series is divided into N/ℓ intervals of equal length, ℓ, the box probability of the j^{th} interval, $\rho_s(j)$, can be defined as,

$$\rho_s(j) \equiv \sum_{i=(j-1)l+1}^{js} x_i \tag{6.2}$$

The scaling exponent, $\tau(q)$, can then be defined via the q^{th} moment of the box probability,

$$Z_q(s) = \sum_{j=1}^{N/s} [\rho_s(j)]^q \sim \ell^{\tau(q)} \tag{6.3}$$

where $\tau(q)$ is derived from the slope of $Z_q(\ell)$ versus ℓ on a log-log plot. For a monofractal, $\tau(q)$ will be a straight line while for a multifractal the slope will vary. A Legendre transformation is often performed on $\tau(q)$ to produce the multifractal spectrum, $f(\alpha)$,

$$\alpha = \frac{d\tau(q)}{dq} \tag{6.4}$$

$$f(\alpha) = q\alpha - \tau(q) \tag{6.5}$$

where, α is a Hölder exponent (Mandelbrot, 1999), while $f(\alpha)$ is the dimension of the subset of the time series that is characterized by α. Figure 6.1 depicts a typical form of a multifractal spectrum. The width of the spectrum, $\Delta\alpha$, is a measure of the multifractal

strength of the time series since the spectrum collapses to a single point when a multifractal becomes a mono-fractal. The maximum value of $f(\alpha)$ is called the support dimension.

6.2.2 Multifractal Detrended Fluctuation Analysis

The Multifractal Detrended Fluctuation Analysis (MFDFA) developed by Kantelhardt *et al.* (2002) consists of five steps, the first three of which are essentially the same as the standard detrended fluctuation analysis. Consider a time series, x, of length, N, that has been normalized in the same fashion as in the multifractal formalism approach outlined above.

1) Determine the profile, or partial cumulative summation, of the time series, Y,

$$Y(k) = \sum_{i=1}^{k} x_i \, , \, k = 1, 2, 3, \ldots N \tag{6.6}$$

2) Divide the profile into N/s non-overlapping intervals of length, ℓ.

3) Calculate the local trend of each segment by a m^{th}-order polynomial least squares fit of the segment and determine the variance about this trend,

$$F^2(\ell, j) = \frac{1}{\ell} \sum_{i=1}^{\ell} \left\{ Y[(j-1)\ell + 1] - y_j(i) \right\}^2 \, , j = 1, 2, \ldots, N/\ell \tag{6.7}$$

where, $y_j(i)$ is the best fitting polynomial. An m^{th}-order polynomial will subtract an $(m\text{-}1)^{\text{th}}$-order trend from the original series, x. In this study, a second order polynomial fit was used to eliminate linear trends.

4) Average over all intervals and calculate the q^{th} order fluctuation function,

$$F_q(\ell) = \left\{ \frac{\ell}{N} \sum_{j=1}^{N/\ell} \left[F^2(\ell, j) \right]^{q/2} \right\}^{1/q} \tag{6.8}$$

5) Determine the scaling behaviour of the fluctuation functions by analyzing log-log plots for each value of q. If the functions are power-law correlated they will scale as,

$$F_q(\ell) \sim \ell^{h(q)} \tag{6.9}$$

For a stationary time series, $h(1)$ is similar to the original Hurst exponent and so Kantelhardt et al. (2002) named $h(q)$ the generalized Hurst exponent. They also showed that $h(q)$ is related to the scaling exponent $\tau(q)$ of standard multifractal formalism by,

$$h(q) = \frac{\tau(q)+1}{q} \tag{6.10}$$

which makes the generalized Hurst exponent identical to the scale factor, σ, of Mandelbrot (1999),

$$\sigma(q) = \frac{\tau(q)+1}{q} \tag{6.11}$$

For a monofractal time series, the scaling behaviour is the same for all intervals and so $h(q)$ is a constant. There will only be a significant dependence of $h(q)$ on q if small and large fluctuations scale differently, with small fluctuations dominating the negative values of q and large fluctuations dominating the positive values of q.

6.2.3 Generalized Multifractal Cascade Model

Koscielny-Bunde *et al.* (2006) developed a generalized form of the multifractal cascade model to serve as a multifractal model for stream flow data. The standard multifractal cascade can be generated recursively as,

1) Start with a set X with 2^n elements all equal to 1.

2) Divide the set into two equal segments of length 2^{n-1} and multiply the first segment by a factor 'a' and the second segment by a factor 'b' such that $0 < a < b < 1$. Usually, in the literature $b = 1 - a$, but this is not required.

3) Divide each remaining segment into two new segments of equal size and multiply the first new segment by a and the second new segment by b.

4) Repeat step (3) until each segment has only one element (i.e. the segments cannot be sub-divided any further).

For example, if we were to start with a set with 8 elements, at the end of this procedure the final set would be: $X = \{a^3, a^2b, a^2b, ab^2, a^2b, ab^2, ab^2, b^3\}$. A randomized version of the multifractal cascade can be produced by randomly selecting which new segment is multiplied by a leaving the other segment to be multiplied by b.

Kantelhardt *et al.* (2002) showed that the scaling exponent for the multifractal cascade is,

$$\tau(q) = \frac{-\ln\left(a^q + b^q\right) + q\ln(a+b)}{\ln 2} \tag{6.12}$$

and,

$$h(q) = \frac{1}{q} - \frac{\ln\left(a^q + b^q\right)}{q\ln 2} + \frac{\ln(a+b)}{\ln 2} \tag{6.13}$$

It can readily be seen that $h(1) = 1$ for any a and b. Since $h(1)$ is similar to the original Hurst exponent, this model is not appropriate for stream flows which almost always exhibit $0.5 < H < 1$. To generalize this model, Koscielny-Bunde *et al.* (2006) subtracted an offset, Δh, from Equation 6.13,

$$\Delta h = \frac{\ln(a+b)}{\ln 2} \tag{6.14}$$

to produce a new relationship,

$$h(q)=\frac{1}{q}-\frac{\ln\left(a^q+b^q\right)}{q\ln 2} \tag{6.15}$$

This is done by fast Fourier transforming (FFT) the generated multifractal cascade and multiplying all Fourier coefficients by $f^{\Delta h}$, where f is the frequency. This reduces the slope of the power spectrum, $E(f) \sim f^{\beta}$, where,

$$\beta = 2h(2)-1 \tag{6.16}$$

from,

$$\beta = 2h(2)-1=\frac{-\ln\left(a^2+b^2\right)+2\ln(a+b)}{\ln 2} \tag{6.17}$$

to,

$$\beta = 2[h(2)-\Delta h]-1=\frac{-\ln\left(a^2+b^2\right)}{\ln 2} \tag{6.18}$$

which is consistent with Equation 6.15. Backward FFT is then used to transform the new Fourier coefficients back to the time domain.

From Equation 6.15, the multifractal spectrum equations for the generalized multifractal cascade can be derived to be,

$$\alpha = h(q)+q\frac{dh(q)}{dq}=-\frac{1}{\ln 2}\frac{a^q\ln a+b^q\ln b}{a^q+b^q} \tag{6.19}$$

$$f(\alpha)=q[\alpha-h(q)]+1=\frac{\ln\left(a^q+b^q\right)}{\ln 2}-\frac{q}{\ln 2}\frac{a^q\ln a+b^q\ln b}{a^q+b^q} \tag{6.20}$$

From which the width and maximum of the multifractal spectrum, the support dimension, can be shown to be,

$$\Delta\alpha=\frac{\ln b-\ln a}{\ln 2} \tag{6.21}$$

$$f_{max} = f(q=0) = 1 \tag{6.22}$$

6.3 |Research Methodology

Given that we rely mostly on simulated streamflow to project the potential impact of climate change on basin hydrology (e.g. Lettenmaier and Gan, 1990), the objective of this study is to compare the unconditional uncertainty of observed and simulated streamflow of two major river systems in Western Canada, the Fraser River Basin (FRB) and the Athabasca River Basin (ARB). The results will provide us with an insight into various studies on Monte Carlo simulations, and especially into the possible effects of climatic change.

The Fraser and Athabasca Rivers are represented by the Water Survey of Canada stations at Hope, British Columbia, and Fort McMurray, Alberta respectively. The observed daily stream flow data and the daily stream flows from the MISBA/ERA-40/GEM simulations of these two basins described in previous chapters will be used to establish the multifractal properties of the observed and simulated flows. Seven GCM simulations (CCSRNIES, CGCM2, CSIROMk2b, ECHAM4, GFDLR30, HadCM3, and NCARPCM) for four SRES climate scenarios (A1FI, A2, B1, and B2) over three 30-year time periods (2010-2039, 2040-2069, 2070-2199) were used to generate 54 future climate scenarios for each river basin. Several researchers have observed that stream flows exhibit different scaling properties at small (less than 30 days) and large (more than 100 days) time scales (Tessier *et al.*, 1996; Kantelhardt *et al.*, 2003; and Koscielny-Bunde *et al.*, 2006). Because we are interested in determining the sample error over a time scale of 30 years (the time scale of the 1961-1990 climate baseline and the SRES climate scenarios), this study will focus on time scales over 300 days. The unconditional

uncertainty of each scenarios prediction of the mean annual flow was then evaluated by four methods: Classical statistics, Hurst exponent, autocorrelation, and a multifractal approach.

6.3.1 Classical Statistics Method

The classical statistics approach assumes that each year's mean annual flow is statistically independent of the previous year, and therefore standard deviation varies inversely with the square root of scale, *k*,

$$\sigma^k = \frac{\sigma}{\sqrt{k}} \tag{6.23}$$

where, σ is the standard deviation of the mean annual flow series at the scale of one year. The upper and lower bounds of the confidence interval due to unconditional uncertainty using a two-sided test are,

$$u(x), l(x) = \bar{x} + z\frac{s}{\sqrt{k}} \pm t_{\upsilon,(1-\alpha)/2}\varepsilon s \tag{6.24}$$

where, *u(x)* and *l(x)* are the upper and lower bounds respectively, $\bar{x}$ is the sample mean, *z* is the quantile of the normal distribution, *s* is the sample standard deviation, *k* is the scale of interest, *t* is the student's t-score with ν degrees of freedom at confidence level α, and ε is,

$$\varepsilon = \frac{1}{\sqrt{n}}\sqrt{1+\frac{z^2}{2k}} \tag{6.25}$$

where, *n* is the size of the sample from which $\bar{x}$ and *s* were calculated.

6.3.2 Hurst Exponent Method

In this method, the Hurst exponent, *H*, is estimated from the slope on a log-log plot of sample standard deviation versus scale for time scales greater than 300 days. Koutsoyiannis *et al.* (2007) derived a variation of classical statistics approach to estimating unconditional uncertainty for time series that scale with a Hurst exponent,

$$u(x), l(x) = \bar{x} + z\frac{s}{k^{1-H}} \pm t_{(1+\alpha)/2}\varepsilon_H s \tag{6.26}$$

where, ε_H is,

$$\varepsilon_H = \frac{1}{n^{1-H}}\sqrt{1 + \frac{\phi(n,H)}{2n^{2H-1}}\left(\frac{z}{k^{1-H}}\right)^2} \tag{6.27}$$

$$\phi(n,H) = (0.1n + 0.8)^{0.088\left(4H^2-1\right)^2} \tag{6.28}$$

6.3.3 Autocorrelation Method

In the autocorrelation method, the autocorrelation, ρ, of each time series for a 365-day lag is calculated by,

$$\rho(lag) = \frac{1}{n}\frac{\sum_{i=1}^{n}(x_i - \bar{x})(x_{i+lag} - \bar{x})}{\sigma_x^2} \tag{6.29}$$

An effective sample size, n', can be calculated from,

$$n' = n\frac{1-\rho}{1+\rho} \tag{6.30}$$

The upper and lower bounds can then be calculated from classical statistics as (Koutsoyiannis *et al.*, 2007),

$$u(x), l(x) = \bar{x} + z\frac{s}{\sqrt{k'}} \pm t_{(1+\alpha)/2}\varepsilon_a s \tag{6.31}$$

where,

$$\varepsilon_a = \frac{1}{\sqrt{n'}}\sqrt{1+\frac{z^2}{2k'}} \tag{6.32}$$

and,

$$k' = k\frac{1-\rho}{1+\rho} \tag{6.33}$$

6.3.4 Multifractal Method

The general procedure to estimate the sample uncertainty based on fractal properties is,

1) Subtract the mean annual daily stream flows from the historical and simulated SRES scenario time series.
2) Perform the MFDFA analysis on the observed and simulated historical flows.
3) Find the best fitting multifractal cascade parameters, a and b, for the observed and simulated historical flows.
4) Determine the difference in these two parameters,

$$\Delta a = a_{obs} - a_{sim} \tag{6.34}$$

$$\Delta b = b_{obs} - b_{sim} \tag{6.35}$$

5) Perform the MFDFA analysis on the simulated flows from each of the 54 climate scenarios.
6) Find the best fitting multifractal cascade parameters, a and b, and shift them by Δa and Δb, respectively.
7) Generate a randomised multifractal cascade with 2^{19} time steps using the adjusted a and b values. With daily time steps, this is the equivalent of a 1435-year time series.

8) Shift the mean and standard deviation of the multifractal cascade to match the mean and standard deviation of the simulated SRES time series (after the mean annual cycle has been removed). Such shifts do not change the fractal properties of a time series.

9) Add the mean annual cycle that was removed in step (1) to the adjusted multi-fractal cascade

10) Determine the 95% confidence limits directly from the resulting time series.

6.4 Results

6.4.1 Observed and Simulated Historical River Flows

Figure 6.2 shows the 365-day moving averages of the observed and simulated daily flows in the ARB (1961-2002) and FRB (1957-2002). Both simulations show systematic bias towards low flows in the late 1950s and early 1960s, mostly due to limitations of the ERA-40 dataset due to the quality and resolution of the observed data upon which the re-analysis data are based. After 1969, with the inclusion of satellite data, the ERA-40 data improve significantly and as a result, so do the hydrologic simulations. Both simulations reproduce the long-term fluctuations in the basin quite well, especially in the FRB ($R^2 = 0.63$). In the ARB ($R^2 = 0.59$), the simulations tend to under predict some of the downswings, most notably in the early 1980s. Again, this is most likely due to the low resolution of the ERA-40 data set, especially the low resolution of the data. In each these years, the simulations overestimated the size of the spring melt wave, which is usually a reflection of too much winter precipitation being supplied to the model.

Figure 6.3 shows how the standard deviation of the observed and simulated flows varies with scale (or sample size) for time scales between one and ten years (365 and 3650 days). The straight lines indicate the lines of best fit and their slopes are $1 - H$. Although both models overestimate the standard deviation at these scales, their slopes (and therefore their Hurst exponents, are similar. The observed and simulated Hurst exponents for the FRB are 0.59 and 0.55 respectively, while the observed and simulated Hurst exponents for the ARB are 0.62 and 0.60 respectively, which are close to each other.

Figure 6.4 is a plot of the autocorrelation functions of the 365-day moving average of the observed and simulated historical flows. For both basins, the simulated results exhibit higher autocorrelation at time scales between 100 and 1000 days. This may due to the properties of the ERA-40 dataset but could indicate that the model structure of MISBA incorporates too much memory in the hydrological systems, most likely via the relationship between deep soil moisture and baseflow. The original ISBA model tended to predict erratic peaks and troughs that were not reflected in the observed data (Kerkhoven and Gan, 2006). The modifications introduced to ISBA were designed to reduce this behaviour by greatly increasing the residence time of moisture in relatively dry soils. It is possible that the mechanism used introduces too much memory at larger time scales than can be readily identified from a hydrograph.

Figure 6.5 shows the results of the MFDFA analysis for the observed and simulated flows in the FRB and ARB, along with the best fitting parameters for the generalized multifractal cascade model. The excellent match between the data and the fractal model is consistent with the observations of Kantelhardt *et al.* (2003) and

Koscielny-Bunde *et al.* (2006). The derived values of fractal parameters *a* and *b* for the FRB are 0.48 and 0.69, respectively, for the observed data, and 0.55 and 0.74, respectively for the simulated data. For the ARB, the derived vales of *a* and *b* are 0.48 and 0.71, respectively, for the observed data, and 0.49 and 0.74, respectively for the simulated data. Again, these results are consistent with the observations of Koscielny-Bunde et al. (2006) who, in their study of 41 international river basins ranging in size from a few hundred to a few million square kilometres, found that values of *a* ranged from 0.39 to 0.57 and *b* ranged from 0.52 to 0.81. Although the differences in the derived values of a and b for the observed and modelled hydrographs are relatively small, it can be seen in Figure 6.5 that this translates to clear differences in the generalized Hurst exponents.

The multifractal spectra of the observed and simulated flows are shown in Figure 6.6. In both cases the simulated and observed data exhibit similar multifractal strength, as measured by the width of the multifractal spectrum, with the primary difference being a leftward shift of the simulated spectra with respect to the observed spectra. Again, this indicates that while the simulated and observed data fall into the same general class of multifractal behaviour, and have similar statistical properties, there is a mismatch in the precise scaling behaviour.

It is beyond the scope of this research to determine whether this mismatch occurs in the ERA-40 dataset, the hydrologic model structure, or (most likely) some combination of the two. However, the fact that the simulated data exhibits the same general fractal properties as the observed data (i.e. they are both consistent with the multifractal cascade and can be represented by similar parameter values) suggests that these differences can

be alleviated correcting this "fractal bias" when further analyzing the model results by shifting the derived values of a and b for the climate scenario simulations by Δa and Δb (Equations 6.34 and 6.35).

The unconditional uncertainties, in terms of an individual year and a 30-year climatology, of the observed and simulated flows in each basin were calculated using the classical, autocorrelation, Hurst exponent, and multifractal approaches (see Table 6.1). The Hurst and autocorrelation methods produce results that are fairly similar to the classical approach. This is not surprising in this case since the Hurst coefficients and autocorrelations of these rivers are relatively low (i.e. close to the values of a statistically independent time series). The multifractal approach, however, produces significantly different results from classical theory, especially in terms of the 30-year upper bound. The reason for this is the significant departure of the probability distribution of the generated multifractal series from the normal distribution that is assumed by the classical, autocorrelation and Hurst approaches. While the generated multifractal can be approximated by a normal distribution over relatively short time spans (30 years or less), the presence of relatively rare periods of extended low and especially high flows cause the entire fractal to have significant skew and kurtosis. This can be seen in Figure 6.7, where the cumulative probability distributions of the observed annual flows in the ARB and FRB are plotted with the distributions for the entire multifractal series, and the first 30 years of the multifractal series, hereafter called the "partial multifractal series". The partial multifractal does not exhibit any of the higher order statistical properties of the full multifractal. The full multifractal does have some features that limit its usefulness for hydrologic time series, however. Of particular concern is the multifractal's tendency to a

more distinct lower bound. This means that the structure of the multifractal cascade may be biased towards extended, relatively mild droughts at the expense of shorter severe droughts. This can best be seen in the case of the ARB where one observed year had flows approximately 10% lower than the lowest flows that the multifractal series could produce over a simulated record of more than 1400 years (Figure 6.7).

6.4.2 SRES Climate Scenarios: Fractal Behaviour

MFDFA analysis was performed on the 54 SRES climate change scenario in both river basins. There is a clear tendency for multifractal strength, as measured by $\Delta\alpha$, to increase with increases in the mean annual flow rate (see Figure 6.8a), however the strength of this relationship is different in the two basins, with the ARB having a much stronger relationship then the FRB. In both basins, multifractal strength has a stronger relationship with changes in mean annual temperature (Figure 6.8b) than changes in mean annual precipitation (Figure 6.8c). The two basins, however, exhibit opposite relationships with temperature. While multifractal strength decreases with increasing temperature in the ARB, it increases with increasing temperature in the FRB. This difference in behaviour can be attributed to differences in how temperature increases in the basins manifest themselves in terms of river flows.

In the ARB, there is a consistent decrease in flow throughout the year due primarily to a reduction in the mean annual snow pack as rising winter temperatures shorten the annual snow season (Kerkhoven and Gan, 2006). Figure 6.8d shows the relationship between multifractal strength and changes in the mean annual snow pack in both basins. Changes in snow water equivalent have a much more dramatic effect on the multifractal behaviour in the ARB, even though the FRB experiences more significant

declines to its snow pack. In the FRB however, this decrease comes with an increase in winter flows that does not occur in the ARB (Figure 6.9), although the two warmest scenarios in the ARB (CCSRNIES A1FI and A2, 2070-99) violate the overall trend. These two scenarios consistently lie outside the overall trend for the ARB. They are, in fact, dramatically warmer than the other scenarios (Figure 6.8b). Warm enough, that the long-term average basin temperature falls significantly below zero only in January. Since the FRB is currently significantly warmer in the winter months (–9°C in the FRB versus –16°C in the ARB during January) only the warmest scenarios in the ARB exhibit behaviour similar to the general trend in the FRB where the winters become warm enough that significant portions of the basin lose their snow fed basin characteristics and the large snow melt wave that has historically dominated the annual hydrograph in both basins begins to weaken and disappear. It is this process that is the most likely cause of the increase in multifractal strength with temperature in the FRB. As for the ARB, climatic change scenarios projected by GCMs have not been sufficient to cause the basin to lose its snow-dominated characteristics in the winter months.

6.4.3 Four Methods for Estimating Unconditional Uncertainty

Figure 6.10 shows the results of the uncertainty analysis in the ARB and FRB using the classical, autocorrelation, Hurst, and multifractal methods for mean flow rates over 30-years (i.e. a climatological time scale). Similarly to the historical flows, the Hurst and Classical approaches produce the tightest ranges, followed by the autocorrelation approach, with the multifractal approach predicting the most uncertainty. At the time scale of individual years (Figure 6.11), there is less variance between the predictions of the non-multifractal techniques. Also, the tendency for the multifractal approach to

cluster the low flow seasons in a relatively tight range becomes apparent, as the lower bound at the annual time scale is only slightly lower than the lower bound at the climatological time scale (approximately 5% and 9% for the FRB and ARB, respectively). By comparison, the classical approach predicts much larger differences between the two scales (approximately 40% and 50% for the FRB and ARB, respectively). The relatively small difference between the 30-year and 1-year bounds in the multifractal method is due to its capacity to simulate extended periods of low and high flows because of the higher degree of memory in the multifractal system than in the other three approaches.

There are four major sources of uncertainty in the predictions of the response of a river basin to future climate change: the hydrological model, the global political and economic decisions made in the future, the general circulation model, and the sample uncertainty associated with the natural variability associated with even a perfectly stable climate. The methods of estimating uncertainty described previously in this paper only address the latter source (sample uncertainty). To put this level of uncertainty in perspective, it would be valuable to estimate the uncertainty associated with the other three sources.

6.4.4 Model Structure Uncertainty

The uncertainty associated with the hydrological model was assessed by comparing the predictions of the MISBA/ERA-40/GEM simulations in the ARB with the predictions of another model, SAC-SMA (Sorooshian *et al.*, 1993). SAC-SMA is a lumped, conceptual process model that depends heavily on calibration and therefore represents a completely different modelling approach than the distributed, physical

process model MISBA/ERA-40/GEM, which requires very little calibration. For the purposes of estimating uncertainty due to hydrologic model structure, the two models are assumed to represent a broad range of modelling approaches. The SAC-SMA model consistently predicts higher flows in the ARB under climatic change than MISBA (Figure 6.12). Although the two models produce very similar predictions under historical conditions (i.e. the climate normal dot falls very close to the 45° line), they grow increasingly divergent as the century progresses and the climate begins to become significantly different than during the historical period (e.g. 2010-2039, to 2040-2069, to 2070-2099). To explain the different predictions of the two models, a best-fitted equation was developed relating the difference in the predicted runoff, ΔQ, to the mean annual precipitation, P, and the change in mean annual temperature, ΔT,

$$\Delta Q = 0.0909P[1 - \exp(-0.367\Delta T)] \tag{6.36}$$

Figure 6.13 is a scatter plot comparing the predicted difference in mean runoff based on Equation 6.36 and the actual difference between the two models. The coefficient of determination is 0.902 and therefore Equation 6.36 explains over 90% of the variance. The key feature of Equation 6.36 is the large, negative coefficient in front of ΔT suggesting that the principle source of the different predictions is the fact that SAC-SMA was calibrated under the historic climate. As the climate warms, the calibrated parameters become increasingly less valid. A particular problem is the fact that SAC-SMA uses a simple degree-day approach for snow, with no accommodation for sublimation. This will tend to result in an over-estimation of the available snow pack in the spring. As was shown in Chapter 4, annual flows in the ARB are sensitive to changes

in the spring snow pack. The SAC-SMA model therefore has a bias towards over-estimating annual runoff under a warmer climate.

6.4.5 SRES Climate Scenarios Uncertainty

Although the full range of economic and political decisions is very large, and impossible to account for in any detail, the range of decisions associated with the four SRES climate scenarios used in this study (A1FI, A2, B1, and B2) represent a realtively wide range of changes in population, industrial technology, and regional disparity. If the four scenarios are assumed to be equally likely, a reasonably conservative estimate of uncertainty due to this source can be estimated by comparing the predictions of the two GCMs from which predictions are available for all four scenarios and estimating the upper and lower bounds using the classical approach.

The uncertainty associated with the choice of GCM can be estimated by comparing the results from the two SRES climate scenarios (A2 and B2) for which predictions are available from all seven GCMS. If we assume each GCM is an equally valid model of the Earth's climatological processes, we can estimate the uncertainty associated with this source using the classical approach. However, this can only account for uncertainty associated with differences between the models. It cannot account for uncertainty associated with aspects the models have in common such as relatively low spatial resolution or inadequate treatment of various climate processes due to the lack of current understanding. Uncertainty associated with these sources is beyond the scope of this study. Indeed, uncertainty associated with processes GCMs cannot currently account for is fundamentally impossible to quantify.

Table 6.2 summarizes the relative uncertainty associated with these four sources, with sample uncertainty represented by the multifractal approach for 30-year mean average flow in the ARB and FRB. Uncertainty due to the SRES scenario and GCM selection were calculated based on the t-distribution with unknown variance and the sample uncertainty was determined directly from the multifractal method. In the case of the hydrologic model used in the ARB, uncertainty was determined by directly comparing the predictions of the MISBA and SAC-SMA models. Although the predictions of the physically based MISBA model should be more robust under a changing climate than the SAC-SMA model, the differences between the models is indicative of the potential range of errors that can occur when a model is applied under conditions that it cannot be evaluated at, such as how a basin will respond under a hypothetical future climate.

The uncertainty associated with the hydrological model in the ARB is comparable to uncertainty associated with the choice of the SRES scenario (averaging ±22% and ±20%, respectively). In the ARB, the uncertainty due to GCM selection is of the same order as uncertainty due to multifractal sample uncertainty (averaging –42% to +42% and –33% to +59%, respectively) but in the FRB, uncertainty associated with GCM selection is much smaller than multifractal sample uncertainty (averaging –12% to +12% and –31% to +48%, respectively). This difference is due to the much higher sensitivity in the ARB to shifts from rainfall to snowfall (Chapter 4). Flows in the ARB are therefore more sensitive than flows in the FRB to changes in winter temperature and precipitation, quantities that vary more between GCMs than changes in annual and temperature and

precipitation. This is likely because the ARB's hydrologic regime is more snow dominated then the FRB's.

6.5 Summary and Conclusions

The multifractal properties of observed and simulated hydrographs in the ARB and FRB were calculated using multifractal detrended fluctuation analysis (MFDFA). Although there were some significant differences in the multifractal properties, the simulated and observed hydrographs' featured properties of both river basins that could be closely modelled by the generalized multifractal cascade model.

Other than during the 1960s, when the ERA-40 re-analysis data were less accurate, MISBA could simulate flows that generally agree well with the observed flows in both river basins (R^2 of 0.63 and 0.59). However, the simulated flows exhibit more variability (Figure 6.3) and more memory (Figure 6.4) than the observed streamflows in both basins. Even though simulated and observed flows exhibit similar multifractal strengths, there is a leftward shift of the simulated multifractal spectrum with respect to the observed spectrum in both river basins (Figure 6.6).

For each basin, the multifractal properties of 54 simulated hydrographs based on the predictions of seven general circulation models, for four SRES climate scenarios, over three 30-year periods in the 21st century were evaluated and used to generate extended artificial time series based on the randomized generalized multifractal cascade model. These artificial time series had the same periodic, statistical, and fractal properties as the simulated hydrographs over a much longer time span than could be reasonably modelled by conventional simulation techniques. These time series could therefore provide a basis to estimate the 95% confidence intervals for mean river flows

over short-term (single year) or climatological (30 year) time scales while avoiding some of the difficulties associated with other uncertainty techniques, such as the influence of long-term trends in the original data and the assumption of normally distributed variance.

The multifractal hydrographs featured significant departures from the behaviour of long-term statistical independence with extended periods of low and high flows resulting in a wider range flows over a 30-year time scale than the classical, autocorrelation, and Hurst methods predicted. Furthermore, the multifractal approach predicted a noticeable degree of skew in the distribution of long-term flows. However, there is evidence that the multifractal model is somewhat over skewed, since the greatly extended time series could not reproduce the lowest flow season in the historical record for either basin (Figure 6.7). The artificial time series appear to be biased towards extended periods of relatively mild droughts at the expense of short, severe droughts. This suggests that it would be beneficial to further modify the multifractal cascade model, or develop new multifractal models that can better reproduce the characteristics of droughts.

The two basins' multifractal properties responded differently to climate change. In the FRB, the multifractal strength of river flows tended to increase along with temperature as the snow fed character of the basin began to weaken. In the colder ARB, only the most extreme scenarios hinted this behaviour. Instead, increased temperatures were associated with decreased flows over the entire annual cycle as snow packs declined without a compensating increase in winter flows. This resulted in a decreased multifractal strength in the ARB under rising temperatures.

The uncertainty associated with long-term river flows due to the multifractal character of each basin was compared with other significant sources of uncertainty: global emission patterns in the 21st century, GCM model selection, and confidence in the accuracy of the hydrological model. Uncertainty associated with the hydrological model and global emission patterns were relatively small (on the order of 20% or less) although in the case of global emission patterns, it is difficult to know if the range of SRES climate scenarios is representative of the "true" distribution of future political and economic decisions. Furthermore, it is possible that the seven GCMs have features in common that do not accurately represent the actual physical processes. To the extent that they do, the method used to estimate this source will tend to underestimate uncertainty.

The uncertainties associated with multifractal variation were on the order of ±50% in both basins and represented the largest source of uncertainty. Only the uncertainty due to GCM selection in the ARB produced similar levels of uncertainty, implying that uncertainty in the predictions of individual GCMs on the hydrology of large river basins (~10^5 km^2) at the 30-year time scale is approximately equal to or less than the natural variability expected under a stationary climate. This suggests that further improvement in GCM modelling associated with an increased understanding of the processes involved, and the finer spatial and temporal resolutions future models are expected to use, will not enable the detection of the influence of climate change on streamflows in relatively large individual river basins even over multi-decadal timescales.

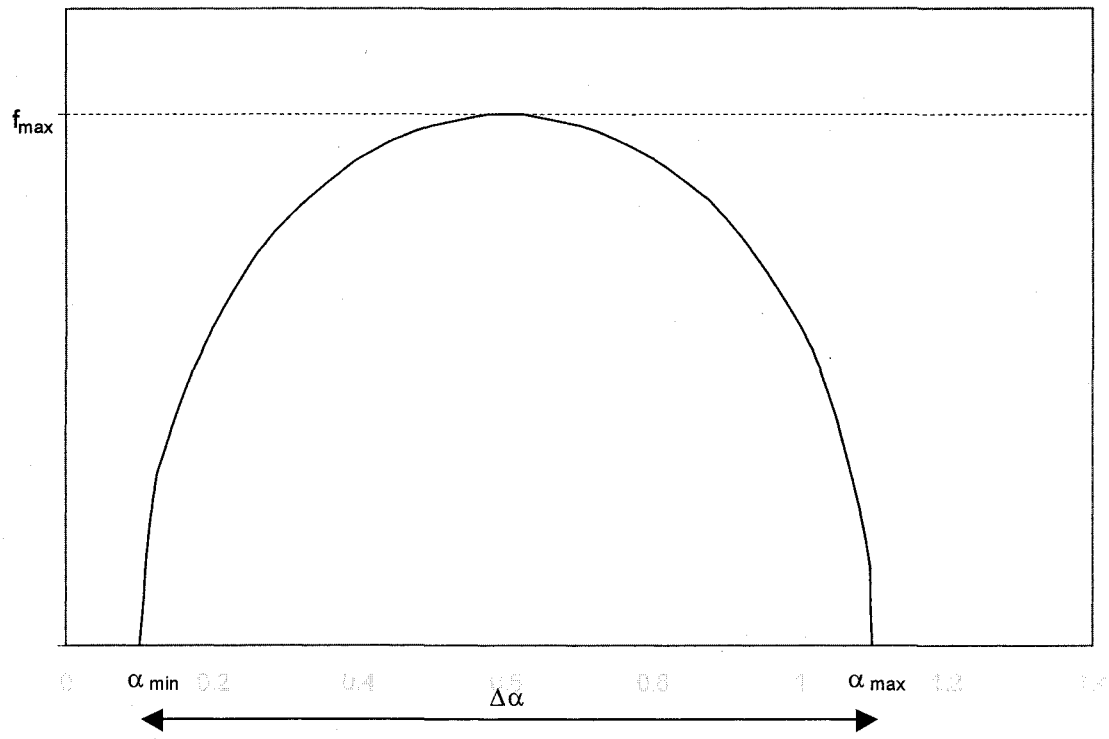

Figure 6.1 - A typical multifractal spectrum indicating the support dimension, f_{max}, and the multifractal strength, $\Delta\alpha$ (Feder, 1988).

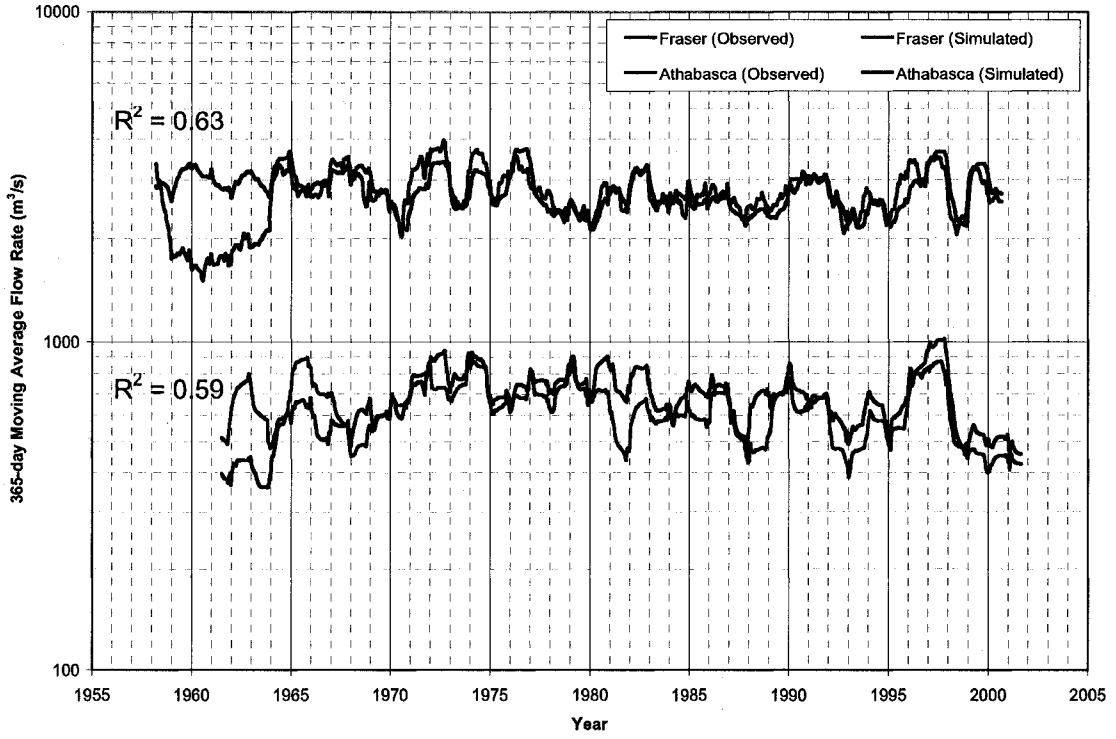

Figure 6.2 - 365-day moving averages of observed and simulated flows in the Athabasca and Fraser River Basins.

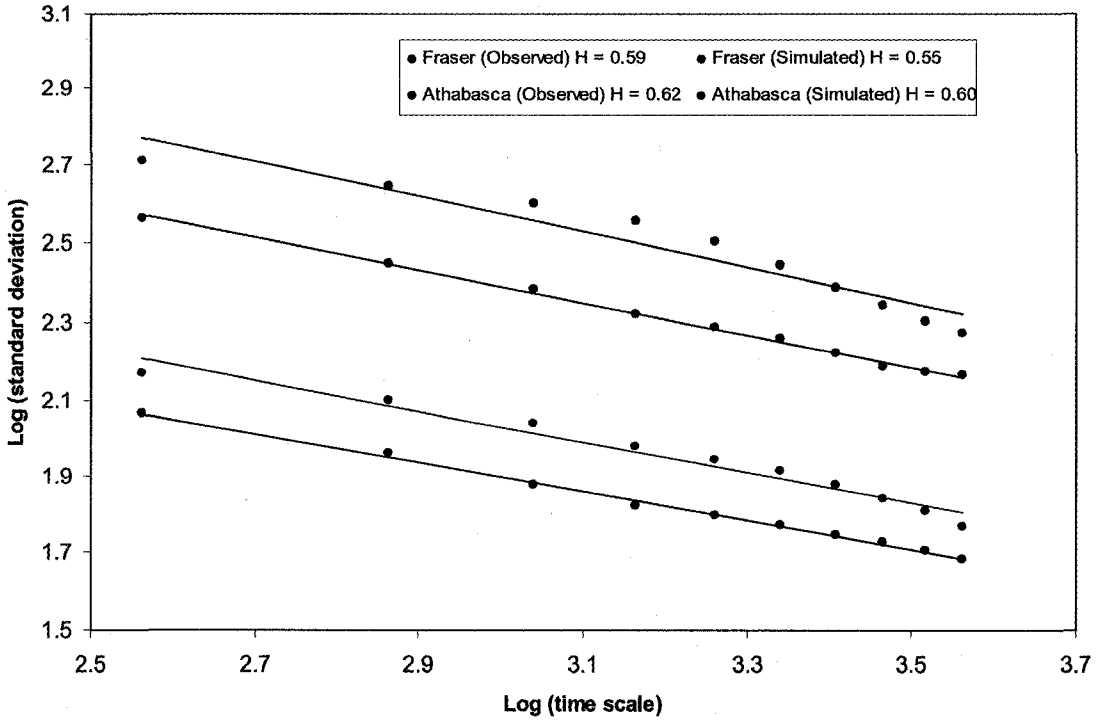

Figure 6.3 - Variation of standard deviation with respect to scale for the observed and simulated historical flows in the Fraser and Athabasca River Basins. Straight lines indicate the line of best fit.

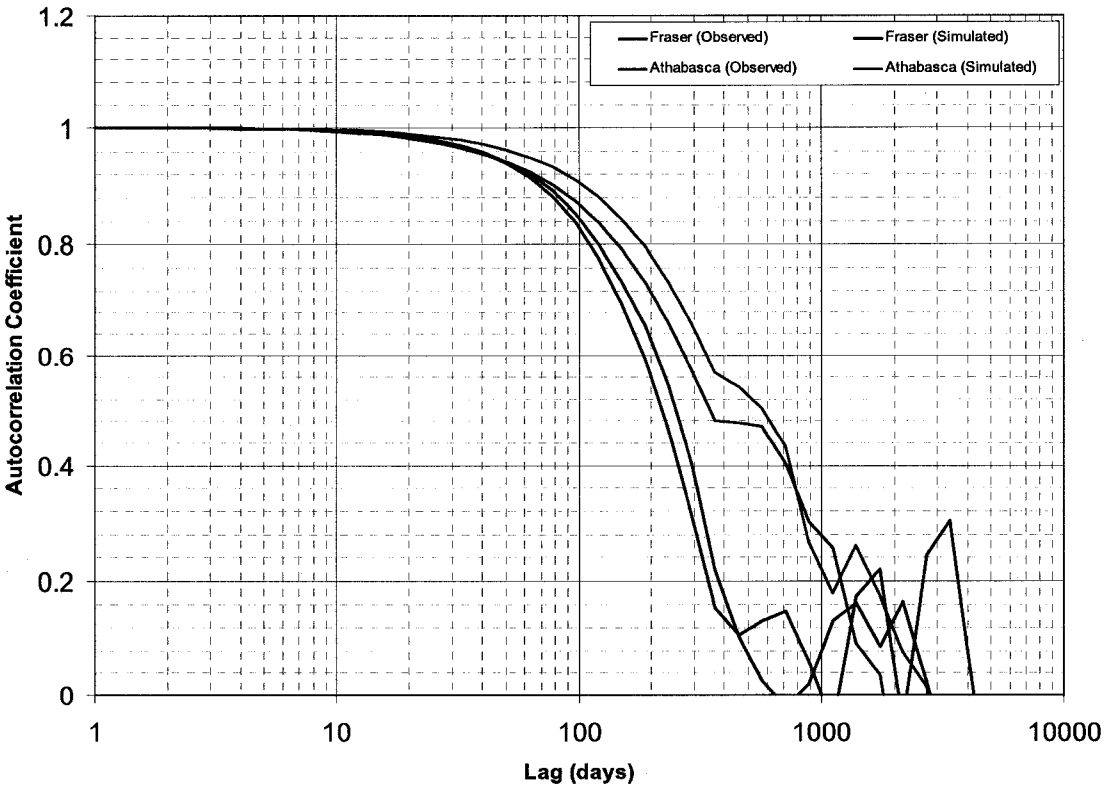

Figure 6.4 - Autocorrelation functions of the 365-day moving average of the observed and simulated historical flows in the Athabasca and Fraser River Basins.

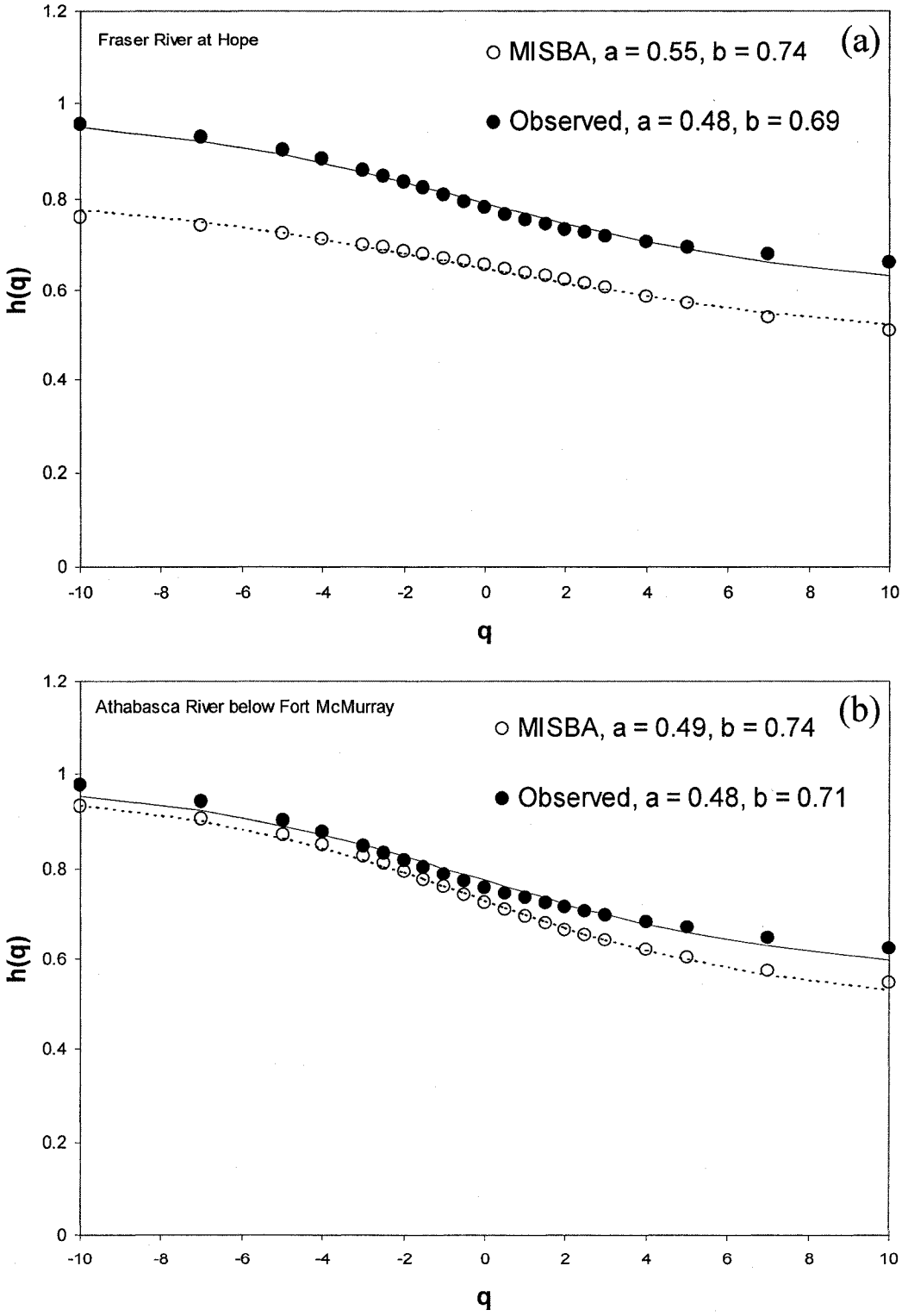

Figure 6.5 - Generalized Hurst exponents of the observed and simulated historical flows in the Fraser (a) and Athabasca (b) River Basins. Values of parameters a and b indicate the parameters for the best fitting multifractal cascade (lines).

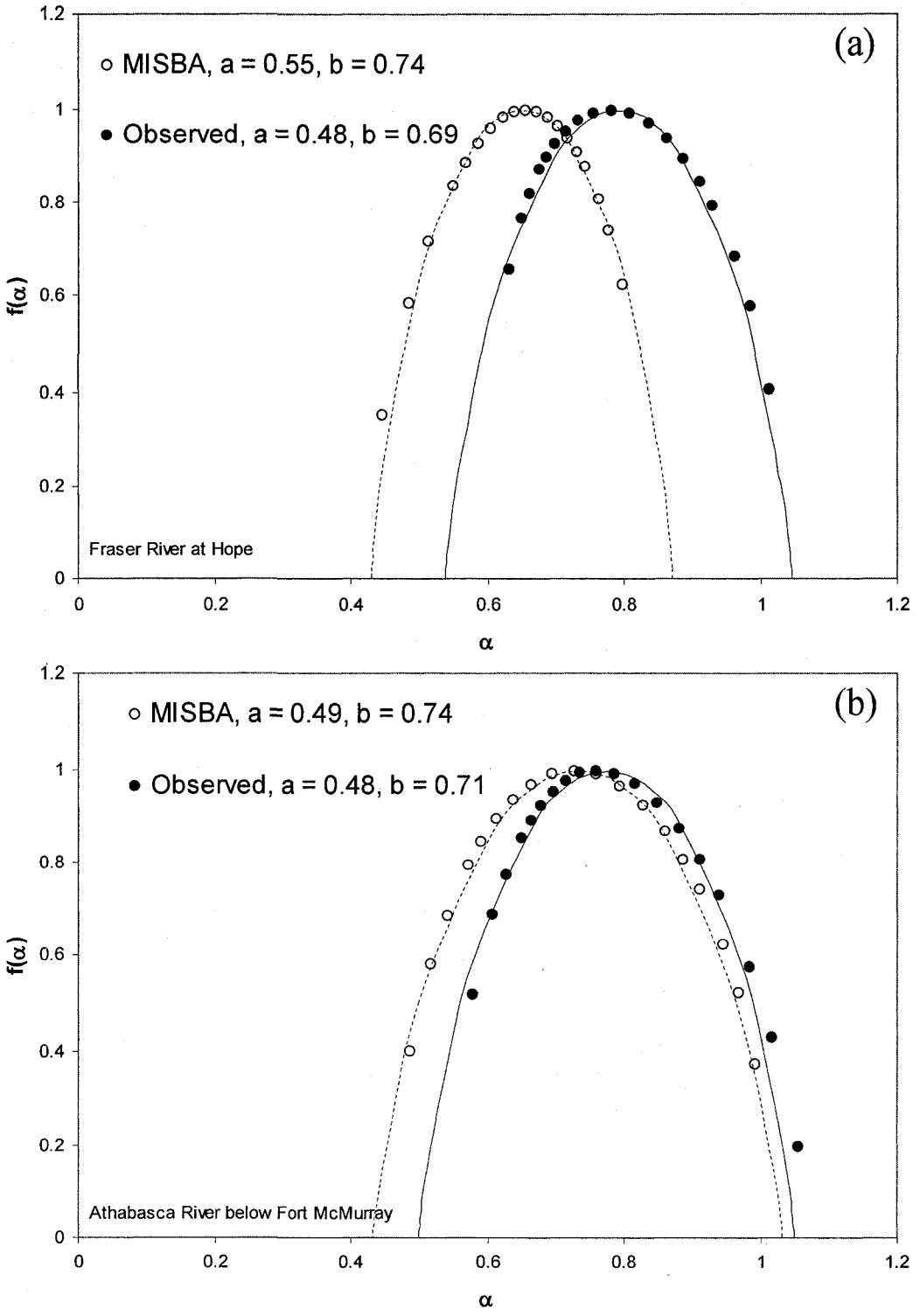

Figure 6.6 - Multifractal spectra of the observed and simulated historical flows in the Fraser (a) and Athabasca (b) River Basins. Values of parameters a and b indicate the parameters for the best fitting multifractal cascade (lines).

Table 6.1 - Estimated 95% confidence limits (upper and lower bounds) for observed and simulated stream flows in the Athabasca and Fraser River Basins based on classical, Hurst, Autocorrelation, and Multifractal approaches. The 1-year and 30-year bounds indicate the range within which an individual year and the average of 30 consecutive years, respectively, can be expected to occur 95% of the time.

All Units in m^3/s	Athabasca River below Fort McMurray							
	Observed				MISBA			
	Classical	Hurst	Autocorrel	Multifractal	Classical	Hurst	Autocorrel	Multifractal
Mean			660				663	
1-year Upper Bound	960	974	978	1148	1043	1057	1125	1203
30-year Upper Bound	745	786	767	1026	770	812	876	1069
30-year Lower Bound	576	534	553	471	555	514	449	461
1-year Lower Bound	361	346	343	443	282	269	200	437
All Units in m^3/s	Fraser River at Hope							
	Observed				MISBA			
	Classical	Hurst	Autocorrel	Multifractal	Classical	Hurst	Autocorrel	Multifractal
Mean			2802				2754	
1-year Upper Bound	3743	3775	3781	4961	4068	4090	4283	5421
30-year Upper Bound	3068	3165	3115	4421	3125	3197	3399	4715
30-year Lower Bound	2536	2439	2489	1970	2382	2310	2108	1418
1-year Lower Bound	1862	1830	1824	1804	1440	1417	1224	1193

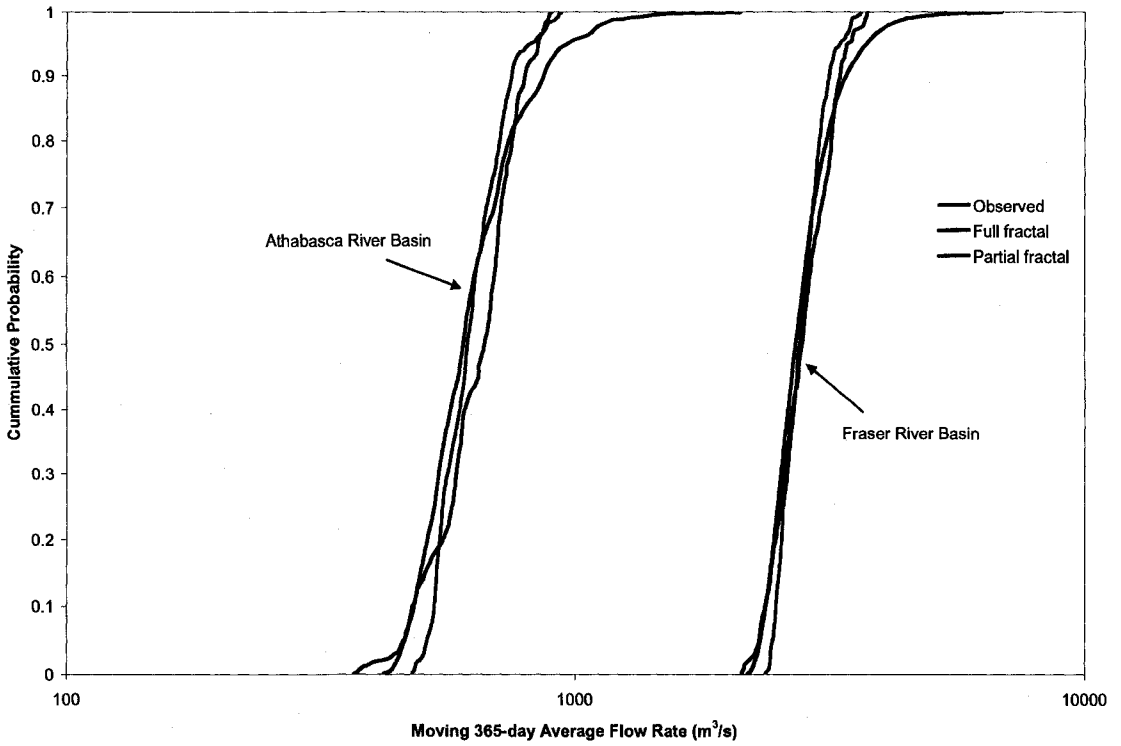

Figure 6.7 - Cumulative probability distributions of observed and fractally generated 365-day moving average flows for the Athabasca and Fraser River Basins

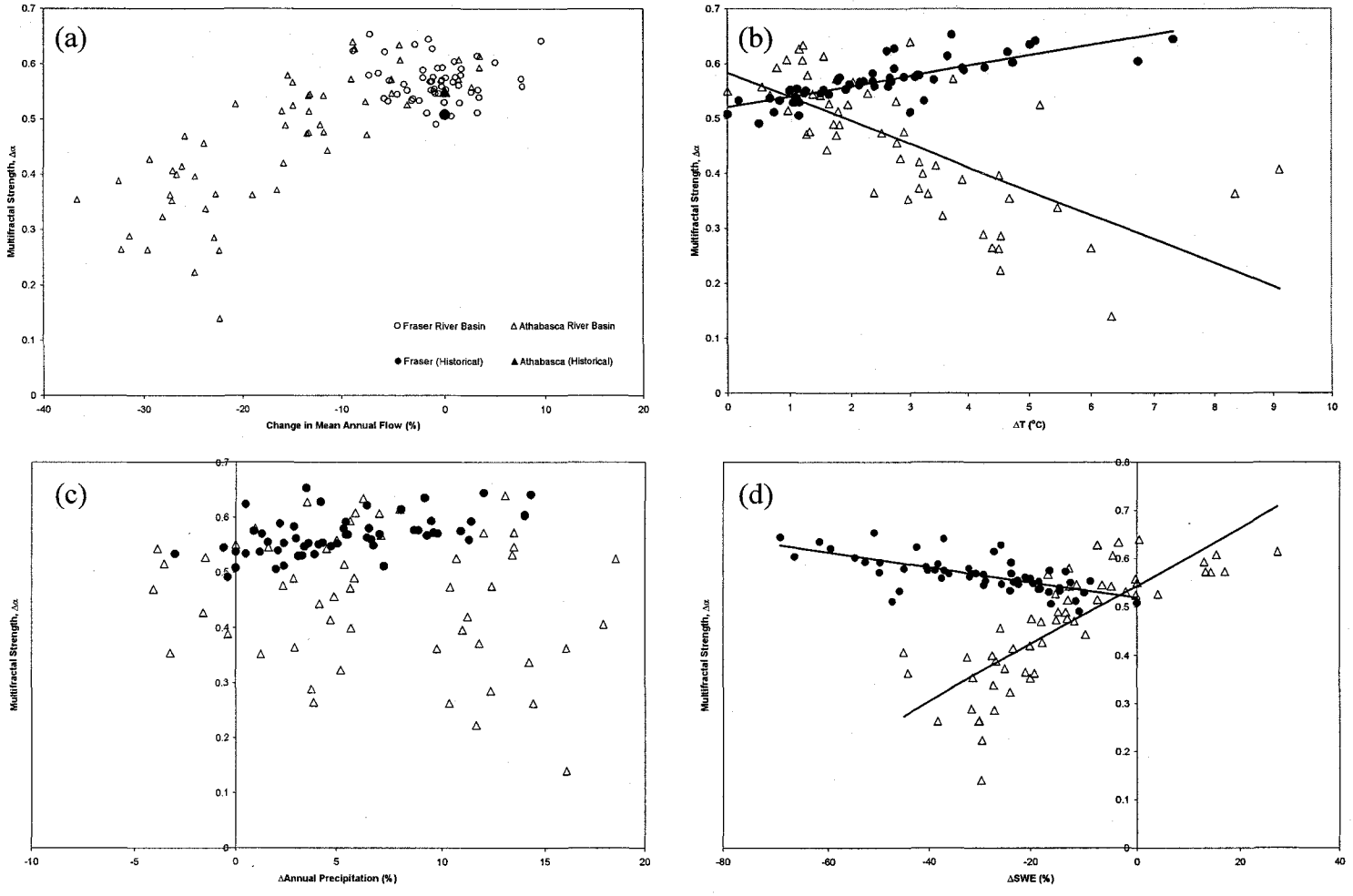

Figure 6.8 - The relationship between multifractal strength and change in (a) mean annual flow, (b) mean annual temperature, (c) mean annual precipitation, and (d) mean annual maximum Snow Water Equivalent for 54 SRES climate scenarios in the Athabasca and Fraser River Basins.

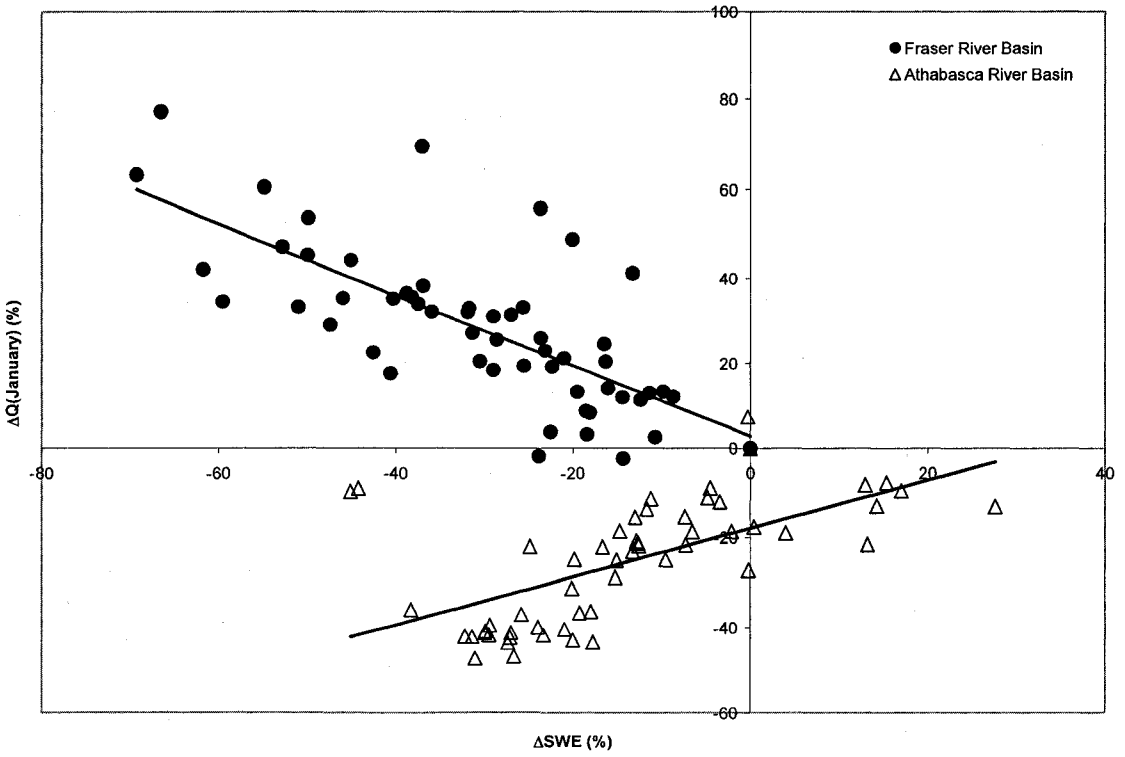

Figure 6.9 - The relationship between Snow Water Equivalent and the change in the change in January flows for 54 SRES climate scenarios in the Athabasca and Fraser River Basins

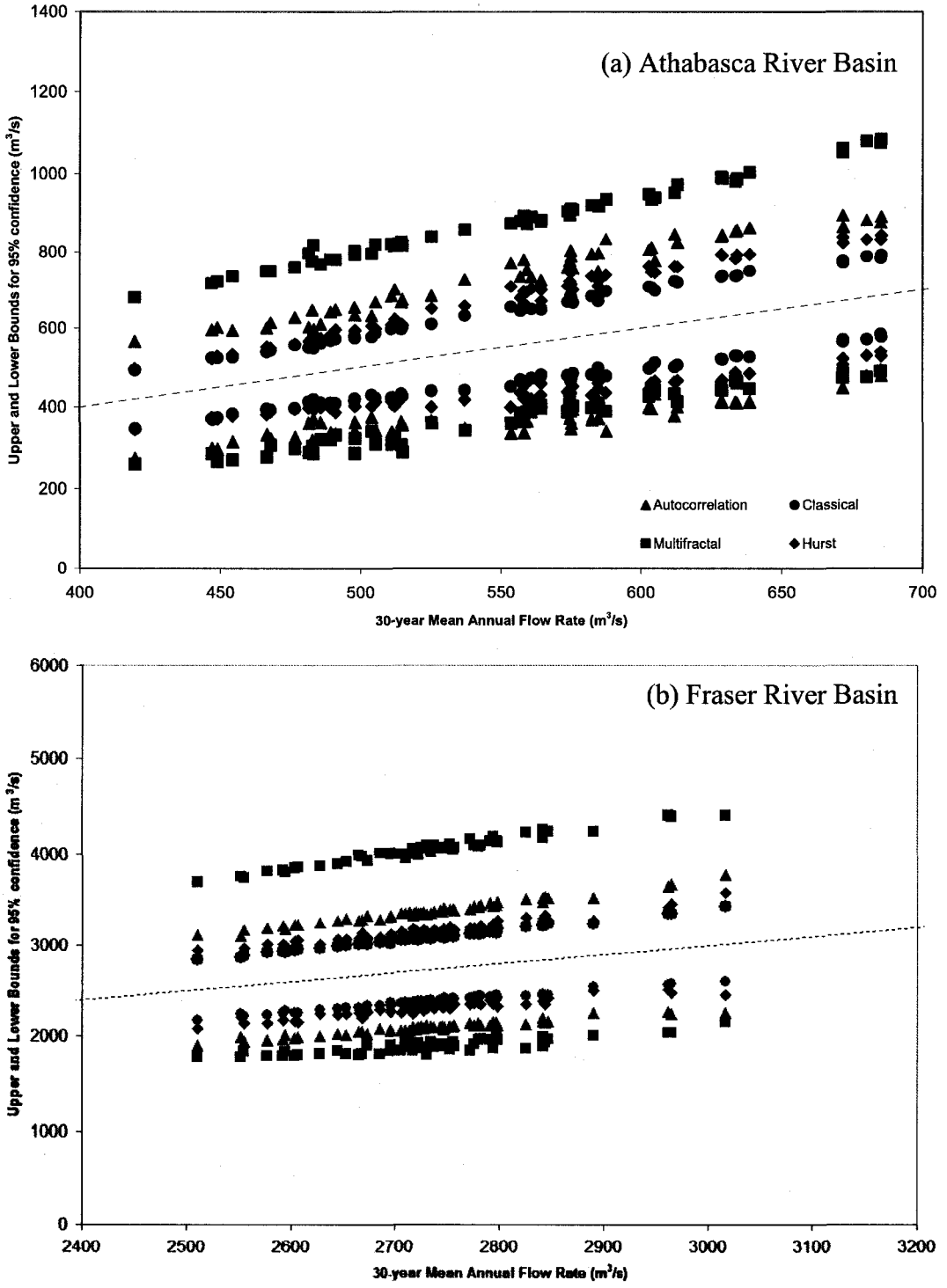

Figure 6.10 - Upper and lower 95% confidence bounds for 30-year mean flow for 54 SRES climate scenarios in the Athabasca and Fraser River Basins.

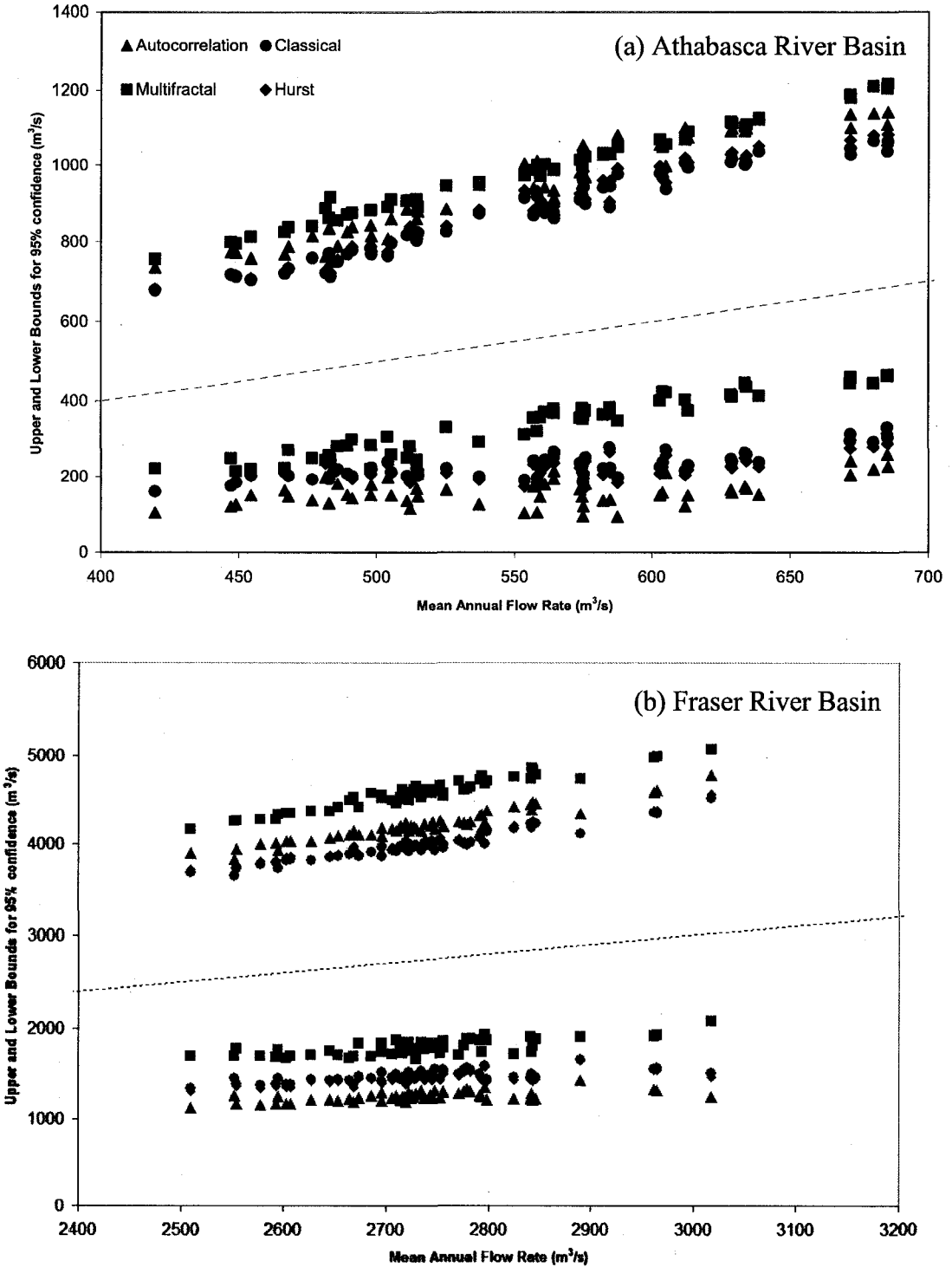

Figure 6.11 - Upper and lower 95% confidence bounds for annual mean flow for 54 SRES climate scenarios in the Athabasca and Fraser River Basins.

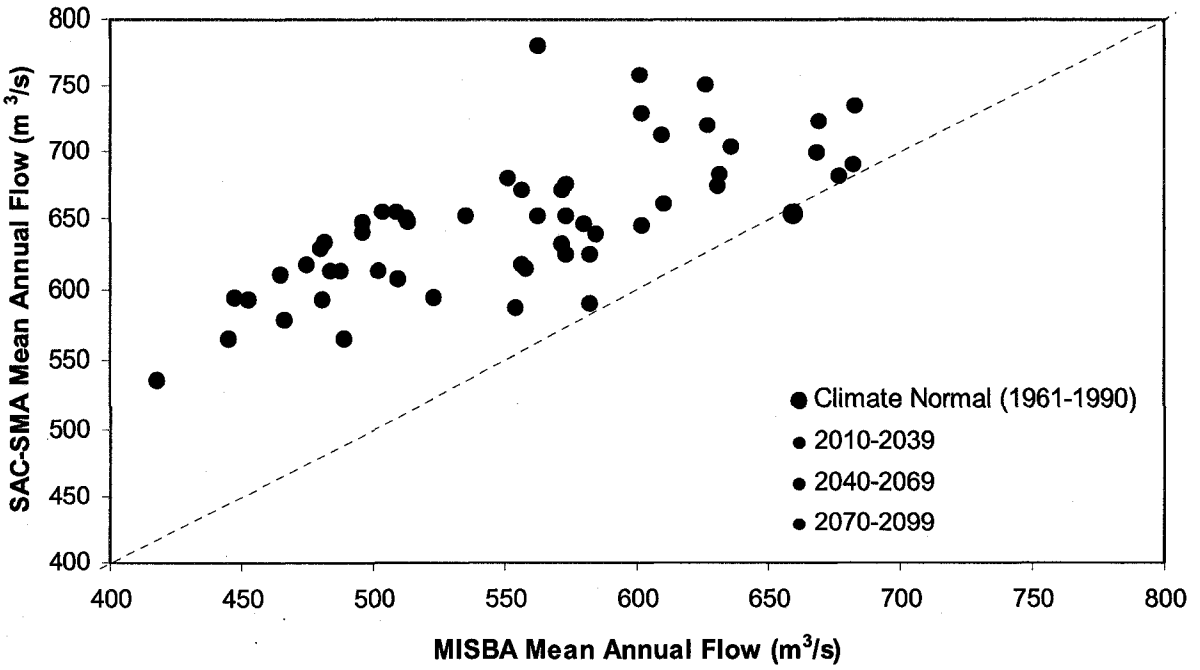

Figure 6.12 – Predictions of mean annual mean flow for historical conditions (black circle) and for 54 SRES climate scenarios (coloured circles) in the Athabasca River Basin for the MISBA and SAC-SMA models.

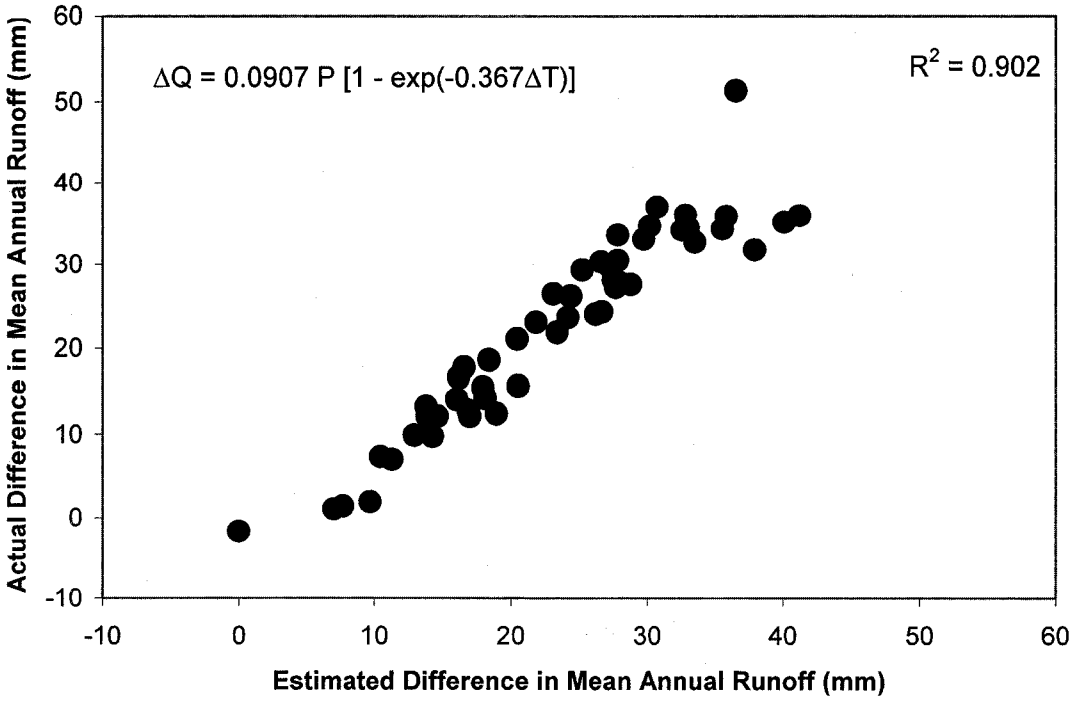

Figure 6.13 – Generalized relationship describing the difference between the predictions of the SAC-SMA and MISBA models for mean annual runoff (ΔQ) due to climatic change in the Athabasca River Basin. P and ΔT indicate the average annual precipitation and the change in mean annual temperature in the basin.

Table 6.2 - 95% confidence limits associated with uncertainty in 30-year average flow due to the hydrologic model, SRES scenario, GCM selection, and multifractal sample uncertainty. Quantities are expressed in terms of the percentage difference with respect to the mean flow.

	Athabasca River below Fort McMurray					
	Average		Maximum		Minimum	
	Upper	Lower	Upper	Lower	Upper	Lower
Type of Hydrologic Model	22.3	-22.3	44.7	-44.7	0.9	-0.9
SRES Scenario	20.1	-20.1	26.2	-26.2	12.6	-12.6
GCM	42.1	-42.1	48.9	-48.9	33.5	-33.5
Sample	58.9	-33.4	69.4	-43.8	55.1	-26.4
	Fraser River at Hope					
	Average		Maximum		Minimum	
	Upper	Lower	Upper	Lower	Upper	Lower
SRES Scenario	12.8	-12.8	21.6	-21.6	5.4	-5.4
GCM	11.6	-11.6	17.1	-17.1	9.0	-9.0
Sample	47.9	-30.9	50.1	-34.0	45.9	-28.2

6.6 Bibliography

Bhatthacharya, R.N., V.K. Gupta, E.C. Waymire, (1983), The Hurst effect under trends, *J. Appl. Probab.* 20, 649–662.

Feder, J., (1988), *Fractals*, Plenum Press, New York.

Gan, T. Y., A.K. Gobena, and Q. Wang, (2007), Precipitation of southwestern Canada: Wavelet, scaling, multifractal analysis, and teleconnection to climate anomalies, *J. Geophys. Res.*, 112, D10110, doi:10.1029/2006JD007157.

Gupta, V.K., and E. Waymire, (1993), A Statistical analysis of mesoscale rainfall as a random cascade, *J. Appl. Meteorol.*, 32, 251-267.

Hurst, H.E., (1951), Long-term storage capacity of reservoirs, *Trans. Am. Soc. Civil Eng.*, 116, 770–799.

Kantelhardt, J.W., S.A. Zschiegner, E.K. Bunde, S. Havlin, A. Bunde, and H.E. Stanley, (2002), Multifractal detrended fluctuation analysis of nonstationary time series, *Physica A*, 316:87–114.

Kantelhardt, J.W., D. Rybski, S.A. Zschiegner, P. Braun, E.K. Bunde, V. Livina, S. Havlin, and A. Bunde, (2003), Multifractality of river runoff and precipitation: Comparison of fluctuation analysis and wavelet methods, *Physica A*, 330:240–5.

Kavasseri R.G., and N. Radhakrishnan, (2005), A multifractal description of wind speed records, *Chaos, Solutions, and Fractals*, 24, 165-173.

Kerkhoven, E., and T.Y. Gan, (2006), A Modified ISBA Surface Scheme for Modeling the Hydrology of Athabasca River Basin with GCM-scale Data, *Advances in Water Resources*, 29 (6), 808-826.

Kolmogorov, A.N., (1962), A Refinement of Previous Hypotheses Concerning the Local Structure of Turbulence in a Viscous Incompressible Fluid at High Reynolds Number. *Journal of Fluid Mechanics*, 13: 82–85.

Koscielny-Bunde, E., J.W. Kantelhardt, P. Braun, A. Bunde, and S. Havlin, (2006), Long-term persistence and multifractality of river runoff records: Detrended fluctuation studies, *Journal of Hydrology*, 322, 120-137.

Koutsoyiannis, D., A. Efstratiadis, and K.P. Georgakakos, (2007), Uncertainty Assessment of Future Hydroclimatic Predictions: A Comparison of Probabilistic and Scenario-Based Approaches, *J. Hydormeteorology*, 8, 261-281.

Lettenmaier, D.P., and T.Y. Gan, (1990), Hydrologic sensitivities of the Sacramento-San Joaquin River Basin to global warming, *Water Resources Research*, American Geophysics Union, 26(1), 69-86.

Lovejoy, S and BB Mandelbrot, (1985), Fractal properties of rain and a fractal model, *Tellus Ser A*, 47, 209.

Lovejoy, S. and D. Schertzer, (1990), Multifractals Universality Classes and Satellite and radar measurements of cloud and rain fields, *J. Geophys. Res.*, 95, 2021.

Mandelbrot, B.B., and J.R. Wallis, (1968), Noah, Joseph, and operational hydrology. *Water Resour. Res.* 4 (5), 909.

Mandelbrot, B.B., (1999), *Multifractals and 1/f noise*, Springer-Verlag, New York.

Schertzer, D., and S. Lovejoy, (1987), Physical modelling and analysis of rain and clouds by anisotropic scaling multiplicative processes. *J. Geophys. Res. Atmosph.* 92, 9693.

Shang, P., L. Yongbo, and S. Kamae, (2008), Detecting long-range correlations of traffic time series with multifractal detrended fluctuation analysis, *Chaos, Solutions, and Fractals*, 36, 82-90.

Sorooshian, S., Q. Duan, and V.K. Gupta, (1993), Calibration of rainfall-runoff models: application of global optimization to the Sacramento Soil Moisture Accounting model, *Water Resour. Res.*, 29, 1185–1194

Tessier, Y., S. Lovejoy, P Hubert, D. Schertzer, and S. Pecknold, (1996), Multifractal analysis and modelling of rainfall and river flows and scaling, causal transfer functions. *J. Geophys. Res. Atmosph.* 101 (D21), 26427–26440.

Chapter Seven: Conclusions and Recommendations

7.1 Conclusions

Although the development of General Circulation Models (GCMs) has allowed for the simulation of nearly all the processes in the global hydrologic cycle, the time and spatial scales at which these models operate are still too coarse to reliably predict hydrologic properties at regional and local scales. Although GCMs are being continually improved to run at smaller scales, the computational requirements remain prohibitive for all but the world's most powerful computer resources available. Unfortunately, hydrologic models capable of capturing these processes at smaller scales are incapable of addressing the large-scale dynamics of the Earth's atmosphere and oceans, which drive the hydrologic variables that hydrologic models depend on. The climatic conditions predicted by GCMs are expected to have large impacts on regional water resources throughout the world. Water management planners therefore require tools that would allow for the assessment of the potential impacts of these changes on flows in river basins that local populations depend on.

The primary objective of this research was to develop a modelling framework capable of combining the large-scale scope of GCMs with the ability of hydrologic models to capture processes at the smaller scales required to accurately simulate river flows, while minimizing the required computational recourses within the limits of a typical home or office computer. The secondary objectives were to apply the resulting model to the Athabasca and Fraser River Basins (ARB and FRB) in order to assess the

potential impact of climate change on streamflows in major river basins, to estimate the uncertainty of these predicted impacts, and to estimate the sensitivity of streamflows in these basins to changes in vegetation.

The modelling framework used was to apply the land surface model Interactions between Soil-Biosphere-Atmosphere (ISBA) within a distributed hydrologic routing model to produce physically based, fully distributed hydrologic model that is compatible with the output of atmospheric models, such as GCMs. New formulations of surface and sub-surface runoff mechanisms, incorporating statistical distributions of soil moisture and precipitation, were developed to improve ISBA's treatment of runoff generation. These modifications simultaneously eliminated two parameters that had a strong influence on predicted runoff, required calibration, and could not be assumed to be homogenous over a large basin. The changes to the surface runoff process also allowed for the simulation of both Dunne and Horton runoff mechanisms. Although these modifications were specifically applied to ISBA, they could easily be applied to almost any land surface model because they only require parameter and state variables that most models provide: soil depth, soil texture, soil hydraulic conductivity, and mean soil moisture.

The projections of seven General Circulation Models (GCMs) from the Third Assessment Report (TAR) of the International Panel on Climate Change (IPCC) were then applied to the ARB and FRB in order to assess the potential impact of climate change on these key western Canadian river basins. In both basins, the GCMs predicted generally similar large-scale trends of increasing temperature and precipitation as the 21st

century progressed reaching average temperature and precipitation changes of +5°C and +10%, respectively in both basins. Furthermore, it was found that most (in excess of 80%) of the variation in key hydrologic variables (mean annual flow, mean maximum annual flow, and mean minimum annual flow) between scenarios could be summarized with relatively simple equations that included only the projected changes in annual rainfall, snowfall, winter temperature, and summer temperature.

Both basins were found to be more sensitive to variations in winter temperature than summer temperature, especially in the case of mean annual minimum flow where relatively minor increases in winter temperature are associated with large decreases in the contribution of precipitation that falls as snow. Both basins also showed similar changes in terms of changes in seasonal flow patterns, such as an earlier onset of spring melt coupled with declines in the amplitude of the snowmelt wave followed by reduced flows in the summer and low flow seasons.

The ARB however, was found to be more sensitive to the shift from snowfall to rainfall due to the shortening of the snow season under a warmer climate because in the drier ARB precipitation that falls as rain is more likely to fall on a dry surface, thus making it more likely that this water will evaporate back to the atmosphere than find its way into the local drainage network. A long term decline in the winter snowpack in the ARB, combined with increased rates of sublimation could well have significant implications for industrial development in the ARB which depends on a stable year-round supply of water from the Athabasca River.

One common concern in the scientific community about the predictions of GCMs has been the fact that these models cannot account for the response of vegetation to climatic change, despite the fact that it has long been recognized that vegetation represents a significant feedback mechanism in both the energy and water budgets and is capable of rapidly responding to climatic change, particularly if these changes result in species die off. However, because of lags in the development of Dynamic General Vegetation Models relative to the development of GCMs, the impact of vegetative response to climatic change on future streamflows has not been assessed. The projections of the seven GCMs under the B2 SRES scenario were repeated in both basins under five vegetative cover scenarios, generated by the vegetation model MAPSS, to estimate the sensitivity of the ARB and FRB to potential vegetative responses to climatic change.

The dominant mechanism in both basins was the tendency for warmer temperatures to increase the areal coverage of grasslands in both basins. Since grassland snowpacks tend to sublimate significantly less than forested snowpacks, this tends to result in proportional increases in the spring snowpack, which in turn results in a increase in annual runoff. In the ARB this represents a consistent strong negative feedback that could potentially mitigate a portion of the flow losses that might otherwise occur in the basin, most notably the potential for a sizable decline in winter flows. The strength of this negative feedback was found to be relatively weak however, with most of the predicted changes in runoff falling within ±3%.

Another issue limiting the application of GCM projections to water management problems is the many sources of uncertainty and the difficulty of quantifying these sources. To this end, recent developments in the multifractal analysis of streamflows were applied to the historical and projected streamflows in the ARB and FRB to better estimate the contribution of variability of flow under a stationary climate to overall streamflow uncertainty. This new approach should provide more reliable estimates of uncertainty in river flows since it allows for the consideration of both the statistical and multifractal properties of streamflow time series.

Streamflows in both river basins showed clear multifractal behaviour that closely followed the qualities of the generalized multifractal cascade, indicating that traditional statistical methods would significantly underestimate uncertainty since they assume statistical independence that fractal time series do not exhibit. The generalized multifractal cascade was then used to generate better estimates of the inter-annual and inter-decadal variability of streamflows, resulting in significantly larger ranges in uncertainty than other methods predict.

In both basins, inter-annual flow variation was at least as large a source of uncertainty as GCM model selection, and a much higher source than either hydrologic model selection or emission scenario selection. This suggests that GCM models, despite their many limitations, have already reached the point where their predictions are precise enough further refinement will not significantly improve our ability to detect the influence of climate change on streamflows in individual basins, although it does not

necessarily preclude detection in an aggregate of river basins or by means of other natural phenomena that exhibit less inter-annual variation than streamflows.

7.2 Recommendations

Based on the results of this study, the following recommendations for future research are made:

- The interaction between the land surface and the atmosphere in the Athabasca Basin, the role of this process in producing convective precipitation within the basin during summer months, the impact of these storms on runoff in the basin, and how these processes might be affected by climatic change should be investigated through the use of a coupled atmosphere/land surface model.
- The sensitivity of the Athabasca basin to the depth of the late winter snowpack suggests that sublimation processes need to be represented as accurately as possible. To this end, a blowing snow module should be added to ISBA.
- The Modified ISBA/ERA-40/GEM framework should be applied to other river basins in Alberta, such as the North and South Saskatchewan River Basins.
- The hydraulic routing component of the Modified ISBA framework cannot directly model the behaviour of lakes. A lake module should be

added to improve model portability to basins with large lakes along the main channel stem, such as the Mackenzie River Basin

- The recent release of the climate projections from the IPCC's Fourth Assessment Report should be applied to the ARB and FRB.
- Tele-connections between long-term climatic indicators such as ENSO and PDO and their impacts on river flows need to be investigated. Of particular importance is the effect climate warming might have on the frequency and amplitude of these oscillations.
- In order to eliminate problems caused by using the predictions of different GCMs under different emission scenarios, the predictions of the dynamic general vegetation models MC1 and BIOMAP under Third and Fourth Assessment Report scenarios should be applied once this data becomes available.
- A detailed hydrologic model that is more capable of representing water and energy fluxes, such as ISBA, should be linked with a dynamic vegetation model such as MC1 to reduce the potential for unrealistic interactions when the results of these models are used to represent the land cover characteristics in hydrologic models.
- The properties of multifractal models such as the generalized multifractal cascade should be further explored in order to improve their ability to generate artificial hydrologic time series

Appendix A: Derivations of Equations 3.2, 3.6, 3.17, 3.22, and 6.19

Derivation of Equation 3.2

Recall Equation 3.1, the Xinanjiang cumulative probability distribution,

$$F(x)=1-\left(1-\frac{x}{x_{\max}}\right)^{\beta} \tag{A.1}$$

From the definition of the probability density function,

$$f(x)=\frac{dF(x)}{dx}=\frac{\beta}{x_{\max}}\left(1-\frac{x}{x_{\max}}\right)^{\beta-1} \tag{A.2}$$

The mean value of variable x is,

$$x_{ave}=\int_0^{x_{\max}} xf(x)dx=\int_0^{x_{\max}} x\frac{\beta}{x_{\max}}\left(1-\frac{x}{x_{\max}}\right)^{\beta-1}dx \tag{A.3}$$

Let $u = x/x_{max}$, $dx = x_{max}du$

$$\frac{x_{ave}}{x_{\max}}=\int_0^1 \beta u(1-u)^{\beta-1}du \tag{A.4}$$

Given,

$$\int x(1-x)^{a-1}dx=-\frac{(1-x)^a(ax+1)}{a(a+1)}+C \tag{A.5}$$

$$\frac{x_{ave}}{x_{\max}}=-\frac{(1-u)^{\beta}(\beta u+1)}{\beta+1}\Bigg|_0^1=\frac{(1-u)^{\beta}(\beta u+1)}{\beta+1}\Bigg|_1^0 \tag{A.6}$$

$$\frac{x_{ave}}{x_{\max}}=\frac{(1-0)^{\beta}(1)}{\beta+1}-\frac{(1-1)^{\beta}(\beta+1)}{\beta+1} \tag{A.7}$$

$$\frac{x_{ave}}{x_{\max}} = \frac{1}{\beta+1} \tag{A.8}$$

Equation A.8 is the same as Equation 3.2.

Derivation of Equation 3.5

Recall Equation 3.2, derived above,

$$\frac{x_{ave}}{x_{\max}} = \frac{1}{\beta+1} \tag{A.9}$$

Replacing x_{ave} with S_{ave}, the average soil moisture retention, and given that the maximum possible soil moisture retention is 1,

$$S_{ave} = \frac{1}{\beta+1} \tag{A.10}$$

$$\beta = \frac{1}{S_{ave}} - 1 \tag{A.11}$$

Equation A.11 is the same as Equation 3.5.

Derivation of Equation 3.6

From Equation A.2, the Xinanjiang probability density function,

$$f(x) = \frac{\beta}{x_{\max}}\left(1 - \frac{x}{x_{\max}}\right)^{\beta-1} \tag{A.12}$$

The definition of the coefficient of variability, CV, is,

$$CV^2 = \frac{\sigma^2}{\mu^2} = \int \frac{(x-\mu)^2}{\mu^2} f(x)dx = \int \frac{(x-x_{ave})^2}{x_{ave}^2} f(x)dx \tag{A.13}$$

$$CV^2 = \int \left(\frac{x}{x_{ave}} - 1\right)^2 \frac{\beta}{x_{\max}}\left(1 - \frac{x}{x_{\max}}\right)^{\beta-1} dx \tag{A.14}$$

$$CV^2 = \int \left((\beta+1)\frac{x}{x_{\max}} - 1 \right)^2 \frac{\beta}{x_{\max}} \left(1 - \frac{x}{x_{\max}} \right)^{\beta-1} dx \tag{A.15}$$

Let $u = x/x_{max}$, $dx = x_{max}du$

$$CV^2 = \int_0^1 ((\beta+1)u - 1)^2 \beta (1-u)^{\beta-1} du \tag{A.16}$$

Given,

$$\int (ax-1)^2 (1-x)^{a-2} dx = -\frac{(1-x)^{a-1}\left(\left(a^2x-2\right)x+1\right)}{a+1} + C \tag{A.17}$$

and substituting $a = \beta + 1$,

$$CV^2 = -\beta \frac{(1-u)^{\beta}\left(\left((\beta+1)^2 u - 2\right)u+1\right)}{\beta+2}\Bigg|_0^1 \tag{A.18}$$

$$CV^2 = \beta \frac{(1-u)^{\beta}\left(\left((\beta+1)^2 u - 2\right)u+1\right)}{\beta+2}\Bigg|_1^0 \tag{A.19}$$

$$CV^2 = \beta \frac{(1)(0+1)}{\beta+2} - 0 = \frac{\beta}{\beta+2} \tag{A.20}$$

$$CV^2 = \frac{\frac{1}{S_{ave}} - 1}{\frac{1}{S_{ave}} + 1} = \frac{1-S_{ave}}{1+S_{ave}} \tag{A.21}$$

Equation A.21 is the same as Equation 3.6.

Derivation of Equation 3.17

Recall Equation 3.15,

$$S_r = \frac{k^2}{P_{ave}(\beta+1)}\left(\frac{\Delta t}{D_{eff}(w_{sat}-w_r)}\right)^{\beta+1}\int_0^{i_{max}} i^{\beta+1}\exp\left(-\frac{ki}{P_{ave}}\right)di + \frac{k^2}{P_{ave}}\int_{i_{max}}^{\infty}\left(\frac{i\Delta t}{D_{eff}(w_{sat}-w_r)}-\frac{\beta}{\beta+1}\right)\exp\left(-\frac{ki}{P_{ave}}\right)di \quad \text{(A.22)}$$

Rewrite this as the sum of two terms,

$$S_r = S_a + S_b \quad \text{(A.23)}$$

where,

$$S_a = \frac{k^2}{P_{ave}(\beta+1)}\left(\frac{\Delta t}{D_{eff}(w_{sat}-w_r)}\right)^{\beta+1}\int_0^{i_{max}} i^{\beta+1}\exp\left(-\frac{ki}{P_{ave}}\right)di \quad \text{(A.24)}$$

and,

$$S_b = \frac{k^2}{P_{ave}}\int_{i_{max}}^{\infty}\left(\frac{i\Delta t}{D_{eff}(w_{sat}-w_r)}-\frac{\beta}{\beta+1}\right)\exp\left(-\frac{ki}{P_{ave}}\right)di \quad \text{(A.25)}$$

The definition of the lower incomplete gamma function is,

$$\gamma(a,x) = \int_0^x t^{a-1}\exp(-t)dt \quad \text{(A.26)}$$

Substituting $x = i_{max}$, $a = \beta+2$, $t=ki/P_{ave}$, and $dt = kdi/P_{ave}$ into Equation A.26,

$$\int_0^{i_{max}} i^{\beta+1}\exp\left(-\frac{ki}{P_{ave}}\right)di = \left(\frac{P_{ave}}{k}\right)^{\beta+2}\gamma\left(\beta+2,\frac{ki_{max}}{P_{ave}}\right) \quad \text{(A.27)}$$

Recall Equation 3.7,

$$\Delta S = \frac{P_{ave}\Delta t}{D_{eff}(w_{sat}-w_r)} \quad \text{(A.28)}$$

and Equation 3.16,

$$i_{\max} = \frac{D_{eff}(w_{sat} - w_r)}{\Delta t} \tag{A.29}$$

Combining Equations A.28 and A.29 yields,

$$\Delta S = \frac{P_{ave}}{i_{\max}} \tag{A.30}$$

Therefore,

$$\int_0^{i_{\max}} i^{\beta+1} \exp\left(-\frac{ki}{P_{ave}}\right) di = \left(\frac{P_{ave}}{k}\right)^{\beta+2} \gamma\left(\beta+2, \frac{k}{\Delta S}\right) \tag{A.31}$$

Substituting Equation A.31 into Equation A.24,

$$S_a = \frac{k^2}{P_{ave}(\beta+1)} \left(\frac{\Delta t}{D_{eff}(w_{sat} - w_r)}\right)^{\beta+1} \left(\frac{P_{ave}}{k}\right)^{\beta+2} \gamma\left(\beta+2, \frac{k}{\Delta S}\right) \tag{A.32}$$

From Equation A.28,

$$\frac{\Delta S}{P_{ave}} = \frac{\Delta t}{D_{eff}(w_{sat} - w_r)} \tag{A.33}$$

Substituting Equation A.33 into Equation A.32 gives,

$$S_a = \frac{k^2}{P_{ave}(\beta+1)} \left(\frac{\Delta S}{P_{ave}}\right)^{\beta+1} \left(\frac{P_{ave}}{k}\right)^{\beta+2} \gamma\left(\beta+2, \frac{k}{\Delta S}\right) \tag{A.34}$$

Simplifying,

$$S_a = \frac{\Delta S^{\beta+1}}{k^{\beta}(\beta+1)} \gamma\left(\beta+2, \frac{k}{\Delta S}\right) \tag{A.35}$$

Recall the definition of S_b from Equation A.25,

$$S_b = \frac{k^2}{P_{ave}} \int_{i_{\max}}^{\infty} \left(\frac{i\Delta t}{D_{eff}(w_{sat} - w_r)} - \frac{\beta}{\beta + 1} \right) \exp\left(-\frac{ki}{P_{ave}} \right) di \tag{A.36}$$

Substituting Equation A.33 gives,

$$S_b = \frac{k^2}{P_{ave}} \int_{i_{\max}}^{\infty} \left(\frac{i\Delta S}{P_{ave}} - \frac{\beta}{\beta + 1} \right) \exp\left(-\frac{ki}{P_{ave}} \right) di \tag{A.37}$$

$$S_b = \frac{k^2}{P_{ave}^2} \Delta S \int_{i_{\max}}^{\infty} i \exp\left(-\frac{ki}{P_{ave}} \right) di - \frac{k^2}{P_{ave}} \frac{\beta}{\beta + 1} \int_{i_{\max}}^{\infty} \exp\left(-\frac{ki}{P_{ave}} \right) di \tag{A.38}$$

Given,

$$\int x \exp(-ax) dx = -\frac{ax + 1}{a^2} \exp(-ax) + C \tag{A.39}$$

$$S_b = -\frac{k^2}{P_{ave}^2} \Delta S \frac{P_{ave}^2}{k^2} \left| \left(\frac{ki}{P_{ave}} + 1 \right) \exp\left(-\frac{ki}{P_{ave}} \right) \right|_{i_{\max}}^{\infty} + \frac{k^2}{P_{ave}} \frac{P_{ave}}{k} \frac{\beta}{\beta + 1} \left| \exp\left(-\frac{ki}{P_{ave}} \right) \right|_{i_{\max}}^{\infty} \tag{A.40}$$

Given,

$$\lim_{x \to \infty} \frac{x + a}{\exp(x)} = 0 \tag{A.41}$$

$$S_b = \Delta S \left(\frac{ki_{\max}}{P_{ave}} + 1 \right) \exp\left(-\frac{ki_{\max}}{P_{ave}} \right) - k \frac{\beta}{\beta + 1} \exp\left(-\frac{ki_{\max}}{P_{ave}} \right) \tag{A.42}$$

Substituting Equation A.30 into Equation A.42 gives,

$$S_b = \Delta S \left(\frac{k}{\Delta S} + 1 \right) \exp\left(-\frac{k}{\Delta S} \right) - k \frac{\beta}{\beta + 1} \exp\left(-\frac{k}{\Delta S} \right) \tag{A.43}$$

$$S_b = \exp\left(-\frac{k}{\Delta S}\right)\left[k + \Delta S - k\frac{\beta}{\beta+1}\right] \tag{A.44}$$

$$S_b = \exp\left(-\frac{k}{\Delta S}\right)\left[\Delta S + k\left(\frac{\beta+1}{\beta+1} - \frac{\beta}{\beta+1}\right)\right] \tag{A.45}$$

$$S_b = \exp\left(-\frac{k}{\Delta S}\right)\left(\Delta S + \frac{k}{\beta+1}\right) \tag{A.46}$$

Substituting Equations A.21 and A.46 into Equation A.23 gives,

$$S_r = \frac{\Delta S^{\beta+1}}{\beta+1}\frac{\gamma(\beta+2, k/\Delta S)}{k^{\beta}} + exp\left(-\frac{k}{\Delta S}\right)\left[\Delta S + \frac{k}{\beta+1}\right] \tag{A.47}$$

Equation A.47 is the same as Equation 3.17.

Derivation of Equation 3.22

Recall Equation 3.21,

$$Q = \beta C_3 D \int_0^1 S^n (1-S)^{\beta-1} dS \tag{A.48}$$

The definition of the beta function, B(x,y), or the Euler integral of the first kind is,

$$B(x,y) = \int_0^1 t^{x-1}(1-t)^{y-1} dt = \frac{\Gamma(x)\Gamma(y)}{\Gamma(x+y)} \tag{A.49}$$

where, $\Gamma(x)$ is Euler's gamma function. Substituting, $n = x\text{-}1$ and $\beta = y$, into Equation A.49 and substituting into Equation A.48,

$$Q = \beta C_3 D \frac{\Gamma(n+1)\Gamma(\beta)}{\Gamma(n+\beta+1)} \tag{A.50}$$

since, $x\Gamma(x) = \Gamma(x+1)$,

$$Q = C_3 D \frac{\Gamma(n+1)\Gamma(\beta+1)}{\Gamma(n+\beta+1)} \tag{A.51}$$

Equation A.51 is the same as Equation 3.22.

Derivation of Equation 6.19

Recall Equation 6.15,

$$h(q) = \frac{1}{q} - \frac{\ln(a^q + b^q)}{q \ln 2} \tag{A.52}$$

which can be rewritten as,

$$h(q) = \frac{1}{q}\left(1 - \frac{\ln(a^q + b^q)}{\ln 2}\right) \tag{A.53}$$

Using the product rule, the derivative of $h(q)$ is,

$$\frac{dh(q)}{dq} = \frac{1}{q}\left(-\frac{a^q \ln a + b^q \ln b}{(a^q + b^q)\ln 2}\right) - \frac{1}{q^2}\left(1 - \frac{\ln(a^q + b^q)}{\ln 2}\right) \tag{A.54}$$

Multiplying both sides by q gives,

$$q\frac{dh(q)}{dq} = \left(-\frac{a^q \ln a + b^q \ln b}{(a^q + b^q)\ln 2}\right) - \frac{1}{q}\left(1 - \frac{\ln(a^q + b^q)}{\ln 2}\right) \tag{A.55}$$

Substituting Equation A.53 for the last term on the left hand side of Equation A.55 gives,

$$q\frac{dh(q)}{dq} = \left(-\frac{a^q \ln a + b^q \ln b}{(a^q + b^q)\ln 2}\right) - h(q) \tag{A.56}$$

which after rearranging gives,

$$h(q) + q\frac{dh(q)}{dq} = -\frac{1}{\ln 2}\frac{a^q \ln a + b^q \ln b}{a^q + b^q} \tag{A.57}$$

The definition of α is,

$$\alpha = h(q) + q\frac{dh(q)}{dq} \tag{A.58}$$

Therefore,

$$\alpha = h(q) + q\frac{dh(q)}{dq} = -\frac{1}{\ln 2}\frac{a^q \ln a + b^q \ln b}{a^q + b^q} \tag{A.59}$$

Equation A.59 is the same as Equation 6.19.

Appendix B: A Comparison of Cumulus Parameterization Schemes in a Numerical Weather Prediction Model for a Monsoon Rainfall Event[2]

B.1 Introduction

In the past, hydrologists have treated precipitation as an input to their hydrological models, while the simulation and prediction of precipitation has been left to atmospheric scientists. The influence of storm velocity and the spatial and temporal distribution of rainfall on runoff have been recognized since the 1960s, but the temporal and spatial resolution of rain gauge data limits our ability to consider these effects. Developments in radar imagery over the past 20 years can estimate the rainfall (Singh, 2002), but not for mountainous terrain. If we rely on precipitation data from radar imageries, then there will be no predictive skill in terms of forecasting runoff beyond the immediate future because we cannot predict radar imageries ahead of time.

One way to address these issues is to use an atmospheric model to simulate precipitation. Developments in numerical weather prediction models and the ever-increasing speed of high performance computers have brought us to the point where mesoscale weather models can be run on a desktop computer. Although there has been a great deal of research into numerical simulation of weather, studies of its applications to watershed hydrology have been limited. Yu *et al.* (1999) used the Pennsylvania State

---

[2] A Version of this chapter has been previously published as, Kerkhoven, E., Gan, T. Y., Shiiba, M., Reuter, G., Tanaka, K.(2006), A comparison of cumulus parameterization schemes in a numerical weather prediction model for a monsoon rainfall event, *Hydrological Processes*, 20(9), 1961-1978.

University/National Center for Atmospheric Research Fifth-Generation Mesoscale Model (MM5) to simulate three storms over a branch of the Susquehanna River in Pennsylvania and the subsequent runoff. Anderson *et al.* (2002) used MM5 to forecast rainfall and runoff in the Calaveras River in Northern California. Both studies found that the runoff derived from MM5 precipitation was lesser than runoff derived from observed rainfall data. Neither study performed sensitivity tests on MM5 parameterizations. Anderson *et al.* (2002) concluded that due to discrepancies between observed and predicted rainfall patterns, the role of MM5's parameterizations schemes should be evaluated.

Because of the difference between the resolution of mesoscale models (20 to 50 km) and the scale of a cumulus cell (1 to 10 km), mesoscale models require the use of convective parameterization (CP) schemes. These schemes must define the trigger of convection, how convection modifies moisture and temperature in a column, and how convection interacts with grid-scale dynamics using the grid-scale information of the main model. Since the 1960s, a number of CP schemes have been developed for use in weather and climate models, many of which are still used today (Kuo, 1965; Arakawa and Schubert, 1974; Anthes, 1977; Fritsch and Chappell, 1980; Betts and Miller, 1986; Kain and Fritsch, 1990; Grell, 1993). Mesoscale models, such as MM5, are usually run with nested grids and have the ability to use different parameterization schemes at different grid scales. The assumptions and simplifications that a scheme makes will limit

its effectiveness, and since there is no universal framework for cumulus parameterization, it is not obvious what the best approach is (Arakawa, 1993).

How CP schemes operate in a mesoscale model is of particular concern for watershed hydrology. In the past, the impacts of CP schemes were usually investigated for climatologic, rather than hydrologic, applications. As a result, the most important factor for a hydrologist, the actual amount of rainfall, was rarely emphasized in past studies. Wang and Seaman (1997) performed a comparison study of the Anthes-Kuo, Betts-Miller, Grell, and Kain-Fritsch schemes using MM5 to simulate six events over the continental United States. The study focussed primarily on rainfall patterns, but they also looked at the total volume of rainfall. They found that while none of the schemes consistently out-performed the others, the Kain-Fritsch and Grell schemes were better than the Anthes-Kuo and Betts-Miller schemes for warm season events.

The purpose of this study is to evaluate the influence of the choice of CP schemes in a mesoscale model on the predicted precipitation, with an emphasis on the accuracy of predicted precipitation amounts in terms of spatial and temporal distributions. Rainfall is the primary input function to basin hydrologic modeling and, as the hydrology community is moving towards driving distributed hydrologic models with meteorological input data, identifying an effective cumulus parameterization scheme for use in a numerical weather model is essential for the accurate forecasting of floods. Since it is the ability of a numerical weather model to predict rainfall that limits its suitability for basin

hydrology applications, this study is limited to comparing predicted and observed rainfall patterns.

B.2 Methodology and Model Descriptions

B.2.1 Methodology

To test how well various CP schemes could predict precipitation during a heavy rainfall event, the MM5 mesoscale model was selected. MM5 is the most recent version of a model first developed in the 1970s by Anthes (Anthes and Warner, 1978). It features multi-nest capability, non-hydrostatic dynamics, four-dimensional data assimilation (FDDA), several physics options, and the ability to be run on most UNIX platforms. A detailed description of MM5 can be found in Grell *et al.* (1995) and Dudhia *et al.* (2000). MM5 includes several CP schemes, five of which were used in this study: Anthes-Kuo, Betts-Miller, Grell, Fritsch-Chappell, and Kain-Fritsch. A summary of these five schemes can be found in Table B.1. MM5 includes the option of using nested sub-grids that can use different parameterizations to take advantage of resolution differences. The sub-grids can be either one-way (from the coarser parent grid to the finer nested grid) or two-way (feedback from the nested grid to the parent grid). For two-way interaction, the parent and nested grid must have a 3:1 resolution ratio. This ensures that every point in the parent grid has a corresponding point in the nested grid.

FDDA is the concept of running a full-physics model while using observed data to "nudge" the results. This allows the model to use physics to maintain dynamical consistency and use observed data to stay close to the true conditions. When properly

done, FDDA minimizes any error caused by gaps in the initial data and deficiencies in the model physics. For more detail on FDDA see Grell *et al.* (1995), and Stauffer and Seaman (1990). In the MM5 model, wind, moisture, and temperature fields can be nudged by the FDDA scheme. In this study, only the wind field was nudged. This was done because FDDA adjustments to humidity and temperature would make it nearly impossible to compare the performance of different CP schemes because these are the variables that are adjusted by these schemes. To ensure that the advection of heat and moisture into the model domain is adequately simulated, MM5 employs a relaxed nudging scheme that is similar to FDDA nudging in its approach. The outer rows and columns are nudged towards the large-scale analysis using a weighting coefficient that decreases linearly to zero at the 5^{th} row/column from the outer boundary.

The model domain consisted of a 111-km resolution grid (Domain 1, mesh size 25 x 31) covering most of China and Japan, and a 37-km resolution grid (Domain 2, mesh size 31 x 31) with two-way interaction, covering East China (Figure B.1). The model was run over a 96 hour period from 0000 UTC 25 June 1998 to 2400 UTC 28 June 1998. Gridded model data was taken from the 0.5°, 12-hour resolution, GAME re-analysis produced by the Japan Meteorological Agency and combined with 12-hour data from a network of meteorological stations. Simulations using all 25 combinations of the 5 schemes over both domains are presented in this paper.

The event simulated was an example of a summer monsoon event over East China, called Mei-yu, or 'plum rain'. A typical monsoon season in China begins when a

quasi-stationary front, called the Mei-yu front, forms in southern China in mid-May, moving northward as the summer progresses passing over the Yangtze River valley and reaching northern China, Korea, and Japan by mid-July. Typically, this progression consists of the front stalling over one location for several days, followed by a sudden northern movement. The strength of the Mei-yu rains is highly variable, both inter-annually and regionally. Heavy flooding often occurs where the front stalls and drought can occur if the front passes over a region too quickly. In 1991 the rain belt remained over the Huaihe Basin for the entire season producing floods while North and South China experienced drought. In 1994, the situation was reversed with the rain belt occurring over North and South China and the Huaihe Basin experiencing drought. A typical Mei-yu season brings about 400 mm of precipitation to East China (Matsumoto, 1998).

B.2.2 Cumulus Parameterization

CP schemes have significant impacts on model predictions, just as cumulus convection does affect the atmosphere circulation by redistributing heat, moisture and momentum. Adjustments to the atmosphere made by different CP schemes can vary significantly. Most CP schemes do not change the horizontal wind field. Instead, the wind field is altered by the release of latent heat. The triggering of convection is highly sensitive to variations in the vertical profile of the atmosphere, both in nature and most CP schemes. Since these variations are smaller than the observational error range, it is virtually impossible for a CP scheme to simulate convection to a high accuracy.

CP schemes were originally developed for very coarse global models to account for diabatic heating in tropical convection, which drives planetary circulations. Because of this, they contain a few legacies of these early applications. CP schemes emphasize heating rates, with precipitation a by-product. Convection is assumed to occur in a small fraction of the grid column. Convective parameterization is particularly difficult in mesoscale modelling. At these scales, the distinction between convective and stratiform precipitation is blurred, resulting in interactions between resolved grid-scale precipitation and parameterized precipitation (Molinari, 1993).

The extent to which convection can be parameterized depends on a separation between the model scale and the convection scale. This suggests that there should exist a statistical equilibrium between the resolved flow and convective energy. Some schemes, like the Arakawa-Schubert scheme (Arakawa and Schubert, 1974), represent this explicitly as a spectrum of cloud sizes. Clouds are often modelled as entraining plumes in CP schemes because of computational efficiency; however, strictly speaking, real clouds are not entraining plumes (Emanuel, 1994). There are also simpler convective adjustment schemes, such as the Betts-Miller scheme (Betts and Miller, 1986), which adjust the atmospheric moisture and temperature to a neutral state, without the use of a cloud model. Some schemes, such as the Anthes-Kuo (Anthes, 1977) are based on moisture convergence.

B.2.3 Anthes-Kuo Scheme

The Anthes-Kuo (AK) scheme is a modification by Anthes (1977) of the Kuo (1965) scheme. Convection is determined from the vertically integrated moisture convergence. The grid-scale moisture convergence is partitioned into two parts: the production of precipitation, and the moistening of the air column. Anthes (1977) set the fraction that goes to precipitation to be a simple function of the mean relative humidity in the troposphere,

$$\alpha = \frac{R_{Hmean} - R_{Hc}}{1 - R_{Hc}} \quad , \quad 0 \le \alpha \le 1 \tag{B.1}$$

where, α is the fraction of moisture convergence to precipitation, R_{Hmean} is the mean relative humidity in the troposphere, and R_{Hc} is a critical relative humidity (50% in MM5). The scheme assumes a dominant cloud size, and does not consider updrafts, downdrafts, or precipitation efficiency.

The Kuo scheme's assumption that convection is generated by moisture convergence has been criticized as inherently flawed in that it violates causality (Raymond and Emanuel, 1993; Emanuel, 1994). To trigger convection, the Kuo scheme requires the presence of available energy and a sufficient moisture supply. Instability produced by energy fluxes can grow unrealistically high until convection is finally triggered, producing "grid-point storms" in which the convective energy of a large area is produced at a single point, sometimes causing numerical instability problems. Also, precipitation is Galilean-invariant, but moisture convergence, which the Kuo scheme assumes is proportional to precipitation, is not Galilean-invariant (i.e. two independent

observers moving at a constant speed relative to each other will measure the same rate of precipitation but different moisture convergences). The changes introduced by Anthes (1977) do not address these problems.

B.2.4 Betts-Miller Scheme

The Betts-Miller (BM) scheme (Betts and Miller, 1986) is a penetrative adjustment scheme without the use of a cloud model. Convectively unstable cloud layers are relaxed to a reference temperature and moisture profile:

$$\frac{\partial T}{\partial t} = \frac{T_{stable} - T_{current}}{t_{convective}} \tag{B.2}$$

$$\frac{\partial q_v}{\partial t} = \frac{q_{v\ stable} - q_{v\ current}}{t_{convective}} \tag{B.3}$$

where $t_{convective}$ is a time scale, T is temperature, q_v is specific humidity, the subscript 'stable' refers to the stable reference profile, and the subscript 'current' refers to the state of the model at the current time step. The stable reference profiles are based on observations, and effectively define a stable humidity profile. Unlike the Kuo scheme, there are no artificial constraints on convection. The scheme initiates convection when the atmosphere is unstable, and continues until the atmosphere stabilizes. The principle weakness is the use of a single stable humidity profile. The scheme does not consider cloud dynamics such as updrafts and downdrafts.

B.2.5 Grell Scheme

This scheme is a simple single cloud version of the Arakawa-Schubert scheme designed to avoid first order sources of error (Grell, 1993; Grell *et al.*, 1995). Clouds are

assumed to be composed of two steady-state circulations caused by updraft and downdraft with the mixing of environmental and cloud air occurring only at the top and bottom of the circulations. This assumption of mixing at the cloud top is consistent with observation and high resolution modelling of deep convective clouds (e.g. Reuter, 1986; Reuter and Yau, 1987a, b). Other CP schemes like the Fritsch–Chappell or the Kain-Fritsch scheme have mixing throughout the entire depth of the cloud. Closure in the Grell scheme is achieved by assuming that the rate at which instability is produced at the resolved grid scale is equal to the rate at which instability is removed at the sub-grid cloud scale. The scheme removes all the available buoyant energy immediately, and converts all liquid water to precipitation, leaving no portion for cloud water. Adjustments to the temperature and moisture profiles are calculated based on the available buoyant energy and the updraft and downdraft mass fluxes. Precipitation efficiency is included in the scheme. Although statistical equilibrium is not explicitly represented in the Grell scheme, the cloud characteristics change at each time step, and over many time steps statistical equilibrium is usually achieved (although not guaranteed). Grell (1993) found that this scheme produced results very similar to the Arakawa-Schubert scheme.

B.2.6 Fritsch-Chappell Scheme

The Fritsch-Chappell (FC) scheme (Fritsch and Chappell, 1980) stabilizes the atmosphere by relaxing the vertical temperature and specific humidity profiles to a stabilized environment. The rate at which the atmosphere is stabilized is controlled by

the difference between the state of the current atmosphere and the stabilized environment, and a convective time scale in a manner similar to the BM scheme. In the FC scheme, the stabilized environment depends on the characteristics of the updraft, downdraft, and the environmental air, using updraft and entraining plume models. The FC scheme was specifically designed for mesoscale modelling.

The key assumption is that adjustments to the temperature and moisture profile depend directly on the convective available potential energy (CAPE), a stability index that measures the buoyant energy in the atmosphere. For closure, the FC scheme assumes that the convective activity must remove most of the CAPE in the convective time scale, which is the time required for mid-level winds to advect convective clouds out of the grid cell (Mailhot *et al.*, 1998). The convective time scale is constrained to be between 30 and 60 minutes. There are three requirements for triggering convection: the CAPE must be positive, there must be sufficient low-level convergence to generate updraft, and the resulting cloud must have at least a minimum depth. The scheme considers the effects of updraft, downdraft and precipitation efficiency, and assumes a single cloud size. As with the Grell scheme, statistical equilibrium tends to occur over several time steps.

B.2.7 Kain-Fritsch Scheme

The Kain-Fritsch (KF) scheme (Kain and Fritsch, 1990) is an extension of the Fritsch-Chappell Scheme. It uses the same assumptions about the removal of CAPE, convective time scale, triggering of convection, and precipitation efficiency. The main

difference is how the KF scheme calculates the inclusion of the characteristics of entrainment/detrainment in the updraft and downdraft when calculating the stabilized temperature and specific humidity profiles (Mailhot *et al.*, 1998). Because the FC scheme was originally intended for short-term modelling (less than a day), it did not explicitly conserve either mass, energy, moisture, or momentum. To ensure the KF scheme could be applied to longer time scales, conservation was rigorously applied (Kain and Fritsch, 1993).

The scheme is well suited for mesoscale models since its assumption about the consumption of CAPE is appropriate for mesoscale time and space scales. The scheme has a realistic convection trigger, and accounts for entrainment and detrainment more realistically than most other schemes. The rate of environmental entrainment and detrainment is assumed to be inversely proportional to the cloud updraft radius. Again, as with the Grell and FC schemes, statistical equilibrium tends to occur over several time steps.

B.3 Synoptic Situation

A large system remained over the southern Yangtze River Valley until June 28, 1998 when the system weakened until it moved north on June 29 to the northern Yangtze-Huaihe River Valley. Figure B.2 is a plot of the June 25 200 mb wind field (2a) and the 850 mb wind field (2b) with the locations of the 500 mb cyclones, 'L', and anti-cyclones, 'H', superimposed. The large-scale features are typical for a Mei-yu event (Lau and Li, 1984; Liang and Wang, 1998). There was a westerly upper-level jet over

northern China and Japan, and easterly flow over the South China Sea and South-East Asia. A southwesterly low-level jet was prominent at the 850 mb level, and westerly flow dominated over Mongolia and northern China. The western Pacific anti-cyclone was situated off the southern Japanese coast, driving warm moist air from the Pacific Ocean to join the monsoon flows over the South China Sea and the Bay of Bengal. A cold low was present over Siberia. Meridional flow south of 30°N is primarily towards the Equator at the upper level, and northward at the lower level. By June 28 (Figure B.3), the upper-level flow was similar but the low-level circulation had changed significantly. The Siberian low moved eastward, and the Pacific anticyclone had moved westward towards the Chinese coast. The low-level jet was forced to shift northward to the Huaihe River Valley (located between the Yellow and Yangtze Rivers, Figure B.4). Very little rainfall was recorded on June 28, but extremely heavy rainfall hit the Huaihe Valley the next day.

B.4 Comparison between Predicted and Observed Rainfall

The event simulated in this study went through three distinct phases: a period of heavy rainfall, followed by a period of moderate rainfall, and a period of low rainfall. The initial 12 hours of each simulation was not used in the analysis since this is the period that the meteorological model is "warming up". The heavy rain phase lasted from hour 12 to hour 36. Average rainfall intensity during this period at the rainfall stations was 20.7 mm/day, and reached as high as 140 mm/day. The moderate rainfall period lasted from hour 36 to hour 72. The average rainfall intensity was 11.4 mm/day, and

reached as high as 50 mm/day. The low rainfall period lasted from hour 72 to hour 96. The average rainfall intensity was 2.3 mm/day, and never went above 10 mm/day.

B.4.1 Evaluation of Precipitation Simulation

To evaluate the quality of each simulation's predicted rainfall field, the model results from Domain 2 were compared to the observations at a network of stations, recording at 12-hour intervals, located between 28° and 36° N and 116° and 122° E (Figure B.4). The model results were interpolated to the station locations using a kriging algorithm.

Table B.2 summarizes the error statistics for simulations that used the same CP scheme in each domain. As can be seen, standard error measures such as mean absolute error (MAE) and root mean square error (RMSE) reward the simulations that most under predict the total volume of rainfall. Because of the highly skewed nature of rainfall patterns, it is common for the difference between the observed and predicted rainfall patterns to be on the same order as the observed rainfall. In fact, with the MAE and the RMSE, a null forecast will often produce a lower error than a forecast with the correct amount of rainfall but with the peaks misplaced. For example, from Table B.2 it can be seen that in terms of MAE a null forecast, where MAE equals mean observed rainfall, would outperform almost every simulation for every rainfall phase. Because of this, weather forecasters usually evaluate model performance based on the frequency with which their models accurately predict the occurrence of events above a threshold, such as rainfall over 50 mm/day. Each observation and simulation pair is categorized in a

contingency table as a *hit* (both over the threshold), a *false alarm* (simulation is over the threshold, but not the observation), a *miss* (observation is over the threshold, but not the simulation), or a *non-event* (both under the threshold). The problem with this approach, from a hydrologist's perspective, is that it does not address the actual volume of rainfall predicted.

Because of these issues, a variation on these error measures is discussed here. At each station, the simulated and observed precipitation were compared and distributed into three categories in a manner similar to the contingency table: accurate prediction (A), over-prediction (B), and under-prediction (C) as follows,

$$A = \sum min(P_{obs,i}, P_{sim,i}) \tag{B.4}$$

$$B = \sum \left(P_{sim,i} - P_{obs,i}\right), \quad where \quad P_{sim,i} > P_{obs,i} \tag{B.5}$$

$$C = \sum \left(P_{obs,i} - P_{sim,i}\right), \quad where \quad P_{sim,i} < P_{obs,i} \tag{B.6}$$

where $P_{obs,i}$ and $P_{sim,i}$ are the observed and the simulated precipitation at station i respectively. Effectively, this approach represents an integration of the contingency table over thresholds from zero to infinity, where A is the integral of the *hits*, B is the integral of the *false alarms*, and C is the integral of the *misses*. The integral of the *non-events* will always be infinite. Simulation performance was evaluated based on the criteria that total error (B + C) and the difference between total simulated rainfall (A + B) and total observed rainfall (A + C) should both be minimized. This was done by calculating an Error Index, *EI*,

$$EI = \max\left(\frac{B}{A+C} \ , \ \frac{C}{A+B}\right) \tag{B.7}$$

Using this index, simulations that produce more rainfall than the observations (i.e. $B > C$) would be evaluated by the first term, while simulations that produce less rainfall (i.e. $C > B$) would be evaluated by the second term. For simulations that produce the same rainfall as observed (i.e. $B = C$) the two terms are the same. The Error Index is minimized if A is large, and if B and C are small and equal. A perfect simulation would produce an Error Index of zero. Recognizing that

$$\sum P_{obs} = A + C \tag{B.8}$$

$$\sum P_{sim} = A + B \tag{B.9}$$

$$\sum \left| P_{obs} - P_{sim} \right| = B + C \tag{B.10}$$

and substituting Equations B.8-B.10 into Equation B.7, it can be shown that

$$EI = \frac{\frac{1}{2}\left(\left|\sum P_{sim} - \sum P_{obs}\right| + \sum \left| P_{sim} - P_{obs} \right|\right)}{\min\left(\sum P_{obs}, \sum P_{sim}\right)} \tag{B.11}$$

The first term in the numerator represents the error in the total volume of rainfall and the second term represents the absolute error of rainfall. The Error Index can therefore be understood as the average of these two errors scaled by the minimum of observed or simulated rainfall. This scaling ensures that the index is not biased towards simulations that under predict rainfall. For example, a simulation that consistently predicts P_{sim} =

nP_{obs} will have the same Error Index as a simulation that consistently predicts $P_{sim} = P_{obs}/n$, namely n-1.

As can be seen in Table B.2, the Anthes-Kuo scheme consistently underestimates rainfall across all three phases. Although the AK scheme also has the lowest MAE and RMSE, this is primarily due to the low rainfall rates predicted by the scheme. When measured by the Error Index, the AK scheme ranks near the bottom. Figure B.5 compares the observed and simulated rainfall patterns for three 12-hour periods, each representing either the heavy, moderate, or light rainfall phases. The AK scheme (Figure B.5b) clearly under simulates the strength of convection at all rainfall intensity scales. This suggests that the AK scheme's assumption that precipitation is limited by large-scale moisture convergence may be inappropriate for this case. Although the scheme does a reasonable job of predicting the location of rainfall, it cannot predict the intensity of atmospheric convection, possibly because it does not adequately consider the effects of buoyant energy in the atmosphere.

The Betts-Miller scheme has a tendency to over-predict rainfall. It also tends to produce narrower rainfall bands of much higher intensity than the other schemes (Figure B.5c). The BM scheme does a good job of simulating light and heavy rain, but for moderate rainfall is inferior to the Grell and Kain-Fritsch schemes, which have better bias, MAE, RMSE, and Error Index scores. In this study, the BM scheme exhibits more "on or off" behaviour than the other schemes, predicting either heavy rainfall or none at all. Because the BM scheme's definition of a stable moisture profile is based on

observations of large-scale tropical storms and hurricanes (Betts and Miller, 1993), it is not surprising that it predicts either severe convection or none at all. This becomes more problematic at smaller grid scales where having heavy rainfall at one grid point and none at an adjacent point becomes less realistic for mesoscale storms.

The weakness of the Fritsch-Chappell scheme is most evident from the very high error scores for the moderate and light rainfall phases (Table B.2). Although it does an adequate job of simulating heavy rainfall, the FC scheme is unable to predict the drop off in rainfall intensity. From Table B.2 and Figure B.5d it can be seen that during the light rainfall phase, the FC scheme predicts more rainfall than it does for the heavy rainfall period. Comparing the FC schemes predictions with the Kain-Fritsch scheme can show the reasons for this.

In this study, the Kain-Fritsch scheme performs better than the FC scheme (for heavy rainfall) or far better (for moderate and light rainfall). The KF scheme uses the same closure and operating principles as the FC scheme but simulates the decrease in rainfall much better. The steady growth of differences between the predictions of the FC and KF schemes can be clearly seen by comparing Figures B.5d and B.5f. The FC scheme continued to predict heavy rainfall when the simulation was started at a later time and therefore the KF scheme's superior performance is probably attributable to the inclusion of detrainment in its cloud model rather than its more rigorous conservation of mass, moisture, energy, and momentum. This suggests that the entrainment/detrainment

processes in the KF scheme may be crucial for realistic simulation of weakening convection.

The Grell scheme is the only CP scheme to perform well at all rainfall intensity scales. The scheme scores the best in terms of bias and the Error Index. In terms of MAE and RMSE, only those simulations that severely under predict rainfall had lower scores. A similar finding was evident in the PSU-NCAR MM5 simulations of two heavy precipitation events over the south-eastern USA (Roebber and Reuter, 2002). The Grell scheme provided the best rainfall on both the outer and inner domain with grid spacing of 54 km and 18 km, respectively. Why does the Grell scheme perform well compared to other CP schemes? It is beyond the scope of our present investigation to determine exactly what the features of the Grell scheme that tends to make it superior. However, it is speculated that a major reason of its superiority is that it accurately captures the cumulus entrainment mechanism. In his review article, Reuter (1986) documented that mixing in deep convection occurs at the cloud top rather than through its sides in plume-like fashion. Grell's formulation captures this mixing by allowing mixing of cloudy and dry environmental air only at the cloud top. In contrast, the other CP schemes tested in this paper assume turbulent mixing throughout the entire cloud depth, have updraft-downdraft circulation, or do not consider mixing at all.

B.4.2 Using Different CP Schemes in each Domain

In this section the potential for improving model performance by using different CP schemes in the two domains will be examined. Evaluation of the CP schemes in this

study is limited here to their influence on cumulus parameterization in the mesoscale Domain 2. From this perspective, the role of Domain 1 is to supply realistic spatial and temporal boundary conditions to Domain 2. Because the assumptions used by different CP schemes are usually more appropriate for some scales rather than others, it is to be expected that changing the CP scheme used in Domain 1 can produce better results. However, doing so also introduces problems related to using different CP concepts simultaneously. How different schemes interact could also be sensitive to the specifics of individual events and model arrangements. Discussion here will therefore be limited to the identification of general patterns and relationships.

Table B.3 summarizes the results of all combinations of the 5 CP schemes used in this study as measured by the Error Index and the ratio of mean simulated to mean observed rainfall. The importance of the Domain 1 CP scheme, however, can be seen in Table B.3 by how simulations with the same Domain 2 scheme (simulations in the same column) vary from each other. In general, the simulations are more sensitive to the selection of the Domain 1 scheme during the heavy rainfall phase than the moderate and light phases, especially if we set aside the exceptional case of the BM-AK (BM in Domain 1 and AK in Domain 2) simulation.

For heavy rain, the Betts-Miller scheme out-performed all other Domain 1 CP schemes, with the notable exception of simulations using the BM scheme in Domain 2 (Table B.3), where the FC-BM and KF-BM performed better than all other combinations for heavy rainfall. This is particularly surprising given that the FC and KF schemes are

otherwise inferior to both the BM and Grell schemes in Domain 1. Figures B.5c and B.5g show the rainfall fields for the BM-BM and FC-BM simulations respectively. The similarity of the BM-BM and FC-BM rainfall patterns in comparison with the other simulations shown in Figure B.5 illustrates the relative importance of the Domain 1 CP scheme. The primary difference between the two figures is that the FC-BM simulation consistently predicts less rainfall than the BM-BM simulation, particularly in the case of heavy rainfall. This indicates that the FC scheme passes less energy and moisture to Domain 2 than the BM scheme. Since the BM scheme tends to produce too much rainfall at the Domain 2 scale, the decreased supply improves the performance. The fact that the FC and BM schemes do not otherwise perform well at the Domain 1 and 2 scales respectively suggests that this improvement is due more to the coincidence of two flaws (too little energy supplied by the FC scheme and too much convection in the BM scheme) than any skill on the part of the schemes.

With the exception of the Grell scheme during the heavy rainfall phase, every simulation that used the same scheme in both domains could be improved by changing the Domain 1 scheme. In terms of the Error Index, the AK-AK simulation was dominated by the Gr-AK and KF-AK simulations; the BM-BM simulation was dominated by the FC-BM and KF-BM simulations; the FC-FC simulation was dominated by the AK-FC, BM-FC and Gr-FC simulations; and the KF-KF simulation was dominated by the Gr-KF simulation. The combination of the BM scheme in Domain 1 and the Grell scheme in Domain 2 (Figure B.5h) was the best simulation in this study,

with the sixth lowest Error Index for heavy rainfall, the lowest for moderate rainfall, and the second lowest for light rainfall.

B.5 Conclusion

A monsoon event in Eastern China in the summer of 1998 was simulated with the Mesoscale meteorological model MM5 using various combinations of five cumulus parameterization schemes: Anthes-Kuo, Betts-Miller, Fritsch-Chappell, Kain-Fritsch, and Grell. It was shown that the ability of the model to predict reasonable rainfall patterns and intensities was heavily dependent on the cumulus parameterization schemes used. This study was based on a single localized event. Therefore, these findings are somewhat speculative in nature and further confirmation is needed to substantiate our conclusions.

The Anthes-Kuo scheme was unable to produce sufficient rainfall due probably to its unrealistic assumptions about the nature of atmospheric convection. The scheme consistently predicted less than two-thirds of the observed rainfall for the heavy, moderate, and light rainfall phases.

The Betts-Miller scheme was the best scheme for the larger scale (111 km) domain, but tended to over-predict rainfall in the mesoscale (37 km) domain by roughly 20%. The scheme's use of a single stable moisture profile based on observations of tropical storms and severe convective tendencies limits its application to other environments and smaller scales.

The Fritsch-Chappell scheme was able to reproduce the heavy rainfall phase of the event but it failed to simulate the decline in rainfall as the simulation progressed, predicting rainfall an order of magnitude too high by the end of the simulation.

The Kain-Fritsch scheme's inclusion of entrainment/detrainment processes made it better than the Fritsch-Chappell scheme at simulating the moderate and light phases of the event without any loss in accuracy in the heavy phase. The scheme simulated the moderate phase of the event well, but could not simulate the light phase as well as the Grell and Betts-Miller schemes. Its tendency to over-predict light rainfall in this study should not be a problem for event scale hydrology applications, but may be problematic for longer-term climatic applications.

The Grell scheme was the only scheme to produce consistently good results in all three rainfall phases and at both domain scales, making it the most robust of all the schemes considered in this study. Unlike the Betts-Miller scheme, the Grell scheme does not make any stability assumptions based on tropical, or any other, environments. This makes it a useful first choice for mesoscale modelling.

While the choice of scheme used in the small scale Domain 2 was the most important factor in determining simulation performance, in every case that a simulation used the same scheme in both domains performance could be improved by changing the Domain 1 scheme. In general, when the Domain 2 scheme included downdrafts (FC, Gr, and KF) performance improved by using a scheme that did not include downdrafts (AK and BM – especially BM) in Domain 1, and when the Domain 2 scheme did not include

downdrafts (AK and BM) performance improved by using a scheme that did include downdrafts (FC, Gr, and KF) in Domain 1. This suggests that the inclusion of downdrafts may improve the accuracy of the simulation, but its use in both domains may cause unrealistic feedbacks and interactions. Although the combination of the Betts-Miller scheme in the large domain and the Grell scheme in the mesoscale domain was found to be best for this event, more research is needed to determine which schemes are appropriate in other environments. The skill of the Grell is speculated to be related to the fact that it allows mixing of cloud and environmental air to occur only at the cloud top. Other schemes allow for mixing throughout the entire depth of the cloud, which is inconsistent with observations, and high-resolution cumulus simulations that show the presence of the cloud top mixing mechanism (Reuter 1986, Reuter and Yau 1987a, b).

Because of the relative coarseness of the mesoscale for many hydrological applications it can be tempting to use these schemes at smaller resolutions, such as 10 km or less. As this study has shown however, the ability of a parameterization scheme to simulate convection at one scale is no indication of its usefulness at smaller scales. Because of this, and due to theoretical evidence that suggests that cumulus parameterization may be impossible at these scales (Molinari, 1993; Emanuel, 1994), it is currently inadvisable to use cumulus parameterization schemes at these smaller scales. Until computational power makes it feasible to incorporate cloud-resolving models, it would be more appropriate to use an explicit moisture scheme or apply downscaling techniques when finer spatial resolutions are required.

CP Scheme	Abreviation	Reference	Cloud Model	Closure Assumption
Anthes-Kuo	AK	Anthes (1977)	Simple 1-D, no downdraft	Precipitation is proportional to large-scale moisture convergence
Betts-Miller	BM	Betts and Miller (1986)	Penetrative adjustment (no cloud model)	Atmosphere is relaxed towards a pre-defined neutral state
Grell	Gr	Grell (1993)	1-D updraft-downdraft couplet, no lateral entrainment	The rate of production of instability at the large scale = the rate of removal of instability at the small scale
Fritsch-Chappell	FC	Fritsch and Chappell (1980)	1-D entraining plume, with downdraft	Convection is proportional to the available buoyant energy.
Kain-Fritsch	KF	Kain and Fritsch (1990)	1-D entraining-detraining plume, with downdraft	Convection is proportional to the available buoyant energy.

Table B.1 - Summary of Cumulus Parameterization Schemes used in this study.

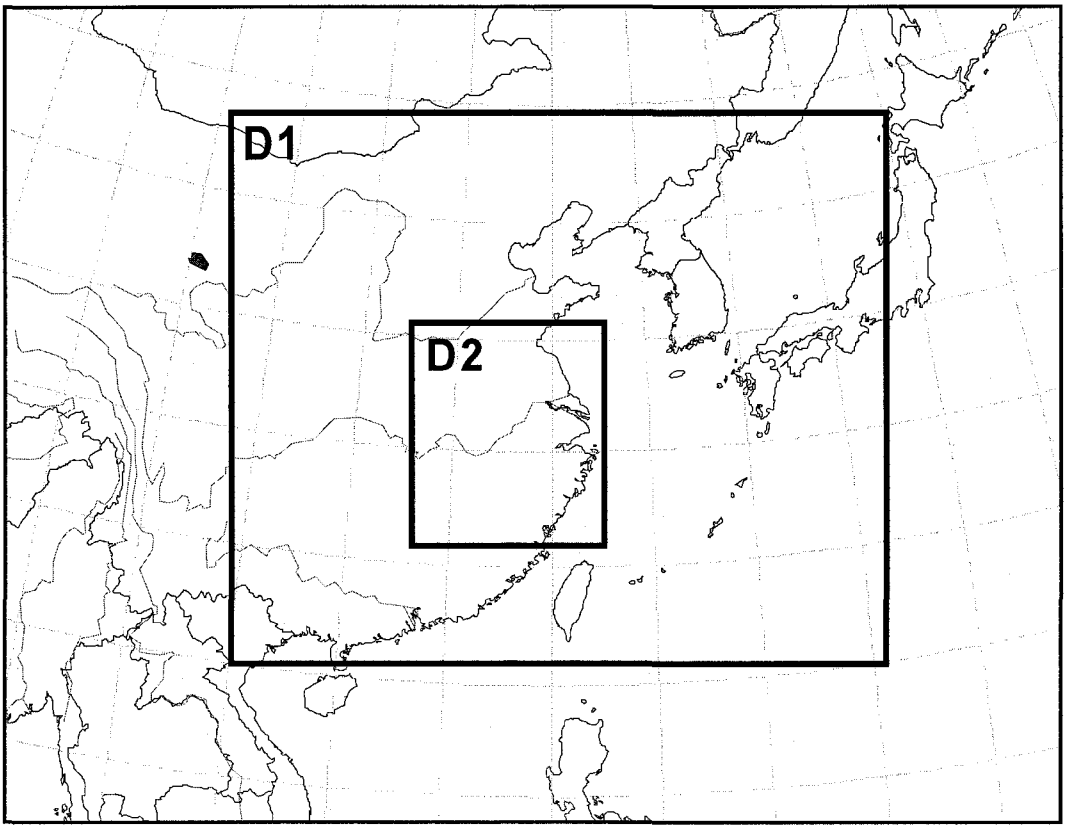

Figure B.1 - Location of MM5 model domains

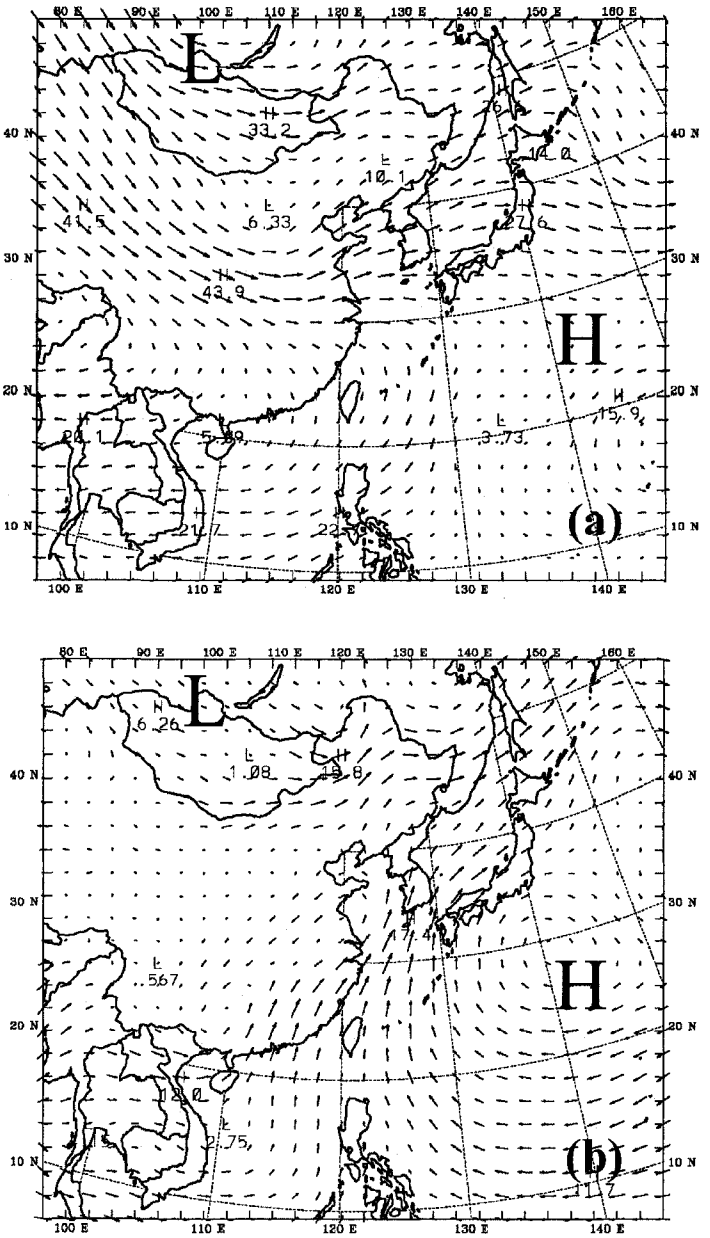

Figure B.2 - (a) 200 mb wind field and (b) the 850 mb wind field at 0000 UTC 28 June 1998. 'L' and 'H' indicates the locations of 500 mb cyclones and anti-cyclones, respectively.

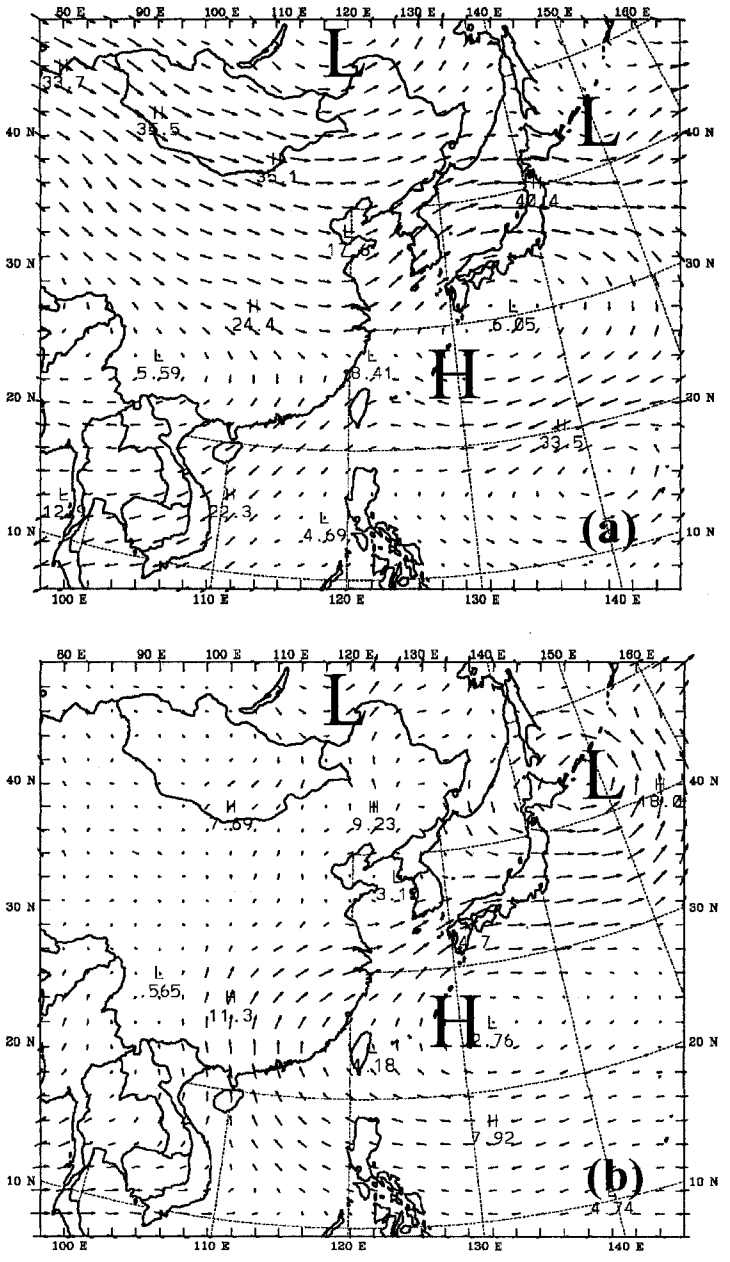

Figure B.3 - (a) 200 mb wind field and (b) the 850 mb wind field at 0000 UTC 28 June 1998. 'L' and 'H' indicates the locations of 500 mb cyclones and anti-cyclones, respectively.

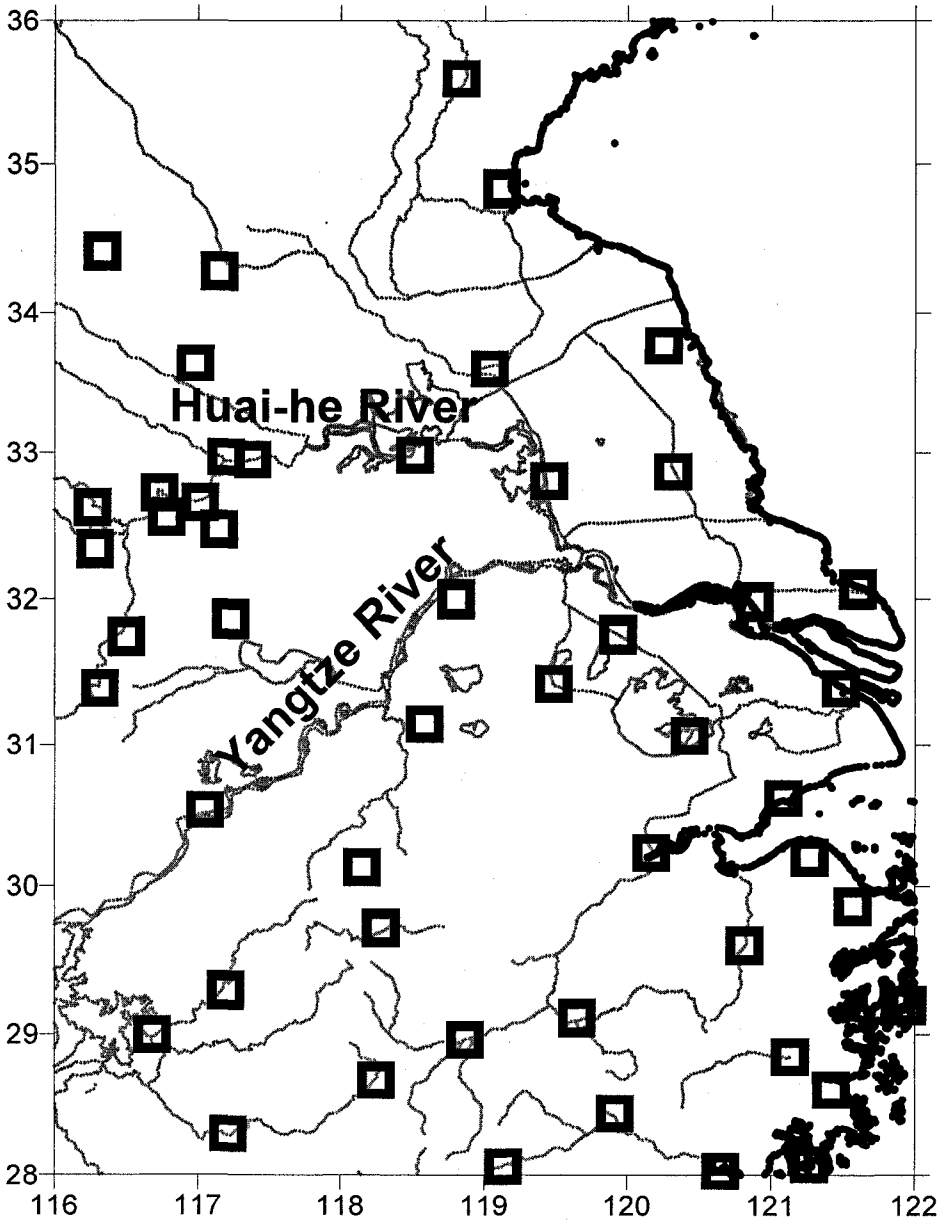

Figure B.4 - Location of rainfall gauge stations (squares) in the analysis region.

Rainfall Phase	Simulation	Mean Observed (mm/day)	Mean Simulated (mm/day)	Sim/Obs (%)	MAE (mm/day)	RMSE (mm/day)	Error Index
Heavy	AK-AK	**20.69**	**10.75**	**52**	**16.19**	**30.54**	**1.22**
	BM-BM	**20.69**	**24.26**	**117**	**23.81**	**48.61**	**0.66**
	FC-FC	**20.69**	**12.39**	**60**	**21.15**	**37.99**	**1.19**
	Gr-Gr	**20.69**	**21.46**	**104**	**25.42**	**54.59**	**0.63**
	KF-KF	**20.69**	**17.82**	**86**	**25.00**	**46.98**	**0.78**
Moderate	AK-AK	**11.42**	**7.30**	**64**	**13.21**	**22.41**	**1.19**
	BM-BM	**11.42**	**16.92**	**148**	**20.91**	**40.31**	**1.16**
	FC-FC	**11.42**	**20.62**	**181**	**20.82**	**34.33**	**1.31**
	Gr-Gr	**11.42**	**13.21**	**116**	**14.66**	**28.58**	**0.72**
	KF-KF	**11.42**	**9.72**	**85**	**14.16**	**25.47**	**0.82**
Light	AK-AK	**2.34**	**0.74**	**32**	**2.66**	**6.55**	**2.90**
	BM-BM	**2.34**	**4.40**	**188**	**5.75**	**11.55**	**1.67**
	FC-FC	**2.34**	**17.60**	**753**	**17.72**	**26.64**	**7.06**
	Gr-Gr	**2.34**	**4.71**	**202**	**5.53**	**8.12**	**1.69**
	KF-KF	**2.34**	**7.47**	**320**	**8.35**	**13.61**	**2.88**

Table B.2 - Error Statistics for simulations using the same CP scheme in both domains.

						HEAVY			Pave =	20.7 mm/day
		Error Index					Simulated/Observed Rainfall			
		Domain 2 CP Scheme (37 km)					Domain 2 CP Scheme (37 km)			
		AK	BM	FC	Gr	KF	AK	BM	FC	Gr	KF
Domain 1 CP Scheme (111 km)	AK	1.217	0.640	0.908	0.675	0.800	0.519	1.075	0.711	0.890	0.808
	BM	0.864	0.663	0.574	0.640	0.634	0.676	1.175	1.031	1.055	0.969
	FC	1.278	0.560	1.193	0.738	1.017	0.325	0.898	0.597	0.823	0.676
	Gr	1.185	0.701	0.705	0.635	0.758	0.524	1.320	0.877	1.039	0.855
	KF	0.983	0.518	0.702	0.690	0.781	0.616	1.056	0.933	0.911	0.862
						MODERATE			Pave =	11.4 mm/day
		Error Index					Simulated/Observed Rainfall			
		AK	BM	FC	Gr	KF	AK	BM	FC	Gr	KF
Domain 1 CP Scheme (111 km)	AK	1.186	1.296	1.179	0.681	0.733	0.639	1.752	1.635	1.050	0.861
	BM	2.551	1.156	1.136	0.623	0.770	0.325	1.482	1.606	1.049	0.839
	FC	1.259	1.130	1.314	0.672	0.828	0.561	1.617	1.810	1.074	0.842
	Gr	1.181	0.978	1.173	0.715	0.642	0.611	1.415	1.714	1.156	1.027
	KF	0.991	1.028	1.067	0.766	0.816	0.694	1.506	1.516	1.137	0.851
						LOW			Pave =	2.3 mm/day
		Error Index					Simulated/Observed Rainfall			
		AK	BM	FC	Gr	KF	AK	BM	FC	Gr	KF
Domain 1 CP Scheme (111 km)	AK	2.897	2.765	6.858	1.450	2.065	0.315	3.010	7.162	1.736	2.424
	BM	2.188	1.673	6.443	1.410	3.228	0.434	1.884	6.852	1.664	3.574
	FC	3.471	1.625	7.056	1.665	2.225	0.275	1.797	7.531	1.845	2.527
	Gr	2.086	2.427	6.547	1.690	2.656	0.432	2.679	6.845	2.015	3.039
	KF	1.355	1.623	8.198	1.709	2.884	0.654	1.757	8.581	1.964	3.196

Table B.3 - Summary of results based on Error Index and the ratio of total simulated to total observed rainfall over each of three rainfall phases.

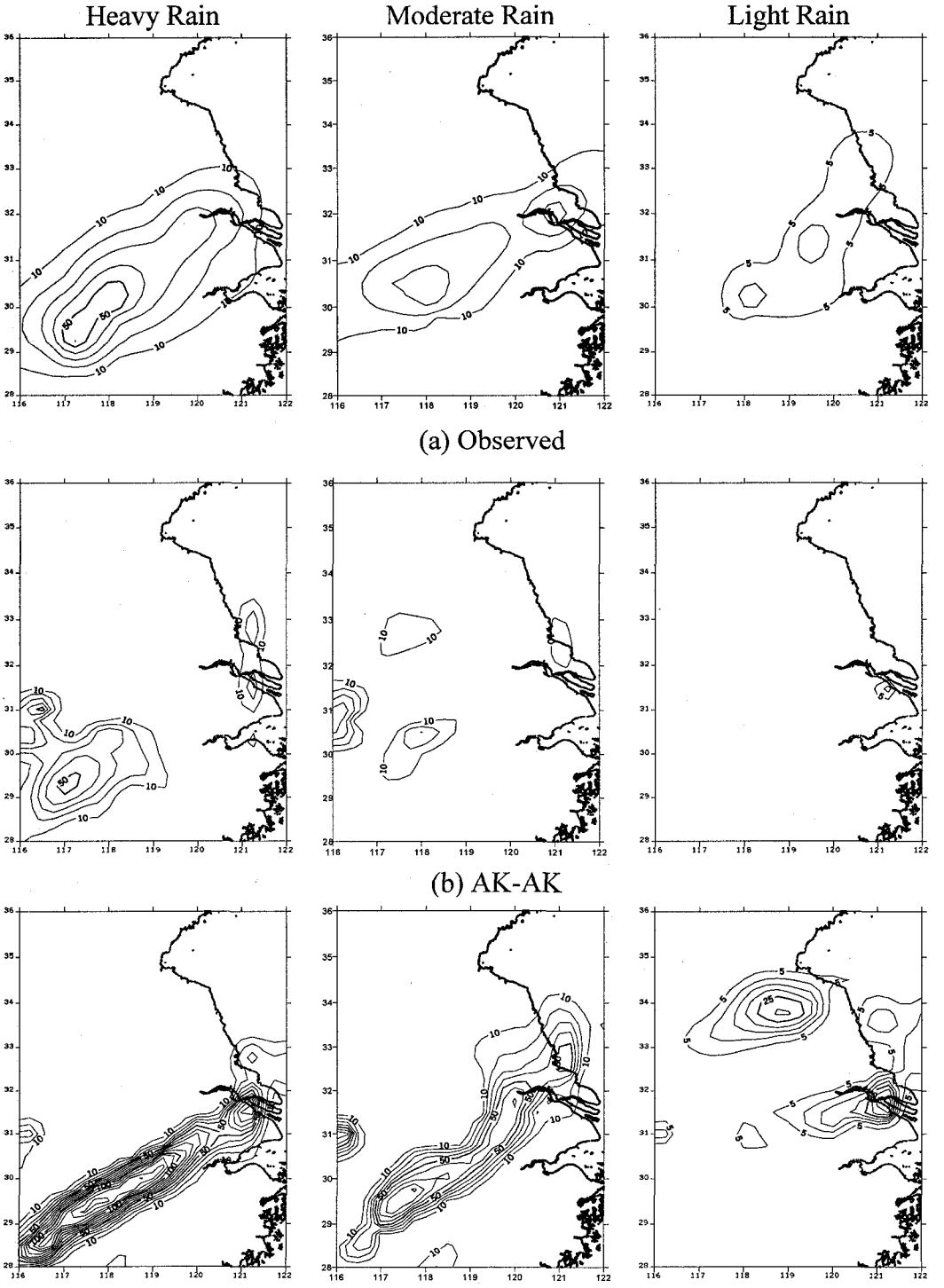
Heavy Rain
Moderate Rain
Light Rain
(a) Observed
(b) AK-AK
(c) BM-BM

Heavy Rain | Moderate Rain | Light Rain

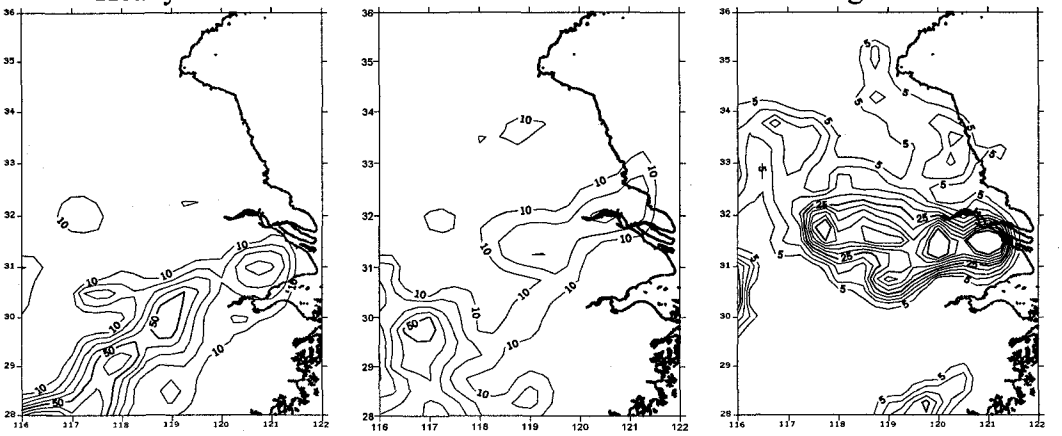

(d) FC-FC

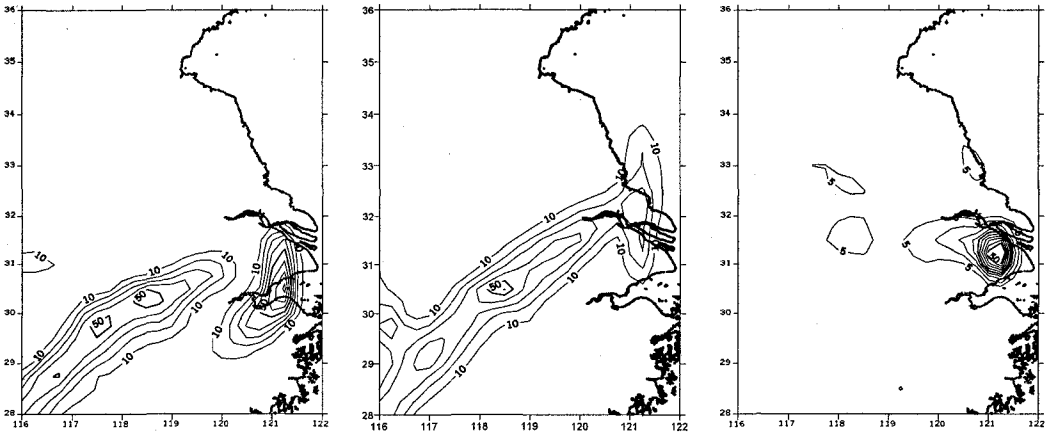

(e) Gr-Gr

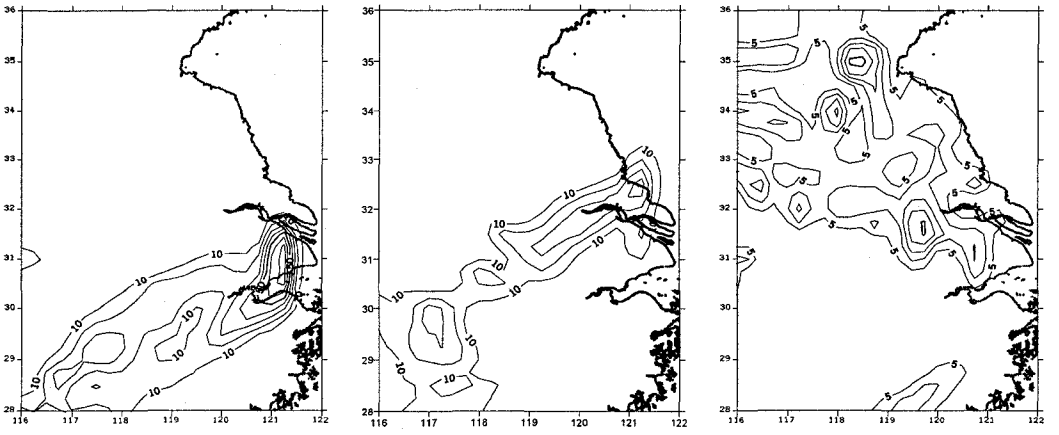

(f) KF-KF

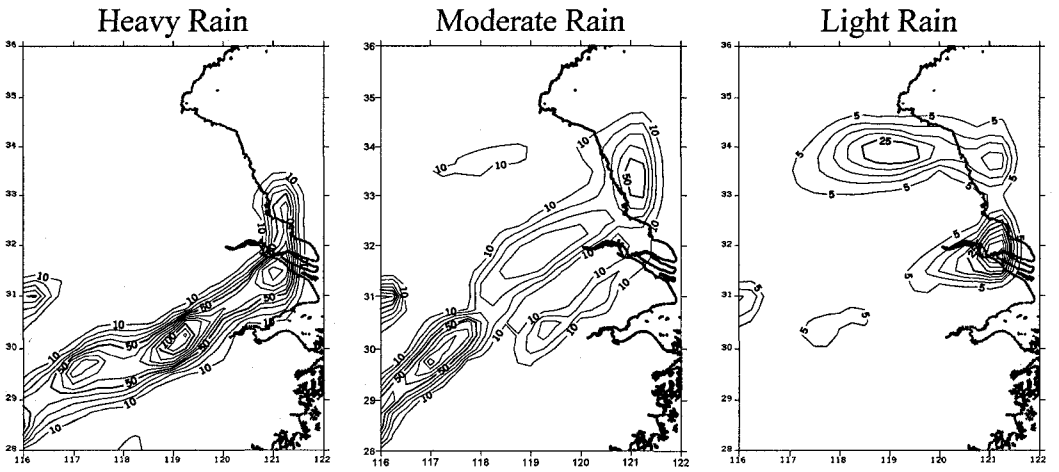

(g) FC-BM

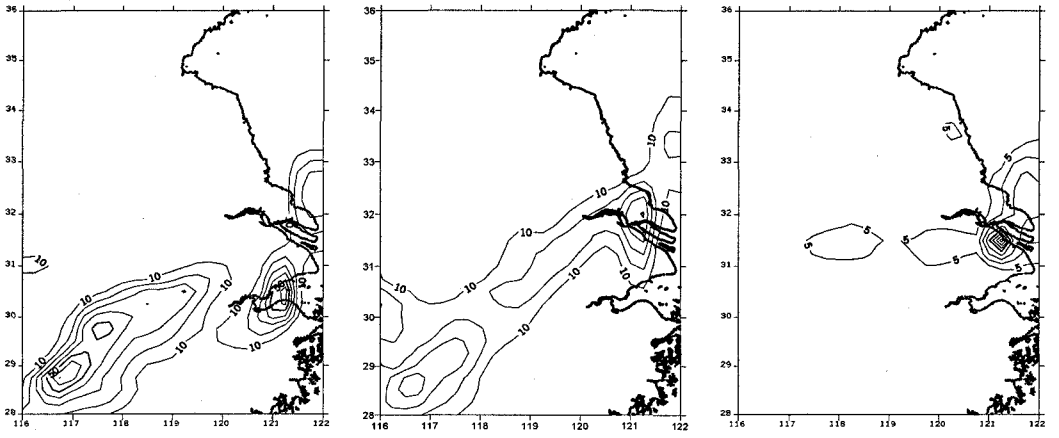

(h) BM-Gr

Figure B.5 - Rainfall patterns for (a) Observed station data, (b) AK-AK, (c) BM-BM, (d) FC-FC, (e) GR-Gr, (f) KF-KF, (g) FC-BM, and (h) BM-Gr. Heavy rainfall (hours 24-36) is on the left, moderate rainfall (hours 36-48) is in the middle, and light rainfall (hours 72-84) is on the right. Heavy and moderate rainfall contours are at 10 mm intervals and light rainfall contours are at 5 mm intervals.

B.6 Bibliography

Anderson, M.L., Z.Q. Chen, M.L. Kavvas, A. Feldman, (2002), Coupling HEC-HMS with Atmpospheric Models for Prediction of Watershed Runoff, *Journal of Hydrologic Engineering,* 7: 312-318.

Anthes, R.A., (1977), A Cumulus Parameterization Scheme utilizing a One-dimensional Cloud Model. *Monthly Weather Review,* 105, 270-286.

Anthes, R.A., and T.T. Warner. (1978). Development of Hydrodynamic Models Suitable for Air Pollution and other Mesometeorological Studies. *Monthly Weather Review* 106, 1045-1078.

Arakawa, A., and W.H. Schubert. (1974). Interaction of a cumulus cloud ensemble with the large-scale environment. Part 1. *Journal of the Atmospheric Sciences* 31: 674-701.

Arakawa, A. (1993). Closure Assumptions in the Cumulus Parameterization Problem, in, *The Representation of Cumulus convection in Numerical Models*, Emanuel KA, Raymond DJ (eds). American Meteorological Society: Boston; 1-15.

Betts, A.K., and M.J. Miller. (1986). A new convective adjustment scheme: Part II: Single column tests using GATE wave, BOMEX, ATEX and arctic air-mass data sets. *Quarterly Journal of the Royal Meteorological Society* 112: 693-709.

Dudhia, J., D. Gill, K. Manning, W. Wang, and C. Bruyere. (2004). *PSU/NCAR Mesoscale Modelling System Tutorial Class Notes and Users' Guide (MM5 Modelling System Version 3)*. National Center for Atmospheric Research: Boulder.

Emanuel, K.A. (1994). *Atmospheric Convection*, Oxford University Press: New York; 580.

Fritsch, J..M.., and C.F. Chappell, (1980). Numerical Prediction of convectively driven mesoscale pressure system. Part 1. *Journal of the Atmospheric Sciences* 37: 1722-1733.

Grell, G.A. (1993) Prognostic evaluation of Assumptions used by Cumulus Parameterizations. *Monthly Weather Review* 121: 765-787.

Grell, G.A., J. Dudhia, and D.R. Stauffer. (1995). *A Description of the Fifth-Generation Penn State/NCAR Mesoscale Model (MM5)*, NCAR Technical Note 398. National Center for Atmospheric Research: Boulder; 117.

Kain, J.S., and J.M. Fritsch. (1990). A one dimensional entraining/detraining plume model and its application in cumulus parameterization. *Journal of the Atmospheric Sciences* 47: 2784-2802.

Kain, J.S., and J.M. Fritsch. (1993) Convective Parameterization for Mesoscale Models: The Kain-Fritsch Scheme. In *The Representation of Cumulus convection in Numerical Models*, K.A. Emanuel, and D.J. Raymond (eds). American Meteorological Society: Boston; 165-170.

Kuo, H.L., (1965) On formation and intensification of tropical cyclone through latent heat release by cumulus convection. *Journal of the Atmospheric Sciences* 22: 456-475.

Liang, X.Z., and W.C. Wang, (1998) Associations between China monsoon rainfall and tropospheric jets. *Quart. J. Roy. Meteor. Soc.*, 124, 2597–2623.

Lau, K.M., and M.T. Li, (1984) The monsoon of east Asia and its global associations—A survey. *Bull. Amer. Meteor. Soc.*, 65, 114–125.

Matsumoto, J., (1998) Climatological study of heavy rainfall in East Asia during Baiu/Mei-yu Season. *International Symposium, Meso-scale Water Cycle and Heavy Rainfall in East Asia*, Nagoya, Japan. 11-14.

Mailhot, J., S. Bélair, R. Benoit, B. Bilodeau, Y. Delage, L. Fillion, L. Garand, C. Girard, and A. Tremblay. (1998) *Scientific Description of RPN Physics Library - Version 3.6*. Atmospheric Environment Service: Toronto; 188.

Molinari, J., (1993) An Overview of Cumulus Parameterization in Mesoscale Models. In *The Representation of Cumulus convection in Numerical Models*, Emanuel KA, Raymond DJ (eds). American Meteorological Society: Boston; 155-158.

Raymond, D.J., and K.A. Emanuel, (1993) The Kuo Cumulus Parameterization. In *The Representation of Cumulus convection in Numerical Models*, Emanuel KA, Raymond DJ (eds). American Meteorological Society: Boston; 165-170.

Reuter, G.W., (1986) A historical review of cumulus entrainment studies. *Bulletin of the American Meteorological Society* 67: 151-154.

Reuter, G.W., and M. Yau, (1987a) Mixing mechanisms in cumulus congestus clouds. Part I: Observations. *Journal of the Atmospheric Sciences* 44: 781-797.

Reuter, G.W., and M. Yau, (1987b) Mixing mechanisms in cumulus congestus clouds. Part II: Numerical simulations. *Journal of the Atmospheric Sciences* 44: 798-827.

Roebber, P.J., and G.W. Reuter, (2002) The sensitivity of precipitation to circulation details. Part II: Mesoscale modelling. *Monthly Weather Review* 130: 3-23.

Singh, V.P., (2002) Mathematical Modeling of Watershed Hydrology. *Journal of Hydrologic Engineering* 7: 270-292.

Stauffer, D.R., and N.L. Seaman, (1990) Use of Four-Dimensional Data Assimilation in a Limited-Area Mesoscale Model. Part I: Experiments with Synoptic Data. *Monthly Weather Review* 118: 1250-1277.

Wang, W., and N.L. Seaman, (1997) A Comparison Study of Convective Parameterization Schemes in a Mesoscale Model. *Monthly Weather Review* 125: 252-278.

Yu, Z., M.N. Lakhatakia, B. Yarnal, R.A. White, D.A. Miller, B. Frakes, E.J. Barron, C. Duffy, and F.W. Schwartz, (1999) Simulating the river-basin response to atmospheric forcing by linking a mesoscale meteorological model and hydrologic model system. *Journal of Hydrology* 218: 72-91.